

Laboratório
Nacional de
Computação
Científica

Programa de Pós Graduação em Modelagem Computacional

**Integrative Computational Modeling & In-vivo
Characterization of Residual Deformations in
Hemodynamics.**

Por

Gonzalo Damián Ares

PETRÓPOLIS, RJ - BRASIL

ABRIL DE 2016

INTEGRATIVE COMPUTATIONAL MODELING & IN-VIVO
CHARACTERIZATION OF RESIDUAL DEFORMATIONS IN
HEMODYNAMICS.

Gonzalo Damián Ares

TESE SUBMETIDA AO CORPO DOCENTE DA COORDENAÇÃO DE FORMAÇÃO
DE RECURSOS HUMANOS DO LABORATÓRIO NACIONAL DE COMPUTAÇÃO
CIENTÍFICA COMO PARTE DOS REQUISITOS NECESSÁRIOS PARA A
OBTENÇÃO DO GRAU DE DOUTOR EM MODELAGEM COMPUTACIONAL.

DOUTOR EM CIÊNCIAS

Aprovado por:

Prof. Pablo Javier Blanco, D.Sc. (PRESIDENTE)

Prof. Anne Marie Robertson, Ph.D.

Prof. Eduardo Alberto Fancello, D.Sc.

Prof. Antonio André Novotny, D.Sc.

Prof. Abimael Fernando Dourado Loula, D.Sc.

PETRÓPOLIS, RJ - BRASIL

ABRIL DE 2016

Ares, Gonzalo Damián

A681i Integrative Computational Modeling & In-vivo Characterization of Residual Deformations in Hemodynamics. / Gonzalo Damián Ares. Petrópolis, R.J. : Laboratório Nacional de Computação Científica, 2016.

xxvii, 155 p. : il.; 29.7 cm

Orientadores: Pablo Javier Blanco, Raúl Antonino Feijóo

Tese (D.Sc.) – Laboratório Nacional de Computação Científica, 2016.

1. preload analysis 2. fluid-structure interaction 3. 3D-1D coupling 4. residual deformations 5. arterial wall I. Blanco, Pablo Javier II. Feijóo, Raúl Antonino III. MCT/LNCC IV. Título

CDD - 612.118 1

Resumo da tese submetida à Coordenação de Pós-Graduação do Laboratório Nacional de Computação Científica - LNCC/MCTI como parte dos requisitos necessários para a obtenção do grau de Doutor em Ciências (D.Sc.)

INTEGRATIVE COMPUTATIONAL MODELING & IN-VIVO CHARACTERIZATION OF RESIDUAL DEFORMATIONS IN HEMODYNAMICS.

Gonzalo Damián Ares

Abril/2016

Orientadores: Pablo Javier Blanco, Diretor de Tese
Raúl Antonino Feijóo, Co-Diretor de Tese

Esta tese aborda dois problemas de relevância na modelagem do sistema cardiovascular humano. O primeiro tema consiste no desenvolvimento de um enfoque abrangente para a simulação do escoamento sanguíneo e sua interação com a parede arterial, e o segundo tópico é a caracterização in-vivo de tensões e deformações residuais na parede arterial baseada em dados fornecidos por imagens médicas.

De maneira específica, em relação ao primeiro tópico, um marco de modelagem é proposto para o tratamento de problemas hemodinâmicos com um alto grau de realismo, apresentando uma combinação de diferentes técnicas de modelagem para levar em conta i) o fato que as geometrias iniciais obtidas a partir de imagens médicas são correspondentes a um sistema de carregamentos não nulos, definido pela existência da pressão interna no lumen e de tensões axiais localizadas nos contornos artificiais do segmento arterial; ii) o problema de interação fluido-estrutura; iii) o complexo comportamento constitutivo da parede arterial; iv) a interação do segmento de interesse com o resto do sistema cardiovascular; e v) a influência dos tecidos circundantes; e vi) a existência de tensões residuais.

Para a abordagem das questões descritas acima, o problema mecânico de precarregamento é resolvido em uma primeira etapa, encontrando a configuração material de carregamento nulo onde as equações constitutivas são usualmente definidas. Isto é realizado encontrando a solução do problema de equilíbrio mecânico da estrutura arterial dada, considerando que o vaso está submetido a um nível de pressão de base e uma tração axial nos contornos artificiais. Vale a pena ressaltar que esta tração axial é correspondente a um nível de pre-estiramento previamente definido.

Uma vez que a configuração de referência é obtida, a simulação fluido-estrutura 3D é realizada, acoplada com um modelo dimensionalmente reduzido do resto do sistema cardiovascular. Um acoplamento forte através de iterações de ponto fixo é empregado para representar a interação fluido-estrutura, enquanto o acoplamento entre modelos dimensionalmente heterogêneos é conseguido usando um método tipo Broyden. Em relação à modelagem constitutiva, um modelo hiperelástico reforçado com fibras é considerado. Além disso, através da análise de vários exemplos numéricos, a sensibilidade com relação à existência de precarregamentos é quantificada para remarcar a relevância desta questão. Tais resultados indicam que o estado de tensão da parede arterial é fortemente influenciado pela existência de precarregamentos. Assim sendo, levar em consideração esse estado de precarga é fundamental para a predição de tensões no tecido arterial.

Em relação ao segundo tópico, um marco conceptual é apresentado para estimação

de tensões e deformações residuais. Consideramos que os dados são um conjunto de configurações de um segmento arterial, as quais poderiam ser obtidas a partir do uso de técnicas de aquisição e , processamento e segmentação de imagens. Utilizando um enfoque variacional, são apresentadas as equações de equilíbrio mecânico para as configurações conhecidas, acentuando o papel desempenhado pelas deformações residuais. Neste contexto, apresenta-se um funcional custo que mede o desbalance mecânico que é originado se um campo de deformações residuais inconsistente é admitido. Este funcional custo está baseado no resíduo generalizado das equações variacionais previamente mencionadas. Como consequência, o problema de estimação de deformações residuais é transformado em um problema de otimização, no qual se procura minimizar o funcional custo proposto. Com este objetivo, neste trabalho de tese são considerados dois métodos, um método de gradiente e um algoritmo de ponto interior para problemas que apresentam restrições.

A metodologia proposta é testada em três exemplos numéricos baseados em soluções manufaturadas: um barra engastada, um cilindro de parede grossa, e uma artéria aorta composta por três camadas. Os resultados obtidos são promissores e sugerem que o método apresentado (ou variantes baseadas nas ideias aqui mostradas) junto com técnicas adequadas para a aquisição de imagens podem conduzir à identificação in-vivo de deformações residuais.

Abstract of a thesis submitted to the Postgraduate Department of the National Laboratory for Scientific Computing - LNCC/MCTI as a partial fulfillment of the requirements for the degree of Doctor in Sciences (Ph.D.)

INTEGRATIVE COMPUTATIONAL MODELING & IN-VIVO CHARACTERIZATION OF RESIDUAL DEFORMATIONS IN HEMODYNAMICS.

Gonzalo Damián Ares

April/2016

Advisors: Pablo Javier Blanco, Thesis Advisor
Raúl Antonino Feijóo, Thesis Co-Advisor

This thesis is concerned with two major problems arising in the modeling of the cardiovascular system. The first topic consists in a comprehensive approach for the simulation of arterial blood flow and its effect on the stress state of the arterial wall, and the second topic is concerned with the in-vivo characterization of residual deformations in arterial wall tissues, based on data provided by medical images.

Specifically, regarding the first topic, an original modeling framework is proposed for the treatment of hemodynamic problems with increased realism, featuring a combination of several modeling techniques in order to account for i) the fact that the initial (image-based) geometry corresponds to a configuration which is at equilibrium with an internal pressure acting over the lumen, and with tethering forces located at the artificial (axial) boundaries delimiting the arterial region of interest; ii) the fluid-structure interaction problem; iii) the complex constitutive behavior of the arterial wall; iv) the influence of surrounding tissues; v) the interaction of the vessel with the rest of the cardiovascular system; and iv) the influence of residual stresses.

In order to tackle the issues described above, the preload mechanical problem is solved in a first stage, finding the zero-load material configuration which is employed to define suitable constitutive equations. This is performed by finding the solution for the mechanical equilibrium of the given image configuration considering the vessel at this state to be loaded by an internal baseline pressure and an axial traction (caused by tethering forces) at the artificial boundaries. It is worthwhile to mention that this axial traction is such that a previously defined pre-stretch level is considered on the equilibrium image configuration.

Once the reference configuration is obtained, the complete 3D fluid-structure interaction simulation is carried out, coupled with a dimensionally reduced 1D model of the rest of the cardiovascular system. Strong coupling via fixed-point iterations is achieved for the fluid-structure interaction, while the dimensionally heterogeneous coupling is achieved through a Broyden method. Regarding the constitutive modeling, a fiber-reinforced hyperelastic constitutive law is considered. Furthermore, through the analysis of several numerical examples, the sensitivity with respect to the existence of the preload stresses is assessed to quantify the importance of this issue. These results indicate that the stress state of the arterial wall is strongly influenced by the existence of preload. Therefore, the consideration of such preload state is mandatory for the prediction of stresses in arterial tissue.

For the second topic, a conceptual framework is presented for the in-vivo estimation

of residual deformations and stresses. As a given data, a set of known configurations for an arterial segment is considered, which can potentially be obtained from medical imaging techniques. The mechanical equilibrium equations corresponding to such configurations are introduced through a variational approach, highlighting the role of the residual deformations and associated stresses. In this context, a cost functional is proposed to measure the imbalance of the mechanical setting arising from the consideration of inconsistent residual deformations, based on the generalized residuals of the associated variational equations. Then, the characterization of residual deformations becomes an optimization problem, focused on the minimization of this cost functional. For this purpose, a simple gradient descent method and an interior-point algorithm for constrained optimization are explored in this work.

The proposed methodology is tested using three numerical examples based on manufactured solutions, a simple clamped bar, a thick-walled cylinder and a three-layered aorta artery. The obtained results are promising and suggest that the present method (or variants based on the present ideas), when coupled with adequate image acquisition techniques, could successfully lead to the in-vivo identification of residual deformations.

Acknowledgments

The realization of this work is result of a joint effort with my advisors, Pablo Blanco and Raúl Feijóo, and our collaborator Santiago Urquiza. I would like to thank them for the opportunity to work together, for the experience and knowledge shared, and for the constant orientation and support provided during the last years.

I would also like to remark that it would not have been possible to achieve results shown in this thesis without the experience acquired and tools developed in previous works performed in the HeMoLab group. I am thankful to be part of this group and I would like to acknowledge my colleges Rafael, Sansuke, Daniel, Paulo Trenhago, Paulo Ziemer, Eduardo, Carla, Igor, Felipe, Alonso, Lucas, Carlos and Gonzalo for our academic and non-academic discussions that constructed an excellent work environment.

Finally, from a personal point of view, I would like to dedicate a few words to those who accompanied and supported me through the development of this thesis. As most of them share my native language, the next lines are written in Spanish.

No me alcanzan las palabras para agradecer a mis padres, María Rosa y Gustavo, por su afecto, sus consejos y su completo apoyo en todos los desafíos que he decidido encarar. Me gustaría agradecer a mi familia y amigos en Argentina, que me han acompañado a la distancia, y que cada vez que vuelvo a Mar del Plata me hacen sentir como si nunca me hubiese ido. Quiero destacar que mi estadía en Petrópolis me ha dejado algo que valoro aún más que los logros profesionales, estoy feliz por haber conocido aquí a un gran grupo de amigos: Lito, Lis, Goga, Camila, Maru, Pablo, Lucas y Wenddi.

Las últimas palabras son para agradecer el apoyo, la paciencia y el amor de mi esposa Carla, que estuvo a mi lado en cada paso de este trayecto, encarando una nueva vida juntos en otro país. Es a ella a quien dedico esta tesis.

GONZALO ARES
MARCH 2016, PETRÓPOLIS - RJ

A Carla

Contents

Acknowledgements	ix
List of Figures	xv
List of Tables	xviii
List of Symbols	xix
1 Introduction	1
1.1 Motivation	1
1.2 State of the art	2
1.3 Objectives	10
1.4 Contributions	10
1.5 Scientific production	11
1.6 Structure of the thesis	12
2 Continuum mechanics models	13
2.1 Introduction	13
2.2 Solid mechanics at finite strains	13
2.3 Fluid mechanics in deformable domains	26
2.4 Dimensionally reduced models	28
3 Integration of hemodynamic models	33
3.1 Introduction	33
3.2 Initially loaded state	33
3.3 External tissue support	34
3.4 Fluid-structure interaction	35
3.5 Dimensionally heterogeneous models	38
3.6 Constitutive modeling	42
3.7 Residual deformations	43
3.8 Numerical approximations	44
4 Applications in computational hemodynamics	51
4.1 Introduction	51
4.2 Problem 1: straight pipe	51
4.3 Problem 2: carotid bifurcation	63
4.4 Problem 3: patient-specific common carotid	68
4.5 Problem 4: aneurysm at the middle cerebral artery	74
4.6 Discussion	79

5	In-vivo characterization of residual deformations	87
5.1	Introduction	87
5.2	Mechanical setting	89
5.3	Recoverable residual deformation characterization problem	93
5.4	Optimization methods	98
5.5	Sensitivity analysis	103
6	Characterization of residual deformations: numerical examples	109
6.1	Introduction	109
6.2	Clamped bar (1D)	109
6.3	Thick-walled cylinder	115
6.4	Three-layered arterial wall	125
6.5	Discussion	140
7	Conclusion	141
7.1	Integrative modeling framework	141
7.2	Characterization of residual deformations	142
7.3	Future work	142
8	Appendices	145
8.1	Appendix A: basic relations in continuum mechanics	145

List of Figures

1.1	Illustrative representation of the interaction of an arterial segment with the rest of the cardiovascular system	2
1.2	Diagram of the major components of an elastic artery	4
1.3	Representative scheme for the in-vivo, zero-load and virtual configurations	6
1.4	Representative scheme introducing the residual deformation decomposition concept	7
2.1	Mechanical equilibrium setting, displaying the load-free and stress-free material configuration Ω_m and the spatial (equilibrium) configuration Ω_s subjected to the load state \mathbf{t}_s in $\partial\Omega_s^N = \partial\Omega_s^W \cup \partial\Omega_s^E \cup \partial\Omega_s^A$	15
2.2	ALE kinematic setting.	26
2.3	Setting for one dimensional model of fluid flow in a vessel.	29
2.4	Windkessel terminal model, electrical analogy.	30
3.1	Graphical example for the treatment of initially loaded vessel geometries extracted from medical images.	34
3.2	Local analysis of external loads in the arterial wall	35
3.3	Fluid-structure iterative coupling scheme	38
3.4	Representations of dimensionally reduced hemodynamic components.	39
3.5	Scheme representing the interaction between black-box components	40
3.6	Auxiliary domain extensions for the determination of tethering forces	44
3.7	Strategy (iii), application of pre-computed tethering forces in the preload problem.	45
3.8	Discretization of the interface between the arterial wall and blood flow domains	49
4.1	Representation of the helicoidal arrangement of collagen fibers	53
4.2	Straight pipe example: summary of results for scenario (a)	56
4.3	Straight pipe example: transmural stress state for scenario (a)	56
4.4	Straight pipe example: blood flow dynamics	57
4.5	Straight pipe example: velocity profile for different scenarios	58

4.6	Distribution of circumferential (top), axial (middle) and von Mises (bottom) stresses at systole along the thickness of the arterial wall for the proposed scenarios -(a) black, (b) blue, (c) red, (d) green, (e) magenta, (f) cyan).	59
4.7	Straight pipe example: difference of stresses between systole and diastole for scenarios (a) and (d)	62
4.8	Carotid bifurcation example: arterial wall mesh	64
4.9	Carotid bifurcation example: computation of material configurations	65
4.10	Carotid bifurcation example: computed stresses for scenarios (a) and (b)	66
4.11	Carotid bifurcation example: through thickness stress distribution at different points for scenarios (a) and (b)	67
4.12	Carotid bifurcation example: velocity profiles for scenarios (a) and (b) at $t = 0.235T$	68
4.13	Carotid bifurcation example: blood flow dynamics results	69
4.14	Common carotid example: image-based fluid and solid domains, discretization and collagen orientation	70
4.15	Common carotid example: computation of material configurations	71
4.16	Common carotid example: stress state at the arterial wall for scenarios (a) and (b)	72
4.17	Common carotid example: relative discrepancy of von Mises stresses between scenarios (a) and (b)	72
4.18	Common carotid example: through thickness stress distribution at different points for scenarios (a) and (b)	73
4.19	Common carotid example: axial stretch at baseline configuration for scenarios (a) and (b)	74
4.20	Common carotid example: comparison of velocity profiles between scenarios (a) and (b)	75
4.21	Common carotid example: blood flow dynamics results	76
4.22	Cerebral aneurysm example: wall thinning ratio concept	77
4.23	Cerebral aneurysm example: arterial wall and fluid meshes	77
4.24	Cerebral aneurysm example: orientation of collagen fibers	77
4.25	Cerebral aneurysm example: highlight of highly curved regions	78
4.26	Cerebral aneurysm example: auxiliary extension domains	78
4.27	Cerebral aneurysm example: computation of material configurations	79
4.28	Cerebral aneurysm example: von Misses equivalent stress field at systole for scenarios (a) and (b).	80

4.29	Cerebral aneurysm example: discrepancy of the von Misses stress between scenarios (a) and (b)	80
4.30	Cerebral aneurysm example: discrepancy of the von Misses equivalent stress field between scenarios (a) and (b) (aneurysm neck and sack)	81
4.31	Cerebral aneurysm example: through thickness stress distribution at different points for scenarios (a) and (b)	82
4.32	Cerebral aneurysm example: axial stretch at baseline configuration for scenarios (a) and (b)	83
4.33	Cerebral aneurysm example: blood flow dynamics results	84
5.1	Problem setting for <i>in-vivo</i> residual stress characterization.	91
5.2	Extended problem setting for <i>in-vivo</i> residual deformation characterization with multiple known configurations	96
6.1	Setting for the clamped bar 1D problem	110
6.2	Clamped bar example: results summary for the RRD characterization problem	114
6.3	Thick-walled cylinder example: objective residual deformations and stresses .	118
6.4	Thick-walled cylinder example: results for the mechanical problem	119
6.5	Thick-walled cylinder example: functional minimization	121
6.6	Thick-walled cylinder example: residual stress results	123
6.7	Thick-walled cylinder example: residual deformation results	124
6.8	Three-layered aorta example: coordinate system and related geometries for the individual layers in their virtual and material configurations	128
6.9	Three-layered aorta example: target residual stresses and deformations	129
6.10	Three-layered aorta example: principal stretches shaping the IPA of the target RRD	130
6.11	Three-layered aorta example: RS fields associated with the IPA of the target RRD	131
6.12	Three-layered aorta: Numerical solution of the forward mechanical problem. .	132
6.13	Three-layered wall example: resulting residual deformations for the three finite elements approximation	135
6.14	Three-layered wall example: resulting residual stresses for the three finite elements approximation	136
6.15	Three-layered wall example: resulting residual deformations for the three finite elements approximation	138
6.16	Three-layered wall example: resulting stresses deformations for the three finite elements approximation	139

List of Tables

1.1	Summary of main contributions on key topics related to hemodynamic modeling	9
4.1	Straight pipe example: description of modeling scenarios	53
4.2	Material properties considered in the numerical simulation of the carotid artery	54
4.3	Straight pipe example: results overview displaying geometrical landmarks for different configurations	58
4.4	Straight pipe example: stress state comparison between scenarios	60
4.5	Straight pipe example: stress state comparison between scenarios (a) and (d), difference between systolic and baseline stresses	60
6.1	Thick-walled cylinder example: identification error summary.	125
6.2	Summary of geometrical parameters employed for the three-layered vessel wall	127
6.3	Summary of material parameters for three-layered wall example	129
6.4	Three-layered aorta example: geometrical landmarks.	133
6.5	Three-layered aorta example: summary of results corresponding to the 3 finite elements approximation	133
6.6	Three-layered wall example: summary of results corresponding to the 8 finite elements approximation	137

List of Symbols

Chapter 1

Ω_{iv}	In-vivo loaded configuration
Ω_0	Zero-load configuration
Ω_{iso}	Zero-load isolated configuration
Ω_v	Virtual zero-stress configuration
\mathbf{u}	Displacement field mapping Ω_0 into Ω_{iv}
\mathbf{v}_{st}	Displacement field mapping Ω_{iso} into Ω_0
$\boldsymbol{\sigma}$	Stress state at Ω_{iv}
$\boldsymbol{\sigma}^r$	Residual stress
$\boldsymbol{\sigma}_{tet}$	Tethering stress
\mathbf{F}^r	Residual deformation
\mathbf{F}_{st}^r	Residual deformation, prestretch component
\mathbf{F}_d^r	Residual deformation, non prestretch component
\mathbf{F}^u	Deformation associated to \mathbf{u}

Chapter 2

Solid mechanics

Ω_s	Spatial (equilibrium) configuration
Ω_m	Material (reference) configuration
$\partial\Omega_j$	Boundary of configuration Ω_j , $j = m, s$
$\partial\Omega_j^D$	Dirichlet boundary of configuration Ω_j , $j = m, s$
$\partial\Omega_j^N$	Neumann boundary of configuration Ω_j , $j = m, s$
$\partial\Omega_j^E$	External boundary of configuration Ω_j , $j = m, s$
$\partial\Omega_j^{A,i}$	Artificial boundaries of configuration Ω_j , $j = m, s$, $i = 1, \dots, C$
$\partial\Omega_{m/s}^W$	Fluid-solid interface
C	Number of artificial boundaries
\mathbf{x}_s	Points in Ω_s
\mathbf{x}_m	Points in Ω_m
χ_m	Diffeomorphic mapping relating configurations Ω_s and Ω_m
$(*)_s$	Field $(*)$ expressed in terms of \mathbf{x}_s
$(*)_m$	Field $(*)$ expressed in terms of \mathbf{x}_m
$(*)^k$	Field $(*)$ at k th iteration within an iterative process
$(\hat{*})$	Admissible variation associated to field $(*)$
$\delta(*)$	Increment in field $(*)$
\mathbf{u}	Displacement field mapping Ω_m into Ω_s
λ	Lagrange multiplier (associated to the incompressibility constraint)
$\boldsymbol{\varepsilon}(*)$	Symmetric gradient of the field $(*)$
\mathbf{F}	Deformation gradient tensor associated to \mathbf{u}

E	Green-Lagrange strain tensor
C	Left Cauchy-Green strain tensor
B	Right Cauchy-Green strain tensor
\mathcal{U}_s	Linear manifold of kinematically admissible functions for \mathbf{u} in Ω_s
\mathcal{V}_s	Linear manifold of kinematically admissible variations associated to \mathcal{U}_s
\mathcal{L}_s	Linear manifold of admissible functions for λ in Ω_s
\mathcal{W}_s	Hilbert space of regular functions compatible with defined operations
t	Generalized traction vector
\mathbf{t}_s^W	Traction acting at $\partial\Omega_s^W$
\mathbf{t}_s^E	Traction acting at $\partial\Omega_s^E$
$\mathbf{t}_s^{A,i}$	Traction acting at $\partial\Omega_s^{A,i}$
\mathbf{n}_s	Unit vector normal to $\partial\Omega_s$
\mathbf{n}_0	Unit vector normal to $\partial\Omega_m$
P	Orthogonal projection operator
$\boldsymbol{\sigma}$	Cauchy stress tensor
S	Second Piola-Kirchhoff stress tensor
\mathcal{M}_s	Bilinear operator associated to the equilibrium equation in Ω_s
\mathcal{N}_s	Linear operator associated to the mass conservation equation in Ω_s
\mathcal{M}_m	Bilinear operator associated to the equilibrium equation in Ω_m
\mathcal{N}_m	Linear operator associated to the mass conservation equation in Ω_m
d_s, e_s, g_s, f_s, h_s	Linear and bilinear forms defining the linearized preload problem
a_m, b_m, l_m, c_m, m_m	Linear and bilinear forms defining the linearized forward problem (expressed in terms of \mathbf{x}_m)
a_s, b_s, l_s, c_s, m_s	Linear and bilinear forms defining the linearized forward problem (expressed in terms of \mathbf{x}_s)
H	Linear operator, defined in (2.2.50)
D_s	Constitutive tangent operator, defined in (2.2.29)
I	Second order identity tensor
II	Fourth order identity tensor
α_{in}	Non-dimensional ratio between inertial and circumferential forces
ρ_w	Density of the arterial wall
r_i	Inner radius of a vessel (in-vivo configuration)
Δr_i	Inner radius variation (in-vivo configuration)
T_p	Time to achieve peak pressure from diastole
h	Arterial wall thickness (in-vivo configuration)

Fluid mechanics

Υ_0	Blood flow reference domain
Υ_t	Blood flow domain at given time t
$\partial\Upsilon$	Blood flow domain boundary
$\partial\Upsilon^{A,i}$	Blood flow domain, inflow/outflow artificial boundaries
$\partial\Upsilon^W$	Blood flow domain boundary, interface with arterial wall
\mathbf{x}_t	Points in Υ_0
\mathbf{x}_0	Points in Υ_t
d	Displacement field mapping Υ_0 into Υ_t
v	Fluid velocity field
p	Fluid pressure field (Lagrange multiplier)

$(*)_t$	Field $(*)$ expressed in terms of \mathbf{x}_t
$(*)_0$	Field $(*)$ expressed in terms of \mathbf{x}_0
$(*)^k$	Field $(*)$ at k th iteration
$(\hat{*})$	Admissible variation associated to field $(*)$
$\delta(*)$	Increment in field $(*)$
\mathbf{F}_t^A	Deformation gradient tensor associated to \mathbf{d}
\mathcal{U}_t	Linear manifold of kinematically admissible functions for \mathbf{v} in Υ_t
\mathcal{V}_t	Linear manifold of kinematically admissible variations associated to \mathcal{U}_t
\mathcal{P}_t	Linear manifold of kinematically admissible functions for p in Υ_t
\mathcal{D}_t	Linear manifold of kinematically admissible functions for the lumen displacement defined in Υ_t
$\mathcal{D}_k^*, \mathcal{U}_k, \mathcal{V}_k, \mathcal{P}_k, \mathcal{D}_k$	Counterparts of $\mathcal{D}_t^*, \mathcal{U}_t, \mathcal{V}_t, \mathcal{P}_t, \mathcal{D}_t$ at the k th iteration
$\bar{\boldsymbol{\sigma}}$	Deviatoric component of the Cauchy stress tensor
t	Given time instant
t_0	Time instant corresponding to reference configuration Υ_0
μ	Dynamic viscosity
\mathbf{v}_R	Velocity of the frame of reference
ρ	Fluid density

Dimensionally reduced models

One dimensional fluid flow model	
t	Given time instant
x	Coordinate along the axis of the vessel
$A(x, t)$	Cross-sectional lumen area
$R(x, t)$	Vessel radius
$Q(x, t)$	Flow rate
$P(x, t)$	Mean pressure
v_x	Axial component of the velocity field
$v(x, t)$	Mean value of v_x in $A(x, t)$
α	Convective acceleration parameter
Arterial junction models	
N_T	Number of converging segments in a junction
Q_i	Flow rate for the i th converging segment in a junction
P_i	Pressure for the i th converging segment in a junction
Arterioles and capillaries	
R_1, R_2, C	Parameters characterizing the behavior of a Windkessel element
P_{te}	Pressure at terminal point
P_r	Low pressure reference
Venous system and pulmonary circulation	
R, L, C	Resistance, inertance and compliance of a compartment
$(P_i, Q_i), (P_o, Q_o)$	Pairs of pressure and flow rate at the input and output of a compartment
P_{ex}	External pressure

Cardiac model: heart and valves	
P_{ex}	External pressure
P_{ch}, V_{ch}	Pressure and volume of a cardiac chamber
$V_{0,ch}$	Dead volume of a cardiac chamber
α_{ch}	Viscoelastic pressure-volume relation parameter
$e(t)$	Variation of elastance normalized function
$T_{vc}, T_{ac}, T_{vr}, T_{ar}$	Contraction and relaxation periods (ventricles and atria)
t_{ac}, t_{ar}	Starting times for contraction and relaxation (ventricles and atria)
L, R, B	Inertance of the fluid, viscous resistance and parameter accounting for flow separation phenomena
P_i, P_o	Input and output pressures
Θ	Coefficient accounting for non-binary valve response
$\theta, \theta_{min}, \theta_{max}$	Valve opening angle with minimum and maximum values
I, k_f, k_p, k_Q, k_V	Parameters controlling the opening angle of cardiac valves

Chapter 3

Initially loaded configuration

Ω_{base}	Arterial wall baseline configuration
Ω_m	Arterial wall material configuration
$\partial\Omega_{base}$	Arterial wall baseline configuration boundary
$\partial\Omega_{base}^W$	Arterial wall baseline configuration boundary, interface with fluid

External tissue support

$\partial\Omega_{base}^E$	Arterial wall baseline configuration boundary, external contour
\mathbf{t}_s^E	Traction acting at $\partial\Omega_{base}^E$
k_e	Effective elastic parameter
k_v	Effective viscoelastic parameter
\mathbf{u}_0	Reference displacement
σ_{tet}	Tethering stress

Fluid structure interaction

σ_s	Cauchy stress, solid domain
σ	Cauchy stress, fluid domain
Q_i	Flow rate at i th artificial boundary
C	Number of coupling points
\mathbf{n}^i	Normal unit vector at i th fluid artificial boundary
ι, n_s	Parameters controlling the gradual load application
κ_a, κ_b	Subrelaxation parameters

Dimensionally heterogeneous coupling

Coupling equations	
DR	Dimensionally reduced component
SV	Specific-vessel component
$\mathbf{Q}_{DR}, \mathbf{Q}_{SV}$	Vectors containing the flow rate at each bond
$\mathbf{P}_{DR}, \mathbf{P}_{SV}$	Vectors containing the normal traction at each bond
\mathbf{P}, \mathbf{Q}	Vectors containing coupling variables at each bond
t_t^i	Normal traction at i th artificial boundary
$\mathcal{R}_{DR}, \mathcal{R}_{SV}$	Residuals for coupling equations

Broyden algorithm	
\mathbf{z}	Vector grouping coupling variables \mathbf{P} and \mathbf{Q}
$\mathcal{R}(\mathbf{z})$	Generalized residual containing \mathcal{R}_{DR} and \mathcal{R}_{SV}
ϵ, ϵ_{abs}	Relative and absolute tolerances for the Broyden algorithm
\mathbf{B}	Jacobian matrix
$\Delta\mathbf{z}$	Solution update
ς	Perturbation for the computation of \mathbf{B}

Constitutive models

Ψ	Strain energy function
$c_{elast}, k_1, k_2, \lambda_i^0$	Parameters for transversely isotropic material
k_{del}, k_x	Parameters for isotropic exponential material
\mathbf{a}_i	Unit vector indicating orientation of i th family of collagen fibers
I_1, I_4, I_6	Invariants of the Cauchy-Green strain tensor
P, R, h_w, A	Pressure, radius, thickness and cross-sectional (1D model)
E_e, K	Effective Young's modulus and effective viscosity (1D model)

Numerical approximations

$\Omega_{base,aux}$	Baseline configuration of auxiliary domains
$\Omega_{base,aux}$	Material configuration of auxiliary domains
$\mathcal{U}^h, \mathcal{P}^h$	Manifolds approximating \mathcal{U} and \mathcal{P} , spanned by finite element shape functions
φ_l	Finite element shape function corresponding to the l th node of a mesh
ϕ_i	Vectorial functions constructed from finite element shape functions
\mathbf{u}^h	Approximated displacement field
λ^h	Approximated Lagrangian field
U	Vector condensing unknowns related to the displacement field
P	Vector condensing unknowns related to the Lagrangian field
$\mathbf{A}, \mathbf{A}^*, \mathbf{B}, \mathbf{C}, \mathbf{D},$ L, M	Building blocks of the system of equations corresponding to the discretized and linearized problems
γ	Zero-order preconditioning parameter
h	Characteristic length of a finite element
ν	Stabilization parameter for the solid problems
θ	Time integration parameter
$\mathcal{V}_k^h, \mathcal{P}_k^h, \mathcal{D}_k^h$	Discrete approximations of the spaces $\mathcal{V}_k, \mathcal{P}_k$ and \mathcal{D}_k
$\mathcal{B}_v, \mathcal{B}_p, \mathcal{B}_d$	Basis of the discrete manifolds $\mathcal{V}_k^h, \mathcal{P}_k^h$ and \mathcal{D}_k^h
N_E^f	Number of tetrahedral finite elements, fluid domain
N_T^f	Number of nodes, fluid domain
$\boldsymbol{\psi}$	Vectorial fields constructed based on linear finite element shaped functions and an additional "bubble" shape function
$\mathbf{v}^h, p^h, \mathbf{d}^h$	Discrete fields approximating \mathbf{v}, p and \mathbf{d}
V, P, D	Vectors condensing unknowns of the discretized Navier-Stokes problem
ϱ	Artificial compressibility parameter for the regularization of the incompressible Navier-Stokes problem
τ_{up}	Upwinding coefficient
Pe	Peclet number

Chapter 4

p_t	Pressure at time t
p^{base}	Baseline pressure
p_t^{rel}	Relative pressure at time t
\mathbf{x}^{base}	Points in Ω_{base}
\mathbf{u}^{base}	Displacement field mapping Ω_m into Ω_{base}
\mathbf{F}^{base}	Deformation gradient tensor associated to \mathbf{u}^{base}
\mathbf{C}^{base}	Cauchy-Green strain tensor associated to \mathbf{u}^{base}
Δt	Time step size
T	Cardiac period
σ_{vm}	Von Mises equivalent stress
$\Delta \boldsymbol{\sigma}$	Difference between systolic and diastolic stresses
λ_C	Prestretch level
r_i, l, e	Internal radius, length and thickness of the arterial wall
β	Characteristic angle of the collagen fiber arrangement
S_1, S_2, S_3	Principal stresses
$\mathcal{S}_1, \mathcal{S}_2, \mathcal{S}_3, \mathcal{S}_4$	Transversal curves (defined for each example)
WTR	Wall thinning ratio

Chapter 5

Recoverable residual deformation characterization problem

Ω_a	Known configuration
Ω_b^j	Known configurations, $j = 1, \dots, N_B$
N_B	Number of known configurations (additional to Ω_a)
Ω_m	Material configuration
Ω_v	Virtual configuration
Γ_a	Boundaries of Ω_a
Γ_a^N	Neumann boundary of Ω_a
Γ_a^D	Dirichlet boundary of Ω_a
Γ_b^j	Boundaries of configurations Ω_b^j
$\Gamma_b^{N,j}$	Neumann boundaries of configurations Ω_b^j
$\Gamma_b^{D,j}$	Dirichlet boundaries of configurations Ω_b^j
Γ_m^D	Dirichlet boundary of Ω_m
\mathbf{v}	Displacement field mapping Ω_m into Ω_a
\mathbf{u}^j	Displacement field mapping Ω_m into Ω_b^j
\mathbf{w}^j	Displacement field mapping Ω_a into Ω_b^j
$\mathbf{x}_v, \mathbf{x}_m, \mathbf{x}_a, \mathbf{x}_b^j$	Points in domains $\Omega_v, \Omega_m, \Omega_a$ and Ω_b^j
$(*)_m$	Field $(*)$ expressed in terms of \mathbf{x}_m
$(*)_a$	Field $(*)$ expressed in terms of \mathbf{x}_a
$(*)_b$	Field $(*)$ expressed in terms of \mathbf{x}_b^j
\mathbf{F}^r	Residual deformation field
$\mathbf{F}^v, \mathbf{F}^{u^j}, \mathbf{F}^{w^j}$	Deformation gradients associated to displacements $\mathbf{v}, \mathbf{u}^j, \mathbf{w}^j$
$\mathbf{F}^{vr}, \mathbf{F}^{u^j r}, \mathbf{F}^{w^j r}$	Total deformation tensors, composition of \mathbf{F}^r with $\mathbf{F}^v, \mathbf{F}^{u^j}$ and \mathbf{F}^{w^j}
\mathbf{C}^i	Cauchy-Green strain tensor related to the deformation field \mathbf{F}^i ($i = r, v, u^j, w^j, vr, u^j r, w^j r$)

\mathbf{S}^i	Second Piola Kirchhoff stress tensor related to the deformation field \mathbf{F}^i ($i = r, \mathbf{v}, \mathbf{u}^j, \mathbf{w}^j, \mathbf{v}r, \mathbf{u}^j r, \mathbf{w}^j r$)
$\boldsymbol{\sigma}_k^i$	Cauchy stress tensor related to the deformation field \mathbf{F}^i ($i = r, \mathbf{v}, \mathbf{u}^j, \mathbf{w}^j, \mathbf{v}r, \mathbf{u}^j r, \mathbf{w}^j r$), transported to configuration Ω_k ($k = m, a, b$) using a Piola transformation
p_a, p_b^j	Pressures acting at Γ_a^N and $\Gamma_b^{N,j}$
$\mathbf{n}_a, \mathbf{n}_b^j$	Unit normal vectors in Γ_a and Γ_b^j
$\mathcal{V}_m, \mathcal{V}_a, \mathcal{V}_b^j$	Manifolds of kinematically admissible variations defined in $\Omega_m, \Omega_a, \Omega_b^j$
Kin_a	Manifold of kinematically admissible displacements defined in Ω_a
$\mathcal{R}_m, \mathcal{R}_{b,j}$	Generalized residuals associated to equilibrium equations corresponding to Ω_m and Ω_b^j
Φ_i	i -th element of a basis of \mathcal{V}_a
$\mathbf{R}_m, \mathbf{R}_{b,j}$	Vectors containing the dual product of the generalized residuals $\mathcal{R}_m, \mathcal{R}_{b,j}$ with each element of a basis of \mathcal{V}_a
$\mathcal{F}(\tilde{\mathbf{F}}_a^r, \tilde{\mathbf{v}}_a)$	Proposed cost functional
η_m, η_b^j	Weighting factors for cost functional \mathcal{F}
$\tilde{\mathbf{F}}_a^r$	Arbitrary residual deformation field
$\tilde{\mathbf{v}}_a$	Arbitrary displacement field
\mathbf{D}	Space of all tensor fields $\tilde{\mathbf{F}}_a^r$ associated with RRDs defined in Ω_a with positive determinant
$\check{\mathbf{v}}_a$	Displacement field obtained as solution of the equilibrium equation for Ω_a given $\tilde{\mathbf{F}}_a^r$
$\mathcal{J}(\tilde{\mathbf{F}}_a^r)$	Proposed cost functional

Optimization methods

\mathbf{D}^h	Finite space approximating \mathbf{D}
$\mathcal{B}_{\mathbf{D}}$	Basis for \mathbf{D}^h
ω_i	i th element of the basis $\mathcal{B}_{\mathbf{D}}$
\mathbf{F}^h	Approximation of \mathbf{F}^r in the space \mathbf{D}^h
\boldsymbol{x}	Linear combination coefficients defining \mathbf{F}^h
$\mathcal{J}(\boldsymbol{x})$	Proposed cost functional expressed in terms of \boldsymbol{x}
Φ_{ij}	Matrix in $\mathbb{R}^{3 \times 3}$
ω_{ij}^e	Element of the basis $\mathcal{B}_{\mathbf{D}}$ for a piecewise constant approximation
Gradient descent method	
$\vartheta, \gamma, \Delta^{MAX}, tol^j$	Parameters controlling the gradient descent method
Interior-point method	
$\mathcal{H}(\boldsymbol{x})$	Functional incorporating equality constraints
$\mathcal{G}(\boldsymbol{x})$	Functional incorporating inequality constraints
v	Barrier parameter
\boldsymbol{s}	Vector of sack variables
\mathcal{L}	Lagrangian form of the barrier subproblem
$\boldsymbol{\chi}_h, \boldsymbol{\chi}_g$	Lagrange multipliers
$\mathcal{A}_h, \mathcal{A}_g$	Gradients of functionals $\mathcal{H}(\boldsymbol{x}), \mathcal{G}(\boldsymbol{x})$
\mathbf{e}	Identity vector

\mathcal{J}	Diagonal matrix containing sack variables
\mathbf{z}	Vector including problem variables (\mathbf{x}) and slack variables (\mathbf{s})
$\mathcal{C}(\mathbf{z})$	Functional of constraints
$\mathcal{Q}(\mathbf{z})$	Functional relating $\mathcal{J}(\mathbf{x})$ and slack variables (\mathbf{s})
\mathbf{d}	Trial vector for barrier subproblem
\mathcal{W}	Hessian matrix of the Lagrangian \mathcal{L}
$\hat{\mathcal{A}}$	Jacobian related to \mathcal{C}
ϵ_T	Trust region radius
ξ_T	Contraction parameter
\mathbf{v}	Transversal step approximated solution
\mathcal{M}	Merit function
p_c	Constraints penalization parameter
$tol^j, tol^h, tol^g, tol^q, tol^c$	Tolerances controlling the behavior of the interior-point algorithm

Sensitivity analysis

$\mathcal{L}(\mathbf{F}_a^{r*}, \mathbf{v}_a^*, \chi^*)$	Lagrangian functional associated to \mathcal{J}
\mathbf{F}_a^{r*}	Residual deformation field
\mathbf{v}_a^*	Displacement field
χ^*	Lagrange multiplier
χ_{adj}	Solution of the adjoint variational equation
$\mathbf{F}^{\check{\mathbf{v}}}$	Deformation field associated to $\check{\mathbf{v}}_a$
$\mathbf{F}^{\check{\mathbf{v}}r}$	Total deformation composed by $\mathbf{F}^{\check{\mathbf{v}}}$ and $\tilde{\mathbf{F}}^r$
$\mathbf{S}^{\check{\mathbf{v}}r}$	Second Piola-Kirchhoff stress associated to $\mathbf{F}^{\check{\mathbf{v}}r}$
$\sigma_a^{\check{\mathbf{v}}r}$	Cauchy stress associated to $\mathbf{F}_a^{\check{\mathbf{v}}r}$
$\delta(*)$	Increment in variable (*)
N_E	Number of non-overlapping subdomains
Ω_a^e	Non-overlapping subdomain
$\mathbf{F}_a^{r,e}$	Local value of residual deformation tensor in Ω_a^e
$\mathbf{T}_m, \mathbf{T}_b, \mathbf{T}_a$	Components of the sensitivity of \mathcal{L}
\mathcal{T}	Transpose operation for a fourth order tensor

Chapter 6

Clamped bar (1D)

f, f_a, f_b	Concentrated loads
S	Second Piola-Kirchhoff stress
k	Elastic parameter
L	Characteristic length
x_m	Material coordinates
F	Total deformation gradient
F^r	Residual deformation
F^v	Deformation gradient
v	Displacement field
P	Material point located at the center of the bar in Ω_m
v^f, v^{f_a}, v^{f_b}	Displacement field for point P associated to the loads f, f_a, f_b
$x_a^{f_a}, x_b^{f_b}$	Load application coordinates for f_a and f_b expressed in terms of x_a and x_b , respectively
ϕ_i	Linear finite element shape function associated to node i

Thick-walled cylinder & Three-layered aorta

ρ_m, θ_m, z_m	Radial, angular and axial coordinates
v^ρ	Radial displacement component of \mathbf{v}
u^ρ	Radial displacement component of \mathbf{u}
C_1, k_{vol}	Shear and bulk material parameters
\bar{I}_1	Isochorized invariant of the total deformation gradient tensor
J	Determinant of the total deformation gradient tensor
r_i, r_e	Inner and external radii
a, b, c	Coefficients defining target residual stress field
Ω_m^e	Finite element domain
$\bar{\boldsymbol{\sigma}}_m^{r,e}$	Constant residual stress field in Ω_m^e
$\mathbf{F}_m^{r,e}$	Constant residual deformation field in Ω_m^e
ψ_m^i	Local finite element functions
$\mathbf{C}^{r,e}$	Cauchy-Green strain tensor associated to $\mathbf{F}_m^{r,e}$
$\lambda_\rho, \lambda_\theta, \lambda_z$	Principal stretches shaping \mathbf{F}^r
$e_\sigma, e_{\mathbf{F}^r}$	Discrepancy measures between results and target field
$e_v^F, e_\sigma^F, e_{\mathbf{F}^r}^F$	Discrepancy measures between results and target field approximation
$c_{elast}, k_1, k_2, \lambda_i^0$	Parameters for transversely isotropic material
$\mathbf{F}^{exp,*}$	Target residual deformation field for each layer, $(*) = I, M, A$
$\lambda_\rho^{(*)}, \lambda_\theta^{(*)}, \lambda_z^{(*)}$	Principal stretches shaping $\mathbf{F}^{exp,*}$ for each layer, $(*) = I, M, A$
$A^{(*)}, B^{(*)}, L^{(*)},$ $k^{(*)}, L_1^{(A)}, L_2^{(A)},$ $L_3^{(A)}$	Geometrical parameters characterizing the excised and separated layers, $(*) = I, M$
$a^{(*)}, b^{(*)}, l, \beta_c, l_m$	Geometrical parameters characterizing the intact vessel, $(*) = I, M, A$

Chapter 1

Introduction

1.1 Motivation

Motivated by the high worldwide impact of cardiovascular diseases in human health (Mendis et al, 2011; Heidenreich et al, 2011), the last decades have seen both biomedical and scientific computing communities being compelled to increase their efforts towards improving computational tools and simulation-based techniques targeting the diagnosis and treatment of cardiovascular diseases under patient-generic and patient-specific paradigms.

As a consequence, these communities have entered a virtuous cycle of reciprocal feedback, leading each time to increasingly realistic modeling of the complex biological structures and the associated physiological processes occurring at all levels of biological organization (Southern et al, 2008). In particular, computational simulations are being used to assess causes, predict the development and optimize treatments and interventions of several pathologies in the cardiovascular system (CVS). This is due to the abilities and potentialities of such techniques in yielding relevant information, with a great level of detail and accuracy. Moreover, individualized -patient specific- computational models are attractive for physicians and scientists, considering the potential benefits (as powerful prognosis tools), the low cost implied in simulations and their associated impact on minimizing invasive procedures (Castro et al, 2011; Lewis and Kerckhoffs, 2010).

In this context, it is worth to remark that understanding the blood flow dynamics and the mechanical behavior of the arterial wall provides valuable information to gain insight into the mechanobiological processes related to the onset and evolution of cardiovascular pathologies. This fact motivates the seeking of increased realism in cardiovascular simulations. This is the general goal of this thesis, targeting the study of specific vascular segments (with particular emphasis in understanding the behavior of the arterial wall tissue) and their integration with the rest of the CVS. To illustrate this paradigm, Figure 1.1 shows an arterial segment corresponding to a middle cerebral artery and its location within an anatomically detailed model of the arterial network (Blanco et al, 2014a).

An adequate modeling of the entire arterial system (as an integrated functional unit) requires the identification of subsystems representing specific zones and/or particular functional aspects. In this analytic way, a mathematical model must be properly set for each subsystem in order to handle the underlying (biological, mathematical and numerical) complexity. Once mathematical models for these components are properly established, it is necessary to integrate them again into a set of coupled units to recreate the original dynamic interactions.

Computational biomechanics models formulated at the continuum level are highly dependent on (i) the simplifying hypotheses about the interaction of the subsystems which are being considered, (ii) the accuracy of the geometric representations of anatomical and functional structures, and (iii) the data that characterizes the behavior of materials involved

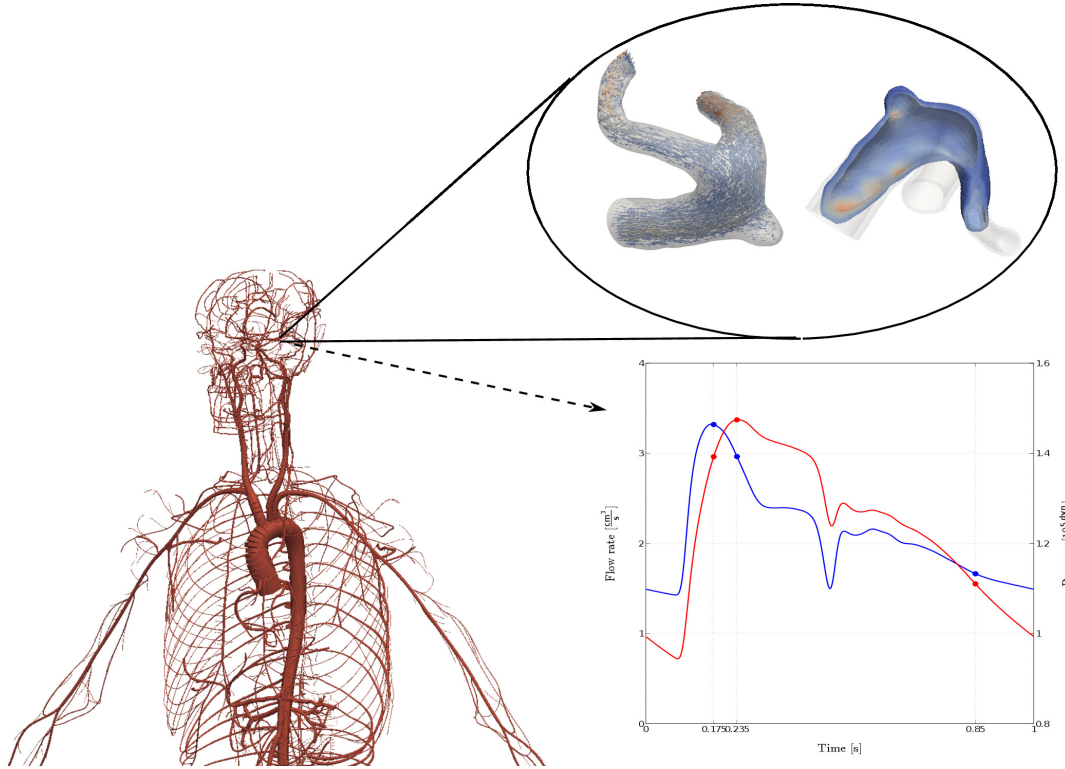


Figure 1.1: Segmentation of an arterial segment obtained from medical images corresponding to a middle cerebral artery bifurcation, featuring an aneurysm. Vascular segment location identified in the anatomically detailed arterial network (ADAN) model (Blanco et al, 2014a).

in the modeling process, for instance, blood and the vascular soft tissues.

In this connection, the development of comprehensive hemodynamic models is fundamental to accurately describe the blood flow dynamics and the mechanical behavior of the arterial wall. As it will be seen, this topic constitutes one of the major objectives of this thesis. Such models must be able to account for the complex composition of the arterial wall tissue, as well as for the interaction with the blood flow and the surrounding bodies.

It has been repeatedly demonstrated that it is key to provide these models with an accurate spatial description of the vascular region to be studied and adequate parameters describing the material behavior. On the one hand, powerful imaging technologies are available (such as IVUS, OCT and 4DMRI) that can offer precise patient-specific information regarding the geometry of vascular structures. On the other hand, current hemodynamic models rely on the information provided by the specialized literature (mostly obtained from ex-vivo studies) for the incorporation of material parameters.

Reciprocally, data assimilation techniques (which have proven to be successful in other areas) are being developed for cardiovascular modeling (see Wittek et al (2013); Bertagna et al (2014) and references therein) to provide simulations with patient-specific parameters characterizing the soft tissue behavior. Remarkably, there are no contributions directed at the in-vivo estimation of residual stresses in arterial walls.

1.2 State of the art

In this section, the key mechanical aspects that are mandatory to account for a truly realistic representation of the physiological conditions in hemodynamic simulations are described. For each topic, relevant contributions are highlighted and the state of the

art is presented. Finally, these articles, together with other major contributions of several research groups working in the area, are contextualized in Table 1.1

1.2.1 Boundary conditions on non-physical interfaces

When a portion of an artery is modeled via a full 3D approach, it must somehow be artificially isolated from the rest of the circulatory system. The simulation results within such arterial district are sensible to the coupling of such isolated segment with the rest of the vascular tree. In fact, a sensitivity analysis presented by Blanco et al (2009) evidenced that the local and global hemodynamics are mutually dependent. This fact suggests that neglecting the interactions between local 3D models with the remaining vasculature leads to the prediction of inconsistent hemodynamic environments which can greatly affect the analysis derived from the predictions of the models. Moreover, the model sensitivity to changes in local/global parameters (e.g. the compliance of the vessels) is also compromised if standalone 3D models are employed.

A suitable approach is to perform an embedding of the 3D model in a dimensionally reduced model (0D-1D for instance) of the entire arterial system to take into account global/local mutual hemodynamic interactions via consistent coupling conditions at the interfaces between these models. This issue was introduced by Formaggia et al (1999) and Formaggia et al (2001) and later exhaustively employed in (Blanco et al, 2007, 2009, 2010; Urquiza et al, 2006; Vignon-Clementel et al, 2006; Migliavacca et al, 2006; Kim et al, 2009a).

1.2.2 Constitutive modeling of the arterial wall

The wall structure of a typical elastic artery is composed of three distinct layers: the intima, the media and the adventitia. Figure 1.2 displays a diagrammatic model of the composition of such layers. The intima is the innermost layer, consisting of a single layer of endothelial cells supported by a thin basal membrane, a subendothelial layer. The media layer is composed by the internal elastic lamina (that separates the media from the intima layer) and a series of circumferentially oriented smooth muscle cells and a helical arrange of collagen fibers embedded in a elastin matrix. These series of smooth muscle cells are separated by elastic laminae. The adventitia is the outermost layer of the arterial wall and consists mainly of fibroblasts and fibrocytes (cells that synthesize collagen and elastin), histological ground and bundles of collagen fibrils forming a fibrous tissue (Holzapfel and Ogden, 2010a). The adventitia layer is separated from the media layer by the external elastic lamina. It is worthwhile to note that, from the mechanical point of view, the relevant constituents are the elastin matrix, the collagen fibers and the smooth muscle cells.

It is widely accepted that the effects of elastin and collagen can be effectively modeled as a fiber reinforced hyperelastic material (see Holzapfel and Ogden (2010a) and references therein). Several constitutive models have been proposed and validated against experimental data. Currently, the most extensively used constitutive model is the transversely isotropic model proposed in Holzapfel and Gasser (2000), where an exponential behavior is considered for the collagen fibers to simulate the progressive recruitment of such curled fibers. Nonetheless, more comprehensive approaches are available. As examples, in Gasser et al (2006), it is further explored the influence of the dispersion of the fiber orientations, and in Hill et al (2012), information regarding the progressive recruitment process of such fibers is introduced. The smooth muscle cells incorporate two additional mechanisms to the arterial wall behavior, an active and a passive action. The passive mechanism introduces a characteristic viscoelastic effect in the soft tissue, and the active component infuses a response to biomechanical stimuli (e.g. blood pressure changes), hormonal stimuli, neural

stimuli and drugs (Zulliger et al, 2004b).

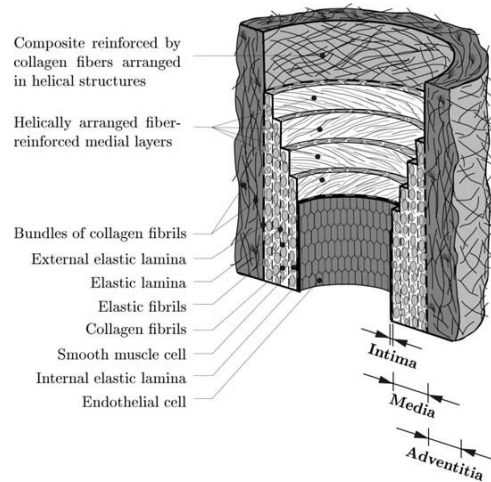


Figure 1.2: Diagram of the major components of an elastic artery, showing the three arterial wall layers: intima, media and adventitia. Figure adapted from Holzapfel and Gasser (2000).

1.2.3 Constitutive modeling of the blood

Blood is a concentrated suspension of formed cellular elements including red blood cells (RBCs), white blood cells and platelets. It is well known that the blood can be characterized as a non-Newtonian fluid. This non-Newtonian behavior is a consequence of the influence of the erythrocytes (RBCs) that form branched three dimensional microstructures at low shear rates and are able to experience deformations. At high shear rates RBCs tend to align with the flow direction and it can be considered that blood flow presents a constant viscosity (Robertson et al, 2008).

As high shear rates are encountered in most parts of the arterial system for healthy individuals, modeling the blood flow as a Newtonian fluid is a reasonable simplifying assumption (Fischer and Rossman, 2009). Actually, the blood exhibits a non-Newtonian behavior in stagnation regions which are typically found in geometrical singularities such as highly curved bifurcations, aneurysms and post-stenotic districts. In this sense, several studies addressing blood flow in aneurysms (Cebal et al, 2005; Fischer and Rossman, 2009) reported a low sensitivity of the hemodynamic variables (wall shear stress, oscillatory shear index, mean velocity) with respect to the constitutive equations employed to model the blood. However, it has been shown that in coiled aneurysms the choice of the constitutive model heavily influences the outcome of the simulations (Morales et al, 2013).

Based on (Fischer and Rossman, 2009), in this work it will be considered that the blood behaves as a Newtonian fluid.

1.2.4 Fluid-structure interaction

Other relevant aspect to be considered is the adequate treatment of the deformation of the domain occupied by the fluid (blood) caused by movement of the distensible arterial walls. It has been pointed out that in some cases the *wall shear stress* (WSS) may be quite overestimated if a rigid arterial wall assumption is considered in blood flow simulations (pure CFD modeling) Hsu and Bazilevs (2011). This stresses the need for including the wall movement in flow simulations. Moreover, this issue goes beyond pure fluid dynamics, *fluid-structure interaction* (FSI) formulations must necessarily be considered if proper determination of stresses within the arterial tissue is required.

Fluid-structure interaction has been largely studied, and a great deal of methods is available to tackle this problem, most of them based on the *Arbitrary Lagrangian-Eulerian* (ALE) formulation introduced by Hughes et al (1981) and firstly applied in the context of hemodynamics by Taylor et al (1998). Iterative and monolithic approaches have been proposed for the FSI system. In this regard the literature is vast, and we limit to mention some relevant works in the field, e.g. (Deparis et al, 2003, 2006) for the former and (Crosetto et al, 2011; Wu and Cai, 2014; Joosten et al, 2009) for the latter.

1.2.5 Surrounding tissues

The arterial vessel is surrounded by tissues, which restrains the movement of the arterial wall, altering the deformation processes, and thence affecting the stress state. Most of current FSI studies neglect this fact considering that the outer surface of the arterial wall is free of loads, leading to unrealistic motions of the artery, as shown in Malossi et al (2013). The main obstacle relies in the determination of the forces acting on the outer boundary. Furthermore, determining the outer boundary itself is a hard task as sometimes there is no clear distinction between adventitia and surrounding tissue. A recent article Moireau et al (2012) deals with this issue by modeling the external tissues as a viscoelastic medium. Reported results show improvements in the accuracy when comparing the predicted results (both considering and neglecting the surrounding tissue interaction) with experimental information extracted from medical images.

1.2.6 Initially loaded configuration

Patient-specific computational models are based on in-vivo geometrical structures obtained from medical image acquisition devices (like MRI and CT). Those images correspond to configurations of anatomical structures in 3D space that are not load-free. On the contrary, those spatial configurations are subjected to the hemodynamic forces acting at the internal wall of the artery and, as afore stated, to forces acting at the external boundary of the vessel due to the interaction with the surrounding media.

In general, in the available literature this aspect is usually disregarded, and only in few publications (see Table 1.1) the configuration initially obtained from the medical images is considered to be equilibrated by an inner baseline pressure. However, there is no clear exposition on how this pressure level is selected. A more realistic approach would be to estimate this inner pressure taking into account the data acquisition technology and the selected reconstruction algorithm; for example, in some cases the given information is a mean over time of the positioning of the artery in the complete cardiac cycle (e.g. in 3D rotational angiographies Orth et al (2009); van Rooij et al (2008)) while in other studies it is possible to synchronize the image acquisition with the patient's electrocardiogram, obtaining images corresponding to a constant time window within the cardiac pulse (e.g. in intravascular ultrasound studies Mintz et al (2001); Honda and Fitzgerald (2008)).

The most common approach to compute the stress state in this *preloaded* configuration is usually referred to as *inverse design analysis* (Govindjee and Mihalic, 1996, 1998) or *inverse elastostatics* (Lu et al, 2007, 2008; Zhou et al, 2010) and focuses on finding the zero load configuration; a different approach is proposed in Gee et al (2009, 2010) introducing *pre-stresses* and *pre-strains* in the image-based geometry. It is important to remark that the first methodology offers a more comprehensive approach to the subject and enables the computation of the elastic energy stored in the tissue, that, as pointed out by Ferruzzi et al (2015), plays a relevant role in arterial wall functioning.

It is also worthwhile to mention that, as stated by Gee et al (2009), neglecting the fact that the image-based geometry corresponds to a loaded state and taking a simplified approach (considering them as load-free configurations being the most common case) leads

to unrealistic evaluation of the quantities of interest such as strain, stress as well as other internal variables involved in the constitutive description.

1.2.7 Residual stresses

Consider the scheme introduced in Figure 1.3, showing three different configurations of an arterial wall segment. Here, Ω_{iv} represents the in-vivo configuration, i.e. a configuration corresponding to the arterial wall segment at equilibrium with hemodynamic and external loads (the image-based configuration). The zero-load (or load-free) configuration Ω_0 is also presented, which represents the state corresponding to a self-equilibrated configuration, where all external loads (both hemodynamic loads and loads acting on the external boundary) have been removed. This configuration is neither stress-free nor strain-free (Fung, 1991; Fung and Liu, 1989). The notation $\boldsymbol{\sigma}^r$ is introduced to refer to the residual stress state induced by the residual deformation field, say \mathbf{F}^r . Note that the stress state $\boldsymbol{\sigma}$ in Ω_{iv} is dependent on these residual deformations and the deformation field originated as response to the load state, here denoted as \mathbf{F}^u . The presence of this residual stress can be manifested performing seizures to the arterial segment. For example, when a cut is performed axially, arteries show a retraction of its length and radial cuts result in an opening angle. If additional cuts are performed, the material will further release stored energy until a virtual stress-free (and strain-free) state is achieved. We will denote this state as the virtual configuration Ω_v of the tissue. Moreover, since there is no energy stored in the body in this configuration, it is possible to regard it as a *material configuration* in the classical sense used to define constitutive laws in continuum mechanics.

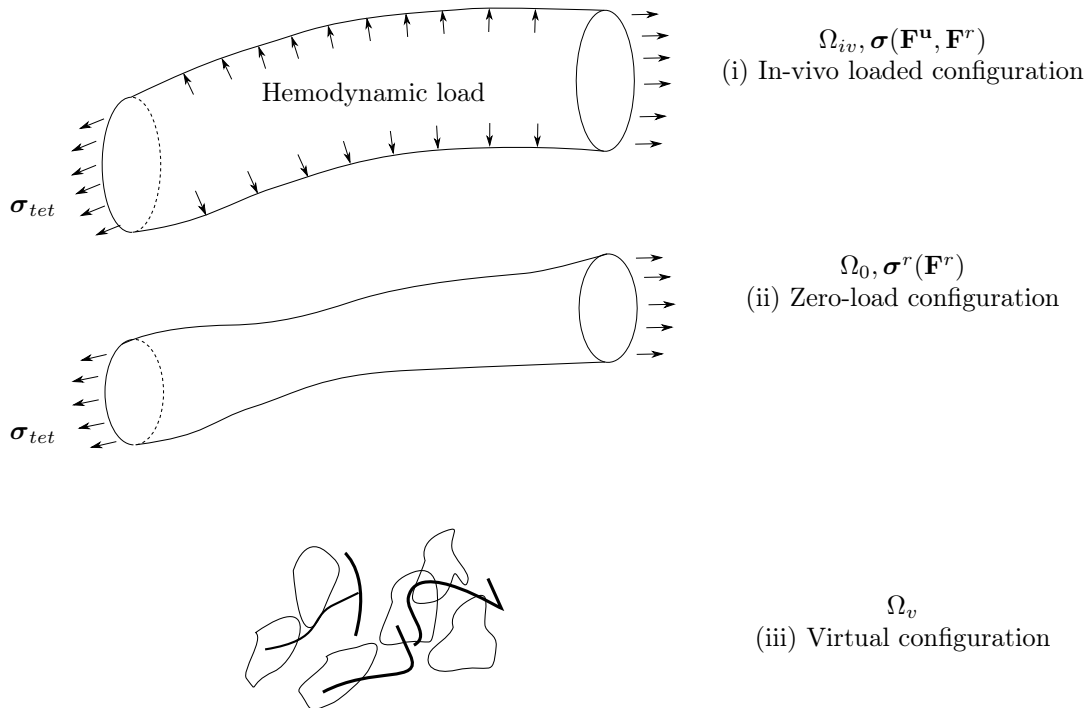


Figure 1.3: Representative scheme introducing (i), the in-vivo configuration Ω_{iv} , corresponding to an in-vivo state of the arterial segment, subjected to hemodynamic and external loads, (ii) the zero-load configuration Ω_0 , featuring a self-equilibrated residual stress state, and (iii) the stress-free virtual configuration Ω_v , a disagggregated state of the arterial wall tissue that serves as a material reference and has no energy stored.

The stretching observed in an arterial segment when it is removed from the rest of

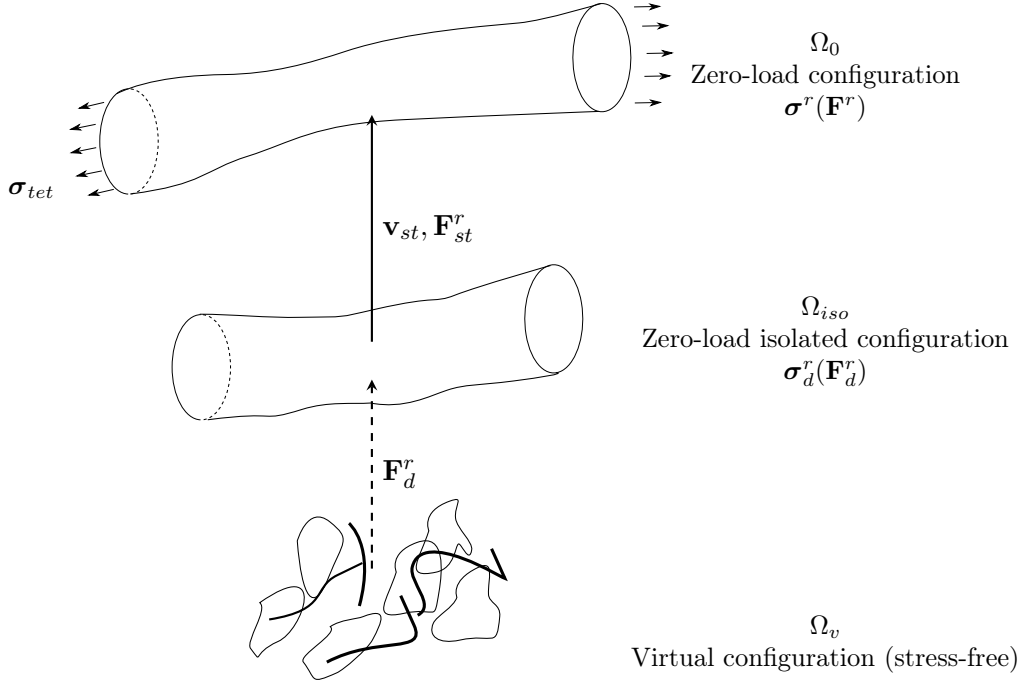


Figure 1.4: Scheme to represent the decomposition of the residual deformation tensor \mathbf{F}^r when considering the pre-stretching component \mathbf{F}_{st}^r . Configuration Ω_{iso} represents an unloaded and isolated arterial segment, at equilibrium with the residual stress $\sigma_d^r(\mathbf{F}_d^r)$. Displacement \mathbf{u}_{st} maps points from Ω_{iso} into Ω_0 inducing the residual deformation \mathbf{F}_{st}^r ; then, the characterization of the total residual deformation tensor is given by $\mathbf{F}^r = \mathbf{F}_{st}^r \mathbf{F}_d^r$.

the CVS is referred to as pre-stretch. This pre-stretch is responsible for a component of the residual deformations. In fact, consider Figure 1.4, which introduces the *zero-load isolated configuration* Ω_{iso} , representing an unloaded arterial segment detached from the rest of the CVS. This configuration features a reduced length (when compared to the in-vivo state) and a different residual stress state, say \mathbf{F}_d^r . The displacement field \mathbf{u}_{st} maps points from Ω_{iso} into Ω_0 , inducing a residual deformation \mathbf{F}_{st}^r . Then the total residual deformation at Ω_0 is given by $\mathbf{F}^r = \mathbf{F}_{st}^r \mathbf{F}_d^r$. Note that, opposed to \mathbf{F}_{st}^r , the deformation \mathbf{F}_d^r is, in the present conceptual framework, not related to a continuous displacement field. Following a similar procedure, it could be possible to decompose \mathbf{F}_d^r into several components resulting from the different deformations caused by the energy release in each cut.

Most efforts to account for residual stresses in arterial wall models are based on the characterization of the deformations resulting from performing seizures in the tissue as described above. Among these, we highlight the contributions of Holzapfel and Gasser (2000), with the first in-depth proposal of this idea; Holzapfel et al (2007) and Holzapfel and Ogden (2010a) performing a layer separation and incorporating further detail to the residual deformation description by accounting for the different behavior presented in each constituent layer; and Pierce et al (2015) displaying a generalization of this technique, mapping information obtained from ex-vivo experiments into patient-specific geometries. It is important to note that the use of these strategies is debatable for the translation of experimental information available in the literature to complex geometries, such as the corresponding to arterial bifurcations or aneurysms. In the present context it is also important to recall the alternative approaches taken in Taber and Humphrey (2001) and Bellini et al (2014), where residual stresses are introduced through growth processes considering that each mechanically relevant component is synthesized and deposited in the tissue with a predefined deformation level. All these approaches rely on experimental ex-vivo measure-

ments, making difficult to devise extensions of those methodologies to in-vivo quantification of residual stresses as required for patient specific simulations.

We emphasize that the introduction of residual stresses in hemodynamic simulations is still an open problem and, up to the author's knowledge, there is no general methodology available to obtain patient-specific information regarding the residual stress state in a vascular region.

Article	Dim. het. coupling	FSI	Finite strains	Histological model	Preloaded state	External tissue	Tethering stress
Grinberg and Karniadakis (2008)	✓	-	-	-	-	-	-
Vignon-Clementel et al (2006)	✓	-	-	-	-	-	-
Urquiza et al (2006)	✓	(α)	-	-	-	-	-
Blanco et al (2010)							
Blanco et al (2013b)							
Torii et al (2006)	-	✓	✓	-	-	-	-
Torii et al (2008)							
Wu and Cai (2014)							
Lu et al (2007)	-	-	✓	-	✓	-	-
Lu et al (2008)							
Holzappel and Gasser (2000)	-	-	✓	✓	(β)	-	✓
Holzappel and Ogden (2010b)							
Crosetto et al (2011)	-	✓	✓	-	-	✓	-
Reymond et al (2013)							
Kim et al (2009b)	✓	✓	✓	-	-	-	-
Kim et al (2009a)							
Gee et al (2009)	-	-	✓	✓	✓	-	-
Gee et al (2010)							
Blanco et al (2013a)	✓	✓	✓	-	-	✓	-
Malossi et al (2013)							
Tezduyar et al (2010)	-	✓	✓	✓	✓	-	-
Hsu and Bazilevs (2011)							
Vavourakis et al (2011)							
Moireau et al (2012)	-	✓	✓	-	✓	✓	-
Pierce et al (2015)	-	-	✓	✓	✓	-	✓
Proposed modeling framework	✓	✓	✓	✓	✓	✓	✓

Table 1.1: Summary of main contributions in modeling issues (see text for further explanation). (α) Using simple 1D models for the arterial wall. (β) This work is based on ex-vivo measures, the initial configurations are truly unloaded.

1.3 Objectives

In view of the context revisited above, the general objective of this thesis is placed on the modeling of blood flow dynamics and its interaction with the arterial wall. That is, it is aimed at studying blood flow in (possibly) patient-specific arterial vessels and their integration with the rest of the CVS, emphasizing the analysis of the mechanical regime of the arterial tissue. Specifically, the particular goals of this work are the following

- to develop and implement an integrative modeling framework capable of dealing with the inherent complexities of hemodynamic problems, addressing the modeling of 3D FSI models with 1D systemic blood flow models and accounting for the effect of existing loads in vascular geometries derived from medical images, and
- to present a novel variational approach for the in-vivo characterization of residual stresses and deformations.

1.4 Contributions

In line with the first main objective of this thesis, a modeling framework that integrates the aspects listed in Section 1.2 is presented. In summary, the strategies to be addressed here will include a full 3D model of a vascular district coupled with a dimensionally reduced model of the rest of the CVS. The dimensionally heterogeneous coupling between models of reduced dimensions with full 3D zones is formulated in a consistent variational framework, following the developments described in Blanco et al (2007). In particular, the 3D model accounts for the solution of the blood flow problem in a moving domain due to the wall compliance. The resulting FSI problem is treated with the ALE method for the fluid problem. The solid problem (arterial wall) is considered to be in the finite strain regime assuming a hyper-elastic material behavior, subjected to the hemodynamic loads exerted by the blood flow, a viscoelastic media surrounding the vessel and a tethering stress state acting at the artificial cross-sectional boundaries (interfaces between 3D and 1D models). The preload problem is also addressed, considering known a pre-strained configuration (for example, the diastolic configuration) and such problem consists in finding the load free reference configuration. Tethering forces are also considered in the preload problem such that a certain level of pre-stretch is achieved. This fact will allow us to take into account the pre-stretch component (\mathbf{F}_{st}^r) of the residual deformation state. Moreover, the variational equilibrium for the solid problem is stated in a given deformed/loaded configuration, which is considered to be extracted from medical images, and the corresponding formulations are consistently linearized.

Related to the development of this modeling framework, the contribution is twofold:

- (i) to present and discuss the conceptual background behind the variational formulations which are required in the hemodynamics field when a realistic mechanical analysis of arterial walls is sought,
- (ii) to introduce, for the first time, hemodynamic simulations integrating the key aspects detailed in Section 1.2, aiming to gain insight on the interplay among modeling ingredients and underlying hypotheses, and their impact in the assessment of the mechanical state of arterial walls.

Additionally, four numerical experiments are analyzed that show the relevance and significance of the proposed integrative approach. Specifically, a sensitivity analysis is performed assessing the relevance of taking into account the complete load state acting over the arterial wall, evidencing the importance of considering both the internal pressure

and residual pre-stretch deformations to appropriately characterize the mechanical state of the arterial wall.

As a contribution related to the second main objective of this thesis, a novel conceptual framework that makes the estimation of residual deformations (and associated stresses) practicable in conditions resembling in-vivo scenarios is presented. This framework combines a variational modeling approach and the kind of data that could be retrieved from medical images. As it will be observed, this formulation consists in the definition of a cost functional which is able to measure the mechanical imbalance due to the assumption of inconsistent residual deformations at a given set of equilibrated configurations of the arterial wall. Thence, the characterization of residual stresses becomes an optimization problem where the residuals of the involved variational equations are minimized by finding the appropriate residual deformation field. In this context, three numerical examples are presented that evidence the suitability and consistency of this novel approach, showing that this methodology is able to identify, with great accuracy, residual stress fields inspired by experimental ex-vivo measures on real human arterial vessels.

1.5 Scientific production

In this Section, the publications derived from this thesis are listed.

Articles in peer-reviewed journals

- Blanco, P.J., Ares, G.D., Urquiza, S.A. & Feijóo, R.A. *On the effect of preload and pre-stretch on hemodynamic simulations: an integrative approach*. Biomechanics and Modeling in Mechanobiology. DOI 10.1007/s10237-015-0712-y (in Press)
- Ares, G.D., Blanco, P.J., Urquiza, S.A. & Feijóo, R.A. *Identification of residual stresses in multi-layered arterial wall tissues using a variational framework* (Submitted to Biomechanics and Modeling in Mechanobiology).

Book chapters

- Urquiza, S.A., Blanco, P.J., Ares, G.D. & Feijóo, R.A. *Implementation issues of large strain formulations of hyperelastic materials for the modeling of arterial wall mechanics*. In: R.A. Feijóo, A. Ziviani & P.J. Blanco.. (Org.). Scientific Computing Applied to Medicine and Healthcare. 1ed., Petrópolis, 2012, v. , p. 79-120.

Complete articles in conference proceedings

- Aranciaga, J., Caballero, D.E., Parisi, N.A., Lombera, G., Blanco, P. J., Ares, G.D. & Urquiza, S. A. *Implementación de una formulación de bajo orden para materiales incompresibles en hemodinámica*. ENIEF 2014, Congreso sobre Métodos Numéricos y sus Aplicaciones, 2014, San Carlos de Bariloche. Mecánica Computacional, 2014. v. 33. p. 2635-2666
- Urquiza, S. A., Parisi, N.A., Caballero, D.E., Lombera, G., Ares, G.D., Blanco, P. J., & Feijóo, R.A. *Un Modelo No Lineal de la Dinámica del Flujo Sanguíneo y la Pared Arterial*. ENIEF 2013, Congreso sobre Métodos Numéricos y sus Aplicaciones, 2013. Mecánica Computacional. v. 32. p. 3885-3902.
- Urquiza, S.A., Blanco, P.J., Ares, G.D. & Feijóo, R.A. *A generic finite element implementation of arterial wall constitutive laws*. MECOM Bicentenario (MECOM 2010 - CILAMSE 2010), 2010, Buenos Aires. Mecánica Computacional, 2010. v. 29. p. 5973-5984

Abstracts in conference proceedings

- Ares, G.D., Blanco, P.J., Urquiza, S.A. & Feijóo, R.A. *Comprehensive computational modeling of brain aneurysms: from preload analysis to 3D-1D FSI simulations*. ESMC 2015. 9th European Solid Mechanics Conference, 2015, Madrid. Proceedings of ESMC 2015, 2015.
- Ares, G.D., Blanco, P.J., Urquiza, S.A. & Feijóo, R.A. *Assessing preload and pre-stretch impact on hemodynamic simulations*. In: ENIEF 2014, Congreso sobre Métodos Numéricos y sus Aplicaciones, 2014, San Carlos de Bariloche. Mecánica Computacional, 2014.
- Urquiza, S.A., Blanco, P.J., Ares, G.D. & Feijóo, R.A. *Implementation of the FSI problem in hemodynamics considering large strains*. In: Congreso sobre Métodos Numéricos y sus Aplicaciones (ENIEF 2011), 2011, Rosario, Argentina. Anais do ENIEF 2011, 2011.

1.6 Structure of the thesis

The thesis is structured as follows. Chapter 2 presents an introduction to the key continuum mechanics concepts and models that integrate the proposed comprehensive modeling framework. There, the topics addressed include finite-strain 3D solid mechanics, 3D fluid dynamics in deformable domains and dimensionally reduced models for the circulatory system. Next, in Chapter 3 the practical strategies adopted to tackle each one of the key aspects in hemodynamic modeling are described. Chapter 4 shows the application of the proposed integrative modeling framework to several study cases, which include two numerical experiments in idealized arterial domains (a straight pipe and a standardized carotid bifurcation) and two patient-specific cases (a common carotid artery and a middle cerebral artery, the latter featuring an aneurysm). Following, in Chapter 5, a variational framework for the characterization of residual deformations in arterial wall tissues is developed, and in Chapter 6 three numerical examples are explored to demonstrate the capabilities of the identification strategy. Finally, concluding remarks and future work are outlined in Chapter 7.

Chapter 2

Continuum mechanics models

2.1 Introduction

In this chapter the key mechanical concepts and models from the continuum mechanics field are introduced. These represent the groundwork for the development of the present work, focusing on the modeling of the arterial wall structure and its interaction with the blood flow.

In a first stage, an introduction to solid mechanics in the finite strain regime is exposed, presenting the kinematic bases along with the mechanical equilibrium concept. In this context, two variational problems (the *preload* and *forward* problems) are presented considering the same equilibrium equations. The difference between these two problems relies in the known data, which amounts to knowing the configuration of the body. For both cases the detailed procedure to perform a consistent linearization through the Newton-Raphson method is presented.

In a second stage, the *Arbitrary Lagrangian Eulerian* (ALE) formulation for the Navier-Stokes equations is summarized, aimed at modeling the blood flow dynamics in three-dimensional moving domains.

Finally, the dimensionally reduced model which accounts for the description of the complete cardiovascular system is presented. It is composed by one-dimensional models for the main arterial vessels and zero-dimensional representations of the remaining part of the cardiovascular components.

2.2 Solid mechanics at finite strains

2.2.1 Kinematics

Let \mathcal{B} be a body for which we identify in the Euclidean space \mathcal{E} its *spatial* configuration Ω_s . Points in this domain are denoted by \mathbf{x}_s . A *material* or *reference* configuration will be referred to as Ω_m , with points \mathbf{x}_m . This material configuration is considered as *load-free* but may be subjected to residual deformations (RDs) and, consequently, to residual stresses (RSs). Although the mathematical developments in this Chapter do not account for residual deformations, this issue will be extensively discussed in Chapter 5.

Remark 2.1. *In the context of hemodynamics, Ω_s may refer to a diastolic, systolic or any other loaded state of the arterial wall. And it stands for the configuration at which mechanical equilibrium is achieved for a given load condition, which in the present context is characterized by blood internal pressure and tethering forces.*

The deformation of the body at the spatial configuration is characterized through

the diffeomorphic mapping χ_m that relates both configurations, that is

$$\begin{aligned}\chi_m : \Omega_m &\rightarrow \Omega_s, \\ \mathbf{x}_m &\mapsto \mathbf{x}_s = \chi_m(\mathbf{x}_m)\end{aligned}\tag{2.2.1}$$

The displacement field which maps the material points into the spatial configuration is denoted by \mathbf{u} . Then, we can also characterize the displacement from Ω_m onto Ω_s and its inverse by the following expressions,

$$\mathbf{x}_s = \chi_m(\mathbf{x}_m) = \mathbf{x}_m + \mathbf{u}_m,\tag{2.2.2}$$

$$\mathbf{x}_m = \chi_s(\mathbf{x}_s) = \chi_m^{-1}(\mathbf{x}_s) = \mathbf{x}_s - \mathbf{u}_s,\tag{2.2.3}$$

where subscripts m and s denote the descriptions of the fields in the material and spatial configurations, respectively. That is, for the displacement vector field it is

$$\mathbf{u}_s(\mathbf{x}_s) = (\mathbf{u}_m(\mathbf{x}_m))_s = \mathbf{u}_m(\chi_m^{-1}(\mathbf{x}_s)).\tag{2.2.4}$$

This notation will be used extensively in the forthcoming developments. The gradients of these mappings are then given by

$$\mathbf{F}_m = \nabla_m \chi_m = \mathbf{I} + \nabla_m \mathbf{u}_m,\tag{2.2.5}$$

$$\mathbf{f}_s = \nabla_s \chi_s = \mathbf{I} - \nabla_s \mathbf{u}_s,\tag{2.2.6}$$

where ∇_m and ∇_s denote the gradients with respect to material and spatial coordinates, respectively. Observe that $(\mathbf{F}_m^{-1})_s = \mathbf{f}_s$ and $(\mathbf{f}_s^{-1})_m = \mathbf{F}_m$.

It is worthwhile to recall that the deformation gradient tensor \mathbf{F}_m characterizes the transformation of a differential segment $d\mathbf{x}_m$ through

$$d\mathbf{x}_s = \mathbf{F}_m d\mathbf{x}_m,\tag{2.2.7}$$

and its determinant measures the volumetric change of a differential volume element $d\Omega_m$ when deformed into $d\Omega_s$ via

$$d\Omega_s = \det \mathbf{F}_m d\Omega_m.\tag{2.2.8}$$

To exclude the possibility of nullifying volume $d\Omega_s$, $\det \mathbf{F}_m > 0$ must be satisfied. Moreover, for incompressible media it follows that

$$\det \mathbf{F}_m = 1,\tag{2.2.9}$$

which represents a reasonable kinematical constraint in the case of dealing with biological tissues (Fung, 1993).

Let us now introduce the Green-Lagrange strain tensor \mathbf{E}_m , which is a measure of the deformation of a segment $d\mathbf{x}_m$ when transformed into $d\mathbf{x}_s$, i.e.

$$d\mathbf{x}_s \cdot d\mathbf{x}_s - d\mathbf{x}_m \cdot d\mathbf{x}_m = (\mathbf{F}_m^T \mathbf{F}_m - \mathbf{I}) d\mathbf{x}_m \cdot d\mathbf{x}_m = 2\mathbf{E}_m d\mathbf{x}_m \cdot d\mathbf{x}_m,\tag{2.2.10}$$

thence

$$\mathbf{E}_m = \frac{1}{2} (\mathbf{F}_m^T \mathbf{F}_m - \mathbf{I}).\tag{2.2.11}$$

Also, the so-called left and right Cauchy-Green strain tensors can be defined as $\mathbf{C}_m = \mathbf{F}_m^T \mathbf{F}_m$ and $\mathbf{B}_m = \mathbf{F}_m \mathbf{F}_m^T$, respectively. Note that the left Cauchy-Green and the Green Lagrange tensors are related by $\mathbf{C}_m = 2\mathbf{E}_m - \mathbf{I}$.

2.2.2 Kinematically admissible fields

In the forthcoming sections, the definition of the mechanical equilibrium will be given in terms of the Virtual Power Principle (Germain, 1973). In such context, it is fundamental to define the sets of kinematically admissible displacement.

Consider the domain Ω_s bounded by $\partial\Omega_s = \partial\Omega_s^D \cup \partial\Omega_s^N$, where $\partial\Omega_s^N$ and $\partial\Omega_s^D$ denote the Neumann and Dirichlet boundaries, respectively. At the Dirichlet boundary, displacements $\bar{\mathbf{u}}_s$ are prescribed. Then, displacement field \mathbf{u}_s is defined in the linear manifold of kinematically admissible functions \mathcal{U}_s , given by

$$\mathcal{U}_s = \left\{ \mathbf{u}_s \in \mathcal{W}_s; \mathbf{u}_s = \bar{\mathbf{u}}_s|_{\partial\Omega_s^D} \right\}, \quad (2.2.12)$$

which is associated to the linear space of kinematically admissible variations \mathcal{V}_s given by

$$\mathcal{V}_s = \left\{ \hat{\mathbf{u}}_s \in \mathcal{W}_s; \hat{\mathbf{u}}_s = \mathbf{0}|_{\partial\Omega_s^D} \right\}. \quad (2.2.13)$$

In the above sets, \mathcal{W}_s is a Hilbert space with functions regular enough for mathematical operations to make sense. In the classical setting, it is $\mathcal{W}_s = \mathbf{H}^1(\Omega_s)$.

2.2.3 Equilibrium equations

Consider the setting presented in Figure 2.1, showing the *load-free* and *stress-free* material configuration Ω_m (that can be thought as the zero-load isolated configuration Ω_{iso} introduced in Section 1.2.7) and the spatial configuration Ω_s with boundary $\partial\Omega_s^N = \partial\Omega_s^W \cup \partial\Omega_s^E \cup \partial\Omega_s^A$, where $\partial\Omega_s^W$ represents the wall interface between the vessel and the blood, $\partial\Omega_s^E$ is the external surface, and $\partial\Omega_s^A = \bigcup_{i=1}^C \partial\Omega_s^{A,i}$ stands for the set of C cross-sectional -non-physical- ring-like boundaries. These non-physical boundaries are generated by the isolation of a given arterial vessel from the rest of the cardiovascular system. Unless stated otherwise, in all these boundaries Neumann conditions will be assumed. This spatial configuration will equivalently be called equilibrium configuration, see Remark 2.1.

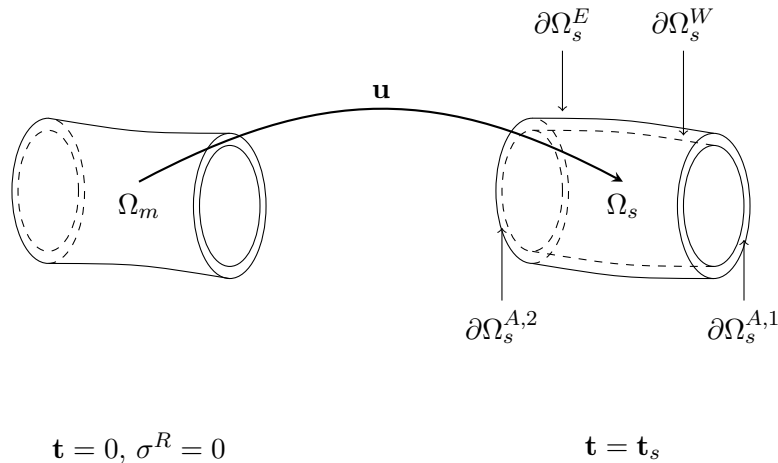


Figure 2.1: Mechanical equilibrium setting, displaying the *load-free* and *stress-free* material configuration Ω_m and the spatial (equilibrium) configuration Ω_s subjected to the load state \mathbf{t}_s in $\partial\Omega_s^N = \partial\Omega_s^W \cup \partial\Omega_s^E \cup \partial\Omega_s^A$

In a general case, the load state of the arterial segment can be characterized as follows: the forces exerted by the blood flow over $\partial\Omega_s^W$, i.e. the traction \mathbf{t}_s^W ; a load \mathbf{t}_s^E acting on the external surface $\partial\Omega_s^E$ due to the presence of surrounding tissues, and a set of tethering tractions $\mathbf{t}_s^{A,i}$ acting over $\partial\Omega_s^{A,i}$, $i = 1, \dots, C$. For notational ease, we group

the tethering tractions into \mathbf{t}_s^A , which is defined over the whole $\partial\Omega_s^A$. We will consider that the load exerted by external tissues, \mathbf{t}_s^E is an active traction, that is, it depends on the solution of the problem (see Section 3.3). It is important to note that the traction due to hemodynamic forces \mathbf{t}_s^W is a follower load, and can be split into normal and tangential components as follows $\mathbf{t}_s^W = t_s^{W,n} \mathbf{n}_s + \mathbf{t}_s^{W,t}$ where $t_s^{W,n} = \mathbf{t}_s^W \cdot \mathbf{n}_s$ is the normal component of the traction and $\mathbf{t}_s^{W,t}$ is the tangential vector which can be characterized as $\mathbf{t}_s^{W,t} = \mathbf{P}_s \mathbf{t}_s^W$, with $\mathbf{P}_s = (\mathbf{I} - \mathbf{n}_s \otimes \mathbf{n}_s)$ being the orthogonal projection operator over the plane with unit normal vector \mathbf{n}_s . Note that we can trivially write $\mathbf{t}_s^{W,t} = \mathbf{P}_s \mathbf{t}_s^{W,t}$.

The variational statement of the Virtual Power Principle will be presented considering the incompressibility as a relaxed kinematical constraint. Then, an independent variable (the pressure in the body) emerges as a Lagrange multiplier to accommodate this distributed constraint. Furthermore, we neglect inertia forces and other forces per unit volume such as gravity. Thus, the mechanical problem is considered to be quasi-static.

Next, we provide the statement of two variational formulations of mechanical equilibrium whose difference is rather subtle: the known domain from which the analysis departs. In Problem 1 below, the given known domain is the domain at which the body is at equilibrium (the spatial domain Ω_s), and the unknown domain is the reference domain used to define the constitutive equations (the material domain Ω_m). In Problem 2, the given domain is the material domain, while the unknown one is the spatial domain.

Problem 1 (Preload problem). Given the equilibrium configuration Ω_s and the load defined in this spatial configuration $(\mathbf{t}_s^W, \mathbf{t}_s^E, \mathbf{t}_s^A)$, the variational equations that govern this problem are those corresponding to the mechanical equilibrium expressed in the *spatial* domain. Hence, the problem reads: given $(t_s^{W,n}, \mathbf{t}_s^{W,t}, \mathbf{t}_s^E, \mathbf{t}_s^A)$, find $(\mathbf{u}_s, \lambda_s) \in \mathcal{U}_s \times \mathcal{L}_s$ such that $\boldsymbol{\sigma}_s$ satisfies

$$\int_{\Omega_s} [-\lambda_s \operatorname{div}_s \hat{\mathbf{u}}_s + \boldsymbol{\sigma}_s \cdot \boldsymbol{\varepsilon}_s(\hat{\mathbf{u}}_s)] d\Omega_s = \int_{\partial\Omega_s^W} \mathbf{P}_s \mathbf{t}_s^{W,t} \cdot \hat{\mathbf{u}}_s d\partial\Omega_s^W + \int_{\partial\Omega_s^W} t_s^{W,n} \mathbf{n}_s \cdot \hat{\mathbf{u}}_s d\partial\Omega_s^W + \int_{\partial\Omega_s^E} \mathbf{t}_s^E \cdot \hat{\mathbf{u}}_s d\partial\Omega_s^E + \sum_{i=1}^C \int_{\partial\Omega_s^{A,i}} \mathbf{t}_s^{A,i} \cdot \hat{\mathbf{u}}_s d\partial\Omega_s^{A,i} \quad \forall \hat{\mathbf{u}}_s \in \mathcal{V}_s, \quad (2.2.14)$$

$$\int_{\Omega_s} [1 - \det \mathbf{F}_s^{-1}] \hat{\lambda}_s d\Omega_s = 0 \quad \forall \hat{\lambda}_s \in \mathcal{L}_s, \quad (2.2.15)$$

where $\boldsymbol{\varepsilon}_s(\hat{\mathbf{u}}) = \frac{1}{2}(\nabla_s \hat{\mathbf{u}} + \nabla_s \hat{\mathbf{u}}^T)$ is the linearized strain rate tensor in the spatial configuration, $\mathcal{L}_s = L^2(\Omega_s)$, and \mathcal{U}_s and \mathcal{V}_s are, respectively, the linear manifolds of kinematically admissible functions and the space of kinematically admissible variations as previously defined in (2.2.12) and (2.2.13). Also, $\boldsymbol{\sigma}_s$ is the Cauchy stress tensor which is related to the second Piola-Kirchhoff stress tensor \mathbf{S}_m through

$$\boldsymbol{\sigma}_s = \frac{1}{\det \mathbf{F}_s} \mathbf{F}_s (\mathbf{S}_m(\mathbf{E}_m))_s \mathbf{F}_s^T. \quad (2.2.16)$$

where the Piola-Kirchhoff stress tensor is a function of the Green-Lagrange deformation tensor (see equation (2.2.11)) via a constitutive equation (see Section 3.6).

Problem 2 (Forward problem). When the material configuration Ω_m is known, the variational equations (2.2.14)-(2.2.15) can be evaluated in terms of such reference domain, yielding what is known as the *forward problem*. In fact, the variational equations that govern the equilibrium problem expressed now in the *material* domain Ω_m are written as

follows: given a load system described in the material description, $(\mathbf{t}_m^{W,n}, \mathbf{t}_m^{W,t}, \mathbf{t}_m^E, \mathbf{t}_m^A)$, find $(\mathbf{u}_m, \lambda_m) \in \mathcal{U}_m \times \mathcal{L}_m$ such that

$$\begin{aligned} \int_{\Omega_m} \left[-\lambda_m (\mathbf{F}_m^{-T} \cdot \nabla_m \hat{\mathbf{u}}_m) \det \mathbf{F}_m + \mathbf{S}_m(\mathbf{E}_m) \cdot \dot{\mathbf{E}}(\hat{\mathbf{u}}_m) d\Omega_m \right] = \\ \int_{\partial\Omega_m^W} (\mathbf{t}_m^{W,n} \mathbf{F}_m^{-T} \mathbf{n}_0^W \cdot \hat{\mathbf{u}}_m) \det \mathbf{F}_m d\partial\Omega_m^W + \int_{\partial\Omega_m^W} \mathbf{P}_m \mathbf{t}_m^{W,t} \cdot \hat{\mathbf{u}}_m |\mathbf{F}_m^{-T} \mathbf{n}_0^W| \det \mathbf{F}_m d\partial\Omega_m^W \\ + \int_{\partial\Omega_m^E} (\mathbf{t}_m^E \cdot \hat{\mathbf{u}}_m) |\mathbf{F}_m^{-T} \mathbf{n}_0^E| \det \mathbf{F}_m d\partial\Omega_m^E + \sum_{i=1}^C \int_{\partial\Omega_m^{A,i}} (\mathbf{t}_m^{A,i} \cdot \hat{\mathbf{u}}_m) |\mathbf{F}_m^{-T} \mathbf{n}_0^{A,i}| \det \mathbf{F}_m d\partial\Omega_m^{A,i} \end{aligned} \quad \forall \hat{\mathbf{u}}_m \in \mathcal{V}_m, \quad (2.2.17)$$

$$\int_{\Omega_m} (\det \mathbf{F}_m - 1) \hat{\lambda}_m d\Omega_m = 0 \quad \forall \hat{\lambda}_m \in \mathcal{L}_m, \quad (2.2.18)$$

where $\dot{\mathbf{E}}(\hat{\mathbf{u}}_m) = \frac{1}{2}[\mathbf{F}_m^T(\nabla_m \hat{\mathbf{u}}_m) + (\nabla_m \hat{\mathbf{u}}_m)^T \mathbf{F}_m]$, \mathbf{n}_0 is the unit normal vector in the material configuration, \mathbf{P}_m is the projection operator in material description, which is given by

$$\mathbf{P}_m = \mathbf{I} - \frac{\mathbf{F}_m^{-T} \mathbf{n}_0^W}{|\mathbf{F}_m^{-T} \mathbf{n}_0^W|} \otimes \frac{\mathbf{F}_m^{-T} \mathbf{n}_0^W}{|\mathbf{F}_m^{-T} \mathbf{n}_0^W|}, \quad (2.2.19)$$

and $\mathcal{U}_m, \mathcal{V}_m$ and \mathcal{L}_m are the counterparts of $\mathcal{U}_s, \mathcal{V}_s$ and \mathcal{L}_s , respectively, with functions defined in Ω_m .

Remark 2.2. *The Forward problem stated above is the classical equilibrium problem in solid mechanics when the material configuration is known, while the preload problem is a non-traditional formulation of the very same variational equation when the equilibrated (deformed) spatial configuration is known. Therefore, as expected, both mechanical problems, which are non-linear, are governed by the same equilibrium equation, and the difference simply lies in the available data for the problem, and therefore in the corresponding linearized expressions.*

Remark 2.3. *The Preload problem stated above is a mandatory step towards characterizing the mechanical state, i.e. the stress state, of the arterial wall at the spatial configuration (a baseline geometry, e.g. the end-diastolic geometry) with a given so-called baseline hemodynamics loads (e.g. the end-diastolic pressure and tethering stresses). The material configuration is required because it is used to define constitutive equations. Such baseline configuration is usually obtained from medical images, while the baseline hemodynamics loads can be easily estimated either from measurements or from the domain knowledge. Just after solving the Preload problem, the baseline mechanical state (the stress state due to preload) is adequately determined and the Forward problem involving fluid-structure interaction and dimensionally-heterogeneous coupling can be solved to determine the equilibrium configuration for other hemodynamics loads occurring during the cardiac cycle. This is the reason why we need the use of the two forms associated with the evaluation of the mechanical equilibrium. Note that this Preload problem is solved only once, for a given set of loads, and, then, the Forward problem is solved with a time-evolving set of loads given by the action of the blood flow during the cardiac cycle driven by the pulsation of the heart imposed through the coupling with the dimensionally reduced model of the cardiovascular system.*

2.2.4 On the hypothesis of negligible inertial forces

We emphasize that the inertial term could be easily incorporated in the solid problem. However, for the arterial districts investigated in Chapter 4 the stresses associated to inertial forces can be disregarded without affecting the predictive capabilities of the model of the arterial wall. This is easily justified by a straightforward nondimensionalization of the equations (consider for simplicity a cylindrical geometry), which shows that the non-dimensional number α_{in} , representing the ratio between inertial and circumferential stresses arising within the cardiac cycle is of the order of 10^{-6} . In fact, α_{in} can be approximated by

$$\alpha_{in} = \frac{\rho_w \Delta r_i h}{T_p^2 p_i}, \quad (2.2.20)$$

where r_i denotes the inner radius, h the wall thickness, p_i the transmural pressure, Δr_i the inner radius variation, ρ_w the density of the wall and T_p the time it takes to achieve the peak pressure from diastole, all these quantities are corresponding to the current configuration. Given the following values within the physiological range, $r_i = 0.4[cm]$, $\Delta r_i = 0.2r_i$, $h = 0.2r_i$, $p_i = 15 \cdot 10^4 [\frac{dyn}{cm^2}]$, $\rho_w = 1 [\frac{gr}{cm^3}]$ and $T_p = 0.1[s]$, through equation (2.2.20) $\alpha_{in} = 4.267 \cdot 10^{-6}$ is obtained. This also holds for the *Preload problem*, but in order to account for the inertial term the velocity of the body at the equilibrium configuration should be also given. Nevertheless, the inertial term will be negligible due to the image-based geometries being corresponding to diastolic relaxed states with low wall velocities and accelerations.

2.2.5 Linearization procedure of the equilibrium problem

For the two non-linear equilibrium problems formulated in Section 2.2.3, i.e. (i) the mechanical equilibrium when the material configuration Ω_m is known (see (2.2.14) and (2.2.15)), and (ii) the mechanical equilibrium when the spatial configuration Ω_s is known (see (2.2.17) and (2.2.18)), the corresponding linearized forms via the Newton method are here detailed. Furthermore and for the sake of simplicity, in these derivations we limit our presentation to evaluate the contribution of the follower loads ($\mathbf{t}_s^{W,n}$ and $\mathbf{t}_s^{W,t}$) and a general static load \mathbf{t}_s^N acting on a boundary $\partial\Omega_s^N$.

Newton-Raphson method for Preload Problem (data Ω_s ; unknown Ω_m)

For the preload problem the linearization of the variational expressions (2.2.14)-(2.2.15) is here presented. In compact form Problem 1 reads: find $(\mathbf{u}_s, \lambda_s) \in \mathcal{U}_s \times \mathcal{L}_s$ such that

$$\begin{cases} \langle \mathcal{M}_s(\mathbf{u}_s, \lambda_s), \hat{\mathbf{u}}_s \rangle_{\Omega_s} = 0 & \forall \hat{\mathbf{u}}_s \in \mathcal{V}_s \\ \langle \mathcal{N}_s(\mathbf{u}_s), \hat{\lambda}_s \rangle_{\Omega_s} = 0 & \forall \hat{\lambda}_s \in \mathcal{L}_s \end{cases} \quad (2.2.21)$$

We recall that for this case Ω_s is fixed and for each Newton-Raphson iteration a new material configuration Ω_m^k is obtained, with points $\mathbf{x}_m^k = \mathbf{x}_s - \mathbf{u}_s^k$. The Newton-Raphson linearization applied to the above expression at the point $(\mathbf{u}_s^k, \lambda_s^k) \in \mathcal{U}_s \times \mathcal{L}_s$ (displacement and pressure fields at the previous iteration) and the increment/perturbation $(\delta\mathbf{u}_s, \delta\lambda_s) \in \mathcal{V}_s \times \mathcal{L}_s$ gives:

$$\langle \mathcal{M}_s(\mathbf{u}_s^k, \lambda_s^k), \hat{\mathbf{u}}_s \rangle_{\Omega_s} + \frac{d}{d\tau} \langle \mathcal{M}_s(\mathbf{u}_s^k + \tau\delta\mathbf{u}_s, \lambda_s^k + \tau\delta\lambda_s), \hat{\mathbf{u}}_s \rangle_{\Omega_s} \Big|_{\tau=0} = 0 \quad \forall \hat{\mathbf{u}}_s \in \mathcal{V}_s \quad (2.2.22)$$

$$\langle \mathcal{N}_s(\mathbf{u}_s^k), \hat{\lambda}_s \rangle_{\Omega_s} + \frac{d}{d\tau} \langle \mathcal{N}_s(\mathbf{u}_s^k + \tau\delta\mathbf{u}_s), \hat{\lambda}_s \rangle_{\Omega_s} \Big|_{\tau=0} = 0 \quad \forall \hat{\lambda}_s \in \mathcal{L}_s \quad (2.2.23)$$

As shown in Appendix A, to denote the presence of the perturbation $(\tau\delta\mathbf{u}_s)$ into the

quantities that depend on \mathbf{u}_s , we introduce the additional index τ , i.e. $\mathbf{F}_s^{-1} = \mathbf{I} - \nabla_s \mathbf{u}_s$ results in $\mathbf{F}_{s,\tau}^{-1} = \mathbf{I} - \nabla_s \mathbf{u}_{s,\tau} = \mathbf{I} - \nabla_s (\mathbf{u}_s + \tau \delta \mathbf{u}_s)$. For the sake of clarity we omit index k on the displacement field \mathbf{u}_s (and also on quantities that are updated at each iteration, such as \mathbf{F}_s). The expanded expression for the perturbed residual in the material configuration in equation (2.2.22) takes the form

$$\begin{aligned} \langle \mathcal{M}_s(\mathbf{u}_s + \tau \delta \mathbf{u}_s, \lambda_s + \tau \delta \lambda_s), \hat{\mathbf{u}}_s \rangle_{\Omega_s} &= \int_{\Omega_s} [-(\lambda_s + \tau \delta \lambda_s) \operatorname{div}_s \hat{\mathbf{u}}_s + \boldsymbol{\sigma}_{s,\tau} \cdot \boldsymbol{\varepsilon}_s(\hat{\mathbf{u}}_s)] d\Omega_s \\ &+ \int_{\partial \Omega_s^W} \mathbf{P}_s \mathbf{t}_s^{W,t} \cdot \hat{\mathbf{u}}_s d\partial \Omega_s^W + \int_{\partial \Omega_s^W} t_s^{W,n} \mathbf{n}_s \cdot \hat{\mathbf{u}}_s d\partial \Omega_s^W + \int_{\partial \Omega_s^N} \mathbf{t}_s^N \cdot \hat{\mathbf{u}}_s d\partial \Omega_s^N, \end{aligned} \quad (2.2.24)$$

where the perturbed expression for the Cauchy stress tensor $\boldsymbol{\sigma}_{s,\tau}$ reads

$$\boldsymbol{\sigma}_{s,\tau} = \left(\frac{1}{\det \mathbf{F}_{s,\tau}} \mathbf{F}_{s,\tau} \mathbf{S}_{s,\tau} \mathbf{F}_{s,\tau}^T \right). \quad (2.2.25)$$

Analogously, for the second term of (2.2.23), the perturbed residual is written as

$$\langle \mathcal{N}_s(\mathbf{u}_s + \tau \delta \mathbf{u}_s), \hat{\lambda}_s \rangle_{\Omega_s} = \int_{\Omega_s} [1 - \det \mathbf{F}_{s,\tau}^{-1}] \hat{\lambda}_s d\Omega_s. \quad (2.2.26)$$

Using equations (8.1.8)-(8.1.11) from Appendix A, we obtain the derivatives of the perturbed expressions as follows

$$\begin{aligned} \frac{d}{d\tau} \langle \mathcal{M}_s(\mathbf{u}_s + \tau \delta \mathbf{u}_s, \lambda_s + \tau \delta \lambda_s), \hat{\mathbf{u}}_s \rangle_{\Omega_s} \Big|_{\tau=0} &= - \int_{\Omega_s} (\mathbf{F}_s^T \cdot \nabla_s \delta \mathbf{u}_s) \boldsymbol{\sigma}_s \cdot \boldsymbol{\varepsilon}_s(\hat{\mathbf{u}}_s) d\Omega_s \\ &+ \int_{\Omega_s} 2(\mathbf{F}_s (\nabla_s \delta \mathbf{u}_s) \boldsymbol{\sigma}_s) \cdot \boldsymbol{\varepsilon}_s(\hat{\mathbf{u}}_s) d\Omega_s + \int_{\Omega_s} \mathbf{D}_s(\mathbf{F}_s \nabla_s \delta \mathbf{u}_s)^S \cdot \boldsymbol{\varepsilon}_s(\hat{\mathbf{u}}_s) d\Omega_s \\ &- \int_{\Omega_s} \delta \lambda_s \operatorname{div}_s \hat{\mathbf{u}}_s d\Omega_s, \end{aligned} \quad (2.2.27)$$

and

$$\frac{d}{d\tau} \langle \mathcal{N}_s(\mathbf{u}_s + \tau \delta \mathbf{u}_s), \hat{\lambda}_s \rangle_{\Omega_s} \Big|_{\tau=0} = - \int_{\Omega_s} (\mathbf{F}_s^T \cdot \nabla_s \delta \mathbf{u}_s) \hat{\lambda}_s d\Omega_s \quad (2.2.28)$$

where S denotes the symmetric part, and $\mathbf{D}_s(\mathbf{F}_s \nabla_s \delta \mathbf{u}_s)^S$ is given by

$$\mathbf{D}_s(\mathbf{F}_s \nabla_s \delta \mathbf{u}_s)^S = \frac{1}{\det \mathbf{F}_s} \mathbf{F}_s \left[\left(\frac{\partial \mathbf{S}_m}{\partial \mathbf{E}_m} \right)_s \mathbf{F}_s^T (\mathbf{F}_s \nabla_s \delta \mathbf{u}_s)^S \mathbf{F}_s \right] \mathbf{F}_s^T. \quad (2.2.29)$$

Collecting equations (2.2.27) and (2.2.28) we can now formulate the linearized problem: given $(\mathbf{u}_s, \lambda_s)$ (displacement and pressure fields at the previous iteration -omitted k index-) find $(\delta \mathbf{u}_s, \delta \lambda_s) \in \mathcal{V}_s \times \mathcal{L}_s$ such that

$$\begin{cases} d_s(\delta \mathbf{u}_s, \hat{\mathbf{u}}_s) + e_s(\delta \lambda_s, \hat{\mathbf{u}}_s) = g_s(\hat{\mathbf{u}}_s) & \forall \hat{\mathbf{u}}_s \in \mathcal{V}_s \\ f_s(\delta \mathbf{u}_s, \hat{\lambda}_s) = h_s(\hat{\lambda}_s) & \forall \hat{\lambda}_s \in \mathcal{L}_s \end{cases} \quad (2.2.30)$$

with

$$d_s(\delta \mathbf{u}_s, \hat{\mathbf{u}}_s) = - \int_{\Omega_s} (\mathbf{F}_s^T \cdot \nabla_s \delta \mathbf{u}_s) \boldsymbol{\sigma}_s \cdot \boldsymbol{\varepsilon}_s(\hat{\mathbf{u}}_s) d\Omega_s + \int_{\Omega_s} 2(\mathbf{F}_s(\nabla_s \delta \mathbf{u}_s) \boldsymbol{\sigma}_s) \cdot \boldsymbol{\varepsilon}_s(\hat{\mathbf{u}}_s) d\Omega_s \\ + \int_{\Omega_s} \mathbf{D}_s(\mathbf{F}_s \nabla_s \delta \mathbf{u}_s)^S \cdot \boldsymbol{\varepsilon}_s(\hat{\mathbf{u}}_s) d\Omega_s, \quad (2.2.31)$$

$$e_s(\delta \lambda_s, \hat{\mathbf{u}}_s) = - \int_{\Omega_s} \delta \lambda_s \operatorname{div} \hat{\mathbf{u}}_s d\Omega_s, \quad (2.2.32)$$

$$g_s(\hat{\mathbf{u}}_s) = - \int_{\Omega_s} [-\lambda_s \operatorname{div} \hat{\mathbf{u}}_s + \boldsymbol{\sigma}_s \cdot \boldsymbol{\varepsilon}_s(\hat{\mathbf{u}}_s)] d\Omega_s + \int_{\partial\Omega_s^W} \mathbf{P}_s \mathbf{t}_s^W \cdot \hat{\mathbf{u}}_s d\partial\Omega_s^W + \\ \int_{\partial\Omega_s^W} t_s^{W,n} \mathbf{n}_s \cdot \hat{\mathbf{u}}_s d\partial\Omega_s^W + \int_{\partial\Omega_s^N} \mathbf{t}_s^N \cdot \hat{\mathbf{u}}_s d\partial\Omega_s^N \quad (2.2.33)$$

$$f_s(\delta \mathbf{u}_s, \hat{\lambda}_s) = - \int_{\Omega_s} (\mathbf{F}_s^T \cdot \nabla_s \delta \mathbf{u}_s) \hat{\lambda}_s d\Omega_s \quad (2.2.34)$$

$$h_s(\hat{\lambda}_s) = - \int_{\Omega_s} [1 - \det \mathbf{F}_s^{-1}] \hat{\lambda}_s d\Omega_s \quad (2.2.35)$$

Newton-Raphson method for Forward Problem (data Ω_m ; unknown Ω_s)

We now apply the Newton-Raphson linearization procedure to equations (2.2.17)-(2.2.18) and write the expressions in the configuration found in the last iteration. Observe that, in this case, the material configuration Ω_m is fixed and the spatial domain Ω_s^k updated at every iteration where, when convergence is achieved, exact equilibrium is satisfied. As before, we omit index k indicating the quantities at the last iteration. Thus, the problem reads: find $(\mathbf{u}_m, \lambda_m) \in \mathcal{U}_m \times \mathcal{L}_m$ such that

$$\begin{cases} \langle \mathcal{M}_m(\mathbf{u}_m, \lambda_m), \hat{\mathbf{u}}_m \rangle_{\Omega_m} = 0 & \forall \hat{\mathbf{u}}_m \in \mathcal{V}_m \\ \langle \mathcal{N}_m(\mathbf{u}_m), \hat{\lambda}_m \rangle_{\Omega_m} = 0 & \forall \hat{\lambda}_m \in \mathcal{L}_m \end{cases} \quad (2.2.36)$$

The Newton-Raphson linearization applied to the above expression at the point $(\mathbf{u}_m^k, \lambda_m^k) \in \mathcal{U}_m \times \mathcal{L}_m$ and for the increment/perturbation $(\delta \mathbf{u}_m, \delta \lambda_m) \in \mathcal{U}_m \times \mathcal{L}_m$ yields:

$$\langle \mathcal{M}_m(\mathbf{u}_m^k, \lambda_m^k), \hat{\mathbf{u}}_m \rangle_{\Omega_m} + \frac{d}{d\tau} \langle \mathcal{M}_m(\mathbf{u}_m^k + \tau \delta \mathbf{u}_m, \lambda_m^k), \hat{\mathbf{u}}_m \rangle_{\Omega_m} \Big|_{\tau=0} \\ + \frac{d}{d\tau} \langle \mathcal{M}_m(\mathbf{u}_m^k, \lambda_m^k + \tau \delta \lambda_m), \hat{\mathbf{u}}_m \rangle_{\Omega_m} \Big|_{\tau=0} = 0 \quad \forall \hat{\mathbf{u}}_m \in \mathcal{V}_m \quad (2.2.37)$$

$$\langle \mathcal{N}_m(\mathbf{u}_m^k), \hat{\lambda}_m \rangle_{\Omega_m} + \frac{d}{d\tau} \langle \mathcal{N}_m(\mathbf{u}_m^k + \tau \delta \mathbf{u}_m), \hat{\lambda}_m \rangle_{\Omega_m} \Big|_{\tau=0} = 0 \quad \forall \hat{\lambda}_m \in \mathcal{L}_m \quad (2.2.38)$$

As shown in Appendix A, to denote the presence of the perturbation $(\tau \delta \mathbf{u}_m)$ into the quantities that depend on \mathbf{u} we introduce the additional index τ , i.e. $\mathbf{F}_{m,\tau} = \mathbf{I} + \nabla_m(\mathbf{u}_m + \tau \delta \mathbf{u}_m) = \mathbf{F}_m + \tau \nabla_m \delta \mathbf{u}_m$. Analyzing the expanded expression for the perturbed

residual in the material configuration, in the second term of equation (2.2.37), we have

$$\begin{aligned}
& \frac{d}{d\tau} \langle \mathcal{M}_m(\mathbf{u}_m + \tau \delta \mathbf{u}_m, \lambda_m), \hat{\mathbf{u}}_m \rangle_{\Omega_m} \Big|_{\tau=0} = - \int_{\Omega_m} \frac{d}{d\tau} [\lambda_m (\mathbf{F}_{m,\tau}^{-T} \cdot \nabla_m \hat{\mathbf{u}}_m) \det \mathbf{F}_{m,\tau}] \Big|_{\tau=0} d\Omega_m \\
& + \int_{\Omega_m} \frac{d}{d\tau} [\mathbf{S}_m(\mathbf{E}_{m,\tau}) \cdot \dot{\mathbf{E}}_\tau(\hat{\mathbf{u}}_m)] \Big|_{\tau=0} d\Omega_m - \int_{\partial\Omega_m^W} \frac{d}{d\tau} (t_m^{W,n} \mathbf{F}_{m,\tau}^{-T} \mathbf{n}_0 \cdot \hat{\mathbf{u}}_m) \det \mathbf{F}_{m,\tau} \Big|_{\tau=0} d\partial\Omega_m^W \\
& \quad - \int_{\partial\Omega_m^W} \frac{d}{d\tau} \mathbf{P}_{m,\tau} \mathbf{t}_m^{W,t} \cdot \hat{\mathbf{u}}_m |\mathbf{F}_{m,\tau}^{-T} \mathbf{n}_0| \det \mathbf{F}_{m,\tau} \Big|_{\tau=0} d\partial\Omega_m^W \\
& \quad - \int_{\partial\Omega_m^N} \frac{d}{d\tau} (\mathbf{t}_m^N \cdot \hat{\mathbf{u}}_m) |\mathbf{F}_{m,\tau}^{-T} \mathbf{n}_0| \det \mathbf{F}_{m,\tau} \Big|_{\tau=0} d\partial\Omega_m^N, \quad (2.2.39)
\end{aligned}$$

where $\dot{\mathbf{E}}_\tau(\hat{\mathbf{u}}_m) = \frac{1}{2} [\mathbf{F}_{m,\tau}^T (\nabla_m \hat{\mathbf{u}}_m) + (\nabla_m \hat{\mathbf{u}}_m)^T \mathbf{F}_{m,\tau}]$.

Using equations (8.1.1)-(8.1.7) detailed in Appendix A to perform the derivation with respect to τ (and evaluate at $\tau = 0$) the following expression is obtained

$$\begin{aligned}
& \frac{d}{d\tau} \langle \mathcal{M}_m(\mathbf{u}_m + \tau \delta \mathbf{u}_m, \lambda_m), \hat{\mathbf{u}}_m \rangle_{\Omega_m} \Big|_{\tau=0} = \int_{\Omega_m} \lambda_m [(\mathbf{F}_m^{-T} (\nabla_m \delta \mathbf{u}_m)^T \mathbf{F}_m^{-T}) \cdot (\nabla_m \hat{\mathbf{u}}_m)] \det \mathbf{F}_m d\Omega_m \\
& \quad - \int_{\Omega_m} \lambda_m [(\mathbf{F}_m^{-T} \cdot (\nabla_m \delta \mathbf{u}_m)) (\mathbf{F}_m^{-T} \cdot (\nabla_m \hat{\mathbf{u}}_m))] \det \mathbf{F}_m d\Omega_m \\
& \quad + \int_{\Omega_m} \left(\frac{\partial \mathbf{S}_m}{\partial \mathbf{E}_m} ((\nabla_m \delta \mathbf{u}_m)^T \mathbf{F}_m)^S \right) \cdot \dot{\mathbf{E}}(\hat{\mathbf{u}}_m) d\Omega_m \\
& \quad + \int_{\Omega_m} \mathbf{S}_m(\mathbf{E}_m) \cdot ((\nabla_m \delta \mathbf{u}_m)^T (\nabla_m \hat{\mathbf{u}}_m))^S d\Omega_m \\
& \quad - \int_{\partial\Omega_m^W} (t_m^{W,n} \mathbf{F}_m^{-T} \mathbf{n}_0 \cdot \hat{\mathbf{u}}_m) \det \mathbf{F}_m (\mathbf{F}_m^{-T} \cdot \nabla_m \delta \mathbf{u}_m) d\partial\Omega_m^W \\
& \quad - \int_{\partial\Omega_m^W} [t_m^{W,n} (-\mathbf{F}_m^{-T} (\nabla_m \delta \mathbf{u}_m)^T \mathbf{F}_m^{-T}) \mathbf{n}_0 \cdot \hat{\mathbf{u}}_m] \det \mathbf{F}_m d\partial\Omega_m^W \\
& \quad - \int_{\partial\Omega_m^W} \left[\frac{d}{d\tau} \frac{\mathbf{F}_{m,\tau}^{-T} \mathbf{n}_0}{|\mathbf{F}_{m,\tau}^{-T} \mathbf{n}_0|} \Big|_{\tau=0} \otimes \frac{\mathbf{F}_m^{-T} \mathbf{n}_0}{|\mathbf{F}_m^{-T} \mathbf{n}_0|} \right]^S \mathbf{t}_m^{W,t} \cdot \hat{\mathbf{u}}_m |\mathbf{F}_m^{-T} \mathbf{n}_0| \det \mathbf{F}_m d\partial\Omega_m^W \\
& \quad - \int_{\partial\Omega_m^W} \mathbf{P}_m \mathbf{t}_m^{W,t} \cdot \hat{\mathbf{u}}_m |\mathbf{F}_m^{-T} \mathbf{n}_0| \det \mathbf{F}_m (\mathbf{F}_m^{-T} \cdot \nabla_m \delta \mathbf{u}_m) d\partial\Omega_m^W \\
& \quad - \int_{\partial\Omega_m^W} \mathbf{P}_m \mathbf{t}_m^{W,t} \cdot \hat{\mathbf{u}}_m \frac{(-\mathbf{F}_m^{-T} (\nabla_m \delta \mathbf{u}_m)^T \mathbf{F}_m^{-T}) \mathbf{n}_0 \cdot \mathbf{F}_m^{-T} \mathbf{n}_0}{|\mathbf{F}_m^{-T} \mathbf{n}_0|} \det \mathbf{F}_m d\partial\Omega_m^W \\
& \quad - \int_{\partial\Omega_m^N} (\mathbf{t}_m^N \cdot \hat{\mathbf{u}}_m) |\mathbf{F}_m^{-T} \mathbf{n}_0| \det \mathbf{F}_m (\mathbf{F}_m^{-T} \cdot \nabla_m \delta \mathbf{u}_m) d\partial\Omega_m^N \\
& \quad - \int_{\partial\Omega_m^N} (\mathbf{t}_m^N \cdot \hat{\mathbf{u}}_m) \frac{(-\mathbf{F}_m^{-T} (\nabla_m \delta \mathbf{u}_m)^T \mathbf{F}_m^{-T}) \mathbf{n}_0 \cdot \mathbf{F}_m^{-T} \mathbf{n}_0}{|\mathbf{F}_m^{-T} \mathbf{n}_0|} \det \mathbf{F}_m d\partial\Omega_m^N, \quad (2.2.40)
\end{aligned}$$

with $\frac{d}{dt} \frac{\mathbf{F}_{m,\tau}^{-T} \mathbf{n}_0}{|\mathbf{F}_{m,\tau}^{-T} \mathbf{n}_0|} \Big|_{\tau=0}$ given by expression (8.1.7) provided in Appendix A. Similarly, for the contribution of the third term of (2.2.37), a perturbation ($\tau \delta \lambda_m$) is introduced, and the expression is derived. The calculation of this term is straightforward since $\langle \mathcal{R}_m, \hat{\mathbf{u}}_m \rangle_{\Omega_m}$ is linear in λ_m , then

$$\frac{d}{d\tau} \langle \mathcal{M}_m(\mathbf{u}_m, \lambda_m + \tau \delta \lambda_m), \hat{\mathbf{u}}_m \rangle_{\Omega_m} \Big|_{\tau=0} = - \int_{\Omega_m} \delta \lambda_m (\mathbf{F}_m^{-T} \cdot \nabla_m \hat{\mathbf{u}}_m) \det \mathbf{F}_m d\Omega_m. \quad (2.2.41)$$

Finally, the second term of (2.2.38) yields

$$\frac{d}{d\tau} \langle \mathcal{N}_m(\mathbf{u}_m + \tau \delta \mathbf{u}_m), \hat{\lambda}_m \rangle_{\Omega_m} \Big|_{\tau=0} = \int_{\Omega_m} \det \mathbf{F}_m (\mathbf{F}_m^{-T} \cdot \nabla_m \delta \mathbf{u}_m) \hat{\lambda}_m d\Omega_m. \quad (2.2.42)$$

With these blocks we are able to write the linear problem: given $(\mathbf{u}_m, \lambda_m)$ (displacement and pressure fields at previous iteration -omitted k index-), find $(\delta \mathbf{u}_m, \delta \lambda_m) \in \mathcal{V}_m \times \mathcal{L}_m$ such that

$$\begin{cases} a_m(\delta \mathbf{u}_m, \hat{\mathbf{u}}_m) + b_m(\delta \lambda_m, \hat{\mathbf{u}}_m) = l_m(\hat{\mathbf{u}}_m) & \forall \hat{\mathbf{u}}_m \in \mathcal{V}_m \\ c_m(\delta \mathbf{u}_m, \hat{\lambda}_m) = m_m(\hat{\lambda}_m) & \forall \hat{\lambda}_m \in \mathcal{L}_m \end{cases} \quad (2.2.43)$$

where the linear and bilinear forms are the following

$$\begin{aligned} l_m(\hat{\mathbf{u}}_m) &= \int_{\Omega_m} \lambda_m (\mathbf{F}_m^{-T} \cdot \nabla_m \hat{\mathbf{u}}_m) \det \mathbf{F}_m d\Omega_m - \int_{\Omega_m} \mathbf{S}_m(\mathbf{E}_m) \cdot \dot{\mathbf{E}}(\hat{\mathbf{u}}_m) d\Omega_m \\ &+ \int_{\partial \Omega_m^W} (t_m^{W,n} \mathbf{F}_m^{-T} \mathbf{n}_0 \cdot \hat{\mathbf{u}}_m) \det \mathbf{F}_m d\partial \Omega_m^W + \int_{\partial \Omega_m^W} \mathbf{P}_m \mathbf{t}_m^{W,t} \cdot \hat{\mathbf{u}}_m \frac{\det \mathbf{F}_m}{|\mathbf{F}_m^{-T} \mathbf{n}_0|} d\partial \Omega_m^W \\ &+ \int_{\partial \Omega_m^N} (\mathbf{t}_m^N \cdot \hat{\mathbf{u}}_m) |\mathbf{F}_m^{-T} \mathbf{n}_0| \det \mathbf{F}_m d\partial \Omega_m^N, \end{aligned} \quad (2.2.44)$$

$$\begin{aligned}
a_m((\delta \mathbf{u}_m), \hat{\mathbf{u}}_m) &= \int_{\Omega_m} \lambda_m \left[\left(\mathbf{F}_m^{-T} (\nabla_m \delta \mathbf{u}_m)^T \mathbf{F}_m^{-T} \right) \cdot (\nabla_m \hat{\mathbf{u}}_m) \right] \det \mathbf{F}_m d\Omega_m \\
&\quad - \int_{\Omega_m} \lambda_m \left[\left(\mathbf{F}_m^{-T} \cdot (\nabla_m \delta \mathbf{u}_m) \right) \left(\mathbf{F}_m^{-T} \cdot (\nabla_m \hat{\mathbf{u}}_m) \right) \right] \det \mathbf{F}_m d\Omega_m \\
+ \int_{\Omega_m} \left(\frac{\partial \mathbf{S}_m}{\partial \mathbf{E}_m} \left((\nabla_m \delta \mathbf{u}_m)^T \mathbf{F}_m \right)^S \right) \cdot \dot{\mathbf{E}}(\hat{\mathbf{u}}_m) d\Omega_m &+ \int_{\Omega_m} \mathbf{S}_m(\mathbf{E}_m) \cdot \left((\nabla_m \delta \mathbf{u}_m)^T (\nabla_m \hat{\mathbf{u}}_m) \right)^S d\Omega_m \\
&\quad - \int_{\partial \Omega_m^W} \left(t_m^{W,n} \mathbf{F}_m^{-T} \mathbf{n}_0 \cdot \hat{\mathbf{u}}_m \right) \det \mathbf{F}_m \left(\mathbf{F}_m^{-T} \cdot \nabla_m \delta \mathbf{u}_m \right) d\partial \Omega_m^W \\
&\quad - \int_{\partial \Omega_m^W} \left[t_m^{W,n} \left(-\mathbf{F}_m^{-T} (\nabla_m \delta \mathbf{u}_m)^T \mathbf{F}_m^{-T} \right) \mathbf{n}_0 \cdot \hat{\mathbf{u}}_m \right] \det \mathbf{F}_m d\partial \Omega_m^W \\
&\quad - \int_{\partial \Omega_m^W} \left[\frac{d}{d\tau} \frac{\mathbf{F}_{m,\tau}^{-T} \mathbf{n}_0}{|\mathbf{F}_{m,\tau}^{-T} \mathbf{n}_0|} \Big|_{\tau=0} \otimes \frac{\mathbf{F}_m^{-T} \mathbf{n}_0}{|\mathbf{F}_m^{-T} \mathbf{n}_0|} \right]^S \mathbf{t}_m^{W,t} \cdot \hat{\mathbf{u}}_m |\mathbf{F}_m^{-T} \mathbf{n}_0| \det \mathbf{F}_m d\partial \Omega_m^W \\
&\quad - \int_{\partial \Omega_m^W} \mathbf{P}_m \mathbf{t}_m^{W,t} \cdot \hat{\mathbf{u}}_m |\mathbf{F}_m^{-T} \mathbf{n}_0| \det \mathbf{F}_m \left(\mathbf{F}_m^{-T} \cdot \nabla_m \delta \mathbf{u}_m \right) d\partial \Omega_m^W \\
&\quad - \int_{\partial \Omega_m^W} \mathbf{P}_m \mathbf{t}_m^{W,t} \cdot \hat{\mathbf{u}}_m \frac{\left(-\mathbf{F}_m^{-T} (\nabla_m \delta \mathbf{u}_m)^T \mathbf{F}_m^{-T} \right) \mathbf{n}_0 \cdot \mathbf{F}_m^{-T} \mathbf{n}_0}{|\mathbf{F}_m^{-T} \mathbf{n}_0|} \det \mathbf{F}_m d\partial \Omega_m^W \\
&\quad - \int_{\partial \Omega_m^N} \left(\mathbf{t}_m^N \cdot \hat{\mathbf{u}}_m \right) |\mathbf{F}_m^{-T} \mathbf{n}_0| \det \mathbf{F}_m \left(\mathbf{F}_m^{-T} \cdot \nabla_m \delta \mathbf{u}_m \right) d\partial \Omega_m^N \\
&\quad - \int_{\partial \Omega_m^N} \left(\mathbf{t}_m^N \cdot \hat{\mathbf{u}}_m \right) \frac{\left(-\mathbf{F}_m^{-T} (\nabla_m \delta \mathbf{u}_m)^T \mathbf{F}_m^{-T} \right) \mathbf{n}_0 \cdot \mathbf{F}_m^{-T} \mathbf{n}_0}{|\mathbf{F}_m^{-T} \mathbf{n}_0|} \det \mathbf{F}_m d\partial \Omega_m^N, \quad (2.2.45)
\end{aligned}$$

$$b_m(\delta \lambda_m, \hat{\mathbf{u}}_m) = - \int_{\Omega_m} \delta \lambda_m \left(\mathbf{F}_m^{-T} \cdot \nabla_m \hat{\mathbf{u}}_m \right) \det \mathbf{F}_m d\Omega_m, \quad (2.2.46)$$

$$c_m(\delta \mathbf{u}_m, \hat{\lambda}_m) = \int_{\Omega_m} \det \mathbf{F}_m \left(\mathbf{F}_m^{-T} \cdot \nabla_m \delta \mathbf{u}_m \right) \hat{\lambda}_m d\Omega_m, \quad (2.2.47)$$

and

$$m_m(\hat{\lambda}_m) = - \int_{\Omega_m} (\det \mathbf{F}_m - 1) \hat{\lambda}_m d\Omega_m \quad (2.2.48)$$

The above linear problem is convenient to be rewritten (evaluated) in terms of the variables now defined in the updated configuration Ω_s^k (written as Ω_s for sake of simplicity, omitting k index as before), with points $\mathbf{x}_s^k = \mathbf{x}_m + \mathbf{u}_m^k$. To do that, as a first step we seek for the spatial expression of the tangent components. With the expressions provided in Appendix

A in mind, we can write the spatial version of (2.2.40) as

$$\begin{aligned}
& \left. \frac{d}{d\tau} \langle \mathcal{M}_s(\mathbf{u}_s^k + \tau \delta \mathbf{u}_s, \lambda_s), \hat{\mathbf{u}}_s \rangle_{\Omega_s} \right|_{\tau=0} = \\
& \int_{\Omega_s} \lambda_s ((\nabla_s \delta \mathbf{u}_s)^T \cdot (\nabla_s \hat{\mathbf{u}}_s) - (\operatorname{div}_s \delta \mathbf{u}_s)(\operatorname{div}_s \hat{\mathbf{u}}_s)) d\Omega_s \\
& + \int_{\Omega_s} (\mathbf{D}_s \boldsymbol{\varepsilon}_s(\delta \mathbf{u}_s) \cdot \boldsymbol{\varepsilon}_s(\hat{\mathbf{u}}_s) + (\nabla_s \delta \mathbf{u}_s) \boldsymbol{\sigma}_s \cdot (\nabla_s \hat{\mathbf{u}}_s)) d\Omega_s \\
& + \int_{\partial \Omega_m^W} [t_s^{W,n} ((\nabla_s \delta \mathbf{u}_s)^T - \mathbf{I}) \mathbf{n}_s \cdot \hat{\mathbf{u}}_s] \operatorname{div}_s \delta \mathbf{u}_s d\partial \Omega_s^W \\
& - \int_{\partial \Omega_s^W} (\mathbf{H}(\delta \mathbf{u}_s) \mathbf{n}_s \otimes \mathbf{n}_s)^S \mathbf{t}_s^{W,t} \cdot \hat{\mathbf{u}}_s d\partial \Omega_s^W - \int_{\partial \Omega_m^W} \mathbf{P}_s \mathbf{t}_s^{W,t} \cdot \hat{\mathbf{u}}_s (\operatorname{div}_s \delta \mathbf{u}_s) d\partial \Omega_s^W \\
& \quad - \int_{\partial \Omega_m^W} \mathbf{P}_s \mathbf{t}_s^{W,t} \cdot \hat{\mathbf{u}}_s (-\nabla_s \delta \mathbf{u}_s)^T \mathbf{n}_s \cdot \mathbf{n}_s d\partial \Omega_s^W \\
& \quad - \int_{\partial \Omega_s^N} (\mathbf{t}_s^N \cdot \hat{\mathbf{u}}_s) [(\operatorname{div}_s \delta \mathbf{u}_s) - (\nabla_s \delta \mathbf{u}_s)^T \mathbf{n}_s \cdot \mathbf{n}_s] d\partial \Omega_s^N \quad (2.2.49)
\end{aligned}$$

where $\mathbf{H}(\delta \mathbf{u}_s)$ stands for

$$\mathbf{H}(\delta \mathbf{u}_s) = \left[-(\nabla_s \delta \mathbf{u}_s)^T + ((\nabla_s \delta \mathbf{u}_s)^T \mathbf{n}_s \cdot \mathbf{n}_s) \mathbf{I} \right], \quad (2.2.50)$$

and recalling (2.2.29) $\mathbf{D}_s \boldsymbol{\varepsilon}_s(\delta \mathbf{u}_s)$ is given by

$$\mathbf{D}_s \boldsymbol{\varepsilon}_s(\delta \mathbf{u}_s) = \frac{1}{\det \mathbf{F}_s} \mathbf{F}_s \left[\left(\frac{\partial \mathbf{S}_m}{\partial \mathbf{E}_m} \right)_s \mathbf{F}_s^T \boldsymbol{\varepsilon}_s(\delta \mathbf{u}_s) \mathbf{F}_s \right] \mathbf{F}_s^T. \quad (2.2.51)$$

Now we add and subtract the term $\lambda_s (\nabla_s \delta \mathbf{u}_s) \cdot (\nabla_s \hat{\mathbf{u}}_s)$ into equation (2.2.49) and consider the operation with second order tensors

$$\lambda_s (\operatorname{div}_s \delta \mathbf{u}_s)(\operatorname{div}_s \hat{\mathbf{u}}_s) = \lambda_s (\mathbf{I} \otimes \mathbf{I}) \boldsymbol{\varepsilon}_s(\delta \mathbf{u}_s) \cdot \boldsymbol{\varepsilon}_s(\hat{\mathbf{u}}_s), \quad (2.2.52)$$

which leads us to

$$\begin{aligned}
& \left. \frac{d}{d\tau} \langle \mathcal{M}_s(\mathbf{u}_s + \tau \delta \mathbf{u}_s, \lambda_s), \hat{\mathbf{u}}_s \rangle_{\Omega_s} \right|_{\tau=0} = \int_{\Omega_s} (\mathbf{D}_s + \lambda_s (2\mathbf{I} - (\mathbf{I} \otimes \mathbf{I}))) \boldsymbol{\varepsilon}_s(\delta \mathbf{u}_s) \cdot \boldsymbol{\varepsilon}_s(\hat{\mathbf{u}}_s) d\Omega_s \\
& + \int_{\Omega_s} (\nabla_s \delta \mathbf{u}_s) \boldsymbol{\sigma}_s \cdot (\nabla_s \hat{\mathbf{u}}_s) d\Omega_s + \int_{\partial \Omega_m^W} [t_s^{W,n} ((\nabla_s \delta \mathbf{u}_s)^T - \mathbf{I}) \mathbf{n}_s \cdot \hat{\mathbf{u}}_s] \operatorname{div}_s \delta \mathbf{u}_s d\partial \Omega_s^W \\
& - \int_{\partial \Omega_s^W} (\mathbf{H}(\delta \mathbf{u}_s) \mathbf{n}_s \otimes \mathbf{n}_s)^S \mathbf{t}_s^{W,t} \cdot \hat{\mathbf{u}}_s d\partial \Omega_s^W - \int_{\partial \Omega_m^W} \mathbf{P}_s \mathbf{t}_s^{W,t} \cdot \hat{\mathbf{u}}_s (\operatorname{div}_s \delta \mathbf{u}_s) d\partial \Omega_s^W \\
& \quad - \int_{\partial \Omega_m^W} \mathbf{P}_s \mathbf{t}_s^{W,t} \cdot \hat{\mathbf{u}}_s (-\nabla_s \delta \mathbf{u}_s)^T \mathbf{n}_s \cdot \mathbf{n}_s d\partial \Omega_s^W \\
& \quad - \int_{\partial \Omega_s^N} (\mathbf{t}_s^N \cdot \hat{\mathbf{u}}_s) [(\operatorname{div}_s \delta \mathbf{u}_s) - (\nabla_s \delta \mathbf{u}_s)^T \mathbf{n}_s \cdot \mathbf{n}_s] d\partial \Omega_s^N \quad (2.2.53)
\end{aligned}$$

where \mathbb{I} and \mathbf{I} are the fourth and second order identity tensors, respectively. Analogously, the spatial expressions (2.2.41) and (2.2.42) result in

$$\frac{d}{d\tau} \langle \mathcal{M}_s(\mathbf{u}_s, \lambda_s + \tau \delta \lambda_s), \hat{\mathbf{u}}_s \rangle_{\Omega_s} \Big|_{\tau=0} = - \int_{\Omega_s} \delta \lambda_s \operatorname{div}_s \hat{\mathbf{u}}_s d\Omega_s, \quad (2.2.54)$$

and

$$\frac{d}{d\tau} \langle \mathcal{N}_s(\mathbf{u}_s + \tau \delta \mathbf{u}_s, \lambda_s), \hat{\lambda}_s \rangle_{\Omega_s} \Big|_{\tau=0} = \int_{\Omega_s} \operatorname{div}_s \delta \mathbf{u}_s \hat{\lambda}_s d\Omega_s. \quad (2.2.55)$$

Hence, from equations (2.2.49), (2.2.54) and (2.2.55), the spatial form of the linearized problem for incompressible materials is formulated as follows: given $(\mathbf{u}_s, \lambda_s)$ (displacement and pressure fields at previous Newton-Raphson iteration -omitted k index-) find $(\delta \mathbf{u}_s, \delta \lambda_s) \in \mathcal{V}_s \times \mathcal{L}_s$ such that

$$\begin{cases} a_s(\delta \mathbf{u}_s, \hat{\mathbf{u}}_s) + b_s(\delta \lambda_s, \hat{\mathbf{u}}_s) = l_s(\hat{\mathbf{u}}_s) & \forall \hat{\mathbf{u}}_s \in \mathcal{V}_s \\ c_s(\delta \mathbf{u}_s, \hat{\lambda}_s) = m_s(\hat{\lambda}_s) & \forall \hat{\lambda}_s \in \mathcal{L}_s \end{cases} \quad (2.2.56)$$

where the bilinear and linear forms are given by

$$\begin{aligned} a_s(\delta \mathbf{u}_s, \hat{\mathbf{u}}_s) &= \int_{\Omega_s} [\mathbf{D}_s + \lambda_s (2\mathbb{I} - (\mathbf{I} \otimes \mathbf{I}))] \boldsymbol{\varepsilon}_s(\delta \mathbf{u}_s) \cdot \boldsymbol{\varepsilon}_s(\hat{\mathbf{u}}_s) d\Omega_s \\ &+ \int_{\Omega_s} (\nabla_s \delta \mathbf{u}_s) \boldsymbol{\sigma}_s \cdot (\nabla_s \hat{\mathbf{u}}_s) d\Omega_s + \int_{\partial \Omega_s^W} [t_s^{W,n} ((\nabla_s \delta \mathbf{u}_s)^T - \mathbf{I}) \mathbf{n}_s^W \cdot \hat{\mathbf{u}}_s] \operatorname{div}_s \delta \mathbf{u}_s d\partial \Omega_s^W \\ &- \int_{\partial \Omega_s^W} (\mathbf{H}(\delta \mathbf{u}_s) \mathbf{n}_s \otimes \mathbf{n}_s)^S \mathbf{t}_s^{W,t} \cdot \hat{\mathbf{u}}_s d\partial \Omega_s^W - \int_{\partial \Omega_m^W} \mathbf{P}_s \mathbf{t}_s^{W,t} \cdot \hat{\mathbf{u}}_s (\operatorname{div}_s \delta \mathbf{u}_s) d\partial \Omega_s^W \\ &- \int_{\partial \Omega_m^W} \mathbf{P}_s \mathbf{t}_s^{W,t} \cdot \hat{\mathbf{u}}_s \left(-(\nabla_s \delta \mathbf{u}_s)^T \mathbf{n}_s \cdot \mathbf{n}_s \right) d\partial \Omega_s^W \\ &- \int_{\partial \Omega_s^N} (\mathbf{t}_s^N \cdot \hat{\mathbf{u}}_s) \left[(\operatorname{div}_s \delta \mathbf{u}_s) - (\nabla_s \delta \mathbf{u}_s)^T \mathbf{n}_s \cdot \mathbf{n}_s \right] d\partial \Omega_s^N \end{aligned} \quad (2.2.57)$$

$$b_s(\delta \lambda_s, \hat{\mathbf{u}}_s) = - \int_{\Omega_s} \delta \lambda_s \operatorname{div}_s \hat{\mathbf{u}}_s d\Omega_s, \quad (2.2.58)$$

$$\begin{aligned} l_s(\hat{\mathbf{u}}_s) &= - \int_{\Omega_s} [-\lambda_s \operatorname{div}_s \hat{\mathbf{u}}_s + \boldsymbol{\sigma}_s \cdot \boldsymbol{\varepsilon}_s(\hat{\mathbf{u}}_s)] d\Omega_s + \int_{\partial \Omega_s^W} \mathbf{P}_s \mathbf{t}_s^W \cdot \hat{\mathbf{u}}_s d\partial \Omega_s^W + \int_{\partial \Omega_s^W} t_s^{W,n} \mathbf{n}_s \cdot \hat{\mathbf{u}}_s d\partial \Omega_s^W \\ &+ \int_{\partial \Omega_s^N} \mathbf{t}_s^N \cdot \hat{\mathbf{u}}_s d\partial \Omega_s^N, \end{aligned} \quad (2.2.59)$$

$$c_s(\delta \mathbf{u}_s, \hat{\lambda}_s) = \int_{\Omega_s} \operatorname{div}_s \delta \mathbf{u}_s \hat{\lambda}_s d\Omega_s, \quad (2.2.60)$$

and

$$m_s(\hat{\lambda}_s) = - \int_{\Omega_s} (1 - \det \mathbf{F}_s^{-1}) \hat{\lambda}_s d\Omega_s. \quad (2.2.61)$$

2.3 Fluid mechanics in deformable domains

2.3.1 Setting for ALE formulation

The ALE formulation is particularly useful in flow problems involving deforming domains (Donea and Huerta, 2003; Hughes, 1987; Löhner, 2008), e.g., in FSI problems with finite displacements. Within this framework, a reference deformable domain is introduced and the fluid motion is described in terms of the coordinates of such domain.

Consider the kinematic setting shown in Figure 2.2. Let Υ_t be the domain representing the lumen of the vessel at a given time t , and Υ_0 a reference configuration of this domain at $t = t_0$.

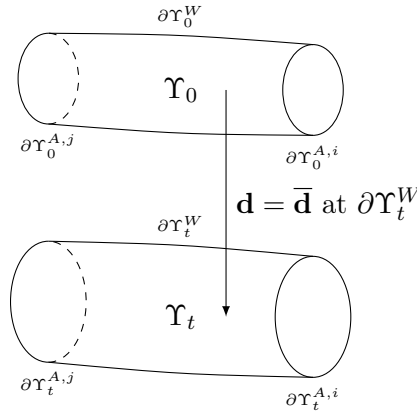


Figure 2.2: ALE kinematic setting.

Considering $t \in \{0, T\}$, the boundary is defined by $\partial\Upsilon_t = \partial\Upsilon_t^{A,i} \cup \partial\Upsilon_t^W$, $i = 1, \dots, C$, where $\partial\Upsilon_t^{A,i}$ is the i th inflow/outflow -artificial- boundary, $i = 1, \dots, C$, being C the number of inflow/outflow artificial boundaries resulting from isolating the vessel geometry from the rest of the cardiovascular system. The interface with the arterial wall is $\partial\Upsilon_t^W$ (fluid-solid interface). Points in the mentioned configurations are denoted by \mathbf{x}_t and \mathbf{x}_0 , accordingly.

In this section, \mathbf{v} and p are employed to denote fluid velocity and pressure, respectively, and \mathbf{d} denotes the displacement (and velocity) of the domain Υ_t with respect to the reference configuration Υ_0 . All these fields are defined in the spatial domain Υ_t .

The displacement (and velocity) of the fluid-solid interface $\partial\Upsilon_t^W$ equals the displacement of the arterial wall. This is the kinematic coupling condition for the FSI problem, that is

$$\mathbf{d}|_{\partial\Upsilon_t^W} = \bar{\mathbf{d}}_t, \quad (2.3.1)$$

where $\bar{\mathbf{d}}_t$ represents the displacement of the arterial wall at the fluid-solid interface. If the reference configuration Υ_0 is chosen to be the lumen enclosed within an image-based configuration (say Ω_I , with displacements \mathbf{u}^I), then it follows that

$$\bar{\mathbf{d}}_t = \mathbf{u}_s|_{\partial\Omega_s^W} - \mathbf{u}_s^I|_{\partial\Omega_s^W}, \quad (2.3.2)$$

where $\mathbf{u}_s|_{\partial\Omega_s^W}$ denotes the solid displacements at the fluid-structure interface for a given time t . As is customary in the specialized literature (Quarteroni et al, 2001), the displacement field on the interior of the deformable domain is obtained through an harmonic extension of the boundary values, that is by solving the problem described next.

Problem 3 (Harmonic extension for deformable domain).

Given the displacement field at the domain boundary $\partial\Upsilon_t^W$, find the displacement field

$\mathbf{d}_t \in \mathcal{D}_t = \mathbf{d} \in \mathbf{H}^1(\Upsilon_t)$, $\mathbf{d}|_{\partial\Upsilon_t^W} = \bar{\mathbf{d}}_t$ such that

$$\int_{\Upsilon_t} \nabla \mathbf{d} \cdot \nabla \hat{\mathbf{d}} \, d\Upsilon_t = 0 \quad \forall \hat{\mathbf{d}} \in \mathcal{D}_t^*, \quad (2.3.3)$$

with $\mathcal{D}_t^* = \mathbf{d} \in \mathbf{H}^1(\Upsilon_t)$, $\mathbf{d}|_{\partial\Upsilon_t^W} = \mathbf{0}$ being the space of kinematically admissible variations associated to \mathcal{D}_t .

Note that, theoretically, it is possible to select any other method to extend the boundary displacements into the domain without modifying the problem, for example, we could take the Navier elasticity equations. It is necessary to avoid mesh deformations that lead to an exaggerated distortion of the elements, hindering the convergence of the numerical methods and degrading the obtained results. This motivates the introduction of constraints over the deformation of the elements in the context of finite element implementations.

2.3.2 Equilibrium equations

Here a variational formulation for the incompressible flow of a Newtonian fluid in a deformable domain expressed in the spatial configuration is presented. Since all the quantities are expressed in terms of spatial coordinates \mathbf{x}_t , subscripts are omitted to simplify the notation. No-slip boundary conditions are imposed on $\partial\Upsilon_t^W$ for the velocity field. Neumann boundary conditions on the artificial boundaries $\partial\Upsilon_t^{A,i}$, $i = 1, \dots, C$, are considered and denoted by \mathbf{t}_t^i . These loads correspond to the action of the rest of the cardiovascular system (CVS) over such boundaries. Such coupling with the rest of the CVS is addressed in Section 3.5. The traction \mathbf{t}_t^i is assumed to be a vector pointing in the direction of the normal vector \mathbf{n}^i , so we directly write $\mathbf{t}_t^i = t_t^i \mathbf{n}^i$, where t_t^i is the magnitude of the traction vector and \mathbf{n}^i is the outward unit normal of $\partial\Upsilon_t^{A,i}$, $i = 1, \dots, C$. Forces per unit volume are neglected. With this setting, the variational problem is formulated as follows.

Problem 4 (Fluid problem in ALE setting).

For every $t \in [0, T]$ find $(\mathbf{v}, p) \in \mathcal{U}_t \times \mathcal{P}_t$ such that

$$\int_{\Upsilon_t} \rho \frac{\partial \mathbf{v}}{\partial t} \cdot \hat{\mathbf{v}} \, d\Upsilon_t + \int_{\Upsilon_t} \rho \nabla \mathbf{v} (\mathbf{v} - \mathbf{v}_R) \cdot \hat{\mathbf{v}} \, d\Upsilon_t - \int_{\Upsilon_t} p \operatorname{div} \hat{\mathbf{v}} \, d\Upsilon_t + \int_{\Upsilon_t} \bar{\boldsymbol{\sigma}}(\mathbf{v}) \cdot \boldsymbol{\varepsilon}(\hat{\mathbf{v}}) \, d\Upsilon_t = \sum_{i=1}^C \int_{\partial\Upsilon_t^{A,i}} t_t^i \mathbf{n}^i \cdot \hat{\mathbf{v}} \, d\partial\Upsilon_t^{A,i} \quad \forall \hat{\mathbf{v}} \in \mathcal{V}_t, \quad (2.3.4)$$

$$\int_{\Upsilon_t} \hat{p} \operatorname{div} \mathbf{v} \, d\Upsilon_t = 0 \quad \forall \hat{p} \in \mathcal{P}_t, \quad (2.3.5)$$

where \mathbf{d} is the solution of (2.3.3), ρ is the fluid density, $\boldsymbol{\sigma}$ is the Cauchy stress tensor such that $\boldsymbol{\sigma} = -p\mathbf{I} + \bar{\boldsymbol{\sigma}}$, which for a Newtonian incompressible fluid it is $\bar{\boldsymbol{\sigma}} = 2\mu\boldsymbol{\varepsilon}(\mathbf{v})$, μ is the dynamic viscosity, and the velocity of the frame of reference is $\mathbf{v}_R = \left(\frac{\partial \mathbf{d}_t}{\partial t}\right)_t = \mathbf{F}_t^A \frac{\partial \mathbf{d}_t}{\partial t}$, where $\mathbf{F}_t^A = \frac{\partial \mathbf{x}_t}{\partial \mathbf{x}_0}$. Also the sets of kinematically admissible functions are given by

$$\begin{aligned} \mathcal{U}_t &= \mathbf{v} \in \mathbf{H}^1(\Upsilon_t), \mathbf{v}|_{\partial\Upsilon_t^W} = \left(\frac{\partial \bar{\mathbf{d}}}{\partial t}\right)_t, \\ \mathcal{P}_t &= L^2(\Upsilon_t), \end{aligned} \quad (2.3.6)$$

and \mathcal{V}_t is the corresponding linear space of kinematically admissible variations obtained from taking differences in the linear manifold \mathcal{U}_t .

2.3.3 Problem linearization

In order to solve numerically the system of equations, a fixed-point linearization method is employed, where the velocity of the reference domain at each iteration is calculated as $\mathbf{v}_R^k = \frac{\mathbf{d}^k - \mathbf{d}^n}{\Delta t}$ (other choices are also viable), where superscripts k and n refer to the previous fixed point iteration and previous time-step, respectively. Hence, the proposed fixed-point method reads: for each iteration $k = 0, 1, \dots$ find $(\mathbf{v}^{k+1}, p^{k+1}, \mathbf{d}^{k+1}) \in (\mathcal{U}_k \times \mathcal{P}_k \times \mathcal{D}_k)$ such that

$$\begin{aligned} \int_{\Upsilon_k} \rho \frac{\partial \mathbf{v}^{k+1}}{\partial t} \cdot \hat{\mathbf{v}} \, d\Upsilon_k + \int_{\Upsilon_k} \rho \nabla \mathbf{v}^{k+1} (\mathbf{v}^k - \mathbf{v}_R^k) \cdot \hat{\mathbf{v}} \, d\Upsilon_k - \int_{\Upsilon_k} p^{k+1} \operatorname{div} \hat{\mathbf{v}} \, d\Upsilon_k \\ + \int_{\Upsilon_k} \bar{\boldsymbol{\sigma}}(\mathbf{v}^{k+1}) \cdot \boldsymbol{\varepsilon}(\hat{\mathbf{v}}) \, d\Upsilon_k = \sum_{i=1}^C \int_{\partial \Upsilon_k^{A,i}} \mathbf{t}_k^i \cdot \hat{\mathbf{v}} \, d\partial \Upsilon_k^{A,i} \quad \forall \hat{\mathbf{v}} \in \mathcal{V}_k, \end{aligned} \quad (2.3.7)$$

$$\int_{\Upsilon_k} \hat{p} \operatorname{div} \mathbf{v}^k \, d\Upsilon_k = 0 \quad \forall \hat{p} \in \mathcal{P}_k, \quad (2.3.8)$$

$$\int_{\Upsilon_k} \nabla \mathbf{d}^{k+1} \cdot \nabla \hat{\mathbf{d}} \, d\Upsilon_k = 0 \quad \forall \hat{\mathbf{d}} \in \mathcal{D}_k^*, \quad (2.3.9)$$

where now the spaces of admissible variations are similar to those described previously, but defined in the current updated domain Υ_k .

Observe that the formulation is such that the equilibrium equations are being solved in the last updated domain of analysis. When convergence is achieved, the domain of analysis should coincide with the *a priori* unknown domain at a given time instant.

2.4 Dimensionally reduced models

In this section we briefly introduce the dimensionally reduced models used to represent the systemic behavior of the cardiovascular system. The system will be represented by a set of one dimensional segments for the main (and larger) arteries combined with zero-dimensional models to model the microvasculature and the venous system. This approach has been extensively used elsewhere (Formaggia et al, 2006; Liang et al, 2009; Blanco and Feijóo, 2013; Watanabe et al, 2013).

2.4.1 One dimensional fluid flow model

The 1D model was rationally introduced in (Hughes and Lubliner, 1973) following a derivation from the Navier-Stokes equations when considering that (a) the axis of the vessel is a straight segment, and (b) the flow is predominantly aligned in the axial direction, implying that the non-axial velocity components are negligible. It is not a requirement to consider the artery to have symmetry of revolution.

Consider the setting shown in Figure 2.3, displaying a vessel domain with its axis aligned with the x direction within a Cartesian 3D frame. We will denote $A(x, t)$ the cross-sectional lumen area at the axial coordinate x and at time t . Also, $R(x, t)$ denotes the vessel radius, and $P(x, t)$ the mean pressure at the same point. The field $\mathbf{v} = (v_x, 0, 0)$

represents the fluid velocity, with $v(x, t)$ the mean value of v_x , i.e.

$$v(x, t) = \frac{1}{A(x, t)} \int_{A(x, t)} v_x dA. \quad (2.4.1)$$

The flow rate, denoted as $Q(x, t)$, is given by

$$Q(x, t) = A(x, t) v(x, t) = \int_{A(x, t)} v_x dA. \quad (2.4.2)$$

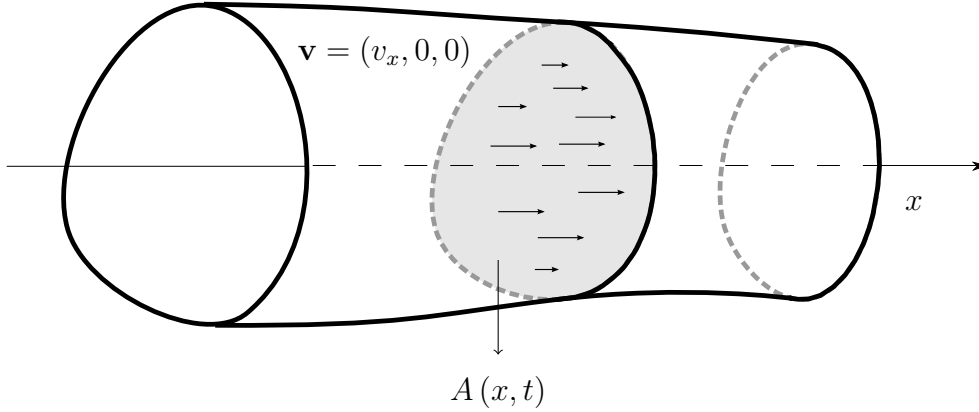


Figure 2.3: Setting for one dimensional model of fluid flow in a vessel.

Considering the above mentioned geometrical and kinematical hypotheses the mass conservation equation for incompressible flows can be expressed as

$$\frac{\partial A}{\partial t} + \frac{\partial Q}{\partial x} = 0 \quad (2.4.3)$$

and the momentum conservation equation reads

$$\frac{\partial Q}{\partial t} + \frac{\partial}{\partial x} \left(\int_A v_x^2 dA \right) = -\frac{A}{\rho} \frac{\partial P}{\partial x} - \frac{2\pi R\tau}{\rho}, \quad (2.4.4)$$

where ρ is the blood density and τ is the wall shear stress, depending on μ , the blood viscosity. In order to rewrite this expression only in terms of the triple (P, Q, A) a convective acceleration parameter $\alpha(x, t)$ depending on the shape of the velocity profile is introduced as follows

$$\alpha = \frac{A}{Q^2} \int_A v_x^2 dA. \quad (2.4.5)$$

For unidirectional velocity fields, this parameter varies within the range of $[1, \frac{4}{3}]$, being, for example, equal to 1 for a flat velocity profile and $\frac{4}{3}$ for a parabolic profile. In this work, $\alpha = 1$ is assumed. In turn, the wall shear stress τ is considered to be given by the formula characterizing Poiseuille flow

$$\tau = \frac{4\mu Q}{\pi R^3}. \quad (2.4.6)$$

In order to close the system of equations, a constitutive equation relating the mean pressure P to the cross sectional area A is required. This topic will be treated along with the constitutive equations for the three-dimensional model in Section 3.6.

2.4.2 Arterial junction models

In order to model the arterial tree as a connection of one-dimensional models for arterial vessels, proper coupling conditions must be formulated. The present model will be used whenever two or more arterial segments meet, that is, at vessel junctions. Then, consider an arterial junction with N_T converging segments, the mass conservation equation reads

$$\sum_{i=1}^{N_T} Q_i = 0, \quad (2.4.7)$$

where Q_i denotes the flow for the i th segment. In addition, it is considered that there is no pressure drop at the junction, thus leading to

$$P_1 = P_i \quad \forall i = 2, \dots, N_T. \quad (2.4.8)$$

These coupling conditions have been extensively used in the literature (Stergiopoulos et al, 1992; Formaggia et al, 2003; Matthys et al, 2007; Blanco et al, 2014b).

2.4.3 Arterioles and capillaries (0D model)

To model the resistive and compliant behaviors of the peripheral beds, Windkessel models at the terminal arterial points are considered (Stergiopoulos et al, 1992). From a mathematical point of view, this model serves to provide appropriate boundary conditions to the network of one-dimensional segments.

An electrical analogy for the Windkessel element consists of a resistance (R_2) connected in parallel with a capacitor (C) and then in series with an additional resistance (R_1). Figure 2.4 represents this setting. Considering that the arterial system presents a pressure P_{te} at the terminal point and it is connected to a low pressure reference point P_r , the governing equation is given by

$$R_1 R_2 C \frac{dQ}{dt} = R_2 C \frac{d}{dt} (P_{te} - P_r) + (P_{te} - P_r) + (R_1 + R_2) Q. \quad (2.4.9)$$

The interested reader is encouraged to see Blanco et al (2014b), where a systematic approach to achieve a physiological blood flow distribution in the CVS through the calibration of the parameters involved in this terminal model is presented.

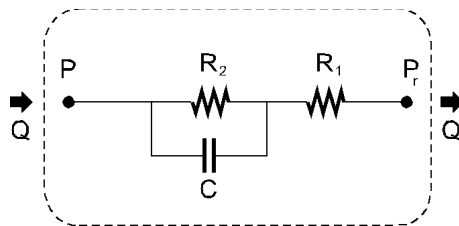


Figure 2.4: Windkessel terminal model, electrical analogy.

2.4.4 Venous system and pulmonary circulation (0D model)

The blood flow through the low-pressure components of the CVS composed by venules, veins, superior and inferior vena cava along with the pulmonary circulation is modeled by a R-L-C analog electric circuit (Liang et al, 2009; Blanco and Feijóo, 2013).

In this case, the components represent the resistance (R), inertance (L) and compliance (C) of a single compartment. (P_i, Q_i) and (P_o, Q_o) are the pairs of pressure and flow rate at the input and output of the compartment, respectively. In addition, P_{ex} stands for

the external pressure, for the examples explored in this thesis $P_{ex} = 0$ is assumed. The equations representing the behavior of this model can be written as

$$\begin{cases} L \frac{dQ_o}{dt} + RQ_o = P_i - P_o, \\ C \frac{d}{dt} (P_i - P_{ex}) = Q_i - Q_o. \end{cases} \quad (2.4.10)$$

2.4.5 Cardiac model: heart and valves (0D models)

These 0D models for the cardiac circulation follow the presentations by Liang et al (2009) and Blanco and Feijóo (2013).

Elastance model for cardiac chambers The four cardiac chambers are described using elastance-based models. Denoting the cardiac chamber pressure as P_i and its volume as V_{ch} , both quantities can be related through

$$P_{ch} - P_{ex} = (E_A e(t) + E_B) (V_{ch} - V_{0,ch}) + \alpha_{ch} |P_{ch}| \frac{dV_{ch}}{dt}, \quad (2.4.11)$$

where $V_{0,ch}$ is the dead volume of the chamber and α_{ch} controls the viscoelastic pressure-volume relation. As usual, the evolution of the chamber volume over time is related to the inflow and outflow by

$$\frac{dV_{ch}}{dt} = Q_i - Q_o. \quad (2.4.12)$$

Also, E_A and E_B are the amplitude and base values for the elastance, and $e(t)$ is a normalized function that controls the variation of the elastance during the cardiac cycle. For the ventricles, this function is given by

$$e_v(t) = \begin{cases} \frac{1}{2} \left\{ 1 - \cos \left(\pi \frac{t}{T_{vc}} \right) \right\} & 0 \leq t \leq T_{vc} \\ \frac{1}{2} \left\{ 1 + \cos \left(\pi \frac{t - T_{vc}}{T_{vr}} \right) \right\} & T_{vc} \leq t \leq T_{vc} + T_{vr} \\ 0 & T_{vc} + T_{vr} \leq t \leq T, \end{cases} \quad (2.4.13)$$

and for atria by

$$e_a(t) = \begin{cases} \frac{1}{2} \left\{ 1 + \cos \left(\pi \frac{t + T - t_{ar}}{T_{ar}} \right) \right\} & 0 \leq t \leq t_{ar} + T_{ar} - T \\ 0 & t_{ar} + T_{ar} - T \leq t \leq t_{ac} \\ \frac{1}{2} \left\{ 1 - \cos \left(\pi \frac{t - t_{ac}}{T_{ac}} \right) \right\} & t_{ac} \leq t \leq t_{ac} + T_{ac} \\ \frac{1}{2} \left\{ 1 - \cos \left(\pi \frac{t - t_{ar}}{T_{ar}} \right) \right\} & t_{ac} + T_{ac} \leq t \leq T. \end{cases} \quad (2.4.14)$$

Here, subscripts v and a denote the ventricles and atria, respectively. In these equations, T is the duration of the cardiac cycle, T_{vc} , T_{ac} , T_{vr} and T_{ar} refer to the duration of contraction and relaxation periods, and t_{ac} , t_{ar} to the starting times for the contraction and relaxation periods.

Non-ideal model for heart valves Cardiac valves are modeled using a non-ideal diode model that allows inverted flow prior to the valve closure. A momentum balance equation governing the behavior of each valve can be expressed as

$$L \frac{dQ_o}{dt} + RQ_o + B |Q_o| Q_o = \Theta (P_i - P_o), \quad (2.4.15)$$

with L representing the inertance of the fluid, R the viscous resistance, B accounting for the flow separation phenomena and, as before, P_i and P_o denote the input and output

pressures. The coefficient Θ introduces a non-binary response of the valve, simulating the orifice of each valve as a function of their opening angle θ . This function reads

$$\Theta = \frac{(1 - \cos \theta)^4}{(1 - \cos \theta_{max})^4}, \quad (2.4.16)$$

where θ_{max} is the maximum angle the valve is able to open. The opening angle is computed using an heuristic angular momentum balance equation (for more details see Korakianitis and Shi (2006)) as follows

$$I \frac{d^2 \theta}{dt^2} + k_f \frac{d\theta}{dt} = k_p (P_i - P_o) + k_Q Q_o \cos \theta + \begin{cases} k_V Q_o \sin(2\theta) & \text{if } P_i \geq P_o \\ 0 & \text{if } P_i \leq P_o \end{cases}, \quad (2.4.17)$$

where I is the moment of the inertia of the valve. The solution of this equation is constrained to

$$\theta = \begin{cases} \theta_{min} & \text{if } \theta \leq \theta_{min}, \\ \theta_{max} & \text{if } \theta \geq \theta_{max}. \end{cases} \quad (2.4.18)$$

The use of this model allows to account for two types of valve malfunctioning, valve narrowing (reduced θ_{max} , related to valve stenosis) and valve insufficiency (increased value of θ_{min}), when the valve is not able to prevent backward flow.

Chapter 3

Integration of hemodynamic models

3.1 Introduction

As already discussed, in order to analyze the mechanical behavior of the arterial wall and the blood flow dynamics, it is fundamental to provide a realistic hemodynamic environment where the following key topics are properly taken into account (see Chapter 1 for further details):

- the fact that image-based configurations correspond to a preloaded state,
- the interaction between the arterial district of interest and the rest of the CVS,
- the complex arterial wall behavior,
- the action of external tissues,
- the fluid-structure interaction, and
- the impact of residual deformations and stresses.

Furthermore, it is necessary to utilize adequate computational tools to approximate and solve the variational equations corresponding to continuum mechanics models (see Chapter 2) representing the behavior of the different components of the system. Also, the efficient coupling between such subsystems is not trivial and requires careful consideration.

Then, the goal of this chapter is to describe the strategies adopted to tackle the mentioned issues. For this purpose, a brief discussion of how the preload problem is addressed is presented in Section 3.2. Next, in Section 3.3 the implemented model for the representation of the action of surrounding tissues is introduced, and a description of the FSI strategy is included in Section 3.4. Next, the methodology implemented for the coupling of dimensionally heterogeneous models is summarized in Section 3.5, and the selection of adequate constitutive equations for the arterial wall is discussed in Section 3.6. Also, the incorporation of axial residual deformations is treated in Section 3.7. Finally, the numerical approximations implemented for this integrative modeling framework, both for the fluid and solid problems, are addressed in Section 3.8.

3.2 Initially loaded state

To account for the fact that vessel geometries extracted from medical images correspond to in-vivo loaded states, the preload problem given by equations (2.2.14)-(2.2.15) introduced in Section 2.2.3 is solved. We will denote the image-based configuration as Ω_{base} and consider a known baseline pressure level (defined for each example) introducing a force acting over the interior boundary on the arterial wall Γ_{base}^W . In this way, the material

reference configuration is obtained and can be utilized for the computation of the arterial wall behavior in the 1D-3D fluid-structure interaction problem.

Figure 3.1 displays a graphical example of the treatment of initially loaded vessel geometries. In this context, Figure 3.1(a) presents a volume render from a computerized tomography (CT) image of a patient, and Figure 3.1(b) presents the lumen segmentation of the arterial region where the specific segment of interest is located, in this example, the common carotid artery. Also, Figure 3.1(c) introduces a discretization of the arterial wall corresponding to the isolated segment in its in-vivo state Ω_{base} . Figure 3.1(d) shows the material (reference) configuration Ω_m obtained from the solution of the aforementioned preload problem.

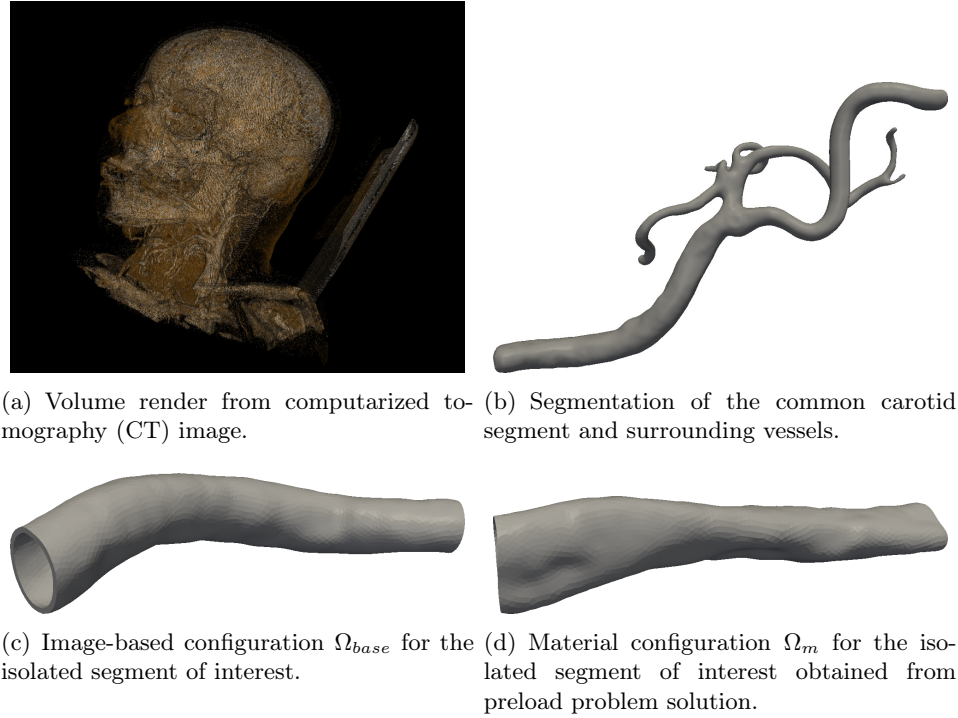


Figure 3.1: Graphical example for the treatment of initially loaded vessel geometries extracted from medical images.

3.3 External tissue support

For the surrounding media we assume that the effective behavior is viscoelastic. Then, the load \mathbf{t}_s^E depends on the displacement and on the velocity of the solid wall at $\partial\Omega_s^E$, that is

$$\mathbf{t}_s^E = k_e (\mathbf{u}_s - \mathbf{u}_0) + k_v \frac{\partial \mathbf{u}_s}{\partial t} \Big|_{\partial\Omega_s^E}, \quad (3.3.1)$$

where k_e and k_v are effective elastic and viscoelastic parameters, respectively, and \mathbf{u}_0 defines a reference position for the elastic response. A linear approximation is considered for the computation of the time derivative. The parameters will be defined considering the hypothesis that surrounding tissues are more influential over regions featuring larger curvatures. In order to support this hypothesis, let us consider a curved arterial segment subjected to tethering forces at non-physical boundaries and supported by surrounding tissues, as depicted on Figure 3.2. Through a simple analysis of external forces it can be inferred that, in order to avoid the rigid displacement of the arterial segment, the surrounding tissues must compensate the action of tethering forces. Additionally, if the

external tissues act primarily in the normal direction of the surface, the forces exerted by them should be more prominent in the highly curved region.

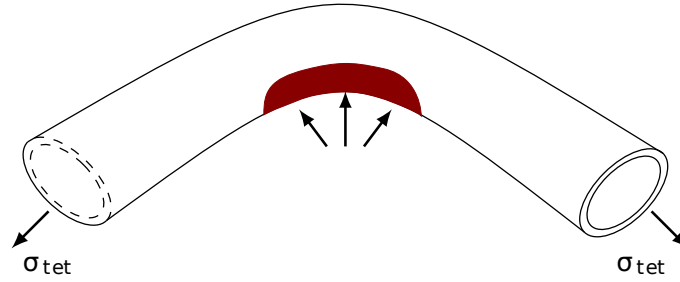


Figure 3.2: Local analysis of external loads in the arterial wall. It is assumed a higher influence of external tissues in curved regions (highlighted in red), so to provide a source of mechanical balance against the tethering forces which are applied at non-physical boundaries.

3.4 Fluid-structure interaction

3.4.1 Interface equations

In this section the fluid-structure interaction technique implemented to perform the coupling between the arterial wall and blood flow models is addressed. For the interface equations, at a given time t , the arterial wall is at equilibrium in a configuration Ω_s . At the interface $\partial\Omega_s^W \equiv \partial\Upsilon_t^W$, the following coupling equations hold

$$\begin{aligned} \mathbf{u}_s &= \mathbf{d}_t & \text{at } \partial\Omega_s^W &\equiv \partial\Upsilon_t^W, \\ (\boldsymbol{\sigma}_s - \boldsymbol{\sigma})\mathbf{n}_s &= 0 & \text{at } \partial\Omega_s^W &\equiv \partial\Upsilon_t^W, \end{aligned} \quad (3.4.1)$$

with \mathbf{n}_s representing the normal vector at the interface, $\boldsymbol{\sigma}_s$ is the Cauchy stress in the solid and $\boldsymbol{\sigma}$ is the Cauchy stress in the fluid. Note that \mathbf{u}_s and \mathbf{d}_t are both expressed in terms of the same reference frame, since at any given time t the arterial wall boundary (corresponding to the spatial configuration) matches the boundary for the blood flow domain.

3.4.2 Fluid-structure interaction in the 3D-1D coupling context

The FSI problem is solved within the context of a dimensionally heterogeneous coupling algorithm (3D-1D coupling, see Section 3.5). Thus, it is actually a black-box component from the point of view of the 3D-1D coupling algorithm. In fact, as time evolves, computations are carried out with the following strategy:

Algorithm 1 1D-3D coupling context

Solve preload problem (eqs. (2.2.14)-(2.2.15))

Loop in time

 Loop for 3D-1D coupling (Broyden iterations, see Section 3.5)

 Data (D) sent to components

 Loop for FSI coupling (fixed-point method, see Section 3.4)

 Outcome (O) retrieved from components

The data for the *FSI black-box component* are

(D.i) at each time step: quantities from previous time step (fluid quantities);

- (D.ii) at each 3D-1D coupling iteration: the normal component of the traction vectors t_t^i at $\partial\Upsilon_t^{A,i}$, $i = 1, \dots, C$, which are provided by the 3D-1D algorithm, and that are incorporated as Neumann boundary conditions on the fluid problem (see equation (2.3.4));
- (D.iii) at each FSI coupling iteration: quantities at previous iteration (fluid and solid quantities).

Solving the FSI problem implies solving the fully coupled system of equations given by (2.2.17)-(2.2.18) (arterial wall mechanics) and (2.3.3)-(2.3.5) (blood flow dynamics). As outcome, the solution of the FSI problem provides the 3D-1D coupling algorithm with the flow rates $Q_i = \int_{\partial\Upsilon_t^{A,i}} \mathbf{v} \cdot \mathbf{n}^i d\partial\Upsilon_t^{A,i}$, $i = 1, \dots, C$.

3.4.3 Coupling algorithm

Figure 3.3 presents the FSI algorithm based on fixed point iterations. The FSI coupling loop corresponds to the circuit of blocks labelled with letters from (a) to (g). Blocks in yellow correspond to the input/output connections with the 3D-1D coupling algorithm. The key blocks of the FSI scheme are the components (b) and (f), highlighted in green.

The key block (b) represents one iteration of the fixed-point scheme introduced in Section 2.3.3. Hence, for each iteration $k = 0, 1, \dots$ of the FSI coupling scheme, block (b) will provide the solution of the following linearized problem: find $(\mathbf{v}^{k+1}, p^{k+1}, \mathbf{d}^{k+1}) \in \mathcal{U}_k \times \mathcal{P}_k \times \mathcal{D}_k$ such that

$$\int_{\Upsilon_k} \rho \frac{\partial \tilde{\mathbf{v}}^{k+1}}{\partial t} \cdot \hat{\mathbf{v}} d\Upsilon_k + \int_{\Upsilon_k} \rho \nabla \tilde{\mathbf{v}}^{k+1} (\mathbf{v}^k - \mathbf{v}_R^k) \cdot \hat{\mathbf{v}} d\Upsilon_k - \int_{\Upsilon_k} \tilde{p}^{k+1} \operatorname{div} \hat{\mathbf{v}} d\Upsilon_k + \int_{\Upsilon_k} \bar{\boldsymbol{\sigma}}(\tilde{\mathbf{v}}^{k+1}) \cdot \boldsymbol{\varepsilon}(\hat{\mathbf{v}}) d\Upsilon_k = \sum_{i=1}^C \int_{\partial\Upsilon_k^{A,i}} \mathbf{t}_k^i \cdot \hat{\mathbf{v}} d\partial\Upsilon_k^{A,i} \quad \forall \hat{\mathbf{v}} \in \mathcal{V}_k, \quad (3.4.2)$$

$$\int_{\Upsilon_k} \hat{p} \operatorname{div} \mathbf{v}^k d\Upsilon_k = 0 \quad \forall \hat{p} \in \mathcal{P}_k, \quad (3.4.3)$$

$$\int_{\Upsilon_k} \nabla \tilde{\mathbf{d}}^{k+1} \cdot \nabla \hat{\mathbf{d}} d\Upsilon_k = 0 \quad \forall \hat{\mathbf{d}} \in \mathcal{D}_k^*, \quad (3.4.4)$$

As input, is necessary to provide this block with the solid displacement at the interface $\partial\Omega_s^W$ at the current FSI iteration (\mathbf{u}_s^k), and the solution corresponding to the fluid problem and the arterial wall for the previous time step (quantities denoted with supra-index n). With this information, the manifolds \mathcal{U}_k and \mathcal{D}_k are defined as

$$\begin{aligned} \mathcal{U}_k &= \left\{ \mathbf{v} \in \mathbf{H}^1(\Upsilon_k), \mathbf{v}|_{\partial\Upsilon_k^W} = \frac{\mathbf{u}_s^k - \mathbf{u}_s^n}{\Delta t} \right\}, \\ \mathcal{D}_k &= \left\{ \mathbf{d} \in \mathbf{H}^1(\Upsilon_k), \mathbf{d}|_{\partial\Upsilon_k^W} = \mathbf{u}_s^k \right\} \end{aligned} \quad (3.4.5)$$

Additionally, the velocity of the reference domain at each iteration is calculated as $\mathbf{v}_R^k = \frac{\mathbf{d}^k - \mathbf{d}^n}{\Delta t}$. This actions are represented in the figure by blocks (i) and (a). Block (c) introduces a subrelaxation step on the output provided by block (c) controlled by the parameter κ_a ,

consequently, the solution is updated as follows

$$\left(\mathbf{v}^{k+1}, p^{k+1}, \mathbf{d}^{k+1}\right) = \kappa_a \left(\tilde{\mathbf{v}}^{k+1}, \tilde{p}^{k+1}, \tilde{\mathbf{d}}^{k+1}\right) + (1 - \kappa_a) \left(\mathbf{v}^k, p^k, \mathbf{d}^k\right). \quad (3.4.6)$$

Key block (f) represents one step of the Newton-Raphson linearization of the solid (forward) problem, as formerly introduced in Section 2.2.5: given $(\mathbf{u}_s, \lambda_s)$ (displacement and pressure fields at previous Newton-Raphson iteration -omitted k index-) find $(\delta\mathbf{u}_s, \delta\lambda_s) \in \mathcal{V}_s \times \mathcal{L}_s$ such that

$$\begin{cases} a_s(\delta\mathbf{u}_s, \hat{\mathbf{u}}_s) + b_s(\delta\lambda_s, \hat{\mathbf{u}}_s) = l_s(\hat{\mathbf{u}}_s) & \forall \hat{\mathbf{u}}_s \in \mathcal{V}_s \\ c_s(\delta\mathbf{u}_s, \hat{\lambda}_s) = m_s(\hat{\lambda}_s) & \forall \hat{\lambda}_s \in \mathcal{L}_s \end{cases} \quad (3.4.7)$$

where the bilinear and linear forms are given by

$$\begin{aligned} a_s(\delta\mathbf{u}_s, \hat{\mathbf{u}}_s) &= \int_{\Omega_s} [\mathbf{D}_s + \lambda_s (2\mathbb{I} - (\mathbf{I} \otimes \mathbf{I}))] \boldsymbol{\varepsilon}_s(\delta\mathbf{u}_s) \cdot \boldsymbol{\varepsilon}_s(\hat{\mathbf{u}}_s) d\Omega_s \\ &+ \int_{\Omega_s} (\nabla_s \delta\mathbf{u}_s) \boldsymbol{\sigma}_s \cdot (\nabla_s \hat{\mathbf{u}}_s) d\Omega_s + \int_{\partial\Omega_s^W} [t_s^{W,n} ((\nabla_s \delta\mathbf{u}_s)^T - \mathbf{I}) \mathbf{n}_s^W \cdot \hat{\mathbf{u}}_s] \operatorname{div}_s \delta\mathbf{u}_s d\partial\Omega_s^W \\ &- \int_{\partial\Omega_s^W} (\mathbf{H}(\delta\mathbf{u}_s) \mathbf{n}_s \otimes \mathbf{n}_s)^S \mathbf{t}_s^{W,t} \cdot \hat{\mathbf{u}}_s d\partial\Omega_s^W - \int_{\partial\Omega_m^W} \mathbf{P}_s \mathbf{t}_s^{W,t} \cdot \hat{\mathbf{u}}_s (\operatorname{div}_s \delta\mathbf{u}_s) d\partial\Omega_s^W \\ &- \int_{\partial\Omega_m^W} \mathbf{P}_s \mathbf{t}_s^{W,t} \cdot \hat{\mathbf{u}}_s \left(-(\nabla_s \delta\mathbf{u}_s)^T \mathbf{n}_s \cdot \mathbf{n}_s \right) d\partial\Omega_s^W \\ &- \int_{\partial\Omega_s^N} (\mathbf{t}_s^N \cdot \hat{\mathbf{u}}_s) \left[(\operatorname{div}_s \delta\mathbf{u}_s) - (\nabla_s \delta\mathbf{u}_s)^T \mathbf{n}_s \cdot \mathbf{n}_s \right] d\partial\Omega_s^N, \end{aligned} \quad (3.4.8)$$

$$b_s(\delta\lambda_s, \hat{\mathbf{u}}_s) = - \int_{\Omega_s} \delta\lambda_s \operatorname{div}_s \hat{\mathbf{u}}_s d\Omega_s, \quad (3.4.9)$$

$$\begin{aligned} l_s(\hat{\mathbf{u}}_s) &= - \int_{\Omega_s} [-\lambda_s \operatorname{div}_s \hat{\mathbf{u}}_s + \boldsymbol{\sigma}_s \cdot \boldsymbol{\varepsilon}_s(\hat{\mathbf{u}}_s)] d\Omega_s + \int_{\partial\Omega_s^W} \mathbf{P}_s \mathbf{t}_s^W \cdot \hat{\mathbf{u}}_s d\partial\Omega_s^W + \int_{\partial\Omega_s^W} t_s^{W,n} \mathbf{n}_s \cdot \hat{\mathbf{u}}_s d\partial\Omega_s^W \\ &+ \int_{\partial\Omega_s^N} \mathbf{t}_s^N \cdot \hat{\mathbf{u}}_s d\partial\Omega_s^N, \end{aligned} \quad (3.4.10)$$

$$c_s(\delta\mathbf{u}_s, \hat{\lambda}_s) = \int_{\Omega_s} \operatorname{div}_s \delta\hat{\mathbf{u}}_s \hat{\lambda}_s d\Omega_s, \quad (3.4.11)$$

and

$$m_s(\hat{\lambda}_s) = - \int_{\Omega_s} (1 - \det \mathbf{F}_s^{-1}) \hat{\lambda}_s d\Omega_s. \quad (3.4.12)$$

The Neumann boundary condition for the inner surface of the solid (block (e)) is updated at each FSI iteration through $\mathbf{t}_s^W = \iota \cdot \mathbf{t}_s^{W,k} + (1 - \iota) \cdot \mathbf{t}_s^{W,k-1}$, where $\iota = k/n_s$ if $k < n_s$. This way, the load is applied gradually in the first n_s (problem dependant parameter) steps, avoiding *overshooting* phenomena. Analogously to the procedure taken for the fluid

problem, a subrelaxation controlled by the parameter κ_b is applied (block (g)), yielding

$$(\mathbf{u}_s^{k+1}, \lambda_s^{k+1}) = \kappa_b (\delta \mathbf{u}_s, \delta \lambda_s) + (\mathbf{u}_s^k, \lambda_s^k). \quad (3.4.13)$$

Lastly, convergence is then evaluated (block (h)). If convergence is reached the algorithm proceeds with the next 3D-1D coupling iteration (see Section 3.5) or, otherwise, the next FSI iteration is carried out.

3.5 Dimensionally heterogeneous models

3.5.1 Hemodynamic components

The 3D FSI model, in which a detailed description of the hemodynamics is sought, is embedded into a larger system, the arterial system. Since there is no need for a full blood flow model of the complete circulation, dimensionally reduced models are instead employed to provide a fair description of the global dynamics which remains very accurate in terms of average quantities, such as average pressure and flow rate.

Within this context, we consider two different approaches for the embedding of the 3D FSI model. As first option we consider the ADAN model Blanco et al (2014a,b), a highly detailed model of the arterial circulation, featuring an accurate spatial description of more than 2000 arteries, as shown in Figure 3.5.1. This model is currently the most detailed description of the arterial circulation and is able to provide with a realistic environment for (virtually) any 3D segment of interest. As a second option we consider a more simple approach, using a complete model of the CVS based on a less detailed model of the arterial tree (inspired in the arterial network proposed in Avolio (1980)) -see Figure 3.5.1- and incorporating venules, veins, cavas, atria, ventricles, and valves, modeled through 0D models. The interested reader is encouraged to see Blanco et al (2013b) for a more detailed description of this closed-loop circulation model.

For both cases, the coupling is performed through a black-box iterative technique. A brief resume of this method is here provided, presenting the coupling strategy for two components listed below. The interested reader is directed to Blanco et al (2013b) for a complete in-depth presentation of this approach.

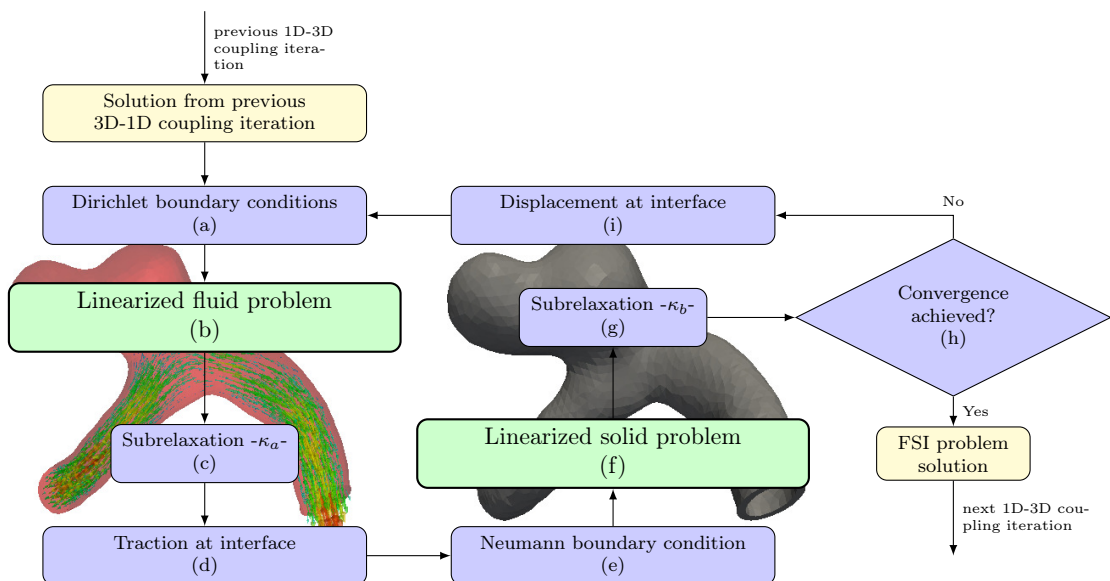


Figure 3.3: Fluid-structure iterative coupling scheme

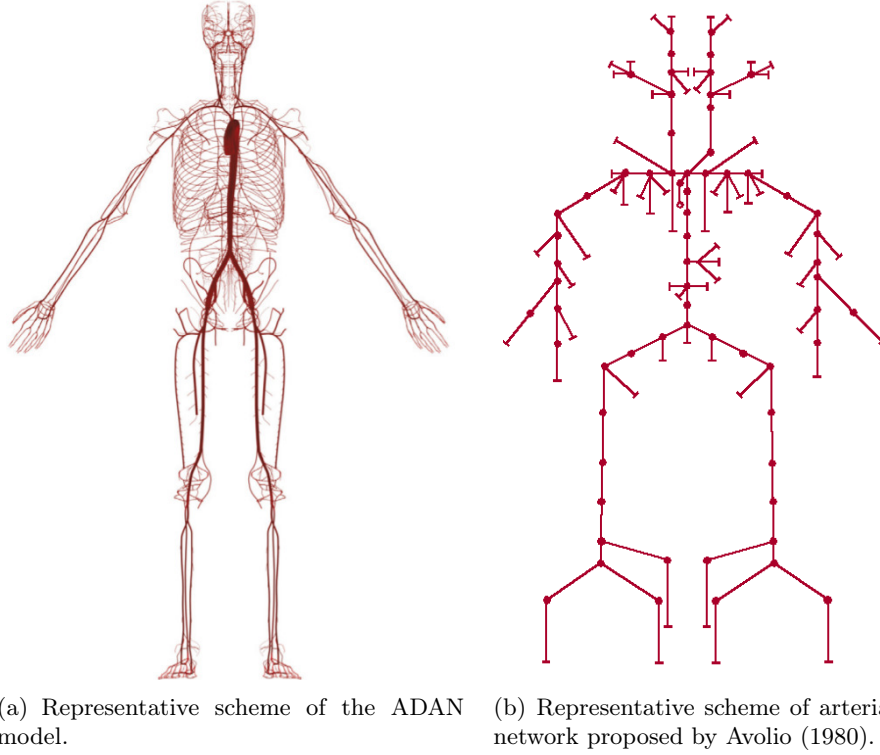


Figure 3.4: Representations of dimensionally reduced hemodynamic components.

Dimensionally reduced component (DR). This component can be either the ADAN model or the simplified closed-loop circulation. For both cases the arterial network is modeled using the governing equations introduced in Section 2.4.

Specific-vessel component (SV). The arterial segment which demands a detailed description of the physical phenomena is represented using the model elaborated above in Section 2.2.3 and Section 3.4, that is: the three-dimensional behavior of the blood flow and its interaction with the arterial wall (see Section 3.4), considering the initially loaded -with pressure and tethering stresses- geometry (see Section 2.2.3). Eventually, coupling with surrounding tissues and residual deformations can be introduced in this component.

3.5.2 Coupling equations

Consider that the dimensionally reduced (DR) component is linked through C bonds to the specific-vessel (SV) component. For the sake of readability we will call simply by “1D-0D” the DR component and by “3D” the SV component. For the i th bond ($i = 1, \dots, C$), consider two coupling variables, namely P_i and Q_i , the normal traction and flow rate at such coupling point. Additionally, we will denote as \mathcal{Q}_c^i and \mathcal{P}_c^i ($c = \text{DR}, \text{SV}$) to the flow rate and normal traction, respectively, given by the corresponding component for the i th bond. Hence, for this bond, the following set of coupling equations can be written:

$$\begin{cases} \mathcal{Q}_{\text{DR}}^i = \mathcal{Q}_{\text{SV}}^i = Q^i \\ \mathcal{P}_{\text{DR}}^i = \mathcal{P}_{\text{SV}}^i = P^i \end{cases}, \quad i = 1, \dots, C. \quad (3.5.1)$$

Consequently, for the complete problem, a system of $2C$ equations is obtained. It is worthwhile to note that for the 3D component, $\mathcal{P}_{\text{SV}}^i$ represents the magnitude of the uniform normal traction vector acting on the fluid non-physical boundaries $\partial\Upsilon_t^{A,i}$. Thence, for the

SV component both quantities are calculated as follows

$$\begin{cases} \mathcal{Q}_{\text{SV}}^i = \int_{\partial\Upsilon_t^{A,i}} \mathbf{v} \cdot \mathbf{n}^i d\partial\Upsilon_t^{A,i}, \\ \mathcal{P}_{\text{SV}}^i = t_t^i \end{cases}, \quad i = 1, \dots, C, \quad (3.5.2)$$

where it is straightforward to see that $t_t^i = (-p + \mu(\nabla\mathbf{v})\mathbf{n} \cdot \mathbf{n})|_{\partial\Upsilon_t^{A,i}}$, $i = 1, \dots, C$.

3.5.3 Strong coupling strategy

In Figure 3.5 the coupling is schematically described. In this scheme a single coupling point condenses the C coupling interfaces. Therefore, at such coupling point we have the unknown vector containing all the unknowns of the coupled system, namely (\mathbf{Q}, \mathbf{P}) , being (Q_i, P_i) , $i = 1, \dots, C$ the pair of coupling variables at each coupling interface. Hence, the

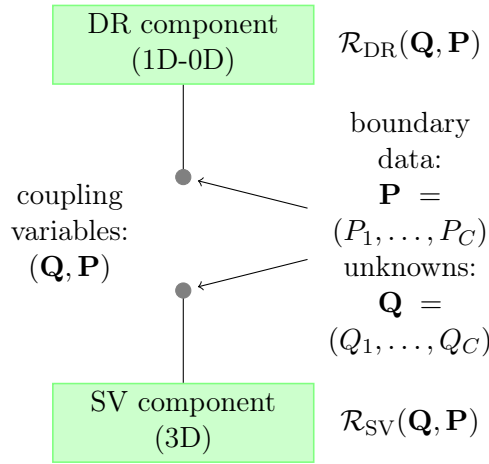


Figure 3.5: Idealization of system as black-box components, coupling variables and chosen boundary data for components.

coupling problem amounts to find the pair (\mathbf{Q}, \mathbf{P}) such that coupling equations (3.5.1) are satisfied, that is

$$\begin{aligned} \mathcal{R}_{\text{DR}}(\mathbf{Q}, \mathbf{P}) &= 0, \\ \mathcal{R}_{\text{SV}}(\mathbf{Q}, \mathbf{P}) &= 0, \end{aligned} \quad (3.5.3)$$

where \mathcal{R}_{DR} and \mathcal{R}_{SV} are residuals defined accordingly. We recall that, in the fluid flow problem, those residuals consist of equations of continuity of mass and continuity of the normal component of the traction vector (hereafter denoted simply by “coupling pressure”).

From the vector of coupling variables (\mathbf{Q}, \mathbf{P}) it is now required to define those quantities that will turn into boundary data for each component within the iterative scheme. Here, we choose the coupling pressure to be boundary data for both components. Hence, the system of coupling equations (3.5.3) results

$$\begin{aligned} \mathcal{R}_{\text{DR}}(\mathbf{Q}, \mathbf{P}) &= \mathbf{Q} - \mathcal{Q}_{\text{DR}}(\mathbf{P}) = 0, \\ \mathcal{R}_{\text{SV}}(\mathbf{Q}, \mathbf{P}) &= \mathbf{Q} - \mathcal{Q}_{\text{SV}}(\mathbf{P}) = 0, \end{aligned} \quad (3.5.4)$$

where \mathcal{Q}_{DR} and \mathcal{Q}_{SV} are compact vector notations for the operators related to the DR and SV components, respectively. These operators encompass the 1D-0D problem (see Blanco et al (2013b)) and the 3D problem (see Sections 2.2.3, 2.3.1, and 3.4) with $\mathbf{P} = (P_1, \dots, P_C)$ as boundary data at the C coupling interfaces. This system contains $2C$ equations, and

can be written as follows

$$\begin{aligned} Q_i - \mathcal{Q}_{\text{DR}}^i(P_1, \dots, P_C) &= 0 & i = 1, \dots, C, \\ Q_i - \mathcal{Q}_{\text{SV}}^i(P_1, \dots, P_C) &= 0 & i = 1, \dots, C. \end{aligned} \quad (3.5.5)$$

Thus, for instance, observe that $\mathcal{Q}_{\text{SV}}^i$ stands for the flow rate given by the SV component at i th coupling interface, after solving the FSI problem, for a given set (P_1, \dots, P_C) of boundary data (see Section 3.4). Regarding the equation (2.3.4), the boundary data is $(t_t^1, \dots, t_t^C) = (P_1, \dots, P_C)$.

In the continuous setting, this system of non-linear equations holds for each time. That is, when approximating in time, system (3.5.5) is solved iteratively until convergence is achieved at each time step.

3.5.4 Solving the coupling equations system

The problem of solving (3.5.4) iteratively can be tackled using any suitable method for systems of non-linear equations. Our previous experience dictates the use of a Broyden algorithm which avoids the computation of derivatives while preserving good convergence properties, as shown in Blanco et al (2013b). In turn, at each coupling iteration (e.g. at each Broyden iteration), the entire FSI algorithm described in Figure 3.3 is executed when solving the SV component. Thus, the iterations ruled by the coupling algorithm embrace the FSI iterations, while such coupling iterations are embraced by the temporal loop.

For a nonlinear equation $\mathcal{R}(\mathbf{z}) = 0$, the plain Broyden method reads

Algorithm 2 Broyden method

1. Given \mathbf{z}^0 and \mathbf{B}^0 do
 2. Compute $\mathbf{r}^0 = \mathcal{R}(\mathbf{z}^0)$
 3. Loop $l = 0, 1, \dots$ until $\frac{\|\mathbf{r}^j\|}{\|\mathbf{r}^0\|} \leq \epsilon$ or $\|\mathbf{r}^j\| \leq \epsilon^{abs}$
 4. $\Delta \mathbf{z} = -(\mathbf{B}^j)^{-1} \mathbf{r}^j$
 5. $\mathbf{z}^{j+1} = \mathbf{z}^j + \Delta \mathbf{z}$
 6. $\mathbf{r}^{j+1} = \mathcal{R}(\mathbf{z}^{j+1})$
 7. $\mathbf{B}^{j+1} = \mathbf{B}^j + \frac{\mathbf{r}^{j+1} \otimes \Delta \mathbf{z}}{\Delta \mathbf{z} \cdot \Delta \mathbf{z}}$
 8. End loop.
-

where ϵ and ϵ^{abs} denote relative and absolute residual tolerances (respectively) controlling the convergence criteria to stop the Broyden algorithm. In the context of our problem \mathbf{z}^j is such that $\mathbf{z}^j = (\mathbf{Q}^j, \mathbf{P}^j)$ and the residual vector \mathbf{r}^j is given by the collected residuals for each component, i.e.

$$\mathbf{r}^j = \begin{pmatrix} \mathcal{R}_{\text{DR}}(\mathbf{Q}^j, \mathbf{P}^j) \\ \mathcal{R}_{\text{SV}}(\mathbf{Q}^j, \mathbf{P}^j) \end{pmatrix}, \quad (3.5.6)$$

thus, at this step it is included the solution of both 1D and 3D problems to obtain $\mathcal{Q}_{\text{DR}}(\mathbf{P})$ and $\mathcal{Q}_{\text{SV}}(\mathbf{P})$, respectively.

Defining initial conditions \mathbf{z}^0

The choice of the initial conditions has a great influence in the capability of the method in achieving convergence. In the presented examples, as a first step we simulate the complete DR component (including a 1D segment that will later be replaced by a 3D counterpart) decoupled until a cyclic solution is achieved. This solution will serve as initial condition for this component. As a second step, we simulate the decoupled SV component for one tenth of the cardiac cycle using as Neumann boundary conditions a normal traction

vector given by the pressure delivered at the coupling points by the DR component. The initial condition for this 3D simulation is given by null velocities and uniform pressure (equal to the magnitude of the traction vector introduced on the main inlet). The solution of this simulation will serve as initial condition for 3D component.

Defining initial matrix \mathbf{B}^0

Along with the initial state \mathbf{z}^0 , it is necessary to provide the method with an initial matrix \mathbf{B}^0 that will be updated at each iteration at step 7 in Algorithm 2. As this is a time-dependent problem, the complete algorithm is repeated at each N time step, and a new initial matrix $\mathbf{B}_{0,N}$ needs to be provided. For the first time step, $\mathbf{B}^{0,1}$ is initialized computing the Jacobian of the system using finite differences. The components of this Jacobian read as follows

$$B_{ab}^{0,1} = \frac{r_a(z_1^0, z_2^0, \dots, z_b^0 + \varsigma, \dots, z_{2C}^0) - r_a(\mathbf{z}^0)}{\varsigma}, \quad (3.5.7)$$

where r_a denotes the a th component of the residual vector and ς is a small enough perturbation. At each new time step, say $N+1$, it is employed the final updated matrix obtained at the previous set of l Broyden iterations which resulted in convergence at the previous time-step N , is employed, that is $\mathbf{B}^{0,N+1} = \mathbf{B}^{l,N}$.

3.6 Constitutive modeling

3.6.1 Constitutive equations for the 3D arterial wall

We make use of the most extensively used constitutive model to represent the behavior of elastin and collagen components in the arterial wall, as proposed in Holzapfel and Gasser (2000).

In this constitutive framework, the tissue is modeled as a hyperelastic composite material in which the elastin matrix is taken into account through a Neo-Hookean isotropic contribution, and the collagen fibers are considered by means of an anisotropic contribution acting in two given directions. In the arterial wall, different layers can be distinguished, and for each layer the same type of strain energy function is assumed, with a different set of material parameters and orientation angles characterizing the families of collagen fibers.

Hence, the strain energy function of the material takes the form:

$$\Psi = \frac{c_{elast}}{2}(I_1 - 3) + \frac{k_1}{2k_2} \sum_{i=4,6} \delta_i \left\{ e^{k_2(I_i - \lambda_i^0)^2} - 1 \right\} \quad (3.6.1)$$

where $\delta_i = 1$ if $I_i > \lambda_i^0$; $\delta_i = 0$ otherwise, and

$$I_1 = \text{tr}(\mathbf{C}_m), \quad I_i = \mathbf{a}_i \cdot (\mathbf{C}_m \mathbf{a}_i), \quad i = 4, 6, \quad (3.6.2)$$

with $\mathbf{C}_m = \mathbf{F}_m^T \mathbf{F}_m$, c_{elast} is the material parameter which characterizes the effective stiffness of the elastin; the effective stiffness of collagen fibers is characterized by k_1 and k_2 , while the recruitment stretch is λ_i^0 , and the directions of orientation of fibers are \mathbf{a}_i , $i = 4, 6$, which are vectors defined in the material configuration Ω_m . The invariants I_4, I_6 measure the stretch in the direction of the fibers as a consequence of the deformation state of the body. The exponential term will be active only if the stretch of the collagen fibers corresponds to a recruited state. The passive response of the smooth muscle is taken into account in a compatible manner with the simplified 1D model through an independent ring model (see viscoelastic terms detailed in Blanco et al (2010)).

We highlight that it is also considered an alternative constitutive equation for the modeling of arterial walls of aneurysms. We make use of an exponential and isotropic strain energy function, based on the hypothesis that collagen fibers are the main energy-storing constituents due to elastin degradation, and acknowledging a lack of information regarding fiber orientations in such environment. This strain energy function, originally introduced in Delfino et al (1997), reads

$$\Psi = \frac{k_{del}}{2k_x} \left\{ \exp[k_x(\bar{I}_1 - 3)] - 1 \right\}, \quad (3.6.3)$$

where, k_{del} is an effective elastic parameter and k_x is a non-dimensional parameter controlling the exponential behavior of the tissue.

3.6.2 Constitutive equations for the 1D arterial wall

To take into account the compliance of the vessel and close the system of equations presented in Section 2.4, a constitutive equation that relates the pressure P to the cross sectional A must be included. In this thesis, it is considered a non-linear viscoelastic model originally proposed by Kivity and Collins (1974), taking following form

$$P = P_0 + \frac{h_{w,0}E_e}{R_0}\varepsilon + \frac{Kh_{w,0}}{R_0}\dot{\varepsilon} \quad (3.6.4)$$

where $\varepsilon = \left(\sqrt{\frac{A}{A_0}} - 1 \right)$, R is the radius of the artery, E_e the effective Young's modulus of the vessel, K is the effective viscosity of the wall, h_w the thickness and subscript '0' indicates that quantities are evaluated for a reference pressure value P_0 .

As shown in Čanić et al (2006), it is important to account for the viscoelasticity of the arterial wall tissue as it plays a major role in the definition of the pulsewave in the CVS.

3.7 Residual deformations

As the application of the in-vivo characterization of residual deformations (see Chapter 5) for complex 3D geometries is matter of current research, in this work we incorporate the axial stretch component through the definition of boundary conditions at the non-physical boundaries when solving the preload problem in order to obtain a “shortened” material geometry. For this purpose in this thesis we explore three different alternatives:

- (i) prescribing axial displacements for every node at the non-physical boundary,
- (ii) applying tethering forces via penalization, related to the mean displacement of the surface, and
- (iii) applying pre-computed tethering forces.

Strategy (i) is the most straightforward approach and is suitable for pipe-like geometries with straight axis. This technique is employed in the idealized common carotid artery example (see Section 4.2).

Strategy (ii) adds tethering forces acting over the axial direction of the non-physical boundary which are proportional to the mean displacement of the boundary, the main difference introduced by this method is the possibility of bending and rotation of the involved surfaces. This technique is used on the examples shown in Sections 4.3 and 4.4.

For the implementation of strategy (iii) the tethering forces applied in each non-physical boundary are previously computed through an auxiliary problem. As a first step

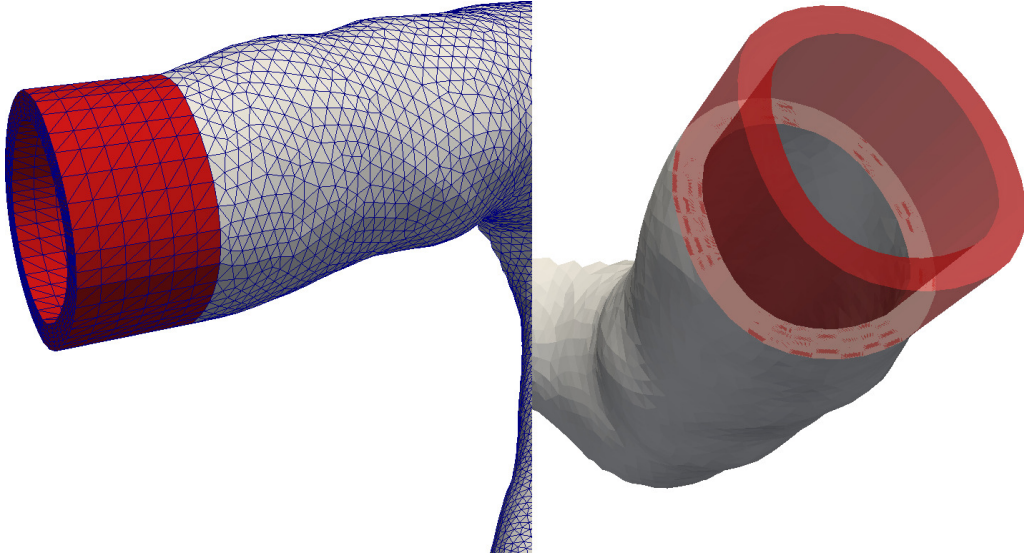


Figure 3.6: Example domain extension (red) at non-physical boundary for the auxiliary problem to determine tethering forces. Left Figure shows mesh details, displaying overlapped nodes at the interface between the original (gray) and the auxiliary (red) geometry. Right Figure evidences the matching cross-sectional shape of the extended domain.

we generate a pipe-like extension of the initial geometry ($\Omega_{base,aux}$ auxiliary domain) at each boundary. This extension presents a linear axis and constant cross-sectional shape, consistent with the original domain as exemplified on Figure 3.6. As a second step a target pre-stretch level and a baseline pressure are defined, and then the preload problem on $\Omega_{base,aux}$ using strategy (ii) is solved to obtain a shortened domain denoted by $\Omega_{m,aux}$ (material counterpart of $\Omega_{base,aux}$). The penalization method in the second step provides us with the tethering force required to acquire the desired pre-stretch level on the auxiliary problem, the reaction of this force is then applied on the original domain to solve the preload problem. Figure 3.7 displays this 3-step process proposed for the computation of the material domain.

With each of these described methodologies a “shortened” material geometry is obtained, when compared with the configuration extracted from the medical images Ω_{base} . For the 1D-3D FSI coupled problem it is considered that during the complete cardiac cycle the position of the non-physical boundaries remains constant. Thence, during the FSI simulation null mean displacements of the boundaries (with respect to Ω_{base}) are enforced using a penalization method analogous to strategy (ii).

3.8 Numerical approximations

The formulations described up to this point are in the continuum setting, and therefore are independent of the numerical method employed to approximate the problem. In this work, for both the fluid and the solid problems the finite element method for the spatial discretization is used. The time integration is treated with an implicit Crank-Nicolson finite-difference method. The finite element techniques employed regarding both solid and fluid problems are detailed next. Also, details for the discretization of the interface between both domains and the shared information among them are provided.

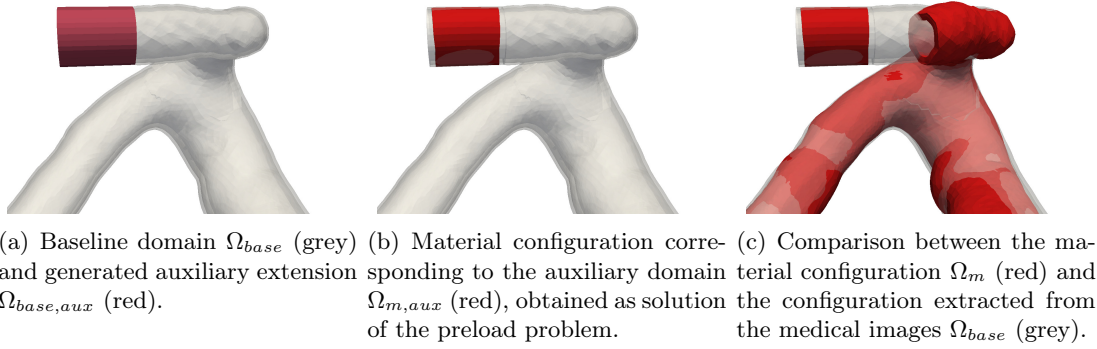


Figure 3.7: Strategy (iii), application of pre-computed tethering forces in the preload problem.

3.8.1 Numerical approximation for the solid problems

Consider ϕ_i , the i th element of the basis \mathcal{B}_u of the discrete space associated to the manifold $\mathcal{U}^h = \text{span}\{\phi_1, \phi_2, \dots, \phi_{3N_T}\}$ approximating \mathcal{U} and φ_l to the l th element of the basis \mathcal{B}_λ of the discrete space $\mathcal{P}^h = \text{span}\{\varphi_1, \varphi_2, \dots, \varphi_{N_T}\}$ approximating \mathcal{P} ; with N_T standing for the total number of nodes in the underlying mesh. As previously mentioned, both ϕ_i and φ_l are constructed based on linear finite element shape functions, and as can be seen, equal order interpolation will be employed. Specifically, φ_l is the scalar field defined by the shape function corresponding to the node l ($l = 1, \dots, N_T$). Also, from each node, three canonical vectorial fields are defined as

$$\begin{cases} \phi_i = (\varphi_l, 0, 0) \\ \phi_{i+1} = (0, \varphi_l, 0) \\ \phi_{i+2} = (0, 0, \varphi_l) \end{cases}, \quad i = 3(l-1). \quad (3.8.1)$$

The approximated displacement and Lagrangean fields (\mathbf{u}_s^h and λ_s^h) are obtained as linear combinations of the elements of the presented basis as

$$\begin{cases} \mathbf{u}_s^h = U_1\phi_1 + U_2\phi_2 + \dots + U_{3N_T}\phi_{3N_T} \\ \lambda_s^h = P_1\varphi_1 + P_2\varphi_2 + \dots + P_{N_T}\varphi_{N_T} \end{cases}, \quad (3.8.2)$$

where U and P condense the unknowns of the discretized equilibrium problem as coefficients of the linear combinations.

The discrete form for the linearized forward problem introduced in (3.4.7) can be written in the following form: given (U, P) (coefficients for the displacement and pressure fields at previous Newton-Raphson iteration -omitted k index-) find $(\delta U, \delta P)$ such that

$$\begin{bmatrix} \mathbf{A} & \mathbf{B} \\ \mathbf{B}^T & \mathbf{0} \end{bmatrix} \begin{bmatrix} \delta U \\ \delta P \end{bmatrix} = \begin{bmatrix} L \\ M \end{bmatrix}, \quad (3.8.3)$$

where the vector δU condenses the unknowns related to $\delta \mathbf{u}_s$ and δP the ones corresponding

to $\delta\lambda_s$. The matrix blocks are given by

$$\begin{aligned}
A_{ij} = & \int_{\Omega_s} [\mathbf{D}_s + \lambda_s (2\mathbb{I} - (\mathbf{I} \otimes \mathbf{I}))] \boldsymbol{\varepsilon}_s(\boldsymbol{\phi}_j) \cdot \boldsymbol{\varepsilon}_s(\boldsymbol{\phi}_i) d\Omega_s \\
& + \int_{\Omega_s} (\nabla_s \boldsymbol{\phi}_j) \boldsymbol{\sigma}_s \cdot (\nabla_s \boldsymbol{\phi}_i) d\Omega_s + \int_{\partial\Omega_s^W} [t_s^{W,n} ((\nabla_s \boldsymbol{\phi}_j)^T - \mathbf{I}) \mathbf{n}_s^W \cdot \boldsymbol{\phi}_i] \operatorname{div}_s \boldsymbol{\phi}_j d\partial\Omega_s^W \\
& - \int_{\partial\Omega_s^W} (\mathbf{H}(\boldsymbol{\phi}_j) \mathbf{n}_s \otimes \mathbf{n}_s)^S \mathbf{t}_s^{W,t} \cdot \boldsymbol{\phi}_i d\partial\Omega_s^W - \int_{\partial\Omega_m^W} \mathbf{P}_s \mathbf{t}_s^{W,t} \cdot \boldsymbol{\phi}_i (\operatorname{div}_s \boldsymbol{\phi}_j) d\partial\Omega_s^W \\
& - \int_{\partial\Omega_m^W} \mathbf{P}_s \mathbf{t}_s^{W,t} \cdot \boldsymbol{\phi}_i \left(-(\nabla_s \boldsymbol{\phi}_j)^T \mathbf{n}_s \cdot \mathbf{n}_s \right) d\partial\Omega_s^W \\
& - \int_{\partial\Omega_s^N} (\mathbf{t}_s^N \cdot \boldsymbol{\phi}_i) \left[(\operatorname{div}_s \boldsymbol{\phi}_j) - (\nabla_s \boldsymbol{\phi}_j)^T \mathbf{n}_s \cdot \mathbf{n}_s \right] d\partial\Omega_s^N, \quad (3.8.4)
\end{aligned}$$

and

$$B_{il} = - \int_{\Omega_s} \varphi_l \operatorname{div}_s \boldsymbol{\phi}_i d\Omega_s, \quad (3.8.5)$$

and the load vectors by

$$\begin{aligned}
L_i = & \int_{\Omega_s} [-\lambda_s \operatorname{div}_s \boldsymbol{\phi}_i + \boldsymbol{\sigma}_s \cdot \boldsymbol{\varepsilon}_s(\boldsymbol{\phi}_i)] d\Omega_s + \int_{\partial\Omega_s^W} \mathbf{P}_s \mathbf{t}_s^W \cdot \boldsymbol{\phi}_i d\partial\Omega_s^W + \int_{\partial\Omega_s^W} t_s^{W,n} \mathbf{n}_s \cdot \boldsymbol{\phi}_i d\partial\Omega_s^W \\
& + \int_{\partial\Omega_s^N} \mathbf{t}_s^N \cdot \boldsymbol{\phi}_i d\partial\Omega_s^N, \quad (3.8.6)
\end{aligned}$$

$$M_l = \int_{\Omega_s} (1 - \det \mathbf{F}_s^{-1}) \varphi_l d\Omega_s. \quad (3.8.7)$$

The *forward* and *preload* problems require further treatment at the discrete level for improving preconditioning, because of the large size of the algebraic system derived from the discretization of realistic patient-specific geometries. This is accomplished by modifying the variational formulations introducing a consistent zero-order term on the linearized (forward and preload) problems. That is, the left hand side of the first equation of (3.4.7) for the forward problem ($a_s(\delta\mathbf{u}_s, \hat{\mathbf{u}}_s)$) includes the additional term

$$\int_{\Omega_s} \gamma \nabla_s \delta\mathbf{u}_s \cdot \nabla_s \hat{\mathbf{u}}_s d\Omega_s \quad (3.8.8)$$

where γ can be regarded as a viscoelastic parameter. Note that this term is nullified when convergence is achieved, i.e. as $\delta\mathbf{u}_s \rightarrow 0$.

Moreover, since tetrahedral elements with linear interpolation for both displacement and pressure fields are used for the space discretization, the problem needs to be stabilized in the sense of the inf-sup condition, the linearized (forward and preload) problems are modified adding a Laplacian-like term in the pressure equation. That is, the left hand side of the second equation of (3.4.7) for the forward problem includes the term

$$\int_{\Omega_s} \frac{h^2}{\nu} \nabla_s \delta\lambda_s \cdot \nabla_s \hat{\lambda}_s d\Omega_s, \quad (3.8.9)$$

where h is a characteristic length of the finite element and ν a given stabilization parameter.

Minding these changes, equation (3.8.3) is redefined as follows

$$\begin{bmatrix} \mathbf{A}^* & \mathbf{B} \\ \mathbf{B}^T & \mathbf{D} \end{bmatrix} \begin{bmatrix} \delta U \\ \delta P \end{bmatrix} = \begin{bmatrix} L \\ M \end{bmatrix}, \quad (3.8.10)$$

where blocks \mathbf{A}^* and \mathbf{D} are given by

$$A_{ij}^* = A_{ij} + \int_{\Omega_s} \gamma \nabla_s \phi_j \cdot \nabla_s \phi_i d\Omega_s, \quad (3.8.11)$$

$$D_{lk} = \int_{\Omega_s} \frac{h^2}{\nu} \nabla_s \varphi_k \cdot \nabla_s \varphi_l d\Omega_s. \quad (3.8.12)$$

The discrete expressions for the linearized form of the preload problem can be obtained analogously following the presented procedure.

3.8.2 Numerical approximation for the fluid problem

As a first step, a θ time integration scheme ($\theta = 1/2$ is Crank-Nicolson) is introduced in the set of linearized equations for the fluid problem presented in -, yielding

$$\begin{aligned} & \int_{\Upsilon_k} \rho \frac{\mathbf{v}^{k+1} - \mathbf{v}^k}{\Delta t} \cdot \hat{\mathbf{v}} d\Upsilon_k + \int_{\Upsilon_k} \rho \nabla \mathbf{v}^{\theta k+1} (\mathbf{v}^{\theta k} - \mathbf{v}_R^k) \cdot \hat{\mathbf{v}} d\Upsilon_k \\ & - \int_{\Upsilon_k} p^{k+1} \operatorname{div} \hat{\mathbf{v}} d\Upsilon_k + \int_{\Upsilon_k} 2\mu \boldsymbol{\varepsilon}(\mathbf{v}^{\theta k+1}) \cdot \boldsymbol{\varepsilon}(\hat{\mathbf{v}}) d\Upsilon_k = \\ & \sum_{i=1}^C \int_{\partial \Upsilon_k^{A,i}} \mathbf{t}_k^i \cdot \hat{\mathbf{v}} d\partial \Upsilon_k^{A,i} \quad \forall \hat{\mathbf{v}} \in \mathcal{V}_k, \end{aligned} \quad (3.8.13)$$

$$\int_{\Upsilon_k} \hat{p} \operatorname{div} \mathbf{v}^{k+1} d\Upsilon_k = 0 \quad \forall \hat{p} \in \mathcal{P}_k, \quad (3.8.14)$$

$$\int_{\Upsilon_k} \nabla \mathbf{d}^{k+1} \cdot \nabla \hat{\mathbf{d}} d\Upsilon_k = 0 \quad \forall \hat{\mathbf{d}} \in \mathcal{D}_k^*, \quad (3.8.15)$$

where it has been considered that the blood behaves as a Newtonian fluid, with $\bar{\boldsymbol{\sigma}}(\mathbf{v}) = 2\mu \boldsymbol{\varepsilon}(\mathbf{v})$. In this context, μ denotes the viscosity of the Newtonian fluid and the velocities $\mathbf{v}^{\theta k+1}$ and $\mathbf{v}^{\theta k}$ are obtained as

$$\mathbf{v}^{\theta k+1} = \theta \mathbf{v}^{k+1} + (1 - \theta) \mathbf{v}^n, \quad \mathbf{v}^{\theta k} = \theta \mathbf{v}^k + (1 - \theta) \mathbf{v}^n, \quad (3.8.16)$$

with \mathbf{v}^n standing for the fluid velocity at the time corresponding to the previous time step t_n .

Next, for the spaces \mathcal{V}_k^h , \mathcal{P}_k^h and \mathcal{D}_k^h (discrete approximations of the corresponding spaces \mathcal{V}_k , \mathcal{P}_k and \mathcal{D}_k , respectively) consider the bases

$$\begin{cases} \mathcal{B}_v = \{\psi_1, \psi_2, \dots, \psi_{3(N_T^f + N_E^f)}\} \\ \mathcal{B}_p = \{\varphi_1, \varphi_2, \dots, \varphi_{N_T^f}\} \\ \mathcal{B}_d = \{\phi_1, \phi_2, \dots, \phi_{3N_T^f}\} \end{cases} \quad (3.8.17)$$

where N_E^f is the total number of tetrahedral elements employed in the discretization of the fluid domain and N_T^f is the total number of nodes in the mesh. Every φ_i in \mathcal{B}_p is a scalar field given by the linear finite element shape functions of these nodes and each ϕ_i in \mathcal{B}_d is a vectorial function as explained in the previous section for the solid problems. Moreover, functions ψ_i in \mathcal{B}_v are a vectorial fields constructed based on these shape functions and an additional ‘‘bubble’’ shape function (see (D.N. Arnold, 1984)) for each tetrahedral element. The addition of these ‘‘bubble’’ functions serves the purpose of satisfying the inf-sup condition corresponding to the null divergence constraint over the velocity field. The approximated velocity, pressure and displacement field are obtained as linear combinations of the corresponding bases elements, i.e.

$$\begin{cases} \mathbf{v}^h = V_1\psi_1 + V_2\psi_2 + \cdots + V_{3(N_T+N_E)}\psi_{3(N_T+N_E)} \\ p^h = P_1\varphi_1 + P_2\varphi_2 + \cdots + P_{N_T}\varphi_{N_T} \\ \mathbf{d}^h = V_1\phi_1 + V_2\phi_2 + \cdots + V_{3N_T}\phi_{3(N_T)} \end{cases}, \quad (3.8.18)$$

where vectors V, P, D condense the linear combination coefficients.

Moreover, since blood flow dynamics can be characterized as a convection-dominated problem, in this work the Streamline Upwind Petrov-Galerkin technique (SUPG, (Hughes et al, 1987)) is employed. Furthermore, an artificial compressibility contribution controlled by the coefficient ϱ is incorporated to regularize the saddle-point problem. Minding these considerations, the discrete system corresponding to equations (3.8.13)-(3.8.15) reads

$$\begin{bmatrix} \mathbf{A} & \mathbf{B} & \mathbf{0} \\ \mathbf{B}^T & \mathbf{C} & \mathbf{0} \\ \mathbf{0} & \mathbf{0} & \mathbf{D} \end{bmatrix} \begin{bmatrix} V^{k+1} \\ P^{k+1} \\ D^{k+1} \end{bmatrix} = \begin{bmatrix} L \\ 0 \\ 0 \end{bmatrix}, \quad (3.8.19)$$

where V^{k+1}, P^{k+1} and D^{k+1} are the vectors of coefficients of the solution for the iteration $k + 1$, and the blocks forming the system matrix are

$$\begin{aligned} A_{ij} = & \int_{\Upsilon_k} \frac{\rho}{\Delta t} \psi_j \cdot \psi_i d\Upsilon_k + \int_{\Upsilon_k} \theta \rho \nabla \psi_j (\mathbf{v}^{\theta k} - \mathbf{v}_R^k) \cdot \psi_i d\Upsilon_k \\ & + \int_{\Upsilon_k} \theta \rho \nabla \psi_j (\mathbf{v}^{\theta k} - \mathbf{v}_R^k) \cdot \tau_{up} \nabla \psi_i (\mathbf{v}^{\theta k} - \mathbf{v}_R^k) d\Upsilon_k + \int_{\Upsilon_k} \theta 2\mu \varepsilon(\psi_j) \cdot \varepsilon(\psi_i) d\Upsilon_k \end{aligned} \quad (3.8.20)$$

$$B_{il} = - \int_{\Upsilon_k} \varphi_l \operatorname{div} \psi_i d\Upsilon_k \quad (3.8.21)$$

$$C_{lm} = - \int_{\Upsilon_k} \varrho \varphi_l \varphi_m d\Upsilon_k, \quad (3.8.22)$$

$$D_{no} = \int_{\Upsilon_k} \nabla \phi_o \cdot \nabla \phi_n d\Upsilon_k, \quad (3.8.23)$$

$$\begin{aligned}
L_i = & \int_{\Upsilon_k} \frac{\rho}{\Delta t} \mathbf{v}^k \cdot \boldsymbol{\psi}_i d\Upsilon_k - \int_{\Upsilon_k} (1 - \theta) \rho \nabla \mathbf{v}^n (\mathbf{v}^{\theta k} - \mathbf{v}_R^k) \cdot \boldsymbol{\psi}_i d\Upsilon_k \\
& - \int_{\Upsilon_k} (1 - \theta) \rho \nabla \mathbf{v}^n (\mathbf{v}^{\theta k} - \mathbf{v}_R^k) \cdot \tau_{up} \nabla \boldsymbol{\psi}_i (\mathbf{v}^{\theta k} - \mathbf{v}_R^k), d\Upsilon_k - \int_{\Upsilon_k} (1 - \theta) 2\mu \boldsymbol{\varepsilon}(\mathbf{v}^n) \cdot \boldsymbol{\varepsilon}(\boldsymbol{\psi}_i) d\Upsilon_k,
\end{aligned} \tag{3.8.24}$$

where τ_{up} is defined at each element considering its characteristic length h and the magnitude of the relative velocity of the fluid with respect to the mesh as follows

$$\tau_{up} = \frac{h}{2|\mathbf{v}^{\theta k} - \mathbf{v}_R^k|} \left(1 - \frac{1}{\text{Pe}}\right), \quad \text{Pe} = \frac{\rho |\mathbf{v}^{\theta k} - \mathbf{v}_R^k| h}{2\mu}. \tag{3.8.25}$$

3.8.3 Interface discretization

Both arterial wall and blood flow domain discretizations are built from a unique surface mesh obtained from the segmentation and mesh preparation process. These constructions preserve the original mesh for the interface in such way that tetrahedral elements for both problems posse matching nodes and faces at the interface boundary ($\partial\Omega_s^W \equiv \partial\Upsilon_t^W$). As consequence, the sharing of information between both problems is straightforward. For example, for the definition of Dirichlet boundary conditions for the fluid problem, as required in (3.4.5), the displacement of the solid is transferred directly between matching nodes on the surface. Similarly, the traction at each node for the fluid domain is computed and then introduced as Neumann boundary data for the solid problem. It is important to note that, when the convergence of the FSI algorithm is achieved, both meshes are compatibly deformed preserving its matching characteristic along the simulation (with an error related to the convergence tolerance of the problem). Figure 3.8 shows an example of a boundary mesh along with two face-matching tetrahedral elements from solid and fluid domains.

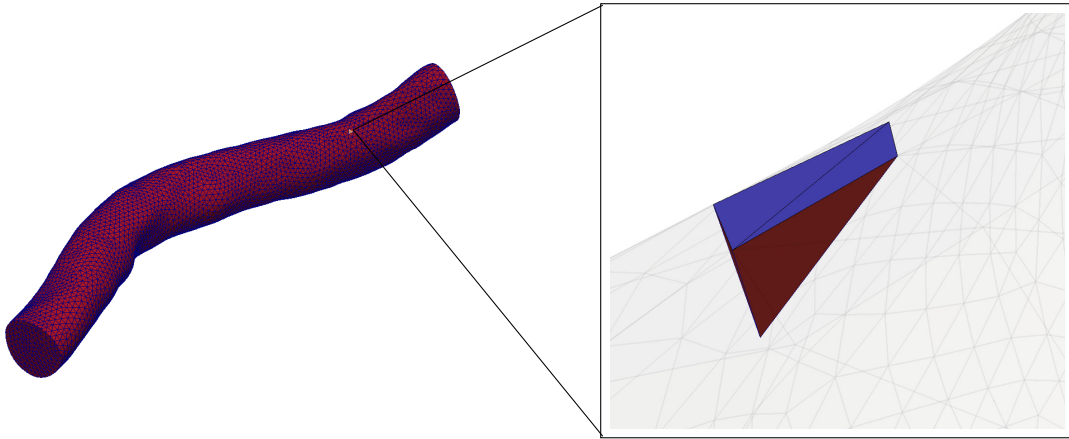


Figure 3.8: Discretization of the interface between the arterial wall and blood flow domains ($\partial\Omega_s^W \equiv \partial\Upsilon_t^W$), displaying the complete triangular mesh -left- and a closeup showing one tetrahedral element from each domain (blue element for arterial wall, red element for fluid domain) with matching faces in the boundary -right-.

Chapter 4

Applications in computational hemodynamics

4.1 Introduction

In this chapter four numerical examples are presented, aiming at showing the potential of the integrative modeling framework described in Chapters 2 and 3 and assessing the influence of initial loads and pre-stretch in hemodynamic simulations.

The first example features a straight pipe representing an idealized human common carotid artery. Six modeling scenarios are analyzed, presenting a comparison between the results obtained using the proposed modeling framework and the ones provided by alternative cases considering different simplifying hypotheses.

In the second example, an idealized common carotid bifurcation is analyzed. In this case, the attention is primarily focused on assessing the impact of tethering forces on the hemodynamic simulation, contrasting two scenarios that differ only in the considered level of pre-stretch ($\lambda_C = 1.2$ and $\lambda_C = 1.0$). The discrepancies between the most frequently used approach in the literature and our proposed modeling framework are highlighted.

For the third example, a patient-specific human common carotid artery is studied. The *baseline diastolic configuration* of the vascular segment of interest is extracted from medical images. Analogous to the analysis presented for the second example, the blood flow dynamics and mechanical response of the vessel are studied for two scenarios corresponding to different levels of pre-stretch.

Finally, in the fourth example, a patient-specific cerebral aneurysm located in the middle cerebral artery is studied. The analysis is focused on the influence of the tethering forces corresponding to different levels of pre-stretch on the aneurysm sack.

4.2 Problem 1: straight pipe

4.2.1 Problem description

A straight pipe representing an idealized human common carotid artery is studied. In the first place the preload problem is solved to obtain the material configuration, assuming that the initial -given- configuration has been extracted from a set of medical images. Then, we proceed to solve the 3D FSI problem coupled with the simplified closed-loop circulation model (see Section 3.5).

Hereafter, we will refer to the fluid pressure field at a given time t as p_t , and define a baseline pressure level $p_{base} = 9 \cdot 10^4 \frac{dyn}{cm^2}$ (67.5 mmHg), and the relative pressure field at any given time is $p_t^{rel} = p_t - p_{base}$.

Six different cases are analyzed with two main objectives: i) to assess the relevance of taking into account the complete load state at the so-called *initial* geometry, separating the inner pressure load and the tethering forces; and ii) to analyze the pitfalls when considering alternative strategies to simulate the system response without having solved the preload problem. Thus, the following scenarios are considered:

- (a) the preload problem is solved considering that the initial geometry is a configuration at mechanical equilibrium with a constant internal reference pressure p_{base} and that presents a known level of pre-stretch $\lambda_C = 1.2$ and the FSI problem is solved from that configuration onwards;
- (b) the preload problem is solved considering that the initial geometry is a configuration at mechanical equilibrium only with a constant internal reference pressure p_{base} , the length of the material configuration is equal to the initial length ($\lambda_C = 1.0$) and the FSI problem is solved from that configuration onwards;
- (c) the preload problem is solved considering that the initial geometry presents a known level of pre-stretch $\lambda_C = 1.2$ and no inner pressure is considered; the FSI problem is solved from that configuration onwards, assuming that the solid is equilibrated by a relative pressure p_t^{rel} ;
- (d) no preload problem is solved and the constitutive equation is defined considering that the initial geometry is the material configuration, for the FSI problem it is considered that the solid is a configuration at mechanical equilibrium with the defined relative pressure p_t^{rel} , i.e., neither the full level of pressure nor the stretch are considered in the simulation;
- (e) no preload problem is solved and constitutive equations are defined considering that the initial geometry is the material configuration, the FSI problem is set in that configuration by firstly applying a known level of pre-stretch $\lambda_C = 1.2$ as well as the full level of inner pressure p_t exerted by the blood flow at any given time t ;
- (f) no preload problem is solved and constitutive equations are defined considering that the initial geometry is the material configuration, the FSI problem is set in that configuration by applying the full level of inner pressure p_t exerted by the blood flow at any given time t and considering that the length of the vessel is constant and equal to the corresponding for the initial state ($\lambda_C = 1$).

Note that: case (a) corresponds to the most realistic and physiologically accurate scenario. Cases (b) and (c) are expected to give insight about the importance of taking into account the full load state when solving the preload problem (internal pressure and pre-stretch, respectively). Finally, cases (d), (e) and (f) will serve the purpose of comparing against standard approaches to blood flow and arterial wall simulations that completely neglect the preload problem. Table 4.1 summarizes the loading conditions used to solve both the preload and the FSI problems for each test case.

For each case, we will denote as *diastolic baseline configuration* to the equilibrium geometry obtained when the vessel is loaded with the constant reference pressure $p = p_{ref}$ and the corresponding tethering forces. That means that for cases (a), (b), (c) and (d) the geometry will be the one obtained from the image, while for cases (e) and (f) the geometry is considerably different due to loading conditions (see Table 4.3).

4.2.2 Geometrical and constitutive parameters

The idealized arterial segment is assumed to have been extracted from a medical image, with inner radius and thickness equal to $r_i = 0.37$ cm and $e = 0.063$ cm, respectively

Scenario	Mat. configuration	Preload problem loads		FSI and forward problem loads	
		Int. pressure	Tet. stretch	Int. pressure	Tet. stretch
(a)	preload*	p_{base}	$\lambda_C = 1.2$	p_t	$\lambda_C = 1.2$
(b)	preload*	p_{base}	$\lambda_C = 1.0$	p_t	$\lambda_C = 1.0$
(c)	preload*	0	$\lambda_C = 1.2$	p_t^{rel}	$\lambda_C = 1.2$
(d)	image ⁺	-	-	p_t^{rel}	$\lambda_C = 1.0$
(e)	image ⁺	-	-	p_t	$\lambda_C = 1.2$
(f)	image ⁺	-	-	p_t	$\lambda_C = 1.0$

Table 4.1: Description of scenarios considered for the idealized carotid segment. Loading conditions for the preload and FSI forward problems are presented. *: indicates that the material configuration is known after solving the preload problem. ⁺: indicates that the material configuration is directly given by the geometry extracted from the image.

(data consistent with a common carotid artery vessel as given by Avolio (1980)), and the length of the pipe is $l = 8.9$ cm. The arterial wall consists of two layers, being the inner layer (media) two times the size of the external layer (adventitia).

The setting of material parameters is inspired in the data presented in Zulliger et al (2004a) for a rat carotid artery, adapted according to the following criteria:

- (i) adventitia layer mechanical properties are one order of magnitude smaller than the ones corresponding to the media layer;
- (ii) the inner radius of the equilibrium configuration when the vessel is loaded with a constant inner pressure level of $p = 1.6 \cdot 10^5 \frac{dyn}{cm^2}$ (120 mmHg) is approximately 5% bigger than the corresponding to a similar situation when the pressure level is at $p = 8 \cdot 10^4 \frac{dyn}{cm^2}$ (60 mmHg); these pressure levels correspond to reasonable systolic and diastolic pressure values, respectively;
- (iii) two families of collagen fibers are considered with helicoidal structure in the circumferential direction (see Figure 4.1), with a characteristic angle β for each family and material layer. The values of β for media and adventitia layers are taken from Holzapfel and Gasser (2000), the orientation of the fibers is in each case determined for the previously defined *diastolic baseline configuration*.

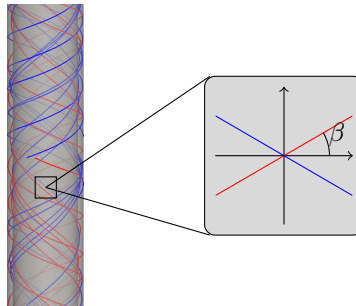


Figure 4.1: Representation of the helicoidal arrangement of collagen fibers for the straight pipe. The orientation of the fibers is defined for media and adventitia layers through the angle β (see Table 4.2 for parameter values).

In addition, these collagen fibers are considered to be recruited when they are stretched beyond the *diastolic baseline configuration* Ω_{base} . Let \mathbf{x}_{base} be the coordinates in this

domain, and \mathbf{u}^{base} be the displacements mapping this configuration with the material domain, with the associated deformation gradient $\mathbf{F}^{base} = \mathbf{I} + \nabla_m \mathbf{u}^{base}$. Then for each scenario the recruitment stretches λ_i^0 are defined via

$$\lambda_i^0 = \mathbf{a}_i \cdot (\mathbf{C}_m^{base} \mathbf{a}_i), \quad i = 4, 6, \quad (4.2.1)$$

with $\mathbf{C}_m^{base} = (\mathbf{F}_m^{base})^T \mathbf{F}_m^{base}$. To obtain a similar collagen behavior (within the physiological pressure range) to the presented in Zulliger et al (2004a) (where collagen is recruited at the zero-load configuration), the parameter k_2 (see equation (3.6.1)) controlling the exponential response of the fiber has been increased. Table 4.2 presents the final material setting for this problem.

Property	Media	Adventitia
Thickness [cm]	0.042	0.021
$c_{elast} [\frac{dyn}{cm^2}]$	$8 \cdot 10^6$	$8 \cdot 10^5$
$k_1 [\frac{dyn}{cm^2}]$	$32 \cdot 10^4$	$32 \cdot 10^3$
k_2	20.0	20.0
β	29.26°	65.37°

Table 4.2: Material properties considered in the numerical simulation of the carotid artery

4.2.3 Discretization

The total number of nodes for the fluid domain is 31251. The fluid mesh is generated using a Delaunay method. The arterial wall is discretized using a semi-structured mesh of tetrahedral elements. This solid mesh was constructed through an extrusion of the surface representing the lumen boundary in the outward normal direction. Prisms were generated from triangles and then tetrahedra were constructed from the prisms. The resulting mesh consists of 6 layers of prisms in the radial direction (the first 4 inner element layers correspond to the media, and the 2 outer layers represent the adventitia). The total number of nodes for the solid domain is 94482. The time-step in the simulation is taken $\Delta t = T/1000$, where $T = 1s$ is the cardiac period.

4.2.4 Parameters for numerical simulation

Numerical parameters used are $\gamma = 0.01c_{elast}$ for the zero-order preconditioning term (see (3.8.8)) and $\nu = 0.1c_{elast}$ for the pressure stabilization (see (3.8.9)).

In the case of the preload problem, a subrelaxation step at each iteration of the Newton-Raphson scheme is introduced, the value adopted for this subrelaxation step is 0.6. The solution is achieved *via* 10 load steps in which the displacement at both ends of the cylinder (to define the pre-stretch, see Section 4.2.5) and the inner pressure (to define the preload pressure) are linearly incremented up to the desired values.

For the FSI problem, the subrelaxation parameters are chosen to be $\kappa_a = \kappa_b = 0.4$ (see equations (3.4.13) and (3.4.13)), while the parameter ι controlling the update of the Neumann boundary condition for the arterial wall at $\partial\Omega_s^W$ is defined by $n_s = 6$ (see Section 3.4.3).

4.2.5 Boundary conditions

Preload problem.

For the preload problem, Dirichlet boundary conditions are imposed to the displacement in the axial direction at non-physical boundaries (following strategy (i) for the incorporation of tethering forces as detailed in Section 3.7), ensuring that a certain level of pre-stretch is achieved. That is, for scenarios (a) and (c) an axial displacement of 0.7416 cm at each end of the cylinder is imposed; while for scenario (b) null axial displacements are considered. Neumann conditions are imposed at $\partial\Omega_s^W$ given by the constant p_{base} pressure load for scenarios (a) and (b), while in scenario (c) $\partial\Omega_s^W$ is set as an homogeneous Neumann boundary. In order to avoid rigid rotations of the entire structure, at non-physical boundaries $\partial\Omega_s^{A,i}$ a penalization over the tangential displacement is added to four diametrical nodes.

Finally, for the force acting on the external boundary $\partial\Omega_s^E$ (see Section 3.3, equation (3.3.1)) the following assumptions are considered:

- the reference displacement for the elastic component is set at the *diastolic baseline configuration*, i.e. $\mathbf{u}_0 = \mathbf{u}_s^{base}$,
- the velocity of the body at the baseline state (relaxed diastolic state) is small.

Hence, the force given by external tissues is neglected in the preload problem, resulting in an homogeneous Neumann boundary condition over the corresponding boundary.

1D-3D FSI problem.

Boundary conditions for both the fluid and the solid at $\partial\Omega_s^W$ are taken as described in Section 3.4. In addition, coupling (Neumann-like) boundary conditions are set at non-physical boundaries for the fluid domain, providing a constant normal traction datum obtained from the 1D model through the dimensionally heterogeneous iterative coupling algorithm. For the arterial wall, and analogously to the preload problem, Dirichlet conditions on the axial displacement are imposed at non-physical boundaries. Furthermore, Robin boundary conditions (at the time-descrete level) are incorporated on $\partial\Omega_s^E$ due to the action of the surrounding tissues (see Section 3.3, expression (3.3.1)). The parameters controlling the response of the external support are $k_e = 2 \cdot 10^2 \frac{dyn}{cm^2}$ and $k_v = 2 \cdot 10^3 \frac{dyn}{cm^2 \cdot s}$, while the reference for the elastic component is given by the displacement at the *diastolic baseline configuration*, i.e. $\mathbf{u}_0 = \mathbf{u}_s^{base}$.

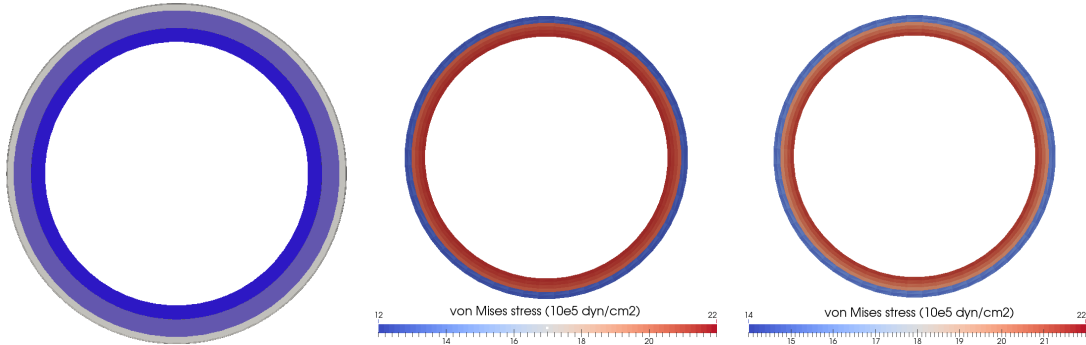
4.2.6 Results

Figure 4.2 summarizes the results obtained for scenario (a); a comparison between the initial (image-based) and material geometries is displayed in Figures 4.2(a) and 4.2(b); the von Mises stress state at the *baseline diastolic* and *systolic* configurations is shown in Figures 4.2(c) and 4.2(d), respectively; and, finally, the velocity profile representing the blood flow behavior is displayed Figure 4.2(e) Since the flow rate contour (not shown here) is given by the 1D model and has a physiological shape, the blood velocity is within the physiological range. Additionally, Figure 4.4 displays the pressure and flow rate (Figure 4.4(a)) at the inlet of the pipe along with the velocity profiles and streamlines for four different time instants within the cardiac cycle (Figures 4.4(b) to 4.4(e)).

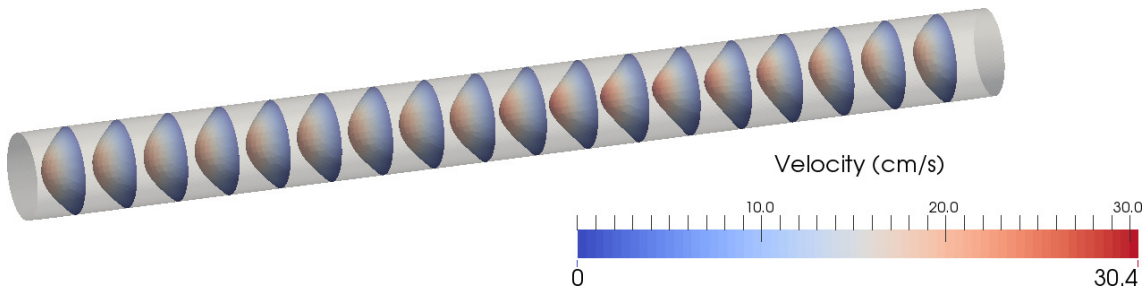
Furthermore, Figure 4.3 features the stress distribution for both diastole and systole states along thickness of the arterial wall. As a consequence of the tethering and internal pressure loads, the material presents a tensile state in both circumferential $\sigma_{\theta\theta}$ and axial σ_{zz} directions. The von Mises equivalent stress (σ_{vm}) is also displayed in the same figure.



(a) Comparison between *baseline diastolic* (blue) and material (translucent grey) configurations (side view).



(b) Comparison between *base-* (c) Von Mises stress distribution (d) Von Mises stress distribution
line diastolic (blue) and material on a central slice of the arterial on a central slice of the arterial
(translucent grey) configurations wall at *baseline diastolic configu-* wall at systole.
(axial view). *ration*.



(e) Velocity profile at systole ($t = 0.35 \cdot T$).

Figure 4.2: Straight pipe example: visualization of results for the 1D-3D FSI simulation of scenario (a). The notable difference on the stress levels is due to the material properties of the media and adventitia layers.

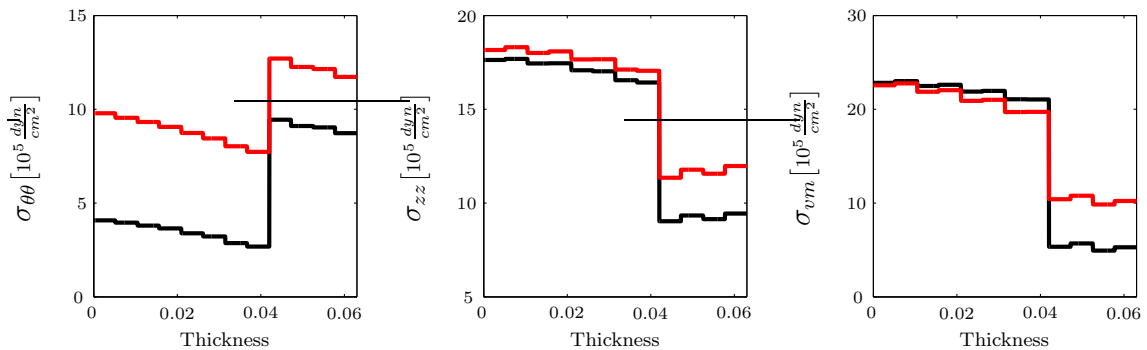
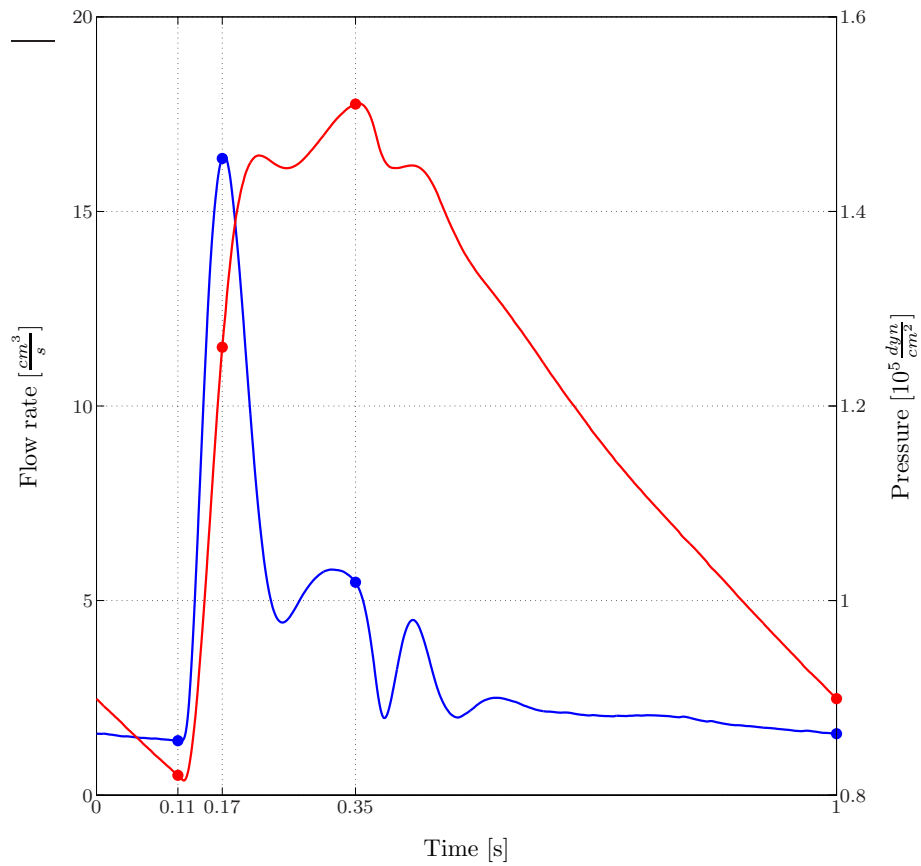
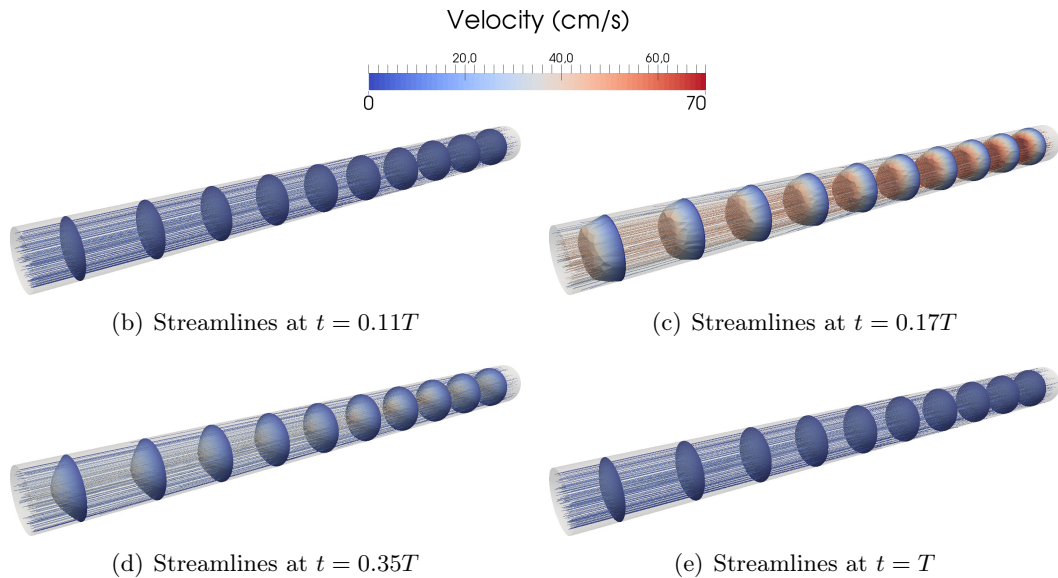


Figure 4.3: Circumferential, longitudinal and von Mises stress distribution along the thickness of the arterial wall for scenario (a) for diastole (black) and systole (red). Note the discontinuity introduced by the different material properties of the media and adventitia layers; also, that stresses are constant within each finite element.



(a) Flow rate (blue) and pressure (red) at the inlet of the straight pipe during the cardiac cycle.



(b) Streamlines at $t = 0.11T$

(c) Streamlines at $t = 0.17T$

(d) Streamlines at $t = 0.35T$

(e) Streamlines at $t = T$

Figure 4.4: Blood flow dynamics for the straight pipe example, displaying pressure (red) and flow rate (blue) at the bifurcation inlet during one cardiac cycle and visualization of velocity profiles and streamlines for four time instants $t = 0.11T$, $t = 0.22T$, $t = 0.35T$ and $t = T$.

It is interesting to highlight that the behavior of the σ_{vm} differs from $\sigma_{\theta\theta}$ and σ_{zz} across the thickness of the arterial wall. While $\sigma_{\theta\theta}$ and σ_{zz} increase at systole in both layers, σ_{vm} slightly decreases in the inner layer and increases in the outer layer. The strong discontinuity is related to the change in material properties from the media to the adventitia layers. All stresses are measured at a central slice of the vessel and mapped back, if required, to the image-based configuration.

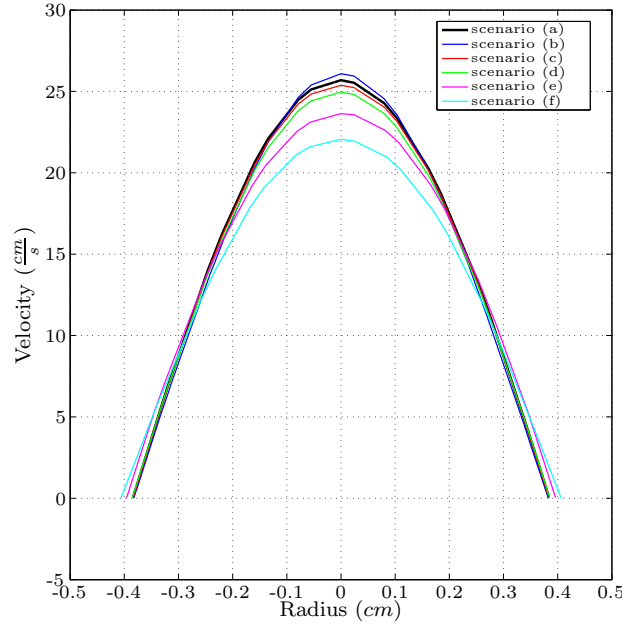


Figure 4.5: Velocity profile for different scenarios at time $t = 0.35T$ measured over a cross sectional line.

In order to establish a comparison of the results for different scenarios, an overview of the predictions performed by the simulations is condensed in Table 4.3 (geometrical landmarks of different configurations), Figure 4.5 (velocity profiles at a given section of the pipe, located at $z = 0.67l$, for $t = 0.35T$), Figure 4.6 (stress distribution along the thickness) and Table 4.4 (relative differences of the average stress at media and adventitia layers with respect to scenario (a)).

- Scenario (a). As said, this ideally represents the most physiologically realistic scenario. That is, the stress state (see Figure 4.6) and the fluid dynamics quantities

Scenario	Geometrical landmarks							
	Zero-load			Diastolic*			Systolic**	
	r_i [cm]	l [cm]	e [cm]	r_i [cm]	l [cm]	e [cm]	r_i [cm]	e [cm]
(a)	0.352	7.42	0.088	0.370	8.90	0.063	0.383	0.060
(b)	0.349 (0.66)	8.90 (19.9)	0.065 (26.5)	0.370 (0.00)	8.90 (0.00)	0.063 (0.00)	0.382 (0.15)	0.060 (0.00)
(c)	0.371 (5.52)	7.42 (0.00)	0.073 (17.9)	0.370 (0.00)	8.90 (0.00)	0.063 (0.00)	0.383 (0.00)	0.060 (0.00)
(d)	0.370 (5.22)	8.90 (19.9)	0.063 (28.7)	0.370 (0.00)	8.90 (0.00)	0.063 (0.00)	0.384 (0.33)	0.061 (0.99)
(e)	0.370 (5.22)	8.90 (19.9)	0.063 (28.7)	0.387 (4.49)	10.89 (20.0)	0.049 (22.7)	0.396 (3.52)	0.051 (16.2)
(f)	0.370 (5.22)	8.90 (19.9)	0.063 (28.7)	0.394 (6.48)	8.90 (00.0)	0.061 (2.86)	0.405 (5.64)	0.059 (1.83)

Table 4.3: Results overview displaying geometrical landmarks (inner radius $-r_i$, length $-l$, and thickness $-t$) of material, diastolic baseline and systolic configurations. Measures are taken at the central slice of the vessel. *Diastolic baseline configuration. ** Configuration at systole ($t = 0.35T$). In parentheses, percent differences with respect to scenario (a) are reported.

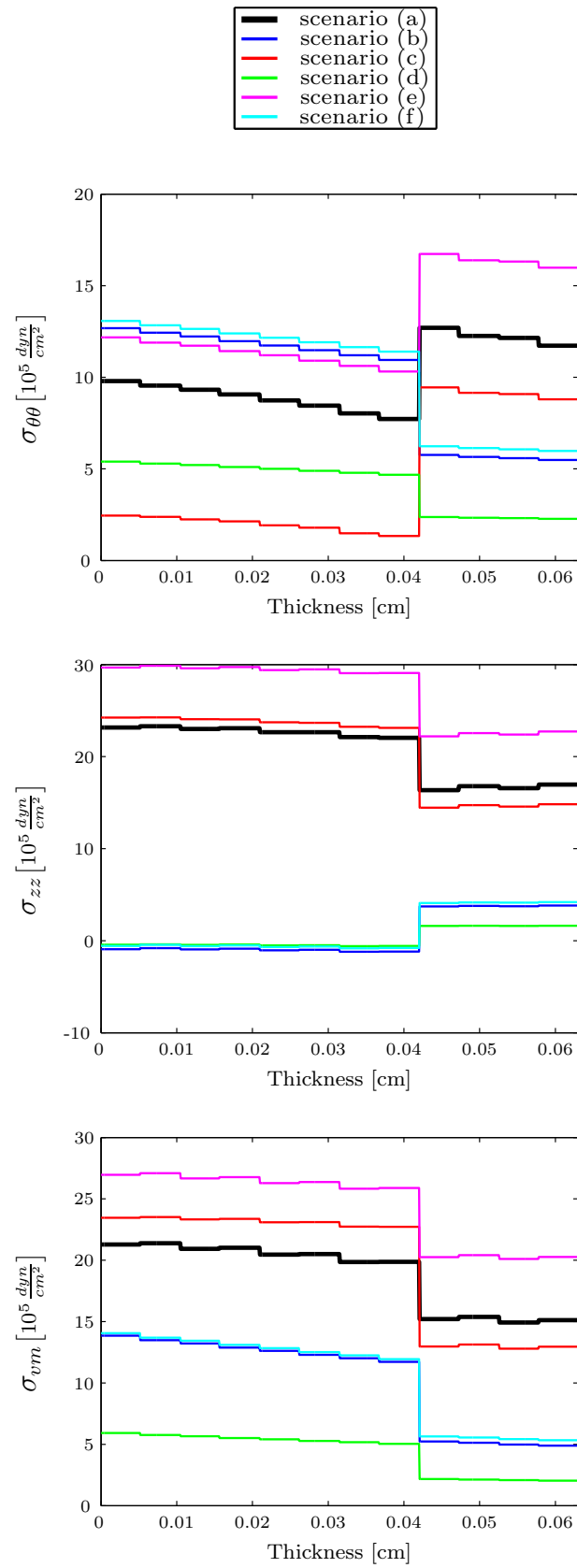


Figure 4.6: Distribution of circumferential (top), axial (middle) and von Mises (bottom) stresses at systole along the thickness of the arterial wall for the proposed scenarios - (a) black, (b) blue, (c) red, (d) green, (e) magenta, (f) cyan.

Scenario	Discrepancies of average stress values [%]					
	Media			Adventitia		
	$\sigma_{\theta\theta}$	σ_{zz}	σ_{vm}	$\sigma_{\theta\theta}$	σ_{zz}	σ_{vm}
(b)	34.0	104	38.3	53.8	77.5	66.5
(c)	77.7	4.59	12.1	25.4	12.1	14.4
(d)	42.9	102	73.5	80.9	90.3	86.1
(e)	27.8	29.6	28.2	33.9	34.8	33.6
(f)	38.8	102.8	37.2	49.8	75.3	63.7

Table 4.4: Percentage differences with respect to scenario (a) of the average circumferential, axial and von Mises stresses for each material layer and proposed scenario. **Measures taken on a central slice of the vessel at $t = 0.35T$.

Scenario (d) : discrepancies of average $\Delta\sigma$ [%]					
Media			Adventitia		
$\Delta\sigma_{\theta\theta}$	$\Delta\sigma_{zz}$	$\Delta\sigma_{vm}$	$\Delta\sigma_{\theta\theta}$	$\Delta\sigma_{zz}$	$\Delta\sigma_{vm}$
6.19	181	2.87	25.8	33.6	26.8

Table 4.5: Percentage discrepancies with respect to scenario (a) of the difference between systolic and *baseline diastolic* stresses ($\Delta\sigma$) for each material layer. Measures taken on a central slice of the vessel at $t = 0.35T$.

(see Figure 4.5) can be considered as reference solution to discuss the differences caused by modeling simplifications in the rest of the scenarios considered (see items below). Such realistic scenario was possible to be simulated through the integrative framework developed in Chapters 2 and 3 of this thesis. For instance, from Figure 4.6 it is seen that the mechanical state of the arterial wall is pretty badly predicted by most of the remaining scenarios, even changing the direction of stresses due to the lack of preload stresses.

- Scenario (b). From Figure 4.6, it can be observed that, despite providing a good approximation of the geometry within the physiological range (see Table 4.3), neglecting the tethering forces given by the pre-stretch leads to major discrepancies when evaluating the stress state of the arterial wall tissue. As it is evident from the same figure, there are significant differences for both the circumferential and axial stresses and, as result, a severe underestimation of the von Mises equivalent stress. As displayed on Table 4.4, in average, the differences in the prediction of stresses reach 54%, 104% and 66% for $\sigma_{\theta\theta}$, σ_{zz} and σ_{vm} , respectively, with respect to scenario (a). As a consequence of the good estimation of the geometry achieved for this simple case, the blood flow behavior is fairly predicted, as can be observed in Figure 4.5. Note that, compared with scenario (a), the shape of the profile has similar characteristics and the maximum velocity presents a difference of approximately 1.5%.
- Scenario (c). Although the approximation of the geometry of the vessel is adequate within the physiological range (see Table 4.3), the estimation of the stress state remains poor. Figure 4.6 clearly shows that the main flaw is in the prediction of the circumferential stress, since axial efforts are fairly represented. Since in this example the von Mises stress invariant is primarily driven by the axial components, this scenario renders a good prediction for this quantity. Table 4.4 shows that the

average stresses present differences up to 78%, 12% and 14% for $\sigma_{\theta\theta}$, σ_{zz} and σ_{vm} , respectively, with respect to scenario (a). Once again, similarly to the findings corresponding to scenario (b) the results for the blood flow behavior are in agreement with those obtained from scenario (a), as shown in Figure 4.5.

- Scenario (d). The geometrical landmarks as well as the hydrodynamics are well predicted by this scenario, as observed in Table 4.3 and Figure 4.5, respectively. As expected, the stress state predicted in this case is substantially different from that obtained in scenario (a). In fact, average relative differences of 81%, 102% and 86% are obtained for $\sigma_{\theta\theta}$, σ_{zz} and σ_{vm} , respectively (see Table 4.4). Recall that, due to the hypothesis considered for this case, stresses at the *baseline diastolic configuration* are null. For this case, it is interesting to contrast the differences of the stresses between diastole and systole (hereafter referred to as $\Delta\sigma$). This comparison is presented in Figure 4.7 and Table 4.5, where it can be appreciated that this scenario is also unable to predict $\Delta\sigma$ accurately, with relative differences up to 25%, 181% and 27% for $\Delta\sigma_{\theta\theta}$, $\Delta\sigma_{zz}$ and $\Delta\sigma_{vm}$, respectively.
- Scenario (e). Differences in geometrical landmarks are significant as observed in Table 4.3, with discrepancies of approximately 4% in the internal radius for both the diastolic and systolic configurations (leading to a disparity of roughly 10% in the lumen area). Also note that the assumptions taken for this case lead to misrepresentation of the tissue thickness; which significantly impacts the mechanical response of the wall. Although similar flow rates are obtained between the current case and scenario (a), the increased cross-sectional area reduces the blood velocity as observed on Figure 4.5, where it is appreciated a decrease of 8% on the maximum velocity. Regarding the stress state, an adequate pattern for both circumferential and axial stresses is predicted, but they are overestimated when compared with scenario (a), as noticed in Figure 4.6. Table 4.4 displays that relative differences reach 33%, 34% and 33% for $\sigma_{\theta\theta}$, σ_{zz} and σ_{vm} , respectively.
- Scenario (f). Significant differences in the geometrical landmarks are obtained for both the diastolic and systolic configurations, i.e., discrepancies of approximately 6% and 13% are reported for the internal radius and lumen area, respectively. Similarly to scenario (e), due to the increased cross-sectional area, the blood velocity is reduced as shown in Figure 4.5. In this case the maximum velocity is underestimated, presenting a discrepancy of 14.1% compared scenario (a). Regarding the stress results, it is evident from Figure 4.6 that this approach is completely unable to characterize the mechanical response of the tissue, since in average, the differences in the prediction of stresses reach 50%, 103% and 64% for $\sigma_{\theta\theta}$, σ_{zz} and σ_{vm} , respectively, with respect to scenario (a).

From the discussion above, it can be inferred that no alternative scenario to case (a) is suitable to accurately evaluate the stress state of the arterial wall, once all the hemodynamic loads acting over arterial vessels are defined. It has been shown that it is mandatory to solve the preload problem taking into account both the internal pressure and the axial prestretch. Moreover, it has been clearly demonstrated even in this simple geometrical model that the tethering forces, usually disregarded, are, as well as the inner pressure load, of the utmost importance for the determination of the stress state of the arterial tissue.

For this particular example, due to the simplicity of geometry and the low compliance of the vessel, all scenarios predict comparable variations of the lumen radius. Consequently, the fluid dynamics variables feature similar behavior in all scenarios. This may not be the

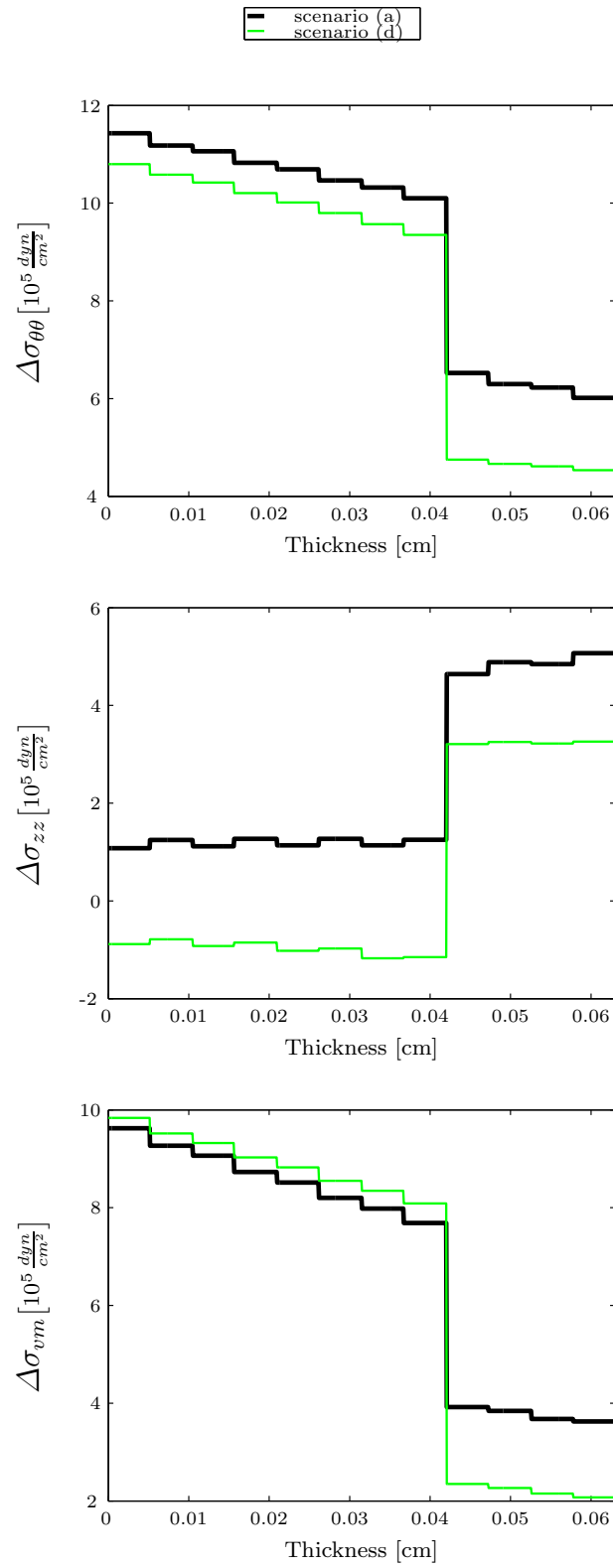


Figure 4.7: Difference of stresses (circumferential, axial and von Mises) between systole and diastole for scenarios (a) and (d) (black and green respectively.)

case for more compliant vessels or more tortuous domains, e.g. for the entire aorta or for some vessels containing aneurysms (see Hsu and Bazilevs (2011)), among others.

4.3 Problem 2: carotid bifurcation

4.3.1 Problem description

This numerical example consists in a standardized geometry of the carotid bifurcation, with the fluid domain defined as in Bharadvaj et al (1982). As before, the preload problem is solved to obtain the material configuration assuming that the initial geometry has been extracted from medical images. Then, the 1D-3D FSI coupled problem is solved. Once again, the baseline pressure level is defined $p_{base} = 9 \cdot 10^4 \frac{dyn}{cm^2}$ (67.5 mmHg), and given the pressure field p_t at the time t the relative pressure level is $p_t^{rel} = p_t - p_{base}$.

In this case we consider the following scenarios:

- (a) the preload problem is solved considering that the initial geometry is a configuration at mechanical equilibrium with a constant internal reference pressure p_{base} and is also subjected to a known level of pre-stretch $\lambda_C = 1.2$. Note that the FSI problem is solved from that configuration onwards,
- (b) the preload problem is solved considering that the initial geometry is a configuration at mechanical equilibrium with a constant internal reference pressure p_{base} and that it is not pre-stretched ($\lambda_C = 1.0$); the FSI problem is solved from that configuration onwards, assuming that the solid is equilibrated by the full level of inner pressure p_t .

Note that, as before, case (a) constitutes the most realistic scenario and case (b) will serve the purpose of comparing with an alternative approach and to further quantify the influence of the tethering forces on the response of the arterial wall.

As performed in the previous example, the 3D segment of interest is coupled with the simplified closed-loop circulation model (see Section 3.5).

4.3.2 Constitutive parameters

Values for the constitutive parameters employed in this example are identical to those presented for the straight pipe. As pointed out in Steinman et al (2002), the carotid bulb and bifurcation zone can be places of elevated thickness values. In accordance to this, we have smoothly increased the thickness towards the bifurcation region up to two times the designated values at the inlet and outlet boundaries; this feature can be appreciated in the inset displayed in Figure 4.8.

Collagen orientation is given at the initial (image-based) configuration Ω^I . A local coordinate system is proposed at each element, where the axial direction is defined through the projection of the lumen's centerline over the internal surface of the vessel and the circumferential direction is an orthogonal vector located over the plane tangential to the same internal surface. In this local coordinate system the preferred acting directions for the collagen fibers are introduced considering that each family forms an angle β with the circumferential direction as presented for the previous example (see Figure 4.1). Moreover, the recruitment stretch for the fibers is defined from this configuration in an analogous manner to the previous example (in that case for Ω^{base}). Note that, for both cases the image based configuration is equivalent to the baseline diastolic domain.

4.3.3 Discretization

The total number of nodes for the discretization of the fluid domain is 27673. The arterial wall is discretized using the same strategy described in Section 4.2.3. The total

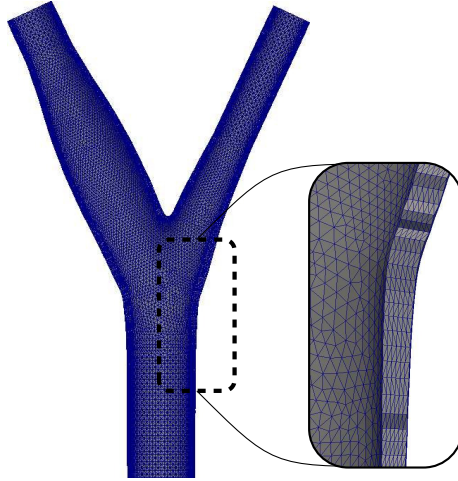


Figure 4.8: Clipping of the arterial wall mesh through the plane of symmetry.

number of nodes for the solid domain is 87751. The time-step in the simulation is taken $\Delta t = T/1000$, where T is the cardiac period.

4.3.4 Boundary conditions

Preload problem.

For the preload problem, Dirichlet boundary conditions are imposed to the displacement in the axial direction at the non-physical boundary corresponding to the inlet, ensuring that a certain level of pre-stretch is achieved. That is, for scenario (a) an axial displacement of 1.05 cm is considered, while for case (b) null axial displacement is imposed. Note that for case (a) the level of pre-stretch is not strictly 20%, but the magnitude of the imposed displacements represents the 20% of the length of the vessel projected to the axis of the common carotid (z cartesian coordinate). Neumann conditions are imposed at $\partial\Omega_s^W$ given by the constant p_{base} pressure load for both scenarios. For the external boundary $\partial\Omega_s^E$ homogeneous Neumann conditions for each case are considered based on the assumptions exposed in Section 4.2.5. Finally, at each distal boundary a penalization over the mean displacement of the surface $\partial\Omega_s^{A,i}$ is considered, thus fixing the center of the outflow area.

1D-3D FSI problem.

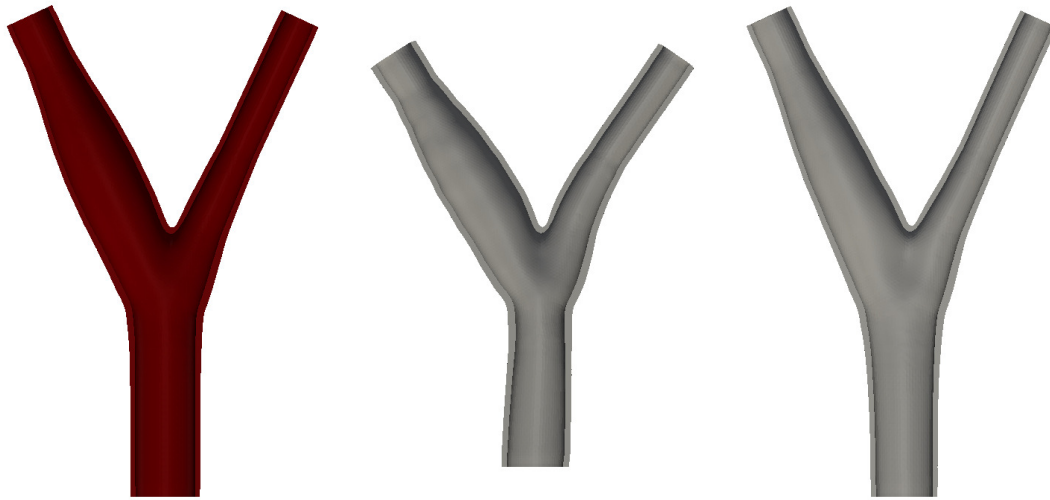
Boundary conditions are analogous to those presented in Section 4.2.5.

4.3.5 Parameters for numerical simulation

The parameter setup for the numerical simulation is identical to the one presented for the straight pipe problem (see Section 4.2.4).

4.3.6 Results

For both cases the baseline diastolic configuration is assumed to be the given one, and the preload is problem solved in order to obtain the material configuration. Figure 4.9(b) and Figure 4.9(c) show the resulting zero-load reference configurations for scenarios (a) and (b), respectively. From these images the influence of the pre-stretch in the computation of the material domain is evident.



(a) Baseline diastolic configuration. (b) Computed zero-load reference configuration for scenario (a). (c) Computed zero-load reference configuration for scenario (b).

Figure 4.9: Computation of material configurations, comparison between scenarios (a) and (b).

Figure 4.10 summarizes the obtained results for both scenarios regarding the mechanical response of the wall tissue, showing the von Mises equivalent stress distribution for the carotid bifurcation at a given time instant during the cardiac systole $t = 0.235T$ and for the baseline diastolic configuration (result given by the preload problem). Moreover, the values of the principal stresses (S_1 , S_2 , S_3) over a curve s going through the interior of the vessel from the inflow boundary to one of the outlets (corresponding to the internal carotid) are detailed on the featured charts. Once again, it can be clearly appreciated that overlooking the tethering forces leads to an unrealistic evaluation of the stress state. Analyzing the principal stresses along the s curve at systole, the relative discrepancies with respect to scenario (a) result in values up to 66%, while for the von Mises stresses the relative discrepancies reach 78%. The discrepancies between the obtained stress fields are further highlighted by Figure 4.11, displaying the stress distribution along four curves crossing the arterial wall at different points for two time instants $t = 0.235T$ and $t = 0.85T$. Here, discrepancies up to 75% can be observed. Also, it is interesting to note in Figures 4.11(b) to 4.11(e), the different stress levels for the media and adventitia layers.

The blood flow behavior is represented in Figure 4.12, featuring the velocity profile in the deformed domain at different slices of the geometry and a chart comparing the velocity magnitude along a line through the bifurcation point at $t = 0.235T$. It is observed that the velocity field shows a good agreement between both cases all over the domain, in the particular case of the velocity over the selected curve it is shown consistency on the shape of the profile and a difference of approximately 5% in the maximum reported value. The same behavior is observed throughout the entire cycle (results not shown). Additional details regarding the blood flow dynamics are presented in Figure 4.13, where the pressure and flow rate at the inlet during the cardiac cycle (Figure 4.13(a)) along with the velocity profiles and streamlines for three time instants $t = 0.22T$, $t = 0.235T$ and $t = 0.85T$ (Figures 4.13(b) to 4.13(d)) are displayed.

In this example the relevance of accounting for the pre-stretch state of the arterial wall is further emphasized, evidencing the influence of the tethering forces on the mechanical response of the tissue. As previously noted in the straight pipe example, due to the

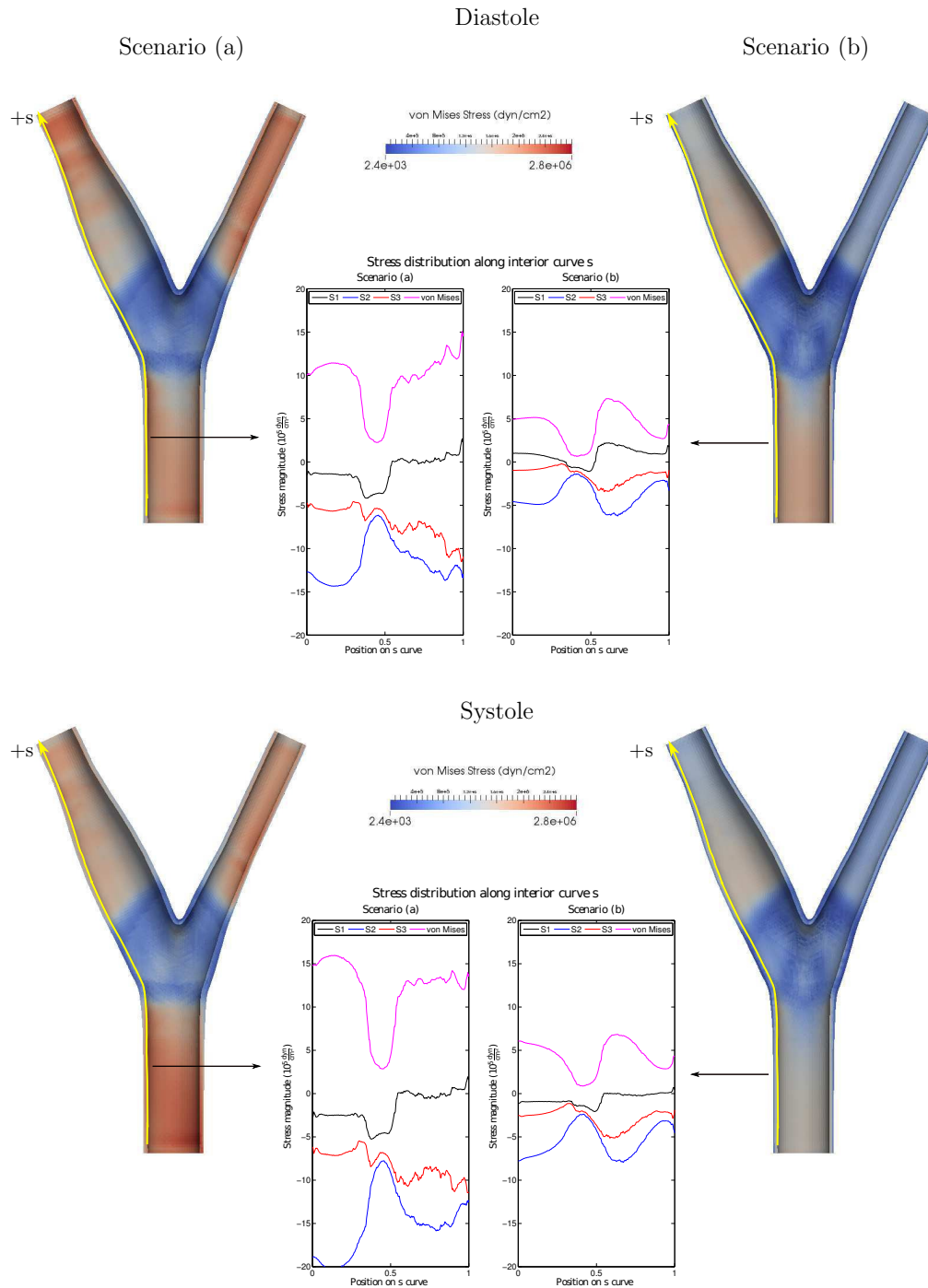
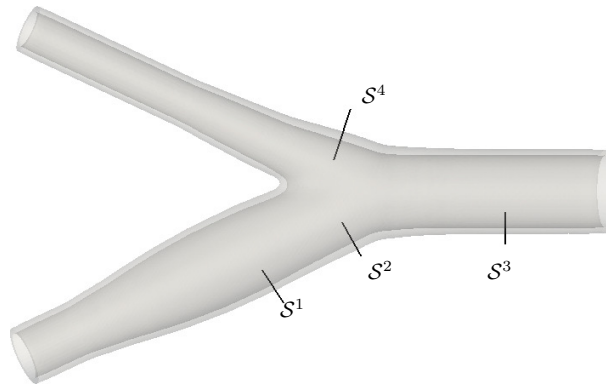


Figure 4.10: Computed stresses for scenarios (a) (left) and (b) (right) mapped into the image-based configuration. Figure displays the von Mises equivalent stress of the arterial wall tissue clipping through the plane of symmetry of the geometry for $t = 0.235T$ (in the context of this figure denoted as systole) and for the baseline diastolic configuration (in the context of this figure denoted as diastole). Charts present the stress distribution (principal stresses in blue (S1), black (S2) and red (S3); von Mises equivalent stress in magenta) over an interior line s going through the common and internal carotid arteries.



(a) Location reference for transversal curves S^1 , S^2 , S^3 and S^4

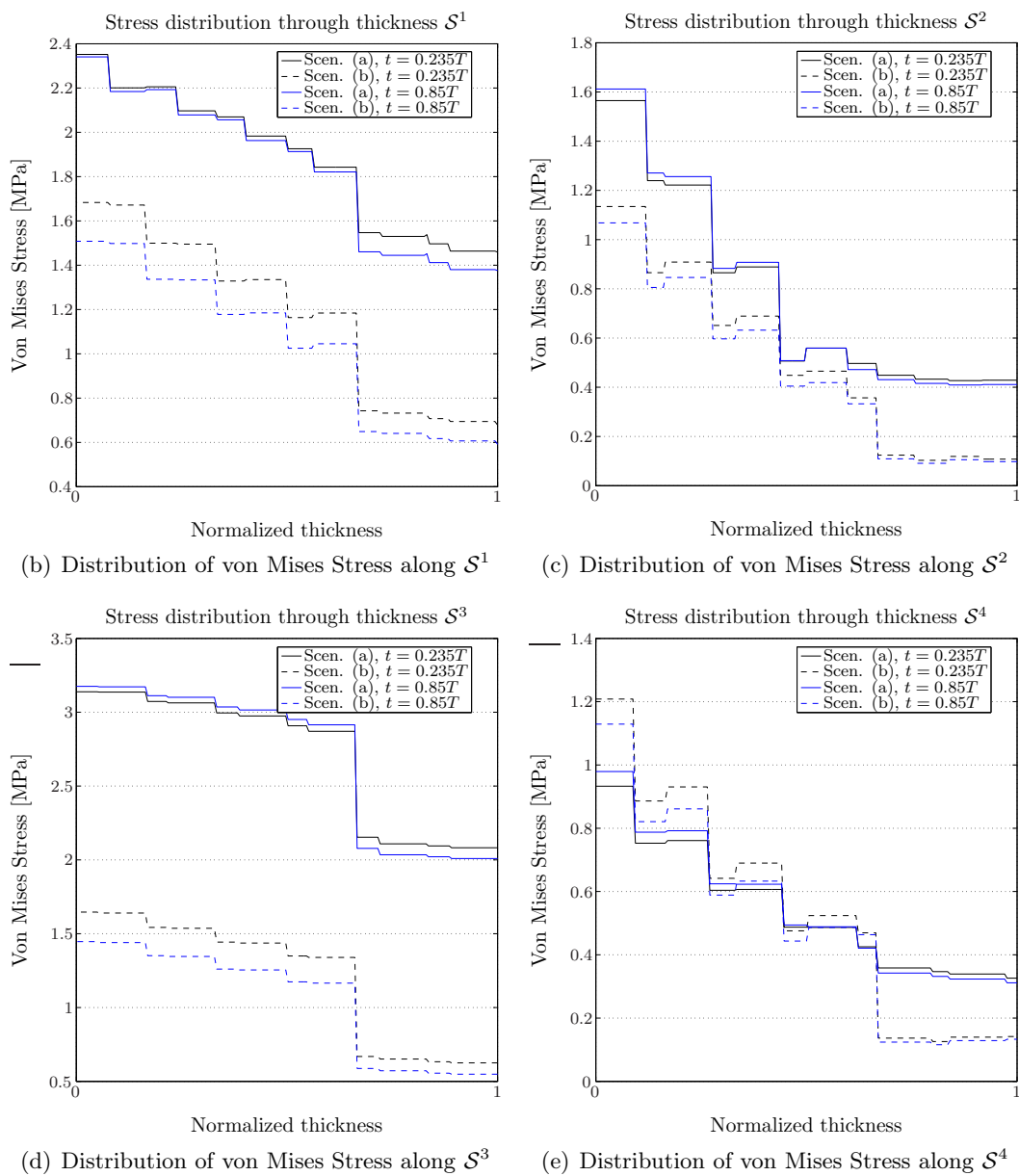


Figure 4.11: Through thickness stress distribution at different points for time instants $t = 0.235T$ (black lines) and $t = 0.85T$ (blue lines). Comparison between results for scenarios (a) -solid lines- and (b) -dashed lines-.

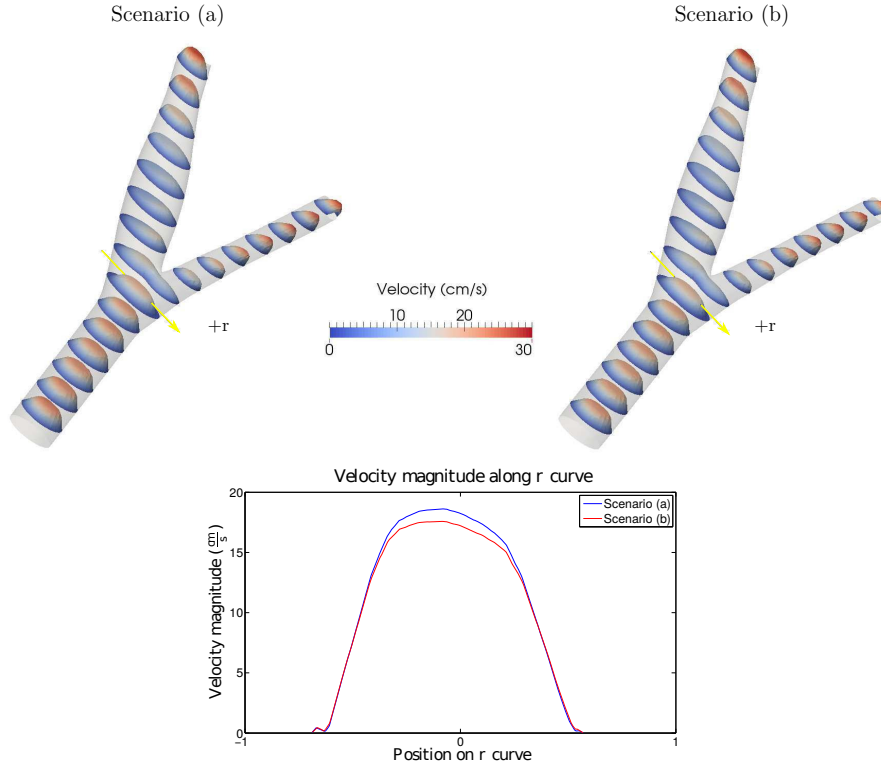


Figure 4.12: Velocity profile for scenarios (a) and (b) at $t = 0.235T$.

low compliance of the vessel and the characteristics of this geometry, scenario (b) shows similar characteristics regarding the blood flow behavior.

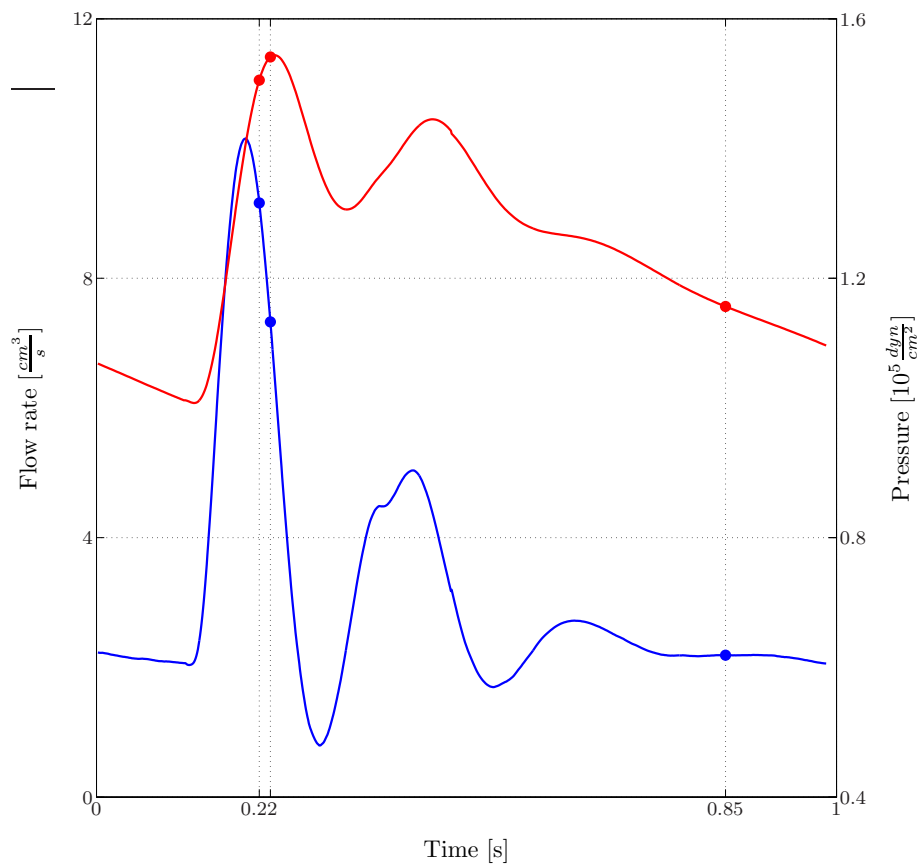
4.4 Problem 3: patient-specific common carotid

4.4.1 Problem description

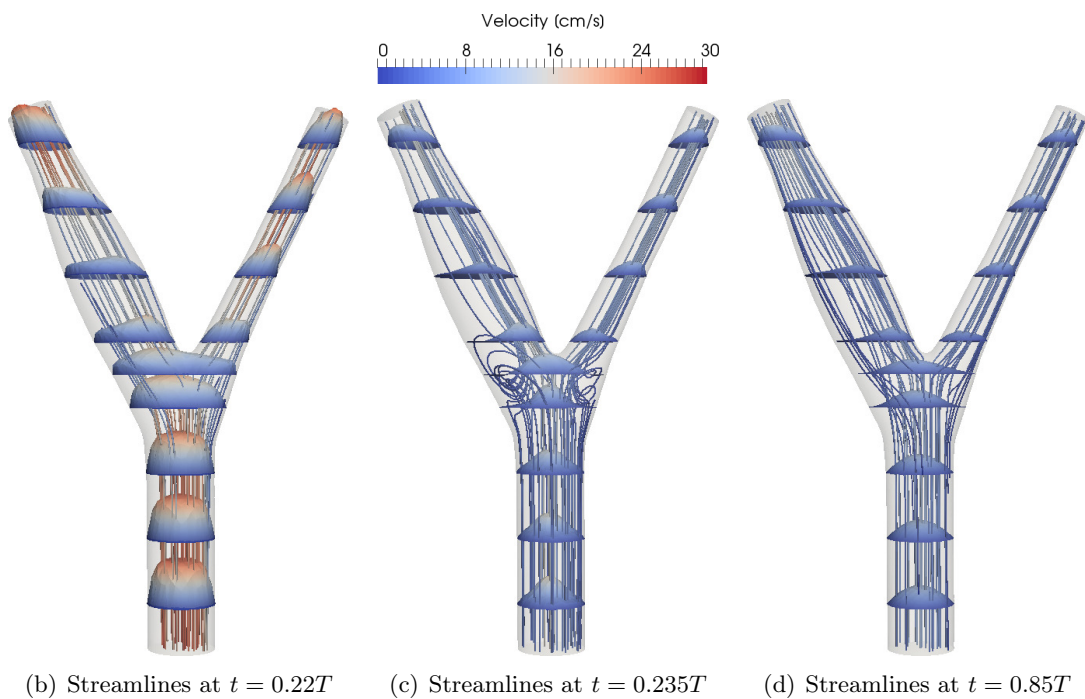
This numerical example consists in a patient-specific left common carotid artery extracted from a medical imaging study (Computed Tomography Angiography). The inner radius of the segment varies between 0.25 cm and 0.33 cm , and its length is $l = 5.75\text{ cm}$ measured over the centerline of the vessel. Both the blood flow domain and the arterial wall domain are presented in Figures 4.14(a) and 4.14(b), respectively. Analogously to the previous examples, two scenarios are analyzed:

- (a) the preload problem is solved considering that the initial geometry is a configuration at mechanical equilibrium with a constant internal reference pressure p_{base} and is also subjected to pre-stretching. Recall that the FSI problem is solved from that configuration onwards,
- (b) the preload problem is solved considering that the initial geometry is a configuration at mechanical equilibrium with a constant internal reference pressure p_{base} and that the position of the non-physical boundaries is fixed; the FSI problem is solved from that configuration onwards, assuming that the solid is equilibrated by the full level of inner pressure p_t .

For this example the pre-stretch in scenario (a) is introduced by setting axial tethering forces at non-physical boundaries such that a certain displacement is prescribed. Through this procedure a shortening of approximately 7% ($\lambda_C \approx 1.07$) is achieved. Also, it is important to remark that fixating the position of these boundaries in scenario (b) does not



(a) Flow rate (blue) and pressure (red) at the inlet of the carotid bifurcation during the cardiac cycle.



(b) Streamlines at $t = 0.22T$

(c) Streamlines at $t = 0.235T$

(d) Streamlines at $t = 0.85T$

Figure 4.13: Blood flow dynamics for the carotid bifurcation example, displaying pressure (red) and flow rate (blue) at the bifurcation inlet during one cardiac cycle and visualization of velocity profiles and streamlines for three time instants $t = 0.22T$ (maximum flow rate), $t = 0.235T$ (maximum mean pressure) and $t = 0.85T$ (diastolic instant).

imply that the length of the segment is constant, in fact, a subtle shortening is observed when solving the preload problem because of the geometrical ability of the vessel to accommodate the curvature, obtaining a pre-stretch of approximately 1.5% ($\lambda_C \approx 1.015$). As before, the baseline pressure level is defined $p_{base} = 9 \cdot 10^4 \frac{dyn}{cm^2}$ (67.5 mmHg).

4.4.2 Constitutive parameters

Values for the constitutive parameters employed in this example are identical to those presented for the straight pipe (see Section 4.2). The thickness of the wall is defined based on the maximum radius observed in the carotid segment, and taking into account the ratio between the inner radius to the thickness presented in Section 4.2, that is, $\frac{r_i}{e} = \frac{0.37}{0.063}$. Hence, the resulting thickness for this test is $e = 0.056 \text{ cm}$. The setting of the collagen fibers is presented in Figure 4.14(c), the definition of the fiber orientations is performed following the strategy discussed in Section 4.3.2.

4.4.3 Discretization

The total number of nodes for the discretization of the fluid domain is 30760. The arterial wall is discretized using the same strategy described in Section 4.2.3. The total number of nodes for the solid domain is 34465. The time-step in the simulation is taken $\Delta t = T/1000$, where T is the cardiac period.

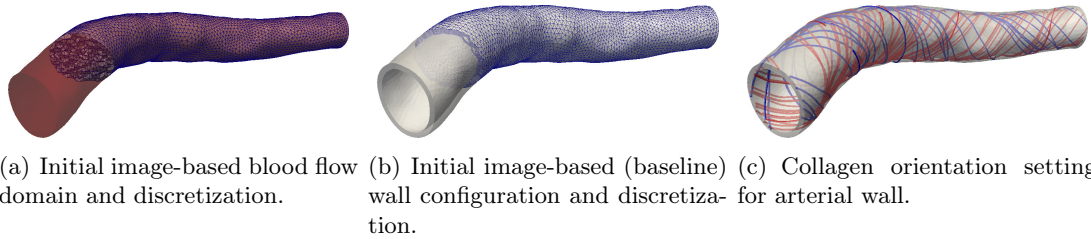


Figure 4.14: Image-based fluid and solid domains, discretization and collagen orientation.

4.4.4 Boundary conditions

Preload problem.

For scenario (a), tethering forces in the normal direction are introduced through penalization, forcing a displacement of the center of both non-physical boundaries to be equal to 0.2 cm (following strategy (ii) detailed in Section 3.7). As stated before, these tethering forces induce a level of pre-stretch of $\lambda_C = 1.07$. For scenario (b) the position of the center of the non-physical boundary is fixed through the same penalization method. Due to the geometrical characteristics of the vessel and the action of the internal pressure, the material configuration results to be shorter than the image-based initial domain, presenting a subtle pre-stretch level of approximately 1.5% ($\lambda_C \approx 1.015$). Neumann conditions are imposed at $\partial\Omega_s^W$ given by the constant p_{base} pressure load for both scenarios. For the external boundary $\partial\Omega_s^E$ homogeneous Neumann conditions for each case are considered based on the assumptions exposed in Section 4.2.5.

1D-3D FSI problem.

Boundary conditions are analogous to those presented in Section 4.2.5.

4.4.5 Parameters for numerical simulation

The parameter setup for the numerical simulation is identical to the one presented for the straight pipe problem (see Section 4.2.4).

4.4.6 Results

As presented for the previous example (see Section 4.3), in this problem the baseline diastolic configuration is assumed to be given and the preload problem is solved in order to obtain the material configuration for the scenarios described above. The initial image-based (baseline) configuration is presented in Figure 4.15(a); while Figures 4.15(b) and 4.15(c) display the resulting zero-load reference configurations for scenarios (a) and (b), respectively. Again, from these images, the great influence of the different hypotheses regarding the tethering forces on the computation of the material domain is evident.

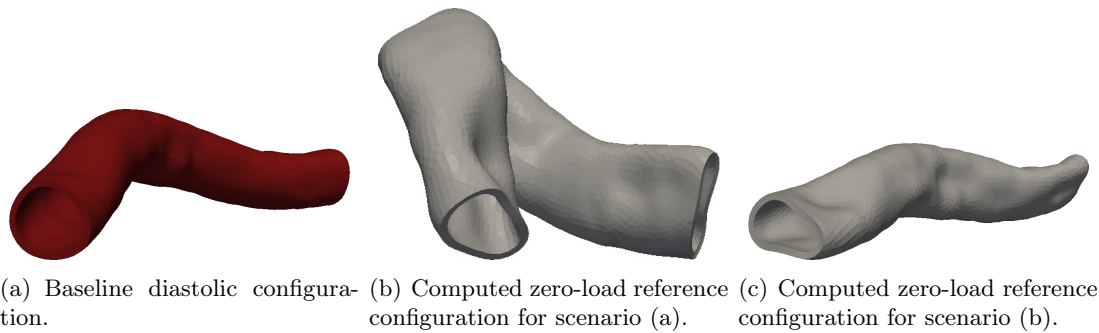


Figure 4.15: Computation of material configurations, comparison between scenarios (a) and (b). The same view and scale is shown for all cases.

Figure 4.16 summarizes the results obtained for both scenarios regarding the mechanical response of the arterial wall. Particularly, the von Mises equivalent stress σ_{vm} at the baseline configuration for scenarios (a) and (b) is presented in Figures 4.16(a) and 4.16(b), respectively. In turn, Figures 4.16(c) and 4.16(d) display the corresponding results for a systolic time instant ($t = 0.35 T$). The above mentioned images feature, for each case, the stress state at the interior surface of the vessel and the transmural distribution along a longitudinal cut (left). Furthermore, areas featuring large stresses are highlighted in a threshold view, where only elements with $\sigma_{vm} \geq 2 \cdot 10^6 \frac{\text{dyn}}{\text{cm}^2}$ are shown (right).

These results show the impact of the different hypotheses assumed for each scenario on a realistic geometry. The vessel curvature leads to different localizations (and values) of stress augmentation in addition to the previously reported differences in the general levels of stress. Moreover, Figure 4.17 presents the relative discrepancy between the von Mises stress values in the baseline and systolic ($t = 0.35 T$) states (reference stress values of $1 \cdot 10^6 \frac{\text{dyn}}{\text{cm}^2}$ and $2 \cdot 10^6 \frac{\text{dyn}}{\text{cm}^2}$ for each case), evidencing differences up to 270%. The discrepancies between the obtained stress fields are further highlighted by Figure 4.18, presenting the transmural distribution of the von Mises equivalent stress along three curves crossing the arterial wall, for two time instants $t = 0.35 T$ (systolic) and $t = T$ (diastolic). The location of those lines is presented in Figure 4.18(a).

Figure 4.19 introduces the level of axial stretch ($\lambda_{ax} = \mathbf{C} \cdot (\mathbf{a}_{ax} \otimes \mathbf{a}_{ax})$, where \mathbf{a}_{ax} is the unit vector indicating the axial direction) at the baseline diastolic configuration corresponding to scenarios (a) and (b). Figures 4.19(a) and 4.19(b) display a comparison between such quantity for both scenarios, while Figures 4.19(c) to 4.19(f) highlight the regions of the arterial wall under axial traction and compression. These figures evidence, again, the paramount influence of the considered hypotheses regarding the tethering forces.



(a) Scenario (a): von Mises equivalent stress for baseline diastolic configuration, interior wall view (left) and threshold displaying most stressed regions ($\sigma_{vm} \geq 2 \cdot 10^6 \frac{dyn}{cm^2}$) (right).



(b) Scenario (b): von Mises equivalent stress for baseline diastolic configuration, interior wall view (left) and threshold displaying most stressed regions ($\sigma_{vm} \geq 2 \cdot 10^6 \frac{dyn}{cm^2}$) (right).



(c) Scenario (a): von Mises equivalent stress for systolic configuration, interior wall view (left) and threshold displaying most stressed regions ($\sigma_{vm} \geq 2 \cdot 10^6 \frac{dyn}{cm^2}$) (right).

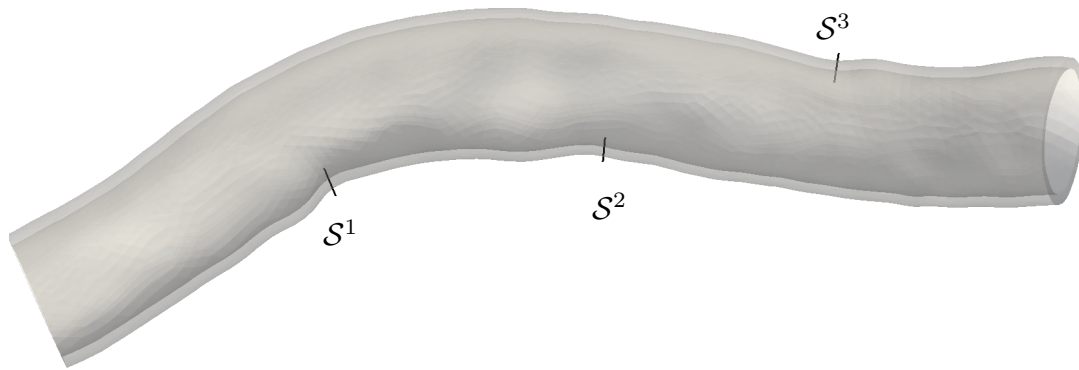


(d) Scenario (b): von Mises equivalent stress for systolic configuration, interior wall view (left) and threshold displaying most stressed regions ($\sigma_{vm} \geq 2 \cdot 10^6 \frac{dyn}{cm^2}$) (right).

Figure 4.16: Stress state at the arterial wall for scenarios (a) and (b) for the baseline diastolic and systolic configurations.



Figure 4.17: Relative discrepancy of von Mises stresses between scenarios (a) and (b) for baseline (left) and systolic (right) configurations. The reference stress level have been defined as $\sigma_{ref} = 1 \cdot 10^6 \frac{dyn}{cm^2}$ and $\sigma_{ref} = 2 \cdot 10^6 \frac{dyn}{cm^2}$, respectively.



(a) Line locations

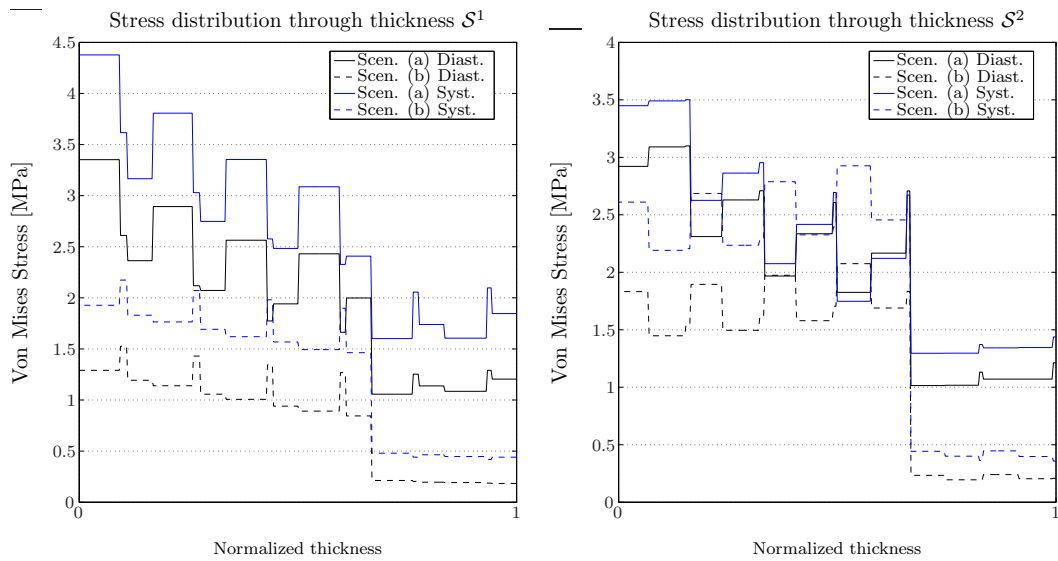
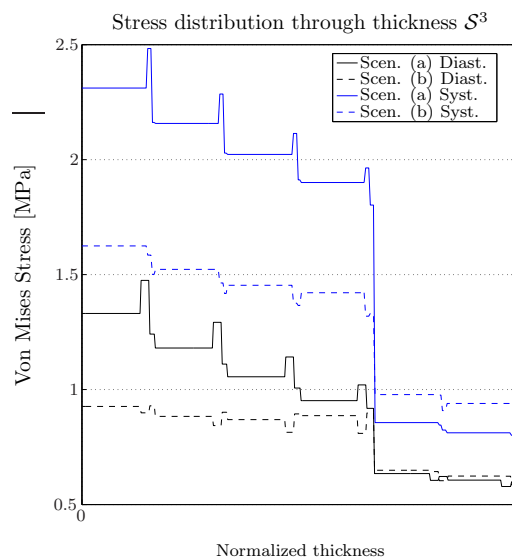
(b) Von Mises Stress through \mathcal{S}^1 (c) Von Mises Stress through \mathcal{S}^2 (d) Von Mises Stress through \mathcal{S}^3

Figure 4.18: Through thickness stress distribution at different points for diastolic ($t = T$, black lines) and systolic ($t = 0.35T$, blue lines) instants. Comparison between results for scenarios (a) -solid lines- and (b) -dashed lines-.

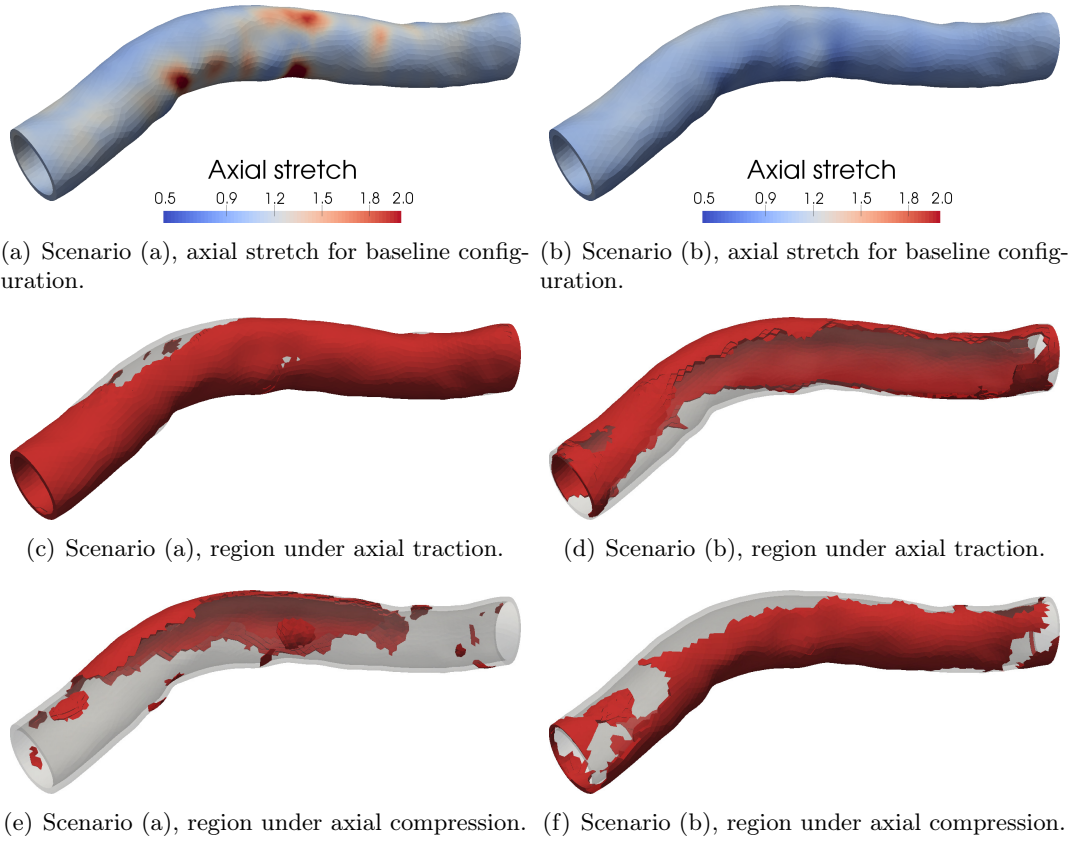


Figure 4.19: Axial stretch at baseline configuration for scenarios (a) and (b). Comparison between regions under axial traction and compression.

A comparison of the obtained blood flow behavior between the two considered scenarios is shown in Figure 4.20. Blood velocity profile in the deformed domain at different slices of the geometry is shown for two characteristic time instants: at systole $t = 0.35T$ and at diastole $t = T$. As reported for the previous numerical examples it is observed that the velocity field shows small sensitivity to the stress state of the arterial wall. Additional details regarding the blood flow dynamics are presented in Figure 4.21, where the pressure and flow rate at the inlet during the cardiac cycle (Figure 4.21(a)) along with the velocity profiles and streamlines for three time instants $t = 0.175T$, $t = 0.35T$ and $t = 0.85T$ (Figures 4.21(b) to 4.21(d)) are displayed.

4.5 Problem 4: aneurysm at the middle cerebral artery

4.5.1 Problem description

For this example, a patient-specific aneurysm located in the bifurcation of the middle cerebral artery into its superior and inferior branches is analyzed. Again, in order to study the influence of tethering stresses two scenarios are taken into account,

- (a) considering tethering forces arising from a level of pre-stretch of approximately 12%, and
- (b) considering tethering forces with null pre-stretch, i.e. the material configuration obtained through the preload problem features the same length as the image-based configuration.

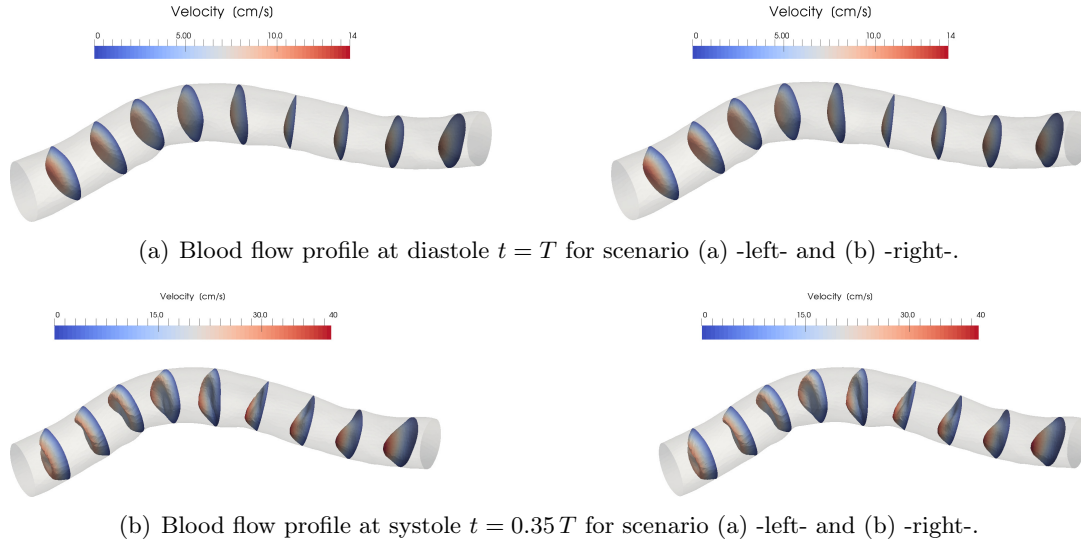


Figure 4.20: Blood flow velocity profiles at diastole $t = T$ and systole $t = 0.35T$, note that the warping factors and color scales differ between the time instants.

The baseline pressure level is defined $p_{base} = 9 \cdot 10^4 \frac{dyn}{cm^2}$ for both scenarios.

The segment of interest is in both cases integrated with the rest of the CVS through the coupling with the ADAN model (see Section 3.5). For the external boundary conditions it is considered an increased influence of the surrounding tissues in regions with high curvature (see Section 4.5.4).

4.5.2 Geometry and discretization

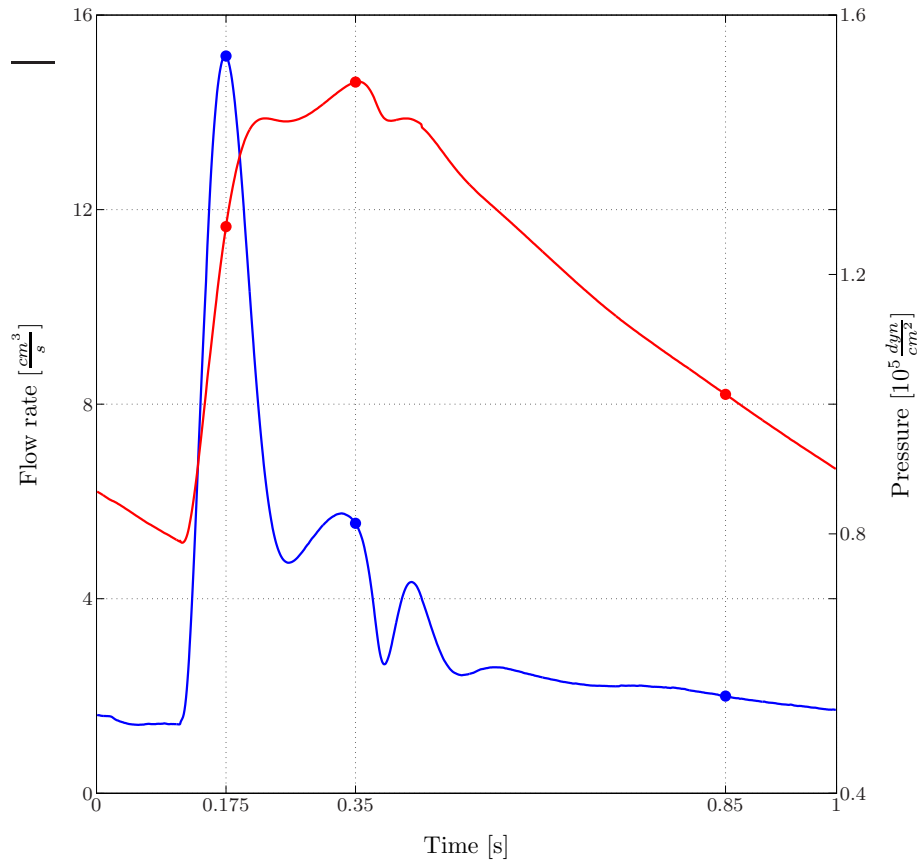
The thickness of the arterial wall is defined as the 30% of the vessel local radius (r_i), i.e. $h = 0.3 r_i$. For the aneurysm sack it is considered a wall thinning ratio (WTR) affecting the local thickness as $e = 0.3 r_i WTR^{-1}$. The WTR is defined as the relation between the surface of the aneurysm sack and the area of the aneurysm neck (as exemplified in Figure 4.5.2), for this case it is obtained $WTR = 1.75$.

The original surface mesh obtained via the segmentation process is refined based on local vessel radius for the complete domain. Moreover, the aneurysm sack area is further refined. This pre-processing for the surface mesh and the generation of the lumen volume is performed using the VMTK package (Antiga et al, 2008), resulting in a tetrahedral mesh with 58691 nodes. The arterial wall discretization is constructed using a similar criteria to the exposed for the previous examples (see Section 4.2.3). For the computation of tethering forces using strategy (iii) (see Section 4.5.4), auxiliary domain extensions are constructed at each non-physical boundary. The total number of nodes for the solid domain used in the 1D-3D FSI computations is 73937. Figure 4.23 showcases the obtained discrete domains. The time-step in the simulation is taken $\Delta t = T/1000$, where $T = 1s$ is the cardiac period.

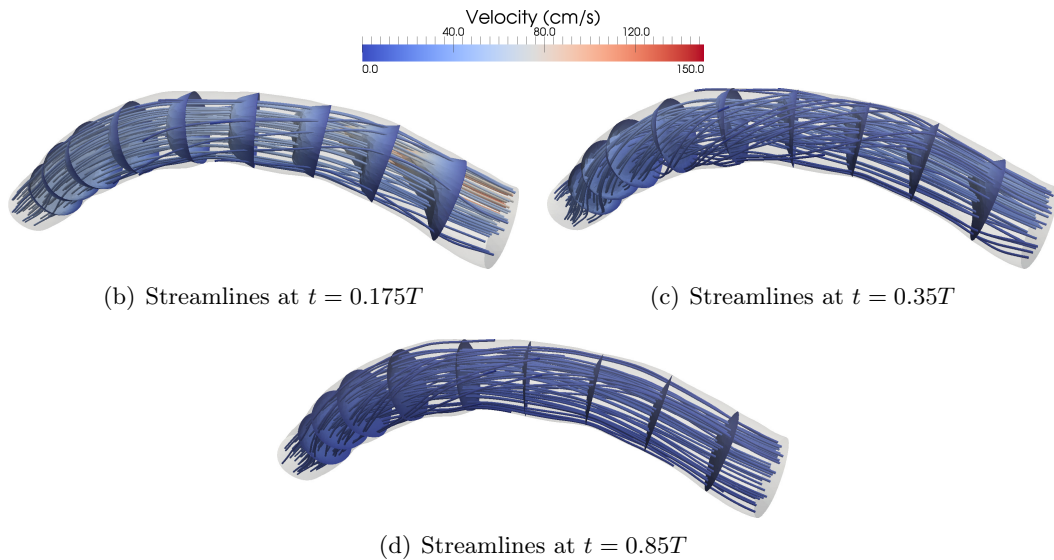
4.5.3 Constitutive modeling

For the healthy region of the arterial wall, the values for the constitutive parameters are identical to those presented for the straight pipe (see Section 4.2). Collagen orientation is given at the initial (image-based) configuration Ω^{base} . Figure 4.24 displays the collagen arrangement in the domain. Additionally, the recruitment stretch for the fibers is defined from this configuration in an analogous manner to the previous examples.

However, for the aneurysm sack area, we consider an isotropic exponential behavior due to elastin degradation as described by equation (3.6.3). The constitutive parameters



(a) Flow rate (blue) and pressure (red) at the inlet of the carotid artery during the cardiac cycle.



(b) Streamlines at $t = 0.175T$

(c) Streamlines at $t = 0.35T$

(d) Streamlines at $t = 0.85T$

Figure 4.21: Blood flow dynamics for the patient-specific common carotid example, displaying pressure (red) and flow rate (blue) at the inlet during one cardiac cycle and visualization of velocity profiles and streamlines for three time instants $t = 0.175T$ (maximum flow rate), $t = 0.35T$ (maximum mean pressure) and $t = 0.85T$ (diastolic instant).

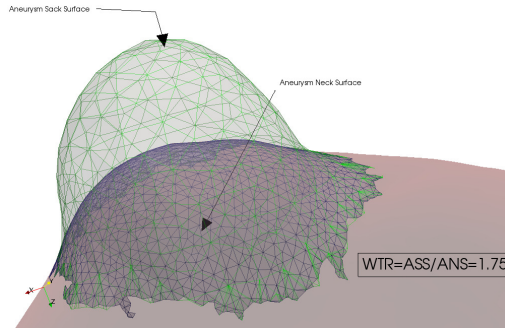


Figure 4.22: Cerebral aneurysm example: wall thinning ratio concept

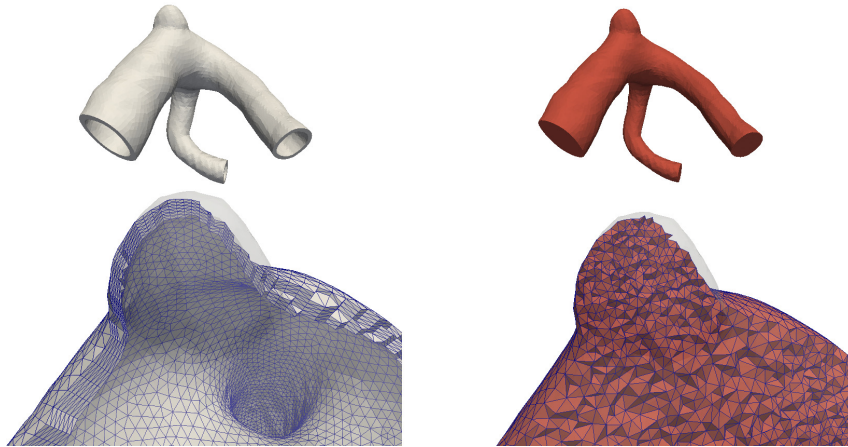


Figure 4.23: Cerebral aneurysm example: arterial wall and fluid meshes

are set as $k_{del} = 8 \cdot 10^5 \frac{\text{dyn}}{\text{cm}^2}$ and $k_x = 20$. This hypothesis is supported by the fact that the collagen response prevails due to elastin degradation and the orientation of such collagen fibers in the diseased vessel is unknown.

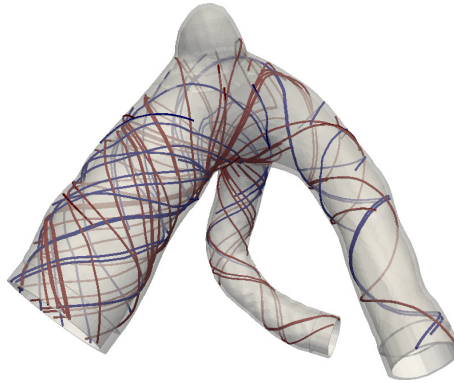


Figure 4.24: Cerebral aneurysm example: orientation of collagen fibers

In this case, the action of the external tissues is considered to be more relevant over highly curved regions (see Figure 4.25). The parameters defining the action of the external tissues are $k_e = 2.0 \cdot 10^5 \frac{\text{dyn}}{\text{cm}^2}$, $k_v = 4.0 \cdot 10^3 \frac{\text{dyn}}{\text{cm}^2 \text{s}}$ and $\mathbf{u}_0 = \mathbf{0}$ for the highly curved regions, and $k_e = 2.0 \cdot 10^2 \frac{\text{dyn}}{\text{cm}^2}$, $k_v = 4.0 \cdot 10^3 \frac{\text{dyn}}{\text{cm}^2 \text{s}}$, and $\mathbf{u}_0 = \mathbf{u}^{base}$ for the remaining parts of the arterial wall (see equation (3.3.1)). This way, it is considered that the baseline configuration is at equilibrium with external forces acting at $\partial\Omega_s^E$ in the highly curved regions, arising from the displacement field mapping the material and baseline configurations.



Figure 4.25: Cerebral aneurysm example: highlight of highly curved regions where the influence of external tissues is considered to be more relevant.



Figure 4.26: Cerebral aneurysm example: auxiliary extension domains for the computation of tethering forces.

4.5.4 Boundary conditions

Preload problem

For the preload problem, Neumann conditions are imposed at $\partial\Omega_s^W$ given by the constant p_{base} pressure load for scenarios (a) and (b). Strategy (iii) is used for the incorporation of tethering forces in scenario (a), as described in Section 3.7. Hence, the preload problem is solved in the auxiliary domain extensions (see Figure 4.26) to prescribe a level of pre-stretch of 12%. For scenario (b), the position of the center of the non-physical boundary is fixed through a penalization method (strategy (ii)).

1D-3D FSI problem

Boundary conditions are analogous to those presented in Section 4.2.5.

4.5.5 Parameters for numerical simulation

The parameter setup for the numerical simulation is based on the presented for the straight pipe problem (see Section 4.2.4).

4.5.6 Results

Figure 4.27 shows the resulting zero-load reference configurations for scenarios (a) and (b). From this image, it is evident the remarkable influence of the tethering forces in the determination of the material configuration. The von Mises equivalent stress state at systole ($t = 0.35T$) for both scenarios is presented in Figure 4.28. It is worthy of notice that this stress state is plotted over the baseline configuration that is common for both scenarios. The image presents the field in a clipping of the original geometry, where it can be appreciated a substantial difference between the results for both scenarios, particularly in the inlet as well as in aneurysm neck regions. The discrepancies between this stress state

is presented in Figure 4.29. Moreover, Figure 4.30 showcases the mentioned discrepancy, focusing in the aneurysm sack area and showing a view from the interior of the sack. In these two figures major discrepancies up to 100% in the domain and up to 70% in the aneurysmal area are observed. Additionally, in order to show the transmural stress distribution, Figure 4.31 displays the von Mises equivalent stress through curves \mathcal{S}^1 , \mathcal{S}^2 , \mathcal{S}^3 and \mathcal{S}^4 (their location is revealed in Figure 4.31(a)) for a systolic ($t = 0.35T$) and the baseline configurations. It can be observed that, in general, the equivalent stress is underestimated in scenario (b) compared to scenario (a) in which tethering forces are considered. Lastly, Figures 4.32(a) and 4.32(b) show the axial stretch at the baseline configuration for both scenarios and Figures 4.32(c) and 4.32(d) highlight the regions under axial compression. In those figures it can be clearly seen that the incorporation of tethering forces leads to prominent axial tractions all over the domain, with impact in the stress state in the aneurysm neck area.

From the present study it is clearly demonstrated that in order to adequately characterize the mechanical state of the arterial wall the incorporation of tethering forces is of the utmost importance.

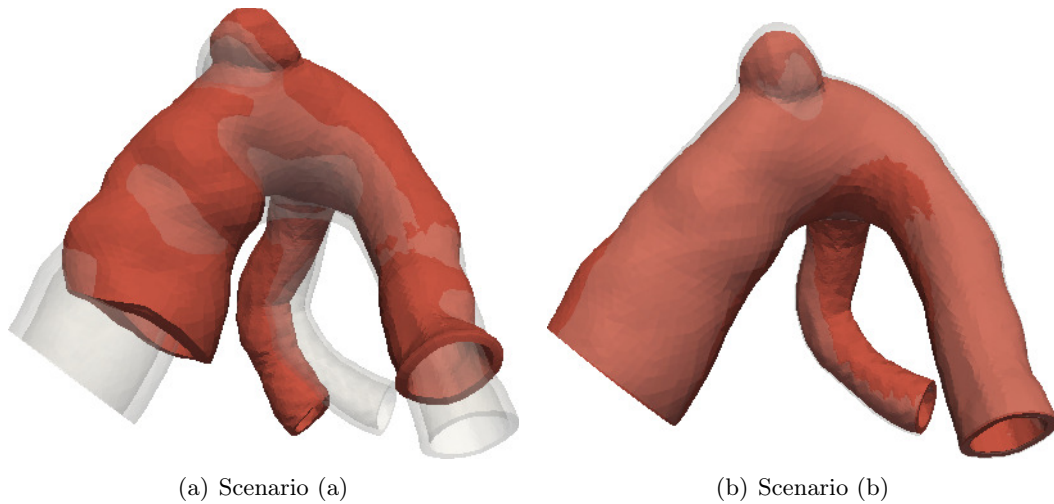


Figure 4.27: Resulting zero-load reference configuration (red) and baseline configuration (translucent grey) for scenarios (a) and (b).

As in the previous examples, relevant differences in the blood flow dynamics were not found. Figure 4.33 presents the pressure and flow rate during the cardiac cycle at the inlet boundary along with the velocity profiles and streamlines for three time instants, $t = 0.175T$ (maximum flow rate), $t = 0.35T$ (maximum pressure) and $t = 0.85T$ (a diastolic instant).

4.6 Discussion

4.6.1 Hemodynamic insight and novel aspects

The examples analyzed in the previous sections shed light on the sensitivity of the arterial wall stress state and blood flow to the definition of the domain of analysis and loads considered to be applied arterial vessels for which the known configuration has been obtained from medical images.

On one hand, these examples demonstrate that blood flow phenomena is not sensitive to the definition of the preload problem. That is, considering the image configuration as material configuration, or considering the true material configuration obtained after solving

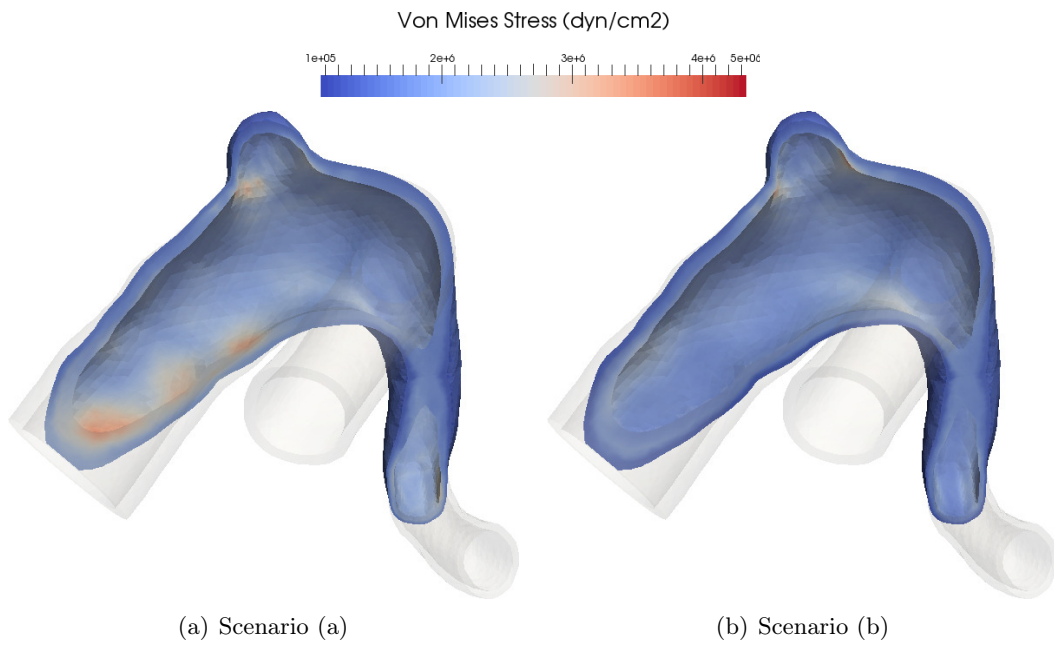


Figure 4.28: Cerebral aneurysm example: von Misses equivalent stress field at systole ($t = 0.35T$) for scenarios (a) and (b).

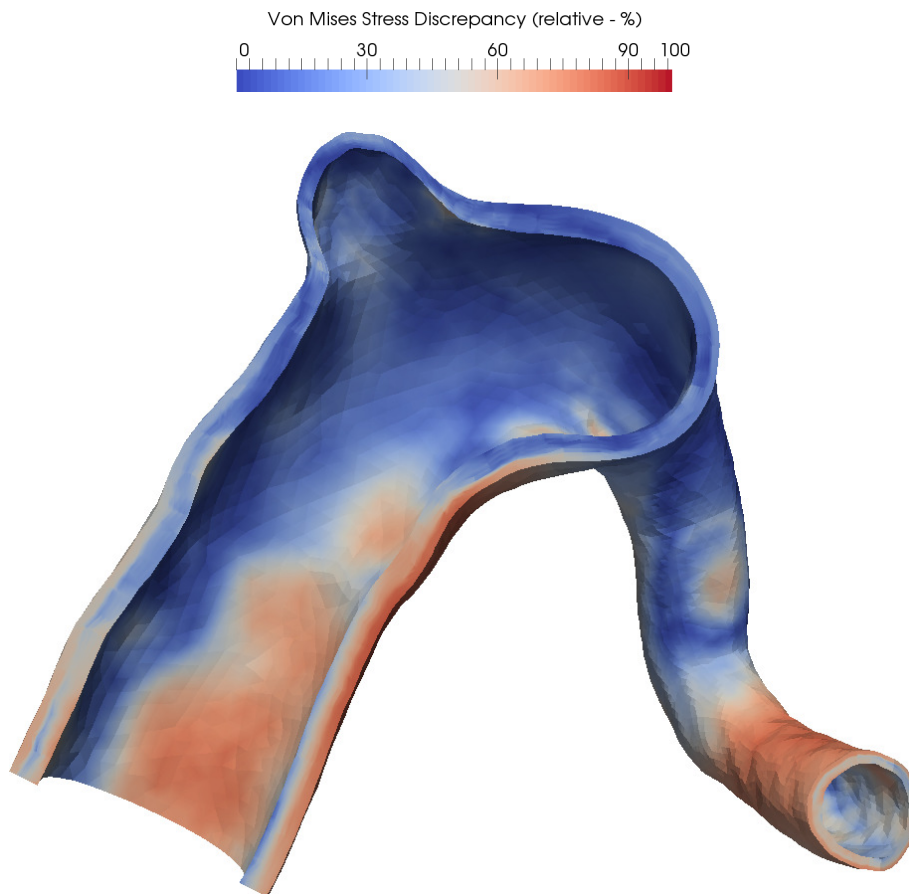


Figure 4.29: Cerebral aneurysm example: discrepancy of the von Misses equivalent stress field at systole ($t = 0.35T$) between scenarios (a) and (b).

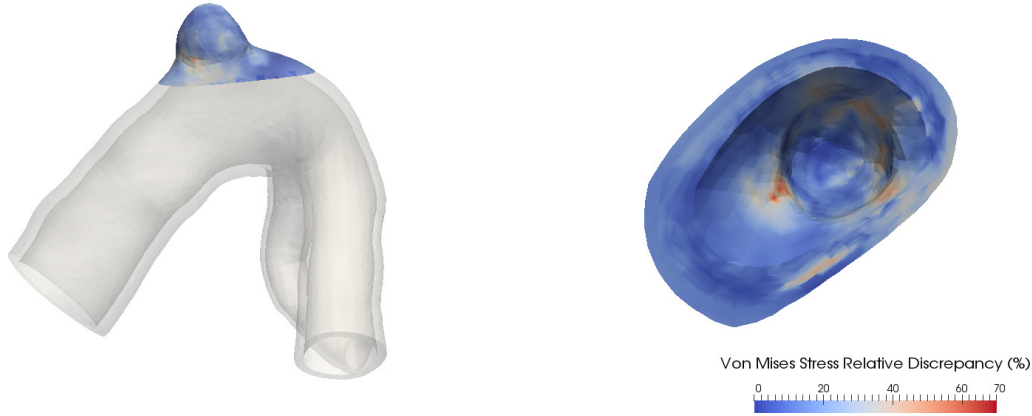


Figure 4.30: Cerebral aneurysm example: discrepancy of the von Mises equivalent stress field at systole ($t = 0.35T$) between scenarios (a) and (b) at the aneurysm neck and sack

the preload problem (whatever the loads are) does not significantly affect the flow patterns. Although some debate may exist in the case of more compliant vessels and different flow regimes, this is reasonable for the cases analyzed within the present thesis. Similar results in this direction support this fact, as shown in Dempere-Marco et al (2006) in the context of blood flow simulation comparing outcomes between compliant and rigid domains.

On the other hand, the reported results show that solving the preload problem (scenario (a)) including pressure and tethering loads is essential to correctly characterize the mechanical state of the arterial wall. In fact, the use of simplifying hypotheses irremediably leads to large deviations from the stresses computed in scenario (a). This implies that there is no simplifying scenario in which the stress state of the arterial vessels is close to the scenario (a).

Moreover, the obtained results, using scenario (a), correspond to the most realistic scenario through the consideration of fluid-structure interaction and coupling with a one-dimensional network of the rest of the arterial tree. This ensures a physiologically consistent hemodynamic environment for the region of interest.

In Chapters 3 and 4, a number of modeling ingredients was considered in an integrated framework implying the consideration of the preload problem to find the material configuration on top of which constitutive equations are defined, including pressure and tethering loads, fluid-structure interaction and coupling with a dimensionally reduced model of the rest of the cardiovascular system. We remark that the integration of these modeling ingredients had no precedents in the specialized literature. Furthermore, the comprehensive approach adopted in this work is crucial (i) to understand the interaction between the different components involved in the physical phenomena and their influence in arterial function, and (ii) to accurately quantify the impact of different modeling hypotheses.

4.6.2 Modeling arterial adaptations

Proper determination of internal stresses in the arterial wall is essential because it poses the mechanical environmental conditions in which living tissues evolve. For instance, growth and remodeling processes are largely known to strongly depend on the homeostatic stress state and to be governed by the level of stress in the vascular tissue (Rodriguez et al, 1994; Baek et al, 2005; Valentín and Humphrey, 2009; Watton et al, 2011). In turn, damage modeling is also acknowledged to be stress-driven (Li and Robertson, 2009; Alastrué et al, 2007; Balzani et al, 2012) which is crucial if the present tools are to be used in the assessment of risk of arterial wall rupture. Another example is the sensitivity of

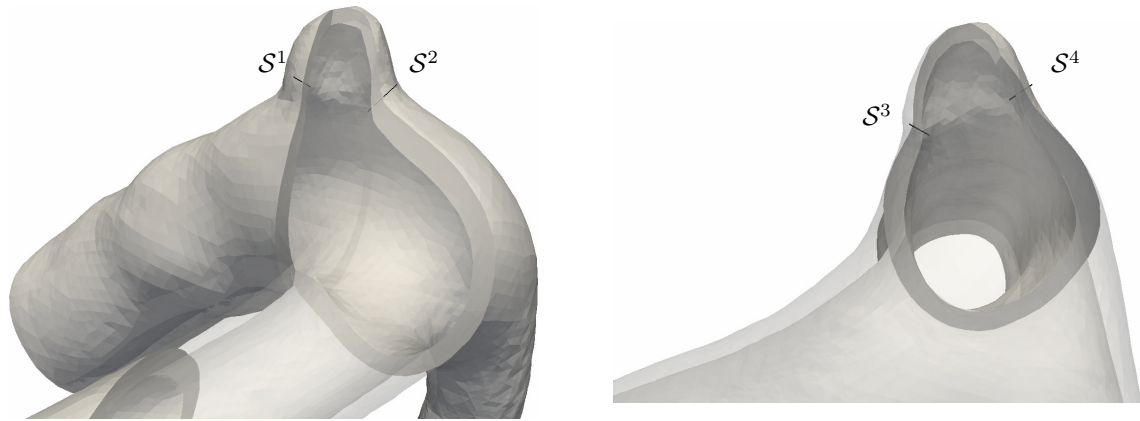
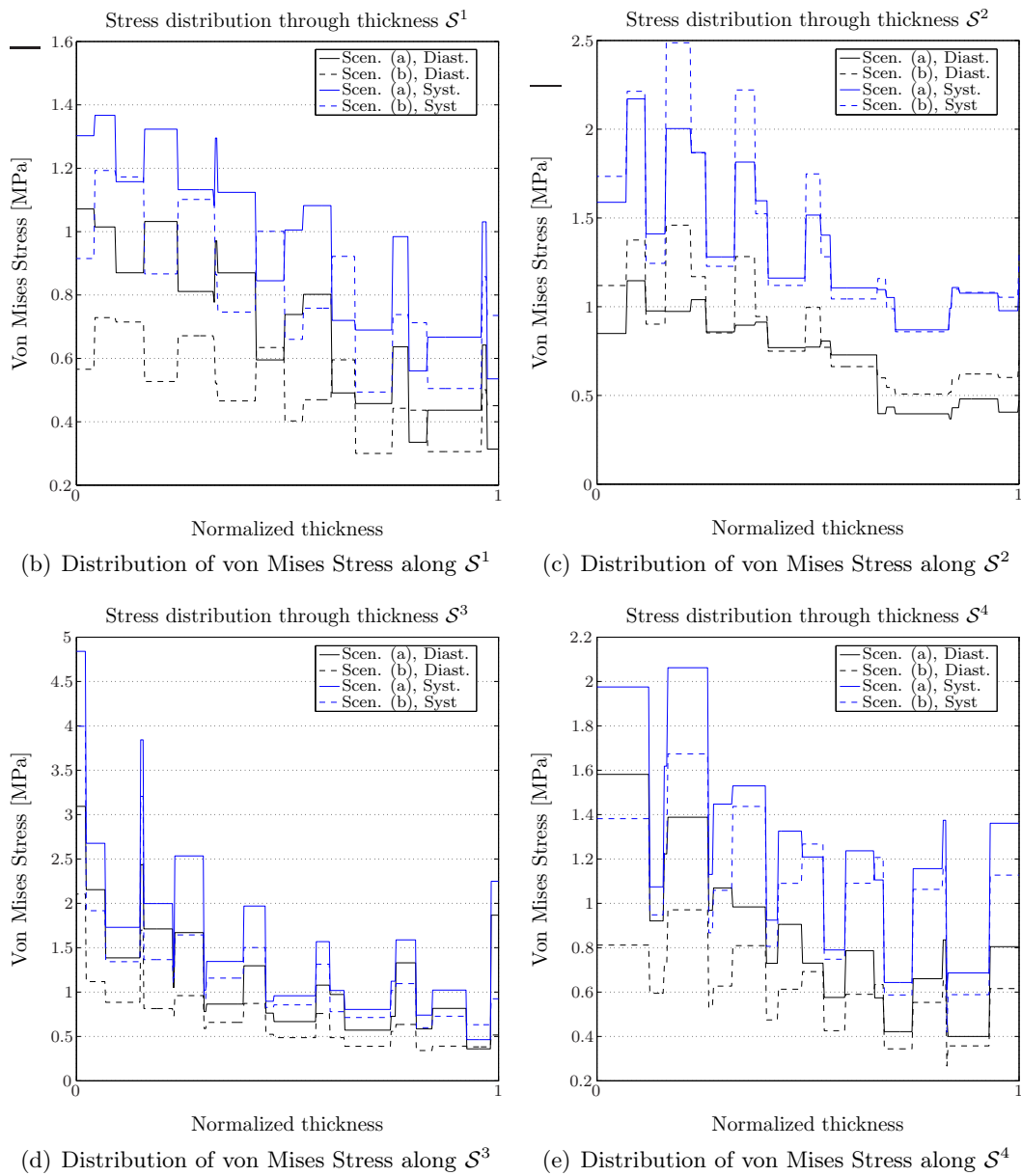
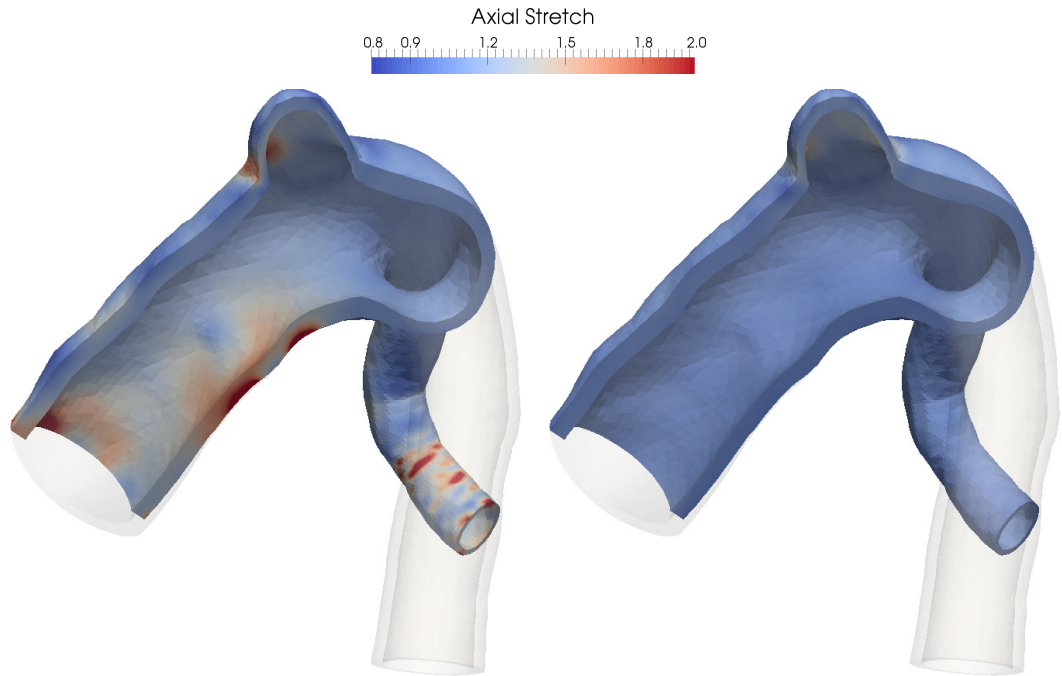
(a) Location reference for curves \mathcal{S}^1 , \mathcal{S}^2 , \mathcal{S}^3 and \mathcal{S}^4 

Figure 4.31: Through thickness stress distribution at different points for time instants $t = 0.235T$ (black lines) and $t = 0.85T$ (blue lines). Comparison between results for scenarios (a) -solid lines- and (b) -dashed lines-.



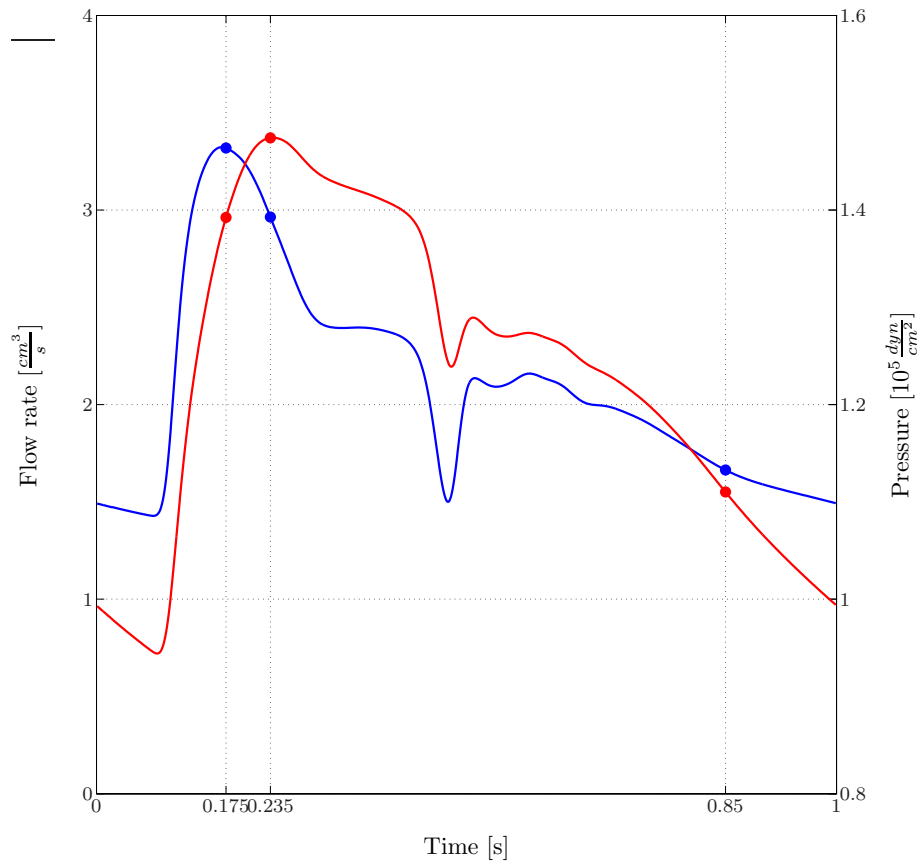
(a) Scenario (a), axial stretch for baseline configuration.

(b) Scenario (b), axial stretch for baseline configuration.

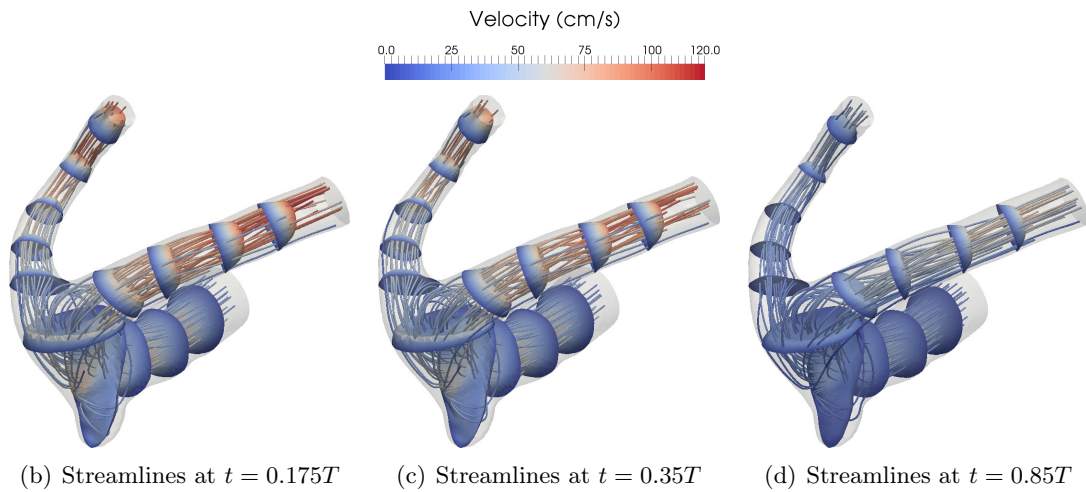


(c) Scenario (a), region under axial compression. (d) Scenario (b), region under axial compression.

Figure 4.32: Axial stretch at baseline configuration for scenarios (a) and (b). Comparison between regions under axial compression.



(a) Flow rate (blue) and pressure (red) at the inlet of the middle cerebral artery during the cardiac cycle.



(b) Streamlines at $t = 0.175T$

(c) Streamlines at $t = 0.35T$

(d) Streamlines at $t = 0.85T$

Figure 4.33: Blood flow dynamics for the patient specific aneurysm (located at middle cerebral artery) example, displaying pressure (red) and flow rate (blue) at the inlet during one cardiac cycle and visualization of velocity profiles and streamlines for three time instants $t = 0.175T$ (maximum flow rate), $t = 0.35T$ (maximum mean pressure) and $t = 0.85T$ (diastolic instant).

mechanoreceptor function to the stretch in arterial tissue (Feng et al, 2007). Lack of arterial stretch has been proved to be related to abnormal firing rate of aortic mechanoreceptors leading to impaired ability of the central nervous system to regulate the arterial pressure. The same can be conjectured for carotid baroreceptors (featuring a similar function).

In all these situations, wrongly estimated stresses certainly would mislead the insight retrieved from models, and obscure the understanding of mechanobiological arterial wall function.

The importance of considering adequate hypotheses regarding the complete loading condition of the vessel is, therefore, capital. As seen, this can be even more critical in patient-specific cases, in which geometrical complexity can contribute to enlarge discrepancies in the calculation of the stress state in the arterial wall.

4.6.3 Limitations

Most of the limitations of the present approach are shared with standard FSI approaches. As for the detailed 3D model, the constitutive parameters of the arterial wall and the definition of the arterial thickness are typical examples.

In turn, little is known about the interaction of the arterial wall with the surrounding media, and much is still to be done. The proposed approach relies on few works available in the literature, and this remains an open problem for the community. In addition, the origin of residual stresses due to growth and remodeling processes and their incorporation in real geometries continues to be matter of debate (see the approach to the problem taken in Chapter 5 for more details). Although residual stresses caused by pre-stretching have been considered in this work, the true impact of residual stresses and deformations is of relevance and will be addressed in the near future.

As for the model of the systemic circulation, limitations are those standard from 1D and 0D models about the calibration of arterial compliances, peripheral resistances and cardiac function. Ultimately, this will have an impact in the definition of pressure and flow waveforms to which the arterial structure under analysis is to be subjected to.

Chapter 5

In-vivo characterization of residual deformations

5.1 Introduction

As it has been pointed out in Chapter 1, it is well known that, in order to realistically model and simulate the behavior of arterial tissues, it is necessary to account for the different composition and role of the arterial wall layers (intima, media, adventitia) as well as for the action of the structurally relevant components, namely elastin, collagen fibers and smooth muscle cells. A considerable amount of literature has been published addressing the study of the constitutive behavior of the soft tissue, developing comprehensive models (Fung, 1991; Holzapfel and Gasser, 2000; Zulliger et al, 2004a; Gundiah et al, 2007), and performing parameter estimation based on ex-vivo experimental data (Weisbecker et al, 2012; Holzapfel and Ogden, 2010a).

However, it is also acknowledged (Fung and Liu, 1989; Fung, 1991; Holzapfel et al, 2007) that the in vivo unloaded configuration of any vascular district (see Chapter 3) is neither stress-free nor strain-free. Hence, an increasing number of studies has been carried out to understand the effects of residual stresses (RSs) in arterial wall mechanics. A shifting in the role researchers assign to RSs has taken place, from conceiving RSs as a mere side effect of growth to a conception in which RSs are viewed as a functionally responsible adaptive and protective mechanism. In fact, nowadays, there is consensus that residual strains and stresses have a functional role in determining suitable mechanobiological conditions in vascular vessels (Driessen et al, 2004; Hariton et al, 2007; Valentín and Humphrey, 2009). Indeed, arteries are living tissues that continuously adapt to their environment and to external stimuli (Humphrey and Rajagopal, 2002; Watton et al, 2011; Cyron and Humphrey, 2014). This adaptation is mediated by growth and remodeling. These processes lead to the occurrence of self-equilibrated RSs, which remain in the body even though all external loads are removed.

In the engineering field, RSs exist in practically all mechanical components. Here, in a similar manner, RSs are usually defined as the stresses which remain in mechanical components when they are not subjected to any external loads. They are the result of the loading history of each piece during its manufacturing and/or loading process. Again, within this context, the “residual” adjective can have a misleading connotation as can be interpreted as being something undesirable or as a collateral effect of the forming process. But, contrariwise, they can be, and in several situations are, intentionally introduced in the design/fabrication process to optimize the performance of mechanical components by acting on the strength of structures and materials. This is the case of steel pipes where plastic deformation is induced to introduce residual compressive stresses (hoop stresses), with the aim of relieving part of the service loads. Similarly, there is consensus in the

scientific community around the fact that the in-vivo stresses are strongly influenced by the existence of RSs (Holzapfel and Gasser, 2000). Furthermore, it has been pointed out that in non-pathological cases RSs contribute to the transmural uniformity of the strain under physiological conditions, consequently leading to relatively low stress gradients across the thickness of the vessel within each layer (Takamizawa and Hayashi, 1987; Destrade et al, 2012).

Reported experimental observations show that when an arterial segment is removed from its surroundings, RSs are manifested through the retraction in the longitudinal direction as well as through the appearance of an opening angle that takes place when the wall is radially cut all along its axis. Moreover, in relatively recent works (Holzapfel et al, 2007; Holzapfel and Ogden, 2010a), it has been observed that different levels of RSs are associated with each constituent layer of the arterial wall. Most efforts to account for RSs in arterial wall models are primarily based on the incorporation of pre-strains acquired from these experimental procedures. In fact, these RSs are caused by the *recoverable residual deformations* (hereafter referred simply as residual deformations -RRDs-) present in the tissue, and which are originated in growth and remodeling processes to keep the structure compatible. Among these, we highlight the contributions of Holzapfel and Gasser (2000) with the first in-depth proposal of this idea, Holzapfel et al (2007); Holzapfel and Ogden (2010a) incorporating further detail accounting for the different behaviors presented for each constituent layer, and Pierce et al (2015) displaying a generalization of this technique to be applied in patient-specific geometries. It is also worthwhile to mention the different approach taken by Taber and Humphrey (2001) and Bellini et al (2014), introducing RSs through growth processes, considering that each mechanically relevant component is synthesized and deposited in the tissue with a predefined deformation (and consequently stress) level.

Fortunately, the limitations in the characterization of constitutive parameters, RSs and RRDs for living tissues obtained through ex vivo experimentation can now be overcome by promoting its integration with computational modeling and data coming from new instruments for measurements and image data acquisition such as IVUS, OCT and 4DMRI among others. Any of these three technologies, when properly combined with motion tracking methods, such as optical-flow (Kirchner and Niemann, 1992) or LDDM (Cao et al, 2005), can definitely be used to reasonably estimate the motion of anatomical structures with an unprecedented level of time and spatial resolution. The integration of these data with computational cardiovascular modeling can help in the identification of patient-specific constitutive parameters, RSs, RRDs, among others relevant parameters, reaching a virtuous cycle of reciprocal feedback leading each time to a more realistic modeling of the complex biological structures and the associated physiological processes, which can be used to aid physicians in their decision-making process.

In particular, the merging between data and computational modeling for real world applications, known as Data Assimilation, is well developed in areas such as geophysics (Blum et al (2009) and references therein), oceanography and meteorology (see (Ghil and Malanotte-Rizzoli, 1991) and references therein) however is only in the beginning in cardiovascular modelling (D’Elia et al (2012); Wittek et al (2013); Rausch and Kuhl (2013); Bertagna et al (2014) and references cited therein). In fact, the “patient-specific” denomination usually stands for the use of image-based geometries, despite the many other physiological variables involved. Currently, constitutive parameters, RSs and RRDs states used in these models are taken from ex vivo experiments and from information collected from the literature and, hence, are not associated with the specific patient. Noteworthy, there is no previous contribution in which the estimation of RSs can be effectively performed from in-vivo data, namely image-based data of the corresponding arterial structures and arterial blood pressure in these sites.

In view of the gap highlighted in the previous paragraph, the aim of this part of the thesis is to develop a novel conceptual framework that makes the estimation of RSs practicable in conditions resembling in-vivo scenarios. For this, data derived from medical images consist of arterial structures imaged at more than one configuration, each of which is associated to a certain level of known arterial pressure.

More specifically, a mechanical framework is presented, explicitly emphasizing the role of RRDs. These deformations can be understood as recoverable as they can be completely released if the arterial district is separated from the surrounding tissues and its material constituents are isolated from their native environment in a hypothetical ex-vivo configuration, denoted hereafter as *virtual configuration*, which is naturally free of RRDs and, therefore, of RSs. Furthermore, the energy stored in the material wall at free load configuration is fully recovered at this virtual configuration (Cowin, 2004; Rodriguez et al, 1994; Ambrosi and Mollica, 2002). As such, these RRDs are the only ones responsible for the RSs present in tissues that manifest through diverse ways as pointed out above (Holzapfel et al, 2007). The problem of the identification of RSs therefore becomes a problem of identification of the RRDs.

Fundamental to our purposes is to have at hand, as input data, at least two configurations of the arterial structure and the displacement field between them. The generalization for more than two configurations is also presented and the influence of the additional data provided is analyzed in the featured examples. This information can be obtained by gating and registering sequences of IVUS images (Hernández-Sabaté et al, 2011; Maso Talou et al, 2015). These known configurations, with properly defined constitutive relations, yield a mechanical imbalance unless the correct RS generated by the adequate RRD tensor field is considered. This is the key for our variational formulation of the identification problem and will be exploited in the construction of a cost functional to be minimized. As we will see, the cost functional is given by the generalized residuals of the variational equations corresponding to the mechanical equilibrium of the known arterial wall configurations. Then, the identification of the RS field is reduced to a minimization of this distance using the variational equilibrium equation at one of these configurations as a constraint (subsidiary condition in variational terms). For the minimization of this cost functional, a simple gradient descent method and an interior-point algorithm for constrained optimization are considered.

The structure of this chapter is organized as follows. The kinematics and the variational framework for the RRD characterization problem is presented in Section 5.2. The formulation of the optimization problem and the proposed cost functionals to be minimized are introduced in Section 5.3. A description of the optimization techniques to be considered for our minimization problem is given in Section 5.4. Finally, the sensitivity analysis of the proposed cost functional with respect to changes in the residual deformations is carried out in Section 5.5.

5.2 Mechanical setting

As mentioned in the Section 5.1, the proposed approach relies in the fact that more than one arterial configuration is known. For simplicity we will consider that two arterial configurations are known, say configuration Ω_a and configuration Ω_b . However, the analysis can straightforwardly be extended to more than two configurations (see Section 5.3.2). For each of these two known configurations we also consider that the arterial blood pressure, which is the external load responsible for part of the total deformation occurring in these configurations, is given. As previously stated, these configurations can be obtained from image data acquisition techniques such as IVUS, OCT and 4DMRI among others. Furthermore, the displacement vector field, say \mathbf{w} , which maps Ω_a into Ω_b is known data

that is somehow retrieved from motion tracking methods, such as optical-flow or LDDM.

In this context, let us present the kinematics setting and the variational formulations corresponding to the equilibrium in these two configurations.

5.2.1 Kinematics

Consider the four-configuration setting displayed on Figure 5.1. The *virtual configuration* Ω_v (with coordinates in this domain denoted as \mathbf{x}_v) represents a state of unloaded and separated material constituents of the arterial wall, serving as a reference for the constitutive equations describing the material behavior. This virtual configuration has a zero stress state and is free of RRDs as result of removing kinematical constraints and loads. Then, this configuration corresponds to a zero elastic strain energy configuration. Moreover, in this configuration the material constituents may have permanent deformation due to plasticity and damage processes occurring along the life of the patient. These are the unrecoverable part of the deformation, and will be disregarded in the present analysis.

The material domain Ω_m (with coordinates \mathbf{x}_m) denotes a zero-load configuration. However, due to processes of growth and remodeling the tissues feature a deformation, characterized in each material point by the RRD tensor \mathbf{F}^r such that each material differential fiber is related with its virtual counterpart by

$$d\mathbf{x}_m = \mathbf{F}^r d\mathbf{x}_v. \quad (5.2.1)$$

This RRD tensor is the recoverable part of the deformation of the tissue, and is responsible for storing energy in the structure still in the case of the zero-load configuration. The associated strain induces a self-equilibrated RS state $\boldsymbol{\sigma}_m^r$ that is dependent on the constitutive behavior of the material. For compressible hyperelastic materials we admit the existence of a scalar strain energy function Ψ , from which the (second) Piola-Kirchhoff and Cauchy stress tensors are obtained by

$$\mathbf{S}^r = \frac{\partial \Psi}{\partial \mathbf{C}^r}, \quad \boldsymbol{\sigma}_m^r = \frac{1}{\det \mathbf{F}^r} \mathbf{F}^r \mathbf{S}_m^r (\mathbf{F}^r)^T, \quad (5.2.2)$$

where \mathbf{F}^r is defined in terms of \mathbf{x}_m , and with \mathbf{C}^r standing for the Cauchy-Green deformation tensor given by $\mathbf{C}^r = (\mathbf{F}^r)^T \mathbf{F}^r$.

The spatial domains Ω_a and Ω_b (with coordinates denoted as \mathbf{x}_a and \mathbf{x}_b , respectively) are configurations at equilibrium with two different levels of blood pressure, say p_a and p_b which are applied over their inner surface of the vessel, Γ_a and Γ_b , respectively. Coordinates on each domain are related through the displacement fields \mathbf{v} and \mathbf{u} as follows

$$\mathbf{x}_a = \mathbf{x}_m + \mathbf{v}_m, \quad (5.2.3)$$

$$\mathbf{x}_b = \mathbf{x}_m + \mathbf{u}_m. \quad (5.2.4)$$

In addition, the relation between configurations Ω_a and Ω_b can be stated in terms of the displacement field \mathbf{w} , as next

$$\mathbf{x}_b = \mathbf{x}_a + \mathbf{w}_a. \quad (5.2.5)$$

Thence, the deformation gradient tensors are obtained as follows

$$\mathbf{F}^{\mathbf{u}} = \mathbf{I} + \nabla_m \mathbf{u}_m, \quad \mathbf{F}^{\mathbf{v}} = \mathbf{I} + \nabla_m \mathbf{v}_m, \quad \mathbf{F}^{\mathbf{w}} = \mathbf{I} + \nabla_a \mathbf{w}_a. \quad (5.2.6)$$

where $\mathbf{F}^{\mathbf{u}}$ and $\mathbf{F}^{\mathbf{v}}$ are defined in terms of \mathbf{x}_m , $\mathbf{F}^{\mathbf{w}}$ in terms of \mathbf{x}_a and $\mathbf{F}^{\mathbf{v}^r}$, $\mathbf{F}^{\mathbf{u}^r}$ (see (5.2.8) below) and \mathbf{F}^r in terms of \mathbf{x}_m . In some cases it will be necessary to express those tensors in an alternative coordinate system; then, an index will be added to symbolize the change in the independent variable (e.g. $\mathbf{F}_b^{\mathbf{u}}$ denotes that the independent variable is \mathbf{x}_b). Also,

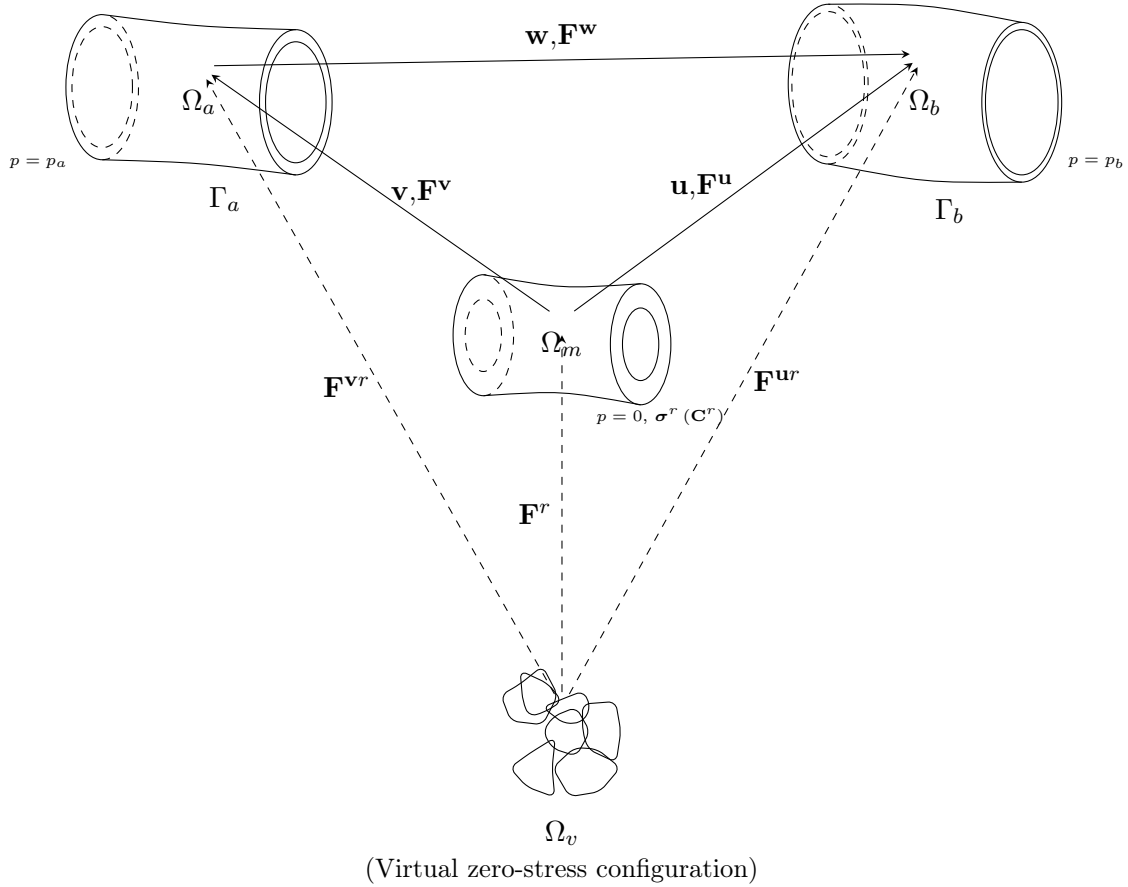


Figure 5.1: Problem setting for *in-vivo* residual deformation characterization. The virtual configuration Ω_v represents a disaggregated state of material particles composing the arterial wall in a zero-stress state and serves as reference configuration for constitutive equations (no elastic energy is stored). The material domain Ω_m is subjected to no external loads, however, due to the existence of RRDs (\mathbf{F}_m^r) developed during the processes of growth/remodelling, a self-equilibrated ² residual stress state (σ_m^r) arises in this configuration. Configurations Ω_a and Ω_b represent two equilibrium configurations with their corresponding external loading system given by the arterial blood pressure (p_a and p_b , respectively). The displacement fields \mathbf{v} and \mathbf{u} map these domains from Ω_m . Tensors \mathbf{F}^v and \mathbf{F}^u denote the corresponding deformation gradient tensors due to the aforementioned displacement fields, and $\mathbf{F}^{vr} = \mathbf{F}^v \mathbf{F}^r$, $\mathbf{F}^{ur} = \mathbf{F}^u \mathbf{F}^r$ are the material expressions for the total deformation tensor with respect to the constitutive reference configuration Ω_v (virtual configuration). For the purposes of the present work, Ω_v will never be practically used, Ω_m is an unknown in the problem, while Ω_a and Ω_b are known data, as well as displacement vector \mathbf{w} .

note that the deformation gradient tensors, \mathbf{F}^v and \mathbf{F}^u , are related through

$$\mathbf{F}^u = \mathbf{F}_m^w \mathbf{F}^v. \quad (5.2.7)$$

The total deformation experienced by the material at these configurations is obtained composing the presented deformation gradient tensors with \mathbf{F}^r , obtaining

$$\mathbf{F}^{ur} = \mathbf{F}^u \mathbf{F}^r = \mathbf{F}_m^w \mathbf{F}^v \mathbf{F}^r, \quad \mathbf{F}^{vr} = \mathbf{F}^v \mathbf{F}^r \quad (5.2.8)$$

Based on the presented definitions, the Cauchy-Green deformation tensors associated

to the mechanical state of the spatial domains are introduced as

$$\mathbf{C}^{vr} = (\mathbf{F}^{vr})^T \mathbf{F}^{vr}, \quad \mathbf{C}^{ur} = (\mathbf{F}^{ur})^T \mathbf{F}^{ur}. \quad (5.2.9)$$

Note that both are naturally defined in Ω_m .

5.2.2 Mechanical equilibrium

In this section the formulations corresponding to the mechanical equilibrium of the tissue in configurations Ω_m , Ω_a and Ω_b are introduced. Moreover, the equations that state the equilibrium will be conveniently rewritten in configuration Ω_a .

5.2.2.1 Mechanical equilibrium in the material configuration Ω_m

The variational equation that defines the mechanical equilibrium of the body in Ω_m reads

$$\int_{\Omega_m} \boldsymbol{\sigma}_m^r \cdot \nabla_m^s \hat{\mathbf{v}} d\Omega_m = 0 \quad \forall \hat{\mathbf{v}} \in \mathcal{V}_m, \quad (5.2.10)$$

where $\boldsymbol{\sigma}_m^r$ is a certain residual stress field, ∇_m^s denotes the symmetric gradient with respect to coordinates \mathbf{x}_m , and \mathcal{V}_m the linear space of kinematic admissible variations in the material configuration considering the Dirichlet boundary Γ_m^D , which is given by

$$\mathcal{V}_m = \left\{ \mathbf{v} \in \mathbf{H}^1(\Omega_m); \mathbf{v}|_{\Gamma_m^D} = 0 \right\}. \quad (5.2.11)$$

Since in the characterization problem Ω_m is unknown, it is worthwhile to express equation (5.2.10) in terms of \mathbf{x}_a , allowing to perform the integration in the known configuration Ω_a . A change of variables leads to

$$\int_{\Omega_a} \boldsymbol{\sigma}_a^r \cdot \left((\mathbf{F}_a^v)^{-T} \nabla_a \hat{\mathbf{v}} \right)^s d\Omega_a = 0 \quad \forall \hat{\mathbf{v}} \in \mathcal{V}_a, \quad (5.2.12)$$

where \mathcal{V}_a is the counterpart of \mathcal{V}_m in Ω_a , and $\boldsymbol{\sigma}_a^r$ is related to $\boldsymbol{\sigma}_m^r$ and \mathbf{S}^r through the following expressions

$$\boldsymbol{\sigma}_a^r = \frac{1}{\det \mathbf{F}_a^v} \mathbf{F}_a^v (\boldsymbol{\sigma}_m^r)_a (\mathbf{F}_a^v)^T = \frac{1}{\det \mathbf{F}_a^{vr}} \mathbf{F}_a^{vr} (\mathbf{S}^r)_a (\mathbf{F}_a^{vr})^T. \quad (5.2.13)$$

5.2.2.2 Mechanical equilibrium in the spatial configuration Ω_a

For simplicity, let us consider that the arterial wall is only subjected to a uniform pressure load p_a applied on the inner surface of the vessel Γ_a . Then the variational equation that characterizes the mechanical equilibrium for the spatial configuration Ω_a reads

$$\int_{\Omega_a} \boldsymbol{\sigma}^{vr} \cdot \nabla_a^s \hat{\mathbf{v}} d\Omega_a = \int_{\Gamma_a} p_a \mathbf{n}_a \cdot \hat{\mathbf{v}} d\Gamma_a \quad \forall \hat{\mathbf{v}} \in \mathcal{V}_a \quad (5.2.14)$$

where \mathcal{V}_a is the space of kinematically admissible virtual actions in Ω_a , and the stress tensor $\boldsymbol{\sigma}^{vr}$ is

$$\boldsymbol{\sigma}^{vr} = \frac{1}{\det \mathbf{F}_a^{vr}} \mathbf{F}_a^{vr} (\mathbf{S}^{vr})_a (\mathbf{F}_a^{vr})^T, \quad (5.2.15)$$

with \mathbf{S}^{vr} representing the Piola-Kirchhoff stress tensor caused by the deformation \mathbf{F}^{vr} .

5.2.2.3 Mechanical equilibrium in the spatial configuration Ω_s

Analogously to the previous case, for a given pressure p_b applied over the inner surface of the vessel wall Γ_b , the variational equation characterizing the mechanical equilibrium in Ω_b is the following

$$\int_{\Omega_b} \boldsymbol{\sigma}^{\mathbf{ur}} \cdot \nabla_b^s \hat{\mathbf{v}} \, d\Omega_b = \int_{\Gamma_b} p_b \mathbf{n}_b \cdot \hat{\mathbf{v}} \, d\Gamma_b \quad \forall \hat{\mathbf{v}} \in \mathcal{V}_b, \quad (5.2.16)$$

where \mathcal{V}_b is the space of kinematically admissible virtual actions in Ω_b , and the constitutive stress tensor $\boldsymbol{\sigma}^{\mathbf{ur}}$ is obtained through

$$\boldsymbol{\sigma}^{\mathbf{ur}} = \frac{1}{\det \mathbf{F}_b^{\mathbf{ur}}} \mathbf{F}_b^{\mathbf{ur}} (\mathbf{S}^{\mathbf{ur}})_b (\mathbf{F}_b^{\mathbf{ur}})^T. \quad (5.2.17)$$

As with equation (5.2.12), it is possible to rewrite this variational equation in configuration Ω_a , leading to

$$\int_{\Omega_a} \boldsymbol{\sigma}_a^{\mathbf{ur}} \cdot \left((\mathbf{F}^{\mathbf{w}})^T \nabla_a \hat{\mathbf{v}} \right)^s \, d\Omega_a = \int_{\Gamma_a} (p_b)_a (\mathbf{F}^{\mathbf{w}})^{-T} \mathbf{n}_a \cdot \hat{\mathbf{v}} \det \mathbf{F}^{\mathbf{w}} \, d\Gamma_a \quad \forall \hat{\mathbf{v}} \in \mathcal{V}_a, \quad (5.2.18)$$

where $\boldsymbol{\sigma}_a^{\mathbf{ur}}$ is written as next

$$\boldsymbol{\sigma}_a^{\mathbf{ur}} = \frac{1}{\det \mathbf{F}_a^{\mathbf{vr}}} \mathbf{F}_a^{\mathbf{vr}} (\mathbf{S}^{\mathbf{ur}})_a (\mathbf{F}_a^{\mathbf{vr}})^T. \quad (5.2.19)$$

Furthermore, since \mathbf{w} is given data, we can reduce the number of unknown variables. In fact, \mathbf{u} can be eliminated considering the identities $\mathbf{u} = \mathbf{v} + \mathbf{w}$ and $\mathbf{F}_a^{\mathbf{ur}} = \mathbf{F}_a^{(\mathbf{v}+\mathbf{w})r} = \mathbf{F}^{\mathbf{w}} \mathbf{F}_a^{\mathbf{vr}}$. To put this in evidence, we introduce the notation

$$\boldsymbol{\sigma}_a^{\mathbf{ur}} = \boldsymbol{\sigma}_a^{(\mathbf{v}+\mathbf{w})r} = \frac{1}{\det \mathbf{F}_a^{\mathbf{vr}}} \mathbf{F}_a^{\mathbf{vr}} \mathbf{S}^{(\mathbf{v}+\mathbf{w})r} (\mathbf{F}_a^{\mathbf{vr}})^T. \quad (5.2.20)$$

Then, equation (5.2.18) takes the final form

$$\int_{\Omega_a} \boldsymbol{\sigma}_a^{(\mathbf{v}+\mathbf{w})r} \cdot \left((\mathbf{F}^{\mathbf{w}})^T \nabla_a \hat{\mathbf{v}} \right)^s \, d\Omega_a = \int_{\Gamma_a} (p_b)_a (\mathbf{F}^{\mathbf{w}})^{-T} \mathbf{n}_a \cdot \hat{\mathbf{v}} \det \mathbf{F}^{\mathbf{w}} \, d\Gamma_a \quad \forall \hat{\mathbf{v}} \in \mathcal{V}_a. \quad (5.2.21)$$

5.3 Recoverable residual deformation characterization problem

In this Section, the RRD problem is introduced as the minimization of a cost functional measuring the mechanical disequilibrium of the setting described above.

5.3.1 Problem statement for two known configurations

As previously mentioned, data acquisition techniques (image acquisition and suitable reconstruction methods) are able to provide the spatial characterization corresponding to configurations Ω_a and Ω_b , each one in equilibrium with well-defined blood pressure levels p_a and p_b . Furthermore, the displacement field \mathbf{w} is considered to be also a given data. Hence, the objective is to find the RRD field \mathbf{F}^r (from which the RS field $\boldsymbol{\sigma}^r$ directly follows) and the material configuration Ω_m (and consequently the displacement fields \mathbf{u}

and \mathbf{v}), such that the three mechanical problems stated in (5.2.12), (5.2.14) and (5.2.18) are satisfied.

Let now $(\mathbf{F}^r, \mathbf{v})$ be the solution of equations (5.2.12), (5.2.14) and (5.2.18) (observe that if the pair is solution of (5.2.12) and (5.2.14), then equation (5.2.21) is automatically satisfied). For the following developments, consider an arbitrary displacement $\tilde{\mathbf{v}} \neq \mathbf{v}$, and an arbitrary deformation tensor $\tilde{\mathbf{F}}^r \neq \mathbf{F}^r$. We refer to $\tilde{\mathbf{v}}_a$ as the description of $\tilde{\mathbf{v}}$ in configuration Ω_a . Also, note that $\tilde{\mathbf{v}}_a \in Kin_a$, where Kin_a stands for the linear manifold of kinematically admissible displacements defined in Ω_a defined as

$$Kin_a = \left\{ \mathbf{v} \in \mathbf{H}^1(\Omega_a); \mathbf{v}|_{\Gamma_a^D} = \bar{\mathbf{v}} \right\}. \quad (5.3.1)$$

As the pair $(\tilde{\mathbf{F}}_a^r, \tilde{\mathbf{v}}_a)$ is not solution of the problem, for a fixed pair, the following functionals can be defined in \mathcal{V}'_a :

- $\mathcal{R}_m = \mathcal{R}_m(\tilde{\mathbf{F}}_a^r, \tilde{\mathbf{v}}_a) \in \mathcal{V}'_a$, associated with the mechanical disequilibrium of the RS field $\boldsymbol{\sigma}_m^r$ in Ω_m ; i.e., with the residual of equation (5.2.12). This functional is defined by

$$\begin{aligned} \langle \mathcal{R}_m(\tilde{\mathbf{F}}_a^r, \tilde{\mathbf{v}}_a), \hat{\mathbf{v}} \rangle &= \int_{\Omega_a} \boldsymbol{\sigma}_a^r \cdot \left((\mathbf{F}_a^{\tilde{\mathbf{v}}})^{-T} \nabla_a \hat{\mathbf{v}} \right)^s d\Omega_a, \\ &= \int_{\Omega_a} \frac{1}{\det \mathbf{F}_a^{\tilde{\mathbf{v}}r}} \mathbf{F}_a^{\tilde{\mathbf{v}}r} (\mathbf{S}^r)_a (\mathbf{F}_a^{\tilde{\mathbf{v}}r})^T \cdot \left((\mathbf{F}_a^{\tilde{\mathbf{v}}})^{-T} \nabla_a \hat{\mathbf{v}} \right)^s d\Omega_a, \quad \text{with } \hat{\mathbf{v}} \in \mathcal{V}_a \end{aligned} \quad (5.3.2)$$

Observe that this functional depends explicitly and implicitly (through \mathbf{S}^r) on $\tilde{\mathbf{F}}_a^r$.

- $\mathcal{R}_b = \mathcal{R}_b(\tilde{\mathbf{F}}_a^r, \tilde{\mathbf{v}}_a) \in \mathcal{V}'_a$, associated with the mechanical disequilibrium in the known spatial domain Ω_b (however written in configuration Ω_a), given by the residual of equation (5.2.18). This functional is defined by

$$\begin{aligned} \langle \mathcal{R}_b(\tilde{\mathbf{F}}_a^r, \tilde{\mathbf{v}}_a), \hat{\mathbf{v}} \rangle &= \int_{\Omega_a} \boldsymbol{\sigma}_a^{(\tilde{\mathbf{v}}+\mathbf{w})r} \cdot \left((\mathbf{F}^{\mathbf{w}})^T \nabla_a \hat{\mathbf{v}} \right)^s d\Omega_a \\ &\quad - \int_{\Gamma_a} (p_b)_a (\mathbf{F}^{\mathbf{w}})^{-T} \mathbf{n}_a \cdot \hat{\mathbf{v}} \det \mathbf{F}^{\mathbf{w}} d\Gamma_a \\ &= \int_{\Omega_a} \frac{1}{\det \mathbf{F}_a^{\tilde{\mathbf{v}}r}} \mathbf{F}_a^{\tilde{\mathbf{v}}r} (\mathbf{S}^{(\tilde{\mathbf{v}}+\mathbf{w})r})_a (\mathbf{F}_a^{\tilde{\mathbf{v}}r})^T \cdot \left((\mathbf{F}^{\mathbf{w}})^T \nabla_a \hat{\mathbf{v}} \right)^s d\Omega_a \\ &\quad - \int_{\Gamma_a} (p_b)_a (\mathbf{F}^{\mathbf{w}})^{-T} \mathbf{n}_a \cdot \hat{\mathbf{v}} \det \mathbf{F}^{\mathbf{w}} d\Gamma_a, \quad \text{with } \hat{\mathbf{v}} \in \mathcal{V}_a \end{aligned} \quad (5.3.3)$$

Again, note that this functional depends explicitly and implicitly (through $\mathbf{S}^{(\tilde{\mathbf{v}}+\mathbf{w})r}$) on $\tilde{\mathbf{F}}_a^r$.

Furthermore, let $\mathcal{V}_a = span \{ \Phi_1, \Phi_2, \dots \}$, where Φ_i denotes the i -th element of a basis of the space of kinematic admissible virtual action at the Ω_a configuration. Then, the above functionals are completely characterized through the dual product with each element Φ_i of the proposed basis, i.e., by the virtual power exerted between the generalized residual forces \mathcal{R}_m and \mathcal{R}_b and each element of the basis.

$$R_m^i(\tilde{\mathbf{F}}_a^r, \tilde{\mathbf{v}}_a) = \langle \mathcal{R}_m(\tilde{\mathbf{F}}_a^r, \tilde{\mathbf{v}}_a), \Phi_i \rangle, \quad i = 1, 2, \dots \quad (5.3.4)$$

$$R_b^i(\tilde{\mathbf{F}}_a^r, \tilde{\mathbf{v}}_a) = \langle \mathcal{R}_b(\tilde{\mathbf{F}}_a^r, \tilde{\mathbf{v}}_a), \Phi_i \rangle, \quad i = 1, 2, \dots \quad (5.3.5)$$

Moreover, $(\mathbf{F}^r, \mathbf{v})$ is the solution of equations (5.2.12), (5.2.14) and (5.2.18) if and only if the pair makes $R_m^i = R_b^i = 0 \quad i = 1, 2, \dots$. Then, we introduce the following *cost functional*

that characterizes the mechanical imbalance as a function of the RRDs

$$\mathcal{F}(\tilde{\mathbf{F}}_a^r, \tilde{\mathbf{v}}_a) = \frac{\eta_m}{2} \mathbf{R}_m(\tilde{\mathbf{F}}_a^r, \tilde{\mathbf{v}}_a) \cdot \mathbf{R}_m(\tilde{\mathbf{F}}_a^r, \tilde{\mathbf{v}}_a) + \frac{\eta_b}{2} \mathbf{R}_b(\tilde{\mathbf{F}}_a^r, \tilde{\mathbf{v}}_a) \cdot \mathbf{R}_b(\tilde{\mathbf{F}}_a^r, \tilde{\mathbf{v}}_a), \quad (5.3.6)$$

where \mathbf{R}_m and \mathbf{R}_b are vectors containing the components defined in (5.3.16) and (5.3.17), respectively. Also, η_m and η_b are weighting factors corresponding the mechanical imbalance at Ω_m and Ω_a , respectively. Note that this weighting factors can be defined to account for the quality of the reconstructions for different domains and the precision on the determination of the \mathbf{w} field, this is particularly interesting for the case on which multiple configurations are known (see Section 5.3.2). Then, the RRD identification problem can be written in the following variational form:

Given Ω_a , Ω_b , \mathbf{w} , the corresponding inner blood pressures p_a, p_b and the material parameters characterizing the arterial wall constitutive behavior, find $(\mathbf{F}_a^r, \mathbf{v}_a)$ such that

$$\begin{aligned} (\mathbf{F}_a^r, \mathbf{v}_a) &:= \arg \min_{\mathbf{D} \times \text{Kin}_a} \left\{ \mathcal{F}(\tilde{\mathbf{F}}_a^r, \tilde{\mathbf{v}}_a) \right\} \\ \text{subjected to } &\int_{\Omega_a} \boldsymbol{\sigma}^{\tilde{\mathbf{v}}_r} \cdot \nabla_a^s \hat{\mathbf{v}} \, d\Omega_a - \int_{\Gamma_a} p_a \mathbf{n}_a \cdot \hat{\mathbf{v}} \, d\Gamma_a = 0 \quad \forall \hat{\mathbf{v}} \in \mathcal{V}_a. \end{aligned} \quad (5.3.7)$$

In the problem described above, \mathbf{D} indicates the space of all tensor fields $\tilde{\mathbf{F}}_a^r$ associated with RRDs defined in Ω_a with positive determinant (i.e. $\det \tilde{\mathbf{F}}_a^r > 0$) for any $\mathbf{x}_a \in \Omega_a$.

Given a fixed $\tilde{\mathbf{F}}_a^r$, consider now $\tilde{\mathbf{v}}_a = \tilde{\mathbf{v}}_a(\tilde{\mathbf{F}}_a^r)$ the unique solution of equation (5.2.14) (see constraint in (5.3.7)). With the introduction of this new variable we define for every $\tilde{\mathbf{F}}_a^r \in \mathbf{D}$ a new cost functional $\mathcal{J}(\tilde{\mathbf{F}}_a^r)$ as

$$\mathcal{J}(\mathbf{F}_a^r) = \mathcal{F}(\tilde{\mathbf{F}}_a^r, \tilde{\mathbf{v}}_a(\tilde{\mathbf{F}}_a^r)), \quad (5.3.8)$$

and problem (5.3.7) can be rewritten as:

Given Ω_a , Ω_b , \mathbf{w} , the corresponding inner pressures p_a, p_b and the material parameters characterizing the arterial wall constitutive behavior, find \mathbf{F}_a^r such that

$$\mathbf{F}_a^r := \arg \min_{\tilde{\mathbf{F}}_a^r \in \mathbf{D}} \left\{ \mathcal{J}(\tilde{\mathbf{F}}_a^r) \right\}. \quad (5.3.9)$$

As $\mathcal{J}(\tilde{\mathbf{F}}_a^r) \geq 0 \quad \forall \tilde{\mathbf{F}}_a^r \in \mathbf{D}$ this problem is well defined, and $\mathcal{J}(\mathbf{F}_a^r) = 0$ if and only if $(\mathbf{F}_a^r, \tilde{\mathbf{v}}_a(\mathbf{F}_a^r)) \in \mathbf{D} \times \text{Kin}_a$ satisfies the mechanical equilibrium equations for Ω_m , Ω_a and Ω_b -given by (5.2.12), (5.2.14) and (5.2.21), respectively-.

We highlight that the proposed cost functional $\mathcal{J}(\tilde{\mathbf{F}}_a^r)$ defined in (5.3.8) introduces a measure of the *error* or *distance* between the variational model and the data provided by medical images. In fact, this *distance* is given by the magnitude of the mechanical equilibrium residuals. The equations presented in the previous Section integrate the available data through the mechanical equilibrium concept, defined by the Virtual Power Principle, and also account for the behavior of arterial wall constituents via corresponding constitutive equations.

Remark 5.1. *The evaluation of the cost functional \mathcal{J} is a two-step process. First, given Ω_a and $\tilde{\mathbf{F}}_a^r$, the mechanical equilibrium given by equation (5.2.14) must be solved, yielding $\tilde{\mathbf{v}}_a$. A linearized form of this preload problem is included in Section 5.5.1, for further discussion about this type of problems see Chapters 2 and 3. Next, the generalized residuals associated with configurations Ω_m and Ω_b must be computed.*

5.3.2 Generalization for multiple known configurations

Let us now consider the mechanical setting presented in Figure 5.2, assuming that more information is available and data acquisition techniques are able provide the known configurations Ω_a and $\Omega_b^1, \dots, \Omega_b^{N_B}$, each one in equilibrium with well-defined blood pressure levels p_a and $p_b^1, \dots, p_b^{N_B}$. Furthermore, the displacement field \mathbf{w}^i that maps points in Ω_a with the corresponding counterpart in Ω_b^i is considered to be also given data for $i = 1, \dots, N_B$.

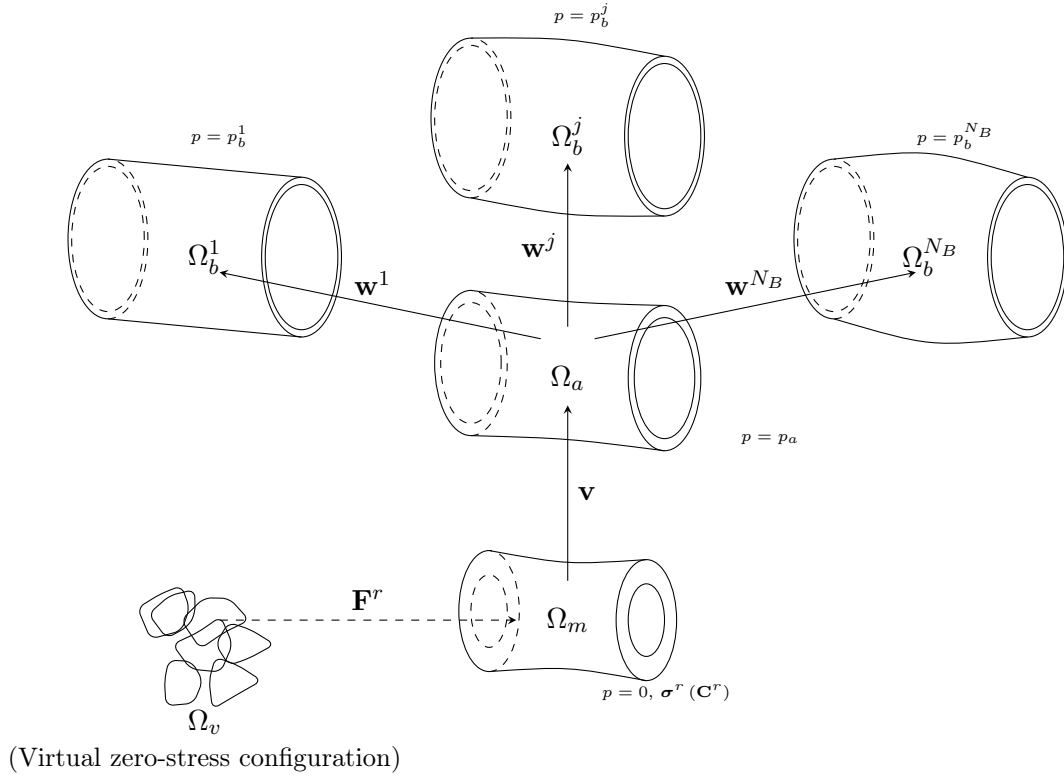


Figure 5.2: Extended problem setting for *in-vivo* residual deformation characterization with multiple known configurations. The virtual configuration Ω_v represents a disaggregated state of material particles composing the arterial wall in a zero-stress state and serves as reference configuration for constitutive equations. The material domain Ω_m is subjected to no external loads, however, is not stress-free due to the existence of RRDs. As before, Ω_a is known, as well as the N_B configurations Ω_b^j ($j = 1, \dots, N_B$). These N_B configurations are represented in the figure by Ω_b^1, Ω_b^j and $\Omega_b^{N_B}$. The displacement fields \mathbf{w}^j mapping Ω_a with Ω_b^j are also known.

For every, configuration Ω_b^j ($j = 1, \dots, N_B$) the mechanical equilibrium equation reads

$$\int_{\Omega_b^j} \boldsymbol{\sigma}^{\mathbf{u}^{j_r}} \cdot \nabla_b^s \hat{\mathbf{v}} \, d\Omega_b^j = \int_{\Gamma_b^j} p_b^j \mathbf{n}_b \cdot \hat{\mathbf{v}} \, d\Gamma_b^j \quad \forall \hat{\mathbf{v}} \in \mathcal{V}_b^j, \quad (5.3.10)$$

where \mathcal{V}_b^j is the space of kinematically admissible virtual actions in Ω_b^j , and the constitutive stress tensor $\boldsymbol{\sigma}^{\mathbf{u}^{j_r}}$ is obtained through

$$\boldsymbol{\sigma}^{\mathbf{u}^{j_r}} = \frac{1}{\det \mathbf{F}_{bj}^{\mathbf{u}^{j_r}}} \mathbf{F}_{bj}^{\mathbf{u}^{j_r}} \left(\mathbf{S}^{\mathbf{u}^{j_r}} \right)_{bj} \left(\mathbf{F}_{bj}^{\mathbf{u}^{j_r}} \right)^T, \quad (5.3.11)$$

where $\mathbf{F}^{\mathbf{u}^{j_r}}$ and $\mathbf{S}^{\mathbf{u}^{j_r}}$ are the deformation and second Piola-Kirchhoff stress tensors associated with the displacement $\mathbf{u}^j = \mathbf{w}^j + \mathbf{v}$.

This variational equation expressed in terms of \mathbf{x}_a coordinates reads

$$\int_{\Omega_a} \sigma_a^{\mathbf{u}^j r} \cdot \left((\mathbf{F}^{\mathbf{w}^j})^T \nabla_a \hat{\mathbf{v}} \right)^s d\Omega_a = \int_{\Gamma_a} \left(p_b^j \right)_a (\mathbf{F}^{\mathbf{w}^j})^{-T} \mathbf{n}_a \cdot \hat{\mathbf{v}} \det \mathbf{F}^{\mathbf{w}^j} d\Gamma_a \quad \forall \hat{\mathbf{v}} \in \mathcal{V}_a, \quad (5.3.12)$$

where $\sigma_a^{\mathbf{u}^j r}$ is written as next

$$\sigma_a^{\mathbf{u}^j r} = \frac{1}{\det \mathbf{F}_a^{\mathbf{v}^r}} \mathbf{F}_a^{\mathbf{v}^r} \left(\mathbf{S}^{\mathbf{u}^j r} \right)_a (\mathbf{F}_a^{\mathbf{v}^r})^T. \quad (5.3.13)$$

Analogously to the procedure followed in the previous section, let now $(\mathbf{F}^r, \mathbf{v})$ be the solution of equations (5.2.12), (5.2.14) and the N_B set of equations defined by (5.3.12). As before, introducing the arbitrary displacement $\tilde{\mathbf{v}} \neq \mathbf{v}$ and the arbitrary deformation tensor $\tilde{\mathbf{F}}^r \neq \mathbf{F}^r$ the following functionals can be defined in \mathcal{V}'_a

- $\mathcal{R}_m = \mathcal{R}_m(\tilde{\mathbf{F}}_a^r, \tilde{\mathbf{v}}_a) \in \mathcal{V}'_a$, associated with the mechanical disequilibrium of the RS field σ_m^r in Ω_m ; i.e., with the residual of equation (5.2.12). This functional is the same as in (5.3.2) but is repeated here for the sake of readability

$$\begin{aligned} \langle \mathcal{R}_m(\tilde{\mathbf{F}}_a^r, \tilde{\mathbf{v}}_a), \hat{\mathbf{v}} \rangle &= \int_{\Omega_a} \sigma_a^r \cdot \left((\mathbf{F}_a^{\tilde{\mathbf{v}}})^{-T} \nabla_a \hat{\mathbf{v}} \right)^s d\Omega_a, \\ &= \int_{\Omega_a} \frac{1}{\det \mathbf{F}_a^{\tilde{\mathbf{v}}^r}} \mathbf{F}_a^{\tilde{\mathbf{v}}^r} (\mathbf{S}^r)_a (\mathbf{F}_a^{\tilde{\mathbf{v}}^r})^T \cdot \left((\mathbf{F}_a^{\tilde{\mathbf{v}}})^{-T} \nabla_a \hat{\mathbf{v}} \right)^s d\Omega_a, \quad \text{with } \hat{\mathbf{v}} \in \mathcal{V}_a \end{aligned} \quad (5.3.14)$$

- The N_B functionals $\mathcal{R}_{b,j} = \mathcal{R}_{b,j}(\tilde{\mathbf{F}}_a^r, \tilde{\mathbf{v}}_a) \in \mathcal{V}'_a$, associated with the mechanical disequilibrium in the known spatial domain Ω_b^j given by the residual of equation (5.3.12). They are defined by

$$\begin{aligned} \langle \mathcal{R}_{b,j}(\tilde{\mathbf{F}}_a^r, \tilde{\mathbf{v}}_a), \hat{\mathbf{v}} \rangle &= \int_{\Omega_a} \frac{1}{\det \mathbf{F}_a^{\tilde{\mathbf{v}}^r}} \mathbf{F}_a^{\tilde{\mathbf{v}}^r} \left(\mathbf{S}^{(\tilde{\mathbf{v}}+\mathbf{w}^j)r} \right)_a (\mathbf{F}_a^{\tilde{\mathbf{v}}^r})^T \cdot \left((\mathbf{F}^{\mathbf{w}^j})^T \nabla_a \hat{\mathbf{v}} \right)^s d\Omega_a \\ &\quad - \int_{\Gamma_a} (p_b)_a \left(\mathbf{F}^{\mathbf{w}^j} \right)^{-T} \mathbf{n}_a \cdot \hat{\mathbf{v}} \det \mathbf{F}^{\mathbf{w}^j} d\Gamma_a, \quad \hat{\mathbf{v}} \in \mathcal{V}_a, \quad i = 1, \dots, N_b \end{aligned} \quad (5.3.15)$$

As in Section 5.3.1, here introduce the virtual power exerted between the generalized residual forces \mathcal{R}_m and \mathcal{R}_b and each i th element of the basis.

$$R_m^i(\tilde{\mathbf{F}}_a^r, \tilde{\mathbf{v}}_a) = \langle \mathcal{R}_m(\tilde{\mathbf{F}}_a^r, \tilde{\mathbf{v}}_a), \Phi_i \rangle, \quad i = 1, 2, \dots \quad (5.3.16)$$

$$R_{b,j}^i(\tilde{\mathbf{F}}_a^r, \tilde{\mathbf{v}}_a) = \langle \mathcal{R}_{b,j}(\tilde{\mathbf{F}}_a^r, \tilde{\mathbf{v}}_a), \Phi_i \rangle, \quad i = 1, 2, \dots \quad j = 1, \dots, N_B \quad (5.3.17)$$

Again, $(\mathbf{F}^r, \mathbf{v})$ is the solution of equations (5.2.12), (5.2.14) and the set of equations defined by (5.3.12) if and only if it makes $R_m^i = R_{b,j}^i = 0$ $i = 1, 2, \dots, j = 1, \dots, N_B$. Then, we introduce the following *cost functional* that characterizes the mechanical imbalance as a function of the RRDs

$$\mathcal{F}(\tilde{\mathbf{F}}_a^r, \tilde{\mathbf{v}}_a) = \frac{\eta_m}{2} \mathbf{R}_m(\tilde{\mathbf{F}}_a^r, \tilde{\mathbf{v}}_a) \cdot \mathbf{R}_m(\tilde{\mathbf{F}}_a^r, \tilde{\mathbf{v}}_a) + \sum_{j=1}^{N_B} \frac{\eta_b^j}{2} \mathbf{R}_{b,j}(\tilde{\mathbf{F}}_a^r, \tilde{\mathbf{v}}_a) \cdot \mathbf{R}_{b,j}(\tilde{\mathbf{F}}_a^r, \tilde{\mathbf{v}}_a), \quad (5.3.18)$$

where η_m and η_b^j are weighting factors corresponding the mechanical imbalances at Ω_m and each Ω_b^j , respectively.

Then, the RRD identification problem can be written in the following variational form: given Ω_a , the N_B configurations Ω_b^j , the N_B displacements fields \mathbf{w}^j , the corresponding inner pressures p_a, p_b^j and the material parameters characterizing the arterial wall constitutive behavior, find $(\tilde{\mathbf{F}}_a^r, \tilde{\mathbf{v}}_a)$ such that

$$\begin{aligned} (\mathbf{F}_a^r, \mathbf{v}_a) &:= \arg \min_{\mathbf{D} \times \text{Kin}_a} \left\{ \mathcal{F} \left(\tilde{\mathbf{F}}_a^r, \tilde{\mathbf{v}}_a \right) \right\} \\ \text{subjected to } &\int_{\Omega_a} \boldsymbol{\sigma}^{\tilde{\mathbf{v}}_a} \cdot \nabla_a^s \hat{\mathbf{v}} \, d\Omega_a - \int_{\Gamma_a} p_a \mathbf{n}_a \cdot \hat{\mathbf{v}} \, d\Gamma_a = 0 \quad \forall \hat{\mathbf{v}} \in \mathcal{V}_a. \end{aligned} \quad (5.3.19)$$

In the problem described above, \mathbf{D} indicates the space of all tensor fields $\tilde{\mathbf{F}}_a^r$ associated with RRDs defined in Ω_a with positive determinant (i.e. $\det \tilde{\mathbf{F}}_a^r > 0$) for any $\mathbf{x}_a \in \Omega_a$.

As shown in Section 5.3.1, a functional \mathcal{J} depending only in $\tilde{\mathbf{F}}_a^r$ can be written if we consider, for a fixed $\tilde{\mathbf{F}}_a^r$, $\tilde{\mathbf{v}}_a = \tilde{\mathbf{v}}_a(\tilde{\mathbf{F}}_a^r)$ the unique solution of equation (5.2.14). \mathcal{J} is defined as

$$\mathcal{J} \left(\tilde{\mathbf{F}}_a^r \right) = \mathcal{F} \left(\tilde{\mathbf{F}}_a^r, \tilde{\mathbf{v}}_a \left(\tilde{\mathbf{F}}_a^r \right) \right), \quad (5.3.20)$$

and problem (5.3.19) can be rewritten as: given Ω_a , the N_B configurations Ω_b^j , the N_B displacements fields \mathbf{w}^j , the corresponding inner pressures p_a, p_b^j and the material parameters characterizing the arterial wall constitutive behavior, find \mathbf{F}_a^r such that

$$\mathbf{F}_a^r := \arg \min_{\mathbf{F}_a^r \in \mathbf{D}} \left\{ \mathcal{J} \left(\tilde{\mathbf{F}}_a^r \right) \right\}. \quad (5.3.21)$$

As $\mathcal{J}(\tilde{\mathbf{F}}_a^r) \geq 0 \quad \forall \tilde{\mathbf{F}}_a^r \in \mathbf{D}$ this problem is well defined, and $\mathcal{J}(\mathbf{F}_a^r) = 0$ if and only if $(\mathbf{F}_a^r, \tilde{\mathbf{v}}_a(\mathbf{F}_a^r)) \in \mathbf{D} \times \text{Kin}_a$ satisfies the mechanical equilibrium equations for Ω_m , Ω_a and Ω_b^j -given by (5.2.12), (5.2.14) and (5.3.10), respectively-.

5.4 Optimization methods

Observe that the RRD characterization problem is completely defined by problem (5.3.21) along with the subsidiary restriction given by (5.2.14), hence leading to a minimization of a highly nonlinear functional (with respect to the unknown variables) subjected to an also nonlinear equality constraint. In order to achieve this minimization two methods are explored in the numerical examples (see Chapter 6), the interior-point algorithm for constrained optimization and the steepest descent method. For the interior-point method we make use of the MATLAB Optimization Toolbox (The MathWorks, 2013) based on the works of Byrd et al (1999, 2000).

For the following presentations, let us consider the base $\mathcal{B}_{\mathbf{D}} = \{\boldsymbol{\omega}_1, \dots, \boldsymbol{\omega}_N\}$ of a finite space \mathbf{D}^h approximating space of RRDs fields \mathbf{D} . Then, an approximation $\mathbf{F}^h \approx \tilde{\mathbf{F}}_a^r$ can be written as a linear combination of the elements of $\mathcal{B}_{\mathbf{D}}$. If \mathbf{x} is a vector containing the coefficients of such linear combination, \mathbf{F}^h can be expressed as

$$\mathbf{F}^h = \mathbf{x} \cdot \mathcal{B}_{\mathbf{D}}, \quad (5.4.1)$$

and using equation (5.3.21) the following minimization problem can be proposed: given Ω_a , Ω_b , \mathbf{w} , the corresponding inner pressures p_a, p_b and the material parameters characterizing the arterial wall constitutive behavior, find $x \in \mathbb{R}^N$ such that

$$\mathbf{x} := \arg \min_{\mathbf{x} \in \mathbb{R}^N} \left\{ \mathcal{J}(\mathbf{x}) \right\}, \quad (5.4.2)$$

where the functional $\mathcal{J}(\mathbf{x}) : \mathbb{R}^N \rightarrow \mathbb{R}$ is defined as $\mathcal{J}(\mathbf{x}) = \mathcal{J}(\mathbf{F}^h)$. Note that, given the vector \mathbf{x} , evaluating $\mathcal{J}(\mathbf{x})$ is a two steps process, involving the solution of the preload mechanical problem corresponding to the equilibrium at Ω_a and the evaluations of the corresponding residuals.

As an example, in a three-dimensional problem, when using a finite element discretization and considering piecewise constant residual deformations, the base $\mathcal{B}_{\mathbf{D}}$ is characterized as follows:

$$\mathcal{B}_{\mathbf{D}} = \{\omega_{ij}^e(\mathbf{x})\}, \quad e = 1, \dots, N_E, \quad i, j = 1, \dots, 3 \quad (5.4.3)$$

where the ω_{ij}^e is

$$\omega_{ij}^e(\mathbf{x}) = \begin{cases} 0, & \mathbf{x} \notin \Omega^e \\ \Phi_{ij}, & \mathbf{x} \in \Omega^e \end{cases}, \quad (5.4.4)$$

where $\Phi_{ij} \in \mathbb{R}^{3 \times 3}$ with ij -th component equal to 1 and null for the rest of the components, e.g.

$$\Phi_{12} = \begin{pmatrix} 0 & 1 & 0 \\ 0 & 0 & 0 \\ 0 & 0 & 0 \end{pmatrix}. \quad (5.4.5)$$

5.4.1 Gradient descent method

Let us consider the following expansion for the functional $\mathcal{J}(\mathbf{x})$ given a perturbation $\delta \mathbf{x}$

$$\mathcal{J}(\mathbf{x} + \delta \mathbf{x}) = \mathcal{J}(\mathbf{x}) + \nabla_x \mathcal{J}(\mathbf{x}) \cdot \delta \mathbf{x} + \mathcal{O}(\delta \mathbf{x}). \quad (5.4.6)$$

Note that, for a sufficiently small $\delta \mathbf{x}$ the high order term $\mathcal{O}(\delta \mathbf{x})$ can be neglected. Considering this, for the minimization process it is proposed to determine $\delta \mathbf{x}$ such that

$$\mathcal{J}(\mathbf{x} + \delta \mathbf{x}) - \mathcal{J}(\mathbf{x}) = \nabla_x \mathcal{J}(\mathbf{x}) \cdot \delta \mathbf{x} \leq 0. \quad (5.4.7)$$

Minding this, we can formulate the following update criterion

$$\delta \mathbf{x} = -\gamma \nabla_x \mathcal{J}(\mathbf{x}), \quad (5.4.8)$$

where γ is a parameter controlling the step size and can be modified along the optimization process. Note that this choice ensures that at each step the functional decreases its value because $-\gamma \nabla_x \mathcal{J}(\mathbf{x}) \cdot \nabla_x \mathcal{J}(\mathbf{x}) \leq 0$. In order to update only the most influential directions (instead of modifying all the components at once) the following modification is introduced

$$\delta x^j = \begin{cases} -\gamma (\nabla_x \mathcal{J}(\mathbf{x}))^j, & \text{if } (\nabla_x \mathcal{J}(\mathbf{x}))^j > \vartheta \max \|\nabla_x \mathcal{J}(\mathbf{x})\| \\ 0, & \text{if } (\nabla_x \mathcal{J}(\mathbf{x}))^j \leq \vartheta \max \|\nabla_x \mathcal{J}(\mathbf{x})\| \end{cases}, \quad (5.4.9)$$

where $\vartheta \in [0, 1]$ is a parameter that defines which directions are considered to be “the most influential”. Additionally, the magnitude of the updates is capped in order to avoid excessive fluctuations on the optimization variables during the minimization process, i.e.

$$\delta x^j = \begin{cases} -\text{sign}(x^j) \Delta^{MAX}, & \text{if } \|\delta x^j\| > \Delta^{MAX} \\ x^j, & \text{if } \|\delta x^j\| \leq \Delta^{MAX} \end{cases}, \quad (5.4.10)$$

where Δ^{MAX} introduces a limit for the magnitude of the updates, observe that this value can be modified along the optimization process.

Considering the convergence tolerance tol^j , the final optimization algorithm takes

the following form

Algorithm 3 Gradient optimization method

1. Set initial value for x .
 2. While $\mathcal{J}(x) > tol^j$ do
 - 2.1 Compute $\nabla_x \mathcal{J}(x)$.
 - 2.2 Update δx^j using (5.4.9)-(5.4.10).
 - 2.3 Solve preload mechanical problem (using 5.5.9).
 - 2.4 Compute residuals \mathcal{R}_m and \mathcal{R}_b using (5.3.16) and (5.3.17).
 - 2.5 Compute functional \mathcal{F} using (5.3.18).
-

It is important to note that for this approach it is necessary to compute the derivative $\nabla_x \mathcal{J}(x)$ (see step 2.1). To do this, two approaches are considered, using finite differences and performing a sensitivity analysis of the functional.

For the first approach, it is a simple straightforward process; however it is important to recall that evaluating $\mathcal{J}(x)$ is a two steps process, in a first step, given $\mathbf{F}^h(x)$, the mechanical equilibrium problem for Ω_a is solved obtaining the displacement field $\mathbf{v}(\mathbf{F}^h)$, next, the residuals \mathbf{R}_m and \mathbf{R}_b are computed.

For the second approach, a complete sensitivity analysis is presented in Section 5.5 considering an approximation for the RRD field using piecewise constant deformations for a finite element discretization.

5.4.2 Interior-point method

For this interior-point method for constrained optimization, consider the smooth functionals $\mathcal{H}(\mathbf{x}) : \mathbb{R}^N \rightarrow \mathbb{R}^L$ and $\mathcal{G}(\mathbf{x}) : \mathbb{R}^N \rightarrow \mathbb{R}^M$ incorporating further constraints on the problem in the following form

$$\mathcal{H}(\mathbf{x}) = \mathbf{0}, \quad \mathcal{G}(\mathbf{x}) \leq \mathbf{0}. \quad (5.4.11)$$

These functionals can introduce different types of nonlinear constraints; in this thesis, for example, they are employed to incorporate restrictions on the determinant of \mathbf{F}^h . Hence, problem (5.4.2) can be re-written adding the presented constraints yielding the constrained optimization problem: given $\Omega_a, \Omega_b, \mathbf{w}$, the corresponding inner pressures p_a, p_b and the material parameters characterizing the arterial wall constitutive behavior, find $x \in \mathbb{R}^N$ such that

$$\begin{aligned} \mathbf{x} &:= \arg \min_{\mathbf{x} \in \mathbb{R}^N} \left\{ \mathcal{J}(\mathbf{x}) \right\}, \\ \text{subjected to } \mathcal{H}(\mathbf{x}) &= \mathbf{0}, \\ \mathcal{G}(\mathbf{x}) &\leq \mathbf{0}. \end{aligned} \quad (5.4.12)$$

The interior-point algorithm (Byrd et al, 2000) is a barrier method in which the sub-problems are solved approximately by a sequential quadratic programming (SQP) iteration within trust-regions. Each barrier subproblem is of the form

$$\begin{aligned} \mathbf{x} &:= \arg \min_{\mathbf{x} \in \mathbb{R}^N} \left\{ \mathcal{J}(\mathbf{x}) \right\} - v \sum_{i=1}^M \ln s_i, \\ \text{subjected to } \mathcal{H}(\mathbf{x}) &= \mathbf{0}, \\ \mathcal{G}(\mathbf{x}) + \mathbf{s} &= \mathbf{0}, \end{aligned} \quad (5.4.13)$$

where $v > 0$ is the penalty parameter and the slack variables \mathbf{s} are assumed to be positive.

The extended Lagrangian form of the barrier subproblem reads

$$\mathcal{L}(\mathbf{x}, \mathbf{s}, \boldsymbol{\chi}_h, \boldsymbol{\chi}_g) = \mathcal{J}(\mathbf{x}) - v \sum_{i=1}^{M_g} \ln s_i + \boldsymbol{\chi}_h \cdot \mathcal{H}(\mathbf{x}) + \boldsymbol{\chi}_g \cdot (\mathcal{G}(\mathbf{x}) + \mathbf{s}) \quad (5.4.14)$$

where $\boldsymbol{\chi}_h \in \mathbb{R}^{M_h}$ and $\boldsymbol{\chi}_g \in \mathbb{R}^{M_g}$ are Lagrange multipliers corresponding to the equality and inequality constraints. At an optimal solution point (\mathbf{x}, \mathbf{s}) it is verified

$$\nabla_{\mathbf{x}} \mathcal{L}(\mathbf{x}, \mathbf{s}, \boldsymbol{\chi}_h, \boldsymbol{\chi}_g) = \nabla_{\mathbf{x}} \mathcal{J}(\mathbf{x}) + \mathcal{A}_h \boldsymbol{\chi}_h + \mathcal{A}_g \boldsymbol{\chi}_g = \mathbf{0} \quad (5.4.15)$$

$$\nabla_{\mathbf{s}} \mathcal{L}(\mathbf{x}, \mathbf{s}, \boldsymbol{\chi}_h, \boldsymbol{\chi}_g) = -v \mathcal{S}^{-1} \mathbf{e} + \boldsymbol{\chi}_g = \mathbf{0} \quad (5.4.16)$$

where \mathcal{A}_h , \mathcal{A}_g , \mathbf{e} , and \mathcal{S} are given by

$$\mathcal{A}_h = (\nabla_{\mathbf{x}} \mathcal{H}_1, \dots, \nabla_{\mathbf{x}} \mathcal{H}_{M_h}) \quad \mathcal{A}_g = (\nabla_{\mathbf{x}} \mathcal{G}_1, \dots, \nabla_{\mathbf{x}} \mathcal{G}_{M_g}) \quad (5.4.17)$$

and

$$e_i = 1 \text{ with } (i = 1, \dots, M_h), \quad \mathcal{S} = \text{diag}(s_1, \dots, s_{M_h}) \quad (5.4.18)$$

where subscripts indicate the number of the corresponding component of the involved vectors.

In order to simplify the presentation the following notation is introduced

$$\mathbf{z} = \begin{pmatrix} \mathbf{x} \\ \mathbf{s} \end{pmatrix}, \quad \mathcal{Q}(\mathbf{z}) = \mathcal{J}(\mathbf{x}) - v \sum_{i=1}^{M_g} \ln s_i, \quad \mathcal{C}(\mathbf{z}) = \begin{pmatrix} \mathcal{H}(\mathbf{x}) \\ \mathcal{G}(\mathbf{x}) + \mathbf{s} \end{pmatrix}, \quad (5.4.19)$$

leading to the following re-expression for problem (5.4.20)

$$\begin{aligned} \mathbf{z} &:= \arg \min_{\mathbf{z} \in \mathbb{R}^{N+M_g}} \left\{ \mathcal{Q}(\mathbf{z}) \right\} \\ &\text{subjected to } \mathcal{C}(\mathbf{z}) = \mathbf{0}, \end{aligned} \quad (5.4.20)$$

Using a SQP approach (Gill et al, 1981) on this problem, the following quadratic program is obtained: for a given \mathbf{z} is, find the trial vector $\mathbf{d} \in \mathbb{R}^{N+M_g}$ such that

$$\begin{aligned} \mathbf{d} &:= \arg \min_{\mathbf{d} \in \mathbb{R}^{N+M_g}} \left\{ \nabla_{\mathbf{z}} \mathcal{Q}(\mathbf{z}) \mathbf{d} + \frac{1}{2} \mathcal{W} \mathbf{d} \cdot \mathbf{d} \right\} \\ &\text{subjected to } \hat{\mathcal{A}}(\mathbf{z}) + \mathcal{C}(\mathbf{z}) = \mathbf{0}, \end{aligned} \quad (5.4.21)$$

with

$$\mathbf{d} = \begin{pmatrix} \mathbf{d}_x \\ \mathbf{d}_s \end{pmatrix}, \quad (5.4.22)$$

and where \mathcal{W} denotes the Hessian matrix of the Lagrangian of the barrier problem (5.4.14) with respect to \mathbf{z} ,

$$\mathcal{W} = \nabla_{\mathbf{z}\mathbf{z}}^2 \mathcal{L} = \begin{pmatrix} \nabla_{\mathbf{x}\mathbf{x}}^2 \mathcal{L} & \mathbf{0} \\ \mathbf{0} & -v \mathcal{S}^{-2} \end{pmatrix}, \quad (5.4.23)$$

and $\hat{\mathcal{A}}$ is the Jacobian related to the constraints functionals \mathcal{C} , given by

$$\hat{\mathcal{A}} = \begin{pmatrix} \mathcal{A}_h & \mathbf{0} \\ \mathcal{A}_g & \mathbf{I} \end{pmatrix}. \quad (5.4.24)$$

In order to facilitate the convergence for cases in which either the initial conditions is distant from the solution or the Hessian matrix \mathcal{W} is not positive definite in the null

space of $\hat{\mathcal{A}}$, a trust region is incorporated for the trial vector as follows

$$\begin{aligned} \mathbf{d} &:= \arg \min_{\mathbf{d} \in \mathbb{R}^{N+M_g}} \left\{ \nabla_{\mathbf{z}} \mathcal{Q}(\mathbf{z}) \mathbf{d} + \frac{1}{2} \mathcal{W} \mathbf{d} \cdot \mathbf{d} \right\} \\ &\text{subjected to } \hat{\mathcal{A}}(\mathbf{z}) \mathbf{d} + \mathcal{C}(\mathbf{z}) = \mathbf{0} \\ &\|\mathbf{d}\|_T \leq \epsilon_T, \end{aligned} \quad (5.4.25)$$

with $\|\cdot\|_T$ indicating an arbitrary norm and $\epsilon_T > 0$ denoting the trust region radius that is updated at every iteration. To avoid incompatibilities between the constraints and the defined trust region (meaning that all possible trial steps \mathbf{d} satisfying constraints lay outside of the trust region) a two step process is followed. First, choosing a contraction parameter $\xi_T \in (0, 1)$ a transversal step is solved finding \mathbf{v} , an approximate solution of

$$\begin{aligned} \mathbf{v} &:= \arg \min_{\mathbf{v} \in \mathbb{R}^{N+M_g}} \left\| \hat{\mathcal{A}}(\mathbf{z}) \mathbf{v} + \mathcal{C}(\mathbf{z}) \right\|_{l^2} \\ &\text{subjected to } \|\mathbf{v}\|_T \leq \xi_T \epsilon_T. \end{aligned} \quad (5.4.26)$$

with $\|\cdot\|_{l^2}$ stands for the vectorial l^2 norm. Note that \mathbf{v} satisfies the proposed constraints and lays within the reduced trust regions. Next, a modification on (5.4.27) is presented to compute \mathbf{d}

$$\begin{aligned} \mathbf{d} &:= \arg \min_{\mathbf{d} \in \mathbb{R}^{N+M_g}} \left\{ \nabla_{\mathbf{z}} \mathcal{Q}(\mathbf{z}) \mathbf{d} + \frac{1}{2} \mathcal{W} \mathbf{d} \cdot \mathbf{d} \right\} \\ &\text{subjected to } \hat{\mathcal{A}}(\mathbf{z}) \mathbf{d} = \hat{\mathcal{A}}(\mathbf{z}) \mathbf{v} \\ &\|\mathbf{d}\|_T \leq \epsilon_T. \end{aligned} \quad (5.4.27)$$

Observe that, for this modified problem both constraints are always consistent since is possible to take $\mathbf{d} = \mathbf{v}$.

Next, the obtained trial step \mathbf{d} is accepted if it provides a sufficient reduction for the following merit function

$$\mathcal{M}(\mathbf{z}, p_c) = \mathcal{Q}(\mathbf{z}) + p_c |\mathcal{C}(\mathbf{z})|, \quad (5.4.28)$$

where p_c is a penalization parameter weighting the influence of the constraints. If this requirement is not met, the trust region ϵ_T is decreased and a new trial step \mathbf{d} is computed. If the step is accepted, the barrier parameter v is decreased and a new barrier problem iterations is initiated. The final structure of the algorithm is outlined next where tol^j is the objective value for the functional in the minimization process, tol^h and tol^g are tolerances for the equality and inequality constraints, and tol^a and tol^c are tolerances related to the barrier subproblems.

It is important to note that the gradient and Hessian of the cost and constraint functionals $\mathcal{J}(x)$, $\mathcal{H}(x)$ and $\mathcal{G}(x)$ are needed for both the computation of the Lagrangian multipliers and the barrier subproblems. We employ the finite differences algorithm included in the MATLAB Optimization Toolbox for the computation of these derivatives, using the BFGS method (Fletcher, 1987) for the Hessian update. For a complete description of the method and its properties the interested reader is encouraged to see Byrd et al (1999, 2000), where details regarding topics such as optimal trust region reduction, the decreasing of the barrier parameters and efficient methods to solve the barrier problem are discussed in depth.

Algorithm 4 Interior-point optimization method

1. Choose initial barrier parameter $v > 0$, set initial state for variables (\mathbf{x}, \mathbf{s}) and Lagrange multipliers λ_h, λ_g
2. While $\mathcal{J}(\mathbf{x}) > tol^j$ or $\mathcal{H}(\mathbf{x}) > tol^h$ or $(\mathcal{G}(\mathbf{x}) + \mathbf{s}) > tol^g$ do
 - 2.1 Define initial ϵ_T, ξ_T and p_c
 - 2.2 While $\mathcal{Q}(\mathbf{z}) > tol^q$ or $\mathcal{C}(\mathbf{z}) > tol^c$ do
 - 2.2.1 Solve transversal problem (5.4.26), obtain v .
 - 2.2.2 Solve modified barrier problem (5.4.27), obtain d .
 - 2.2.3 Evaluate merit function (5.4.28).
 - 2.2.4 If \mathbf{d} is accepted,
 - 2.2.4.1 Set $\mathbf{z} = \mathbf{z} + \mathbf{d}$,
 - 2.2.4.2 Compute Lagrange multipliers using (5.4.15)-(5.4.16).
 - 2.2.4.3 Evaluate $\mathcal{Q}(\mathbf{z})$ and $\mathcal{C}(\mathbf{z})$.
 - else,
 - 2.2.4.4 Decrease ϵ_T and go back to 2.2.1.
 - 2.3 Decrease barrier parameter v .
 - 2.4 Evaluate $\mathcal{J}(\mathbf{x})$, $\mathcal{H}(\mathbf{x})$ and $\mathcal{G}(\mathbf{x})$.

5.5 Sensitivity analysis

In this section, we focus our attention to finding the sensitivity of the functional $\mathcal{J}(\tilde{\mathbf{F}}_a^r)$ with respect to changes in $\tilde{\mathbf{F}}_a^r$. For the sake of simplicity, this calculus will be presented for the three known configurations setting introduced in Section 5.3.1.

Observe that, $\mathcal{J}(\tilde{\mathbf{F}}_a^r)$ can not be written explicitly since the determination of $\check{\mathbf{v}}_a$ is dependent on the solution of equation (5.2.14). As result, the derivative of this functional can not be directly calculated. As a mean to provide an indirect calculation of this derivative a new Lagrangian cost functional is introduced, where the functional dependence between $\check{\mathbf{v}}_a$ and $\tilde{\mathbf{F}}_a^r$ imposed by the equilibrium equation (5.2.14) is removed. This Lagrangian is denoted by \mathcal{L} , and is defined for $(\mathbf{F}_a^{r*}, \mathbf{v}_a^*, \boldsymbol{\chi}^*) \in \mathbf{D} \times \text{Kin}_a \times \mathcal{V}_a$ as follows

$$\mathcal{L}(\mathbf{F}_a^{r*}, \mathbf{v}_a^*, \boldsymbol{\chi}^*) = \mathcal{F}(\mathbf{F}_a^{r*}, \mathbf{v}_a^*) + \int_{\Omega_a} \boldsymbol{\sigma}^{\mathbf{v}^* r} \cdot \nabla_a^s \boldsymbol{\chi}^* d\Omega_a - \int_{\Gamma_a} p_a \mathbf{n}_a \cdot \boldsymbol{\chi}^* d\Gamma_a. \quad (5.5.1)$$

Moreover, evaluating the cost functionals at $(\mathbf{F}_a^r, \check{\mathbf{v}}_a)$ yields

$$\mathcal{L}(\mathbf{F}_a^r, \mathbf{v}_a, \boldsymbol{\chi}^*) = \mathcal{F}(\mathbf{F}_a^r, \mathbf{v}_a) = \mathcal{J}(\mathbf{F}_a^r) \quad \forall \boldsymbol{\chi}^* \in \mathcal{V}_a. \quad (5.5.2)$$

Furthermore, as it is well known, the Gâteaux derivate of \mathcal{J} with respect to \mathbf{F}_a^{r*} evaluated at \mathbf{F}_a^r is given by the derivative of \mathcal{L} with respect to the same \mathbf{F}_a^{r*} evaluated at the point $(\mathbf{F}_a^r, \mathbf{v}_a, \boldsymbol{\chi}_{\text{adj}})$, where $\boldsymbol{\chi}_{\text{adj}}$ is the solution of the adjoint equation associated to \mathcal{L} . In compact notation, the above statement can be written as

$$\left\langle \frac{\partial \mathcal{J}}{\partial \mathbf{F}_a^{r*}}, \delta \tilde{\mathbf{F}}_a^r \right\rangle_{\mathbf{F}_a^r} = \left\langle \frac{\partial \mathcal{L}}{\partial \mathbf{F}_a^{r*}}, \delta \tilde{\mathbf{F}}_a^r \right\rangle_{(\mathbf{F}_a^r, \check{\mathbf{v}}_a, \boldsymbol{\chi}_{\text{adj}})}, \quad (5.5.3)$$

where, as said, $\check{\mathbf{v}}_a$ is the solution of equation (5.2.14), i.e. the solution of the following variational equation

$$\left\langle \frac{\partial \mathcal{L}}{\partial \boldsymbol{\chi}^*}, \hat{\boldsymbol{\chi}} \right\rangle = 0 \quad \forall \hat{\boldsymbol{\chi}} \in \mathcal{V}_a, \quad (5.5.4)$$

and χ_{adj} is the solution of the adjoint variational equation

$$\left\langle \frac{\partial \mathcal{L}}{\partial \mathbf{v}_a^*}, \hat{\mathbf{v}}_a \right\rangle_{\hat{\mathbf{v}}_a} = 0 \quad \forall \hat{\mathbf{v}}_a \in \mathcal{V}_a \quad (5.5.5)$$

where the notation $\left\langle \frac{\partial \mathcal{M}}{\partial \mathbf{a}}, \mathbf{b} \right\rangle_{\mathbf{c}}$ denotes the Gâteaux derivative of the functional \mathcal{M} with respect to $\mathbf{a} = \mathbf{c} + \tau \mathbf{b}$ in the direction given by \mathbf{b} and evaluated at point \mathbf{c} , i.e.

$$\left\langle \frac{\partial \mathcal{M}}{\partial \mathbf{c}}, \mathbf{b} \right\rangle_{\mathbf{c}} = \left. \frac{d}{d\tau} \mathcal{M}(\dots, \mathbf{c} + \tau \mathbf{b}, \dots) \right|_{\tau=0}. \quad (5.5.6)$$

Introducing the approximation presented in Section 5.4, $\mathbf{F}^h \approx \mathbf{F}_a^r$, and recalling that

$$\mathcal{J}(\mathbf{x}) = \mathcal{J}(\mathbf{F}^h), \quad (5.5.7)$$

it is straightforward to observe that this sensitivity analysis allows us to compute the gradient $\nabla_{\mathbf{x}} \mathcal{J}(\mathbf{x})$ required for the gradient descent method (see Section 5.4.1) since

$$\nabla_{\mathbf{x}} \mathcal{J}(\mathbf{x}) = \left\langle \frac{\partial \mathcal{J}}{\partial \mathbf{F}^h}, \delta \mathbf{F}^h \right\rangle \frac{\partial \mathbf{F}^h}{\partial \mathbf{x}} = \left\langle \frac{\partial \mathcal{J}}{\partial \mathbf{F}^h}, \delta \mathbf{F}^h \right\rangle \mathcal{B}_{\mathbf{D}}. \quad (5.5.8)$$

5.5.1 Direct problem

As detailed in the above procedure, the first problem that we need to tackle is related to equation (5.5.4). The problem setting is the following: Given the equilibrium configuration Ω_a , the inner blood pressure p_a acting on the boundary Γ_a and an estimate of the RRD field, say $\tilde{\mathbf{F}}_a^r$, find $\check{\mathbf{v}}_a \in \text{Kin}_a$ such that

$$\left\langle \frac{\partial \mathcal{L}}{\partial \chi^*}, \hat{\chi} \right\rangle = \int_{\Omega_a} \boldsymbol{\sigma}^{\check{\mathbf{v}}r} \cdot \nabla_a^s \hat{\chi} d\Omega_a - \int_{\Gamma_a} p_a \mathbf{n}_a \cdot \hat{\chi} d\Gamma_a = 0 \quad \forall \hat{\chi} \in \mathcal{V}_a, \quad (5.5.9)$$

where $\boldsymbol{\sigma}^{\check{\mathbf{v}}r}$ is defined as

$$\boldsymbol{\sigma}^{\check{\mathbf{v}}r} = \frac{1}{\det \mathbf{F}_a^{\check{\mathbf{v}}r}} \mathbf{F}_a^{\check{\mathbf{v}}r} (\mathbf{S}^{\check{\mathbf{v}}r})_a (\mathbf{F}_a^{\check{\mathbf{v}}r})^T. \quad (5.5.10)$$

By solving this problem, for a given estimate $\tilde{\mathbf{F}}_a^r$, the displacement field $\check{\mathbf{v}}_a$ mapping the known configuration Ω_a from an estimate of the material domain, say $\tilde{\Omega}_m$, is obtained. The above variational equation can be linearized through a Newton-Raphson scheme, leading to the following linear problem: Given $\check{\mathbf{v}}_a$, the displacement field at the previous Newton-Raphson iteration (iteration index omitted in the notation for the sake of clarity), along with the problem data $(\Omega_a, p_a, \tilde{\mathbf{F}}_a^r)$, find $\delta \check{\mathbf{v}}_a \in \mathcal{V}_a$ such that

$$\int_{\Omega_a} \left\langle \frac{\partial \boldsymbol{\sigma}^{\check{\mathbf{v}}r}}{\partial \check{\mathbf{v}}_a}, \delta \check{\mathbf{v}}_a \right\rangle \cdot \nabla_a^s \hat{\chi} d\Omega_a = \int_{\Omega_a} \boldsymbol{\sigma}^{\check{\mathbf{v}}r} \cdot \nabla_a^s \hat{\chi} d\Omega_a - \int_{\Gamma_a} p_a \mathbf{n}_a \cdot \hat{\chi} d\Gamma_a \quad \forall \hat{\chi} \in \mathcal{V}_a, \quad (5.5.11)$$

where $\left\langle \frac{\partial \boldsymbol{\sigma}^{\check{\mathbf{v}}r}}{\partial \check{\mathbf{v}}_a}, \delta \check{\mathbf{v}}_a \right\rangle$ is defined as

$$\begin{aligned} \left\langle \frac{\partial \boldsymbol{\sigma}^{\check{\mathbf{v}}r}}{\partial \check{\mathbf{v}}_a}, \delta \check{\mathbf{v}}_a \right\rangle &= - ((\mathbf{F}_a^{\check{\mathbf{v}}})^T \cdot \nabla \delta \check{\mathbf{v}}_a) \boldsymbol{\sigma}^{\check{\mathbf{v}}r} + 2 (\mathbf{F}_a^{\check{\mathbf{v}}} \nabla \delta \check{\mathbf{v}}_a \boldsymbol{\sigma}^{\check{\mathbf{v}}r})^s \\ &+ \frac{2}{\det \mathbf{F}_a^{\check{\mathbf{v}}r}} \mathbf{F}_a^{\check{\mathbf{v}}r} \left[\left(\frac{\partial \mathbf{S}^{\check{\mathbf{v}}r}}{\partial \mathbf{C}^{\check{\mathbf{v}}r}} \right)_a \left((\mathbf{F}_a^{\check{\mathbf{v}}r})^T (\mathbf{F}_a^{\check{\mathbf{v}}} \nabla \delta \check{\mathbf{v}}_a \mathbf{F}_a^{\check{\mathbf{v}}r}) \right)^s \right] (\mathbf{F}_a^{\check{\mathbf{v}}r})^T \end{aligned} \quad (5.5.12)$$

This problem is usually referred to as a *preload problem* and it is extensively discussed in

Section 2.2.

5.5.2 Adjoint problem

Once $\check{\mathbf{v}}_a$ is obtained from the direct problem (5.5.9), we are ready to solve the adjoint problem (see equation (5.5.5)). The adjoint problem is defined as follows: Given $\tilde{\mathbf{F}}_a^r, p_a, \check{\mathbf{v}}_a$ and Ω_a , find χ_{adj} such that

$$\left\langle \frac{\partial \mathcal{L}}{\partial \mathbf{v}_a^*}, \hat{\mathbf{v}}_a \right\rangle \Big|_{\check{\mathbf{v}}_a} = \left\langle \frac{\partial \mathcal{F}}{\partial \mathbf{v}_a^*}, \hat{\mathbf{v}}_a \right\rangle \Big|_{\check{\mathbf{v}}_a} + \int_{\Omega_a} \left\langle \frac{\partial \boldsymbol{\sigma}_a^{\check{\mathbf{v}}r}}{\partial \mathbf{v}_a^*}, \hat{\mathbf{v}}_a \right\rangle \cdot \nabla_a \chi_{\text{adj}} d\Omega_a = 0 \quad \forall \hat{\mathbf{v}}_a \in \mathcal{V}_a, \quad (5.5.13)$$

where we highlight that $\boldsymbol{\sigma}_a^{\check{\mathbf{v}}r}$ is the Cauchy Stress due to the displacement field $\check{\mathbf{v}}_a$ combined with the residual deformations and

$$\left\langle \frac{\partial \mathcal{F}}{\partial \mathbf{v}_a^*}, \hat{\mathbf{v}}_a \right\rangle \Big|_{\check{\mathbf{v}}_a} = \eta_m \mathbf{R}_m \cdot \left\langle \frac{\partial \mathbf{R}_m}{\partial \mathbf{v}_a^*}, \hat{\mathbf{v}}_a \right\rangle \Big|_{\check{\mathbf{v}}_a} + \eta_b \mathbf{R}_b \cdot \left\langle \frac{\partial \mathbf{R}_b}{\partial \mathbf{v}_a^*}, \hat{\mathbf{v}}_a \right\rangle \Big|_{\check{\mathbf{v}}_a}. \quad (5.5.14)$$

The derivative of the components of the residual vectors in terms of the elements of the basis are obtained through

$$\left\langle \frac{\partial R_m^i}{\partial \mathbf{v}_a^*}, \hat{\mathbf{v}}_a \right\rangle \Big|_{\check{\mathbf{v}}_a} = \int_{\Omega_a} \left\langle \frac{\partial \boldsymbol{\sigma}_a^r}{\partial \mathbf{v}_a^*}, \hat{\mathbf{v}}_a \right\rangle \Big|_{\check{\mathbf{v}}_a} \cdot \left((\mathbf{F}_a^{\check{\mathbf{v}}})^{-T} \nabla_a \Phi_i \right)^s d\Omega_a - \int_{\Omega_a} \boldsymbol{\sigma}_a^r \cdot \left((\nabla_a \hat{\mathbf{v}}_a)^T \nabla_a \Phi_i \right)^s d\Omega_a, \quad (5.5.15)$$

and

$$\left\langle \frac{\partial R_b^i}{\partial \mathbf{v}_a^*}, \hat{\mathbf{v}}_a \right\rangle \Big|_{\check{\mathbf{v}}_a} = \int_{\Omega_a} \left\langle \frac{\partial \boldsymbol{\sigma}_a^{(\check{\mathbf{v}}+\mathbf{w})r}}{\partial \mathbf{v}_a^*}, \hat{\mathbf{v}}_a \right\rangle \Big|_{\check{\mathbf{v}}_a} \cdot \left((\mathbf{F}^{\mathbf{w}})^T \nabla_a \Phi_i \right)^s d\Omega_a. \quad (5.5.16)$$

Moreover, analogously to equation (5.5.12) for the derivative of the stress field in the Ω_a configuration, the detailed expressions for $\left\langle \frac{\partial \boldsymbol{\sigma}_a^r}{\partial \mathbf{v}_a^*}, \hat{\mathbf{v}}_a \right\rangle \Big|_{\check{\mathbf{v}}_a}$ and $\left\langle \frac{\partial \boldsymbol{\sigma}_a^{(\check{\mathbf{v}}+\mathbf{w})r}}{\partial \mathbf{v}_a^*}, \hat{\mathbf{v}}_a \right\rangle \Big|_{\check{\mathbf{v}}_a}$ can be written as

$$\left\langle \frac{\partial \boldsymbol{\sigma}_a^r}{\partial \mathbf{v}_a^*}, \hat{\mathbf{v}}_a \right\rangle \Big|_{\check{\mathbf{v}}_a} = - \left((\mathbf{F}_a^{\check{\mathbf{v}}})^T \cdot \nabla_a \hat{\mathbf{v}}_a \right) \boldsymbol{\sigma}_a^r + 2 \left(\mathbf{F}_a^{\check{\mathbf{v}}} \nabla_a \hat{\mathbf{v}}_a \boldsymbol{\sigma}_a^r \right)^s, \quad (5.5.17)$$

and

$$\begin{aligned} \left\langle \frac{\partial \boldsymbol{\sigma}_a^{(\check{\mathbf{v}}+\mathbf{w})r}}{\partial \mathbf{v}_a^*}, \hat{\mathbf{v}}_a \right\rangle &= - \left((\mathbf{F}_a^{\check{\mathbf{v}}})^T \cdot \nabla_a \hat{\mathbf{v}}_a \right) \boldsymbol{\sigma}_a^{(\check{\mathbf{v}}+\mathbf{w})r} + 2 \left(\mathbf{F}_a^{\check{\mathbf{v}}} \nabla_a \hat{\mathbf{v}}_a \boldsymbol{\sigma}_a^{(\check{\mathbf{v}}+\mathbf{w})r} \right)^s \\ &\quad + \frac{2}{\det \mathbf{F}_a^{\check{\mathbf{v}}r}} \mathbf{F}_a^{\check{\mathbf{v}}r} \left[\left(\frac{\partial \mathbf{S}^{\check{\mathbf{v}}r}}{\partial \mathbf{C}^{\check{\mathbf{v}}r}} \right)_a \left((\mathbf{F}_a^{(\check{\mathbf{v}}+\mathbf{w})r})^T (\mathbf{F}_a^{\mathbf{w}} \mathbf{F}_a^{\check{\mathbf{v}}} \nabla_a \hat{\mathbf{v}}_a \mathbf{F}_a^{\check{\mathbf{v}}r}) \right)^s \right] (\mathbf{F}_a^{\check{\mathbf{v}}r})^T \end{aligned} \quad (5.5.18)$$

5.5.3 Sensitivity evaluation

As a last step, the sensitivity of the Lagrangian cost functional with respect to changes in $\tilde{\mathbf{F}}^r$, denoted as $\delta\tilde{\mathbf{F}}_a^r$, is evaluated as

$$\begin{aligned} \left\langle \frac{\partial \mathcal{L}}{\partial \mathbf{F}_a^{r*}}, \delta\tilde{\mathbf{F}}_a^r \right\rangle \Big|_{\tilde{\mathbf{F}}_a^r, \tilde{\mathbf{v}}_a, \mathcal{X}_{\text{adj}}} &= \eta_m \mathbf{R}_m \cdot \left\langle \frac{\partial \mathbf{R}_m}{\partial \mathbf{F}_a^{r*}}, \delta\tilde{\mathbf{F}}_a^r \right\rangle \Big|_{\tilde{\mathbf{F}}_a^r, \tilde{\mathbf{v}}_a} + \eta_b \mathbf{R}_b \cdot \left\langle \frac{\partial \mathbf{R}_b}{\partial \mathbf{F}_a^{r*}}, \delta\tilde{\mathbf{F}}_a^r \right\rangle \Big|_{\tilde{\mathbf{F}}_a^r, \tilde{\mathbf{v}}_a} \\ &+ \int_{\Omega_a} \left\langle \frac{\partial \boldsymbol{\sigma}_a^{\tilde{\mathbf{v}}r}}{\partial \mathbf{F}_a^{r*}}, \delta\tilde{\mathbf{F}}_a^r \right\rangle \Big|_{\tilde{\mathbf{F}}_a^r, \tilde{\mathbf{v}}_a} \delta\tilde{\mathbf{F}}_a^r \cdot \nabla_a \mathcal{X}_{\text{adj}} d\Omega_a, \end{aligned} \quad (5.5.19)$$

where components $\left\langle \frac{\partial R_m^i}{\partial \mathbf{F}_a^{r*}}, \delta\tilde{\mathbf{F}}_a^r \right\rangle \Big|_{\tilde{\mathbf{F}}_a^r, \tilde{\mathbf{v}}_a}$, $\left\langle \frac{\partial R_b^i}{\partial \mathbf{F}_a^{r*}}, \delta\tilde{\mathbf{F}}_a^r \right\rangle \Big|_{\tilde{\mathbf{F}}_a^r, \tilde{\mathbf{v}}_a}$ are given by

$$\left\langle \frac{\partial R_m^i}{\partial \mathbf{F}_a^{r*}}, \delta\tilde{\mathbf{F}}_a^r \right\rangle \Big|_{\tilde{\mathbf{F}}_a^r, \tilde{\mathbf{v}}_a} = \int_{\Omega_a} \left\langle \frac{\partial \boldsymbol{\sigma}_a^r}{\partial \mathbf{F}_a^{r*}}, \delta\tilde{\mathbf{F}}_a^r \right\rangle \Big|_{\tilde{\mathbf{F}}_a^r, \tilde{\mathbf{v}}_a} \cdot \left((\mathbf{F}_a^{\tilde{\mathbf{v}}})^{-T} \nabla_a \Phi_i \right)^s d\Omega_a, \quad (5.5.20)$$

and

$$\left\langle \frac{\partial R_b^i}{\partial \mathbf{F}_a^{r*}}, \delta\tilde{\mathbf{F}}_a^r \right\rangle \Big|_{\tilde{\mathbf{F}}_a^r, \tilde{\mathbf{v}}_a} = \int_{\Omega_a} \left\langle \frac{\partial \boldsymbol{\sigma}_a^{(\tilde{\mathbf{v}}+\mathbf{w})r}}{\partial \mathbf{F}_a^{r*}}, \delta\tilde{\mathbf{F}}_a^r \right\rangle \Big|_{\tilde{\mathbf{F}}_a^r, \tilde{\mathbf{v}}_a} \cdot \left((\mathbf{F}^{\mathbf{w}})^T \nabla_a \Phi_i \right)^s d\Omega_a. \quad (5.5.21)$$

Observe that the Gâteaux derivative of the stress fields with $\left\langle \frac{\partial \boldsymbol{\sigma}_a^{\tilde{\mathbf{v}}r}}{\partial \mathbf{F}_a^{r*}}, \delta\mathbf{F}_a^r \right\rangle$ is given by

$$\begin{aligned} \left\langle \frac{\partial \boldsymbol{\sigma}_a^{\tilde{\mathbf{v}}r}}{\partial \mathbf{F}_a^{r*}}, \delta\mathbf{F}_a^r \right\rangle \Big|_{\tilde{\mathbf{F}}_a^r, \tilde{\mathbf{v}}_a} &= - \left((\mathbf{F}_a^r)^{-T} \cdot \delta\mathbf{F}_a^r \right) \boldsymbol{\sigma}_a^{\tilde{\mathbf{v}}r} + 2 \left[\left(\mathbf{F}_a^{\tilde{\mathbf{v}}} \delta\mathbf{F}_a^r (\mathbf{F}_a^{\tilde{\mathbf{v}}r})^{-1} \right) \boldsymbol{\sigma}_a^{\tilde{\mathbf{v}}r} \right]^s + \\ &\frac{2}{\det \mathbf{F}_a^{\tilde{\mathbf{v}}r}} \mathbf{F}_a^{\tilde{\mathbf{v}}r} \left\{ \left(\frac{\partial \mathbf{S}^{\tilde{\mathbf{v}}r}}{\partial \mathbf{C}^{\tilde{\mathbf{v}}r}} \right)_a \left((\mathbf{F}_a^{\tilde{\mathbf{v}}r})^T \mathbf{F}_a^{\tilde{\mathbf{v}}} \delta\mathbf{F}_a^r \right)^s \right\} (\mathbf{F}_a^{\tilde{\mathbf{v}}r})^T \end{aligned} \quad (5.5.22)$$

and the corresponding expressions for $\left\langle \frac{\partial \boldsymbol{\sigma}_a^r}{\partial \mathbf{F}_a^{r*}}, \delta\tilde{\mathbf{F}}_a^r \right\rangle \Big|_{\tilde{\mathbf{F}}_a^r, \tilde{\mathbf{v}}_a}$ and $\left\langle \frac{\partial \boldsymbol{\sigma}_a^{\tilde{\mathbf{v}}r}}{\partial \mathbf{F}_a^{r*}}, \delta\tilde{\mathbf{F}}_a^r \right\rangle \Big|_{\tilde{\mathbf{F}}_a^r, \tilde{\mathbf{v}}_a}$ can be obtained analogously as

$$\begin{aligned} \left\langle \frac{\partial \boldsymbol{\sigma}_a^r}{\partial \mathbf{F}_a^{r*}}, \delta\mathbf{F}_a^r \right\rangle \Big|_{\tilde{\mathbf{F}}_a^r, \tilde{\mathbf{v}}_a} &= - \left((\mathbf{F}_a^r)^{-T} \cdot \delta\mathbf{F}_a^r \right) \boldsymbol{\sigma}_a^r + 2 \left[\left(\mathbf{F}_a^{\tilde{\mathbf{v}}} \delta\mathbf{F}_a^r (\mathbf{F}_a^{\tilde{\mathbf{v}}r})^{-1} \right) \boldsymbol{\sigma}_a^r \right]^s + \\ &\frac{2}{\det \mathbf{F}_a^{\tilde{\mathbf{v}}r}} \mathbf{F}_a^{\tilde{\mathbf{v}}r} \left[\left(\frac{\partial \mathbf{S}^r}{\partial \mathbf{C}^r} \right)_a \left((\mathbf{F}_a^r)^T \delta\mathbf{F}_a^r \right)^s \right] (\mathbf{F}_a^{\tilde{\mathbf{v}}r})^T \end{aligned} \quad (5.5.23)$$

and

$$\begin{aligned} \left\langle \frac{\partial \boldsymbol{\sigma}_a^{(\tilde{\mathbf{v}}+\mathbf{w})r}}{\partial \mathbf{F}_a^{r*}}, \delta\mathbf{F}_a^r \right\rangle \Big|_{\tilde{\mathbf{F}}_a^r, \tilde{\mathbf{v}}_a} &= - \left((\mathbf{F}_a^r)^{-T} \cdot \delta\mathbf{F}_a^r \right) \boldsymbol{\sigma}_a^{(\tilde{\mathbf{v}}+\mathbf{w})r} + 2 \left[\left(\mathbf{F}_a^{\tilde{\mathbf{v}}} \delta\mathbf{F}_a^r (\mathbf{F}_a^{\tilde{\mathbf{v}}r})^{-1} \right) \boldsymbol{\sigma}_a^{(\tilde{\mathbf{v}}+\mathbf{w})r} \right]^s + \\ &\frac{2}{\det \mathbf{F}_a^{\tilde{\mathbf{v}}r}} \mathbf{F}_a^{\tilde{\mathbf{v}}r} \left[\left(\frac{\partial \mathbf{S}^{(\tilde{\mathbf{v}}+\mathbf{w})r}}{\partial \mathbf{C}^{(\tilde{\mathbf{v}}+\mathbf{w})r}} \right)_a \left((\mathbf{F}_a^{(\tilde{\mathbf{v}}+\mathbf{w})r})^T \mathbf{F}_a^{(\tilde{\mathbf{v}}+\mathbf{w})} \delta\mathbf{F}_a^r \right)^s \right] (\mathbf{F}_a^{\tilde{\mathbf{v}}r})^T. \end{aligned} \quad (5.5.24)$$

Let us now consider that the domain Ω_a is subdivided into N_E non-overlapping sub-domains Ω_a^e ($e = 1, \dots, N_E$). If a piecewise constant approximation for the deformation field in such sub-domains is employed, we can analyze the derivative of the Lagrangian for changes in the local residual deformation $\mathbf{F}_a^{r,e}$ as

$$\left\langle \frac{\partial \mathcal{L}}{\partial \mathbf{F}_a^{r*}}, \delta\mathbf{F}_a^{r,e} \right\rangle \Big|_{\tilde{\mathbf{F}}_a^r, \tilde{\mathbf{v}}_a, \mathcal{X}_{\text{adj}}} = \eta_m \mathbf{T}_m \cdot \delta\mathbf{F}_a^{r,e} + \eta_s \mathbf{T}_b \cdot \delta\mathbf{F}_a^{r,e} + \mathbf{T}_a \cdot \delta\mathbf{F}_a^{r,e}, \quad (5.5.25)$$

where

$$\mathbf{T}_m \cdot \delta \mathbf{F}_a^{r,e} = \mathbf{R}_m \cdot \left\langle \frac{\partial \mathbf{R}_m}{\partial \mathbf{F}_a^{r*}}, \delta \mathbf{F}_a^{r,e} \right\rangle \Big|_{\tilde{\mathbf{F}}_a^r, \tilde{\mathbf{v}}_a}, \quad (5.5.26)$$

$$\mathbf{T}_b \cdot \delta \mathbf{F}_a^{r,e} = \mathbf{R}_b \cdot \left\langle \frac{\partial \mathbf{R}_b}{\partial \mathbf{F}_a^{r*}}, \delta \mathbf{F}_a^{r,e} \right\rangle \Big|_{\tilde{\mathbf{F}}_a^r, \tilde{\mathbf{v}}_a}, \quad (5.5.27)$$

and

$$\mathbf{T}_a \cdot \delta \mathbf{F}_a^{r,e} = \int_{\Omega_a} \left\langle \frac{\partial \boldsymbol{\sigma}_a^{\check{v}r}}{\partial \mathbf{F}_a^{r*}}, \delta \mathbf{F}_a^{r,e} \right\rangle \Big|_{\tilde{\mathbf{F}}_a^r, \tilde{\mathbf{v}}_a} \cdot \nabla_a \chi_{\text{adj}} d\Omega_a. \quad (5.5.28)$$

Performing some mathematical manipulations, the form of tensors \mathbf{T}_m , \mathbf{T}_b and \mathbf{T}_a can be found as

$$\begin{aligned} \mathbf{T}_a &= \int_{\Omega_a^e} (\mathbf{F}_a^r)^{-T} (\boldsymbol{\sigma}_a^{\check{v}r} \cdot \nabla_a \chi_{\text{adj}}) d\Omega_a^e \\ &+ \int_{\Omega_a^e} 2 (\mathbf{F}_a^{\check{v}})^T (\nabla_a \chi_{\text{adj}}) \boldsymbol{\sigma}_a^{\check{v}r} (\mathbf{F}_a^{\check{v}})^{-T} d\Omega_a^e \\ &+ \left\{ \int_{\Omega_a^e} \frac{1}{\det \mathbf{F}_a^{\check{v}r}} \left[\left(\frac{\partial \mathbf{S}^{\check{v}r}}{\partial \mathbf{C}^{\check{v}r}} \right)_a^T \left((\mathbf{F}_a^{\check{v}r})^T (\nabla_a \chi_{\text{adj}}) \mathbf{F}_a^{\check{v}r} \right) \right] (\mathbf{F}_a^{\check{v}r})^T \mathbf{F}_a^{\check{v}} d\Omega_a^e \right\}^T \\ &+ \int_{\Omega_a^e} (\mathbf{F}_a^{\check{v}})^T \mathbf{F}_a^{\check{v}r} \frac{1}{\det \mathbf{F}_a^{\check{v}r}} \left[\left(\frac{\partial \mathbf{S}^{\check{v}r}}{\partial \mathbf{C}^{\check{v}r}} \right)_a^T \left((\mathbf{F}_a^{\check{v}r})^T (\nabla_a \chi_{\text{adj}}) \mathbf{F}_a^{\check{v}r} \right) \right] d\Omega_a^e, \quad (5.5.29) \end{aligned}$$

$$\begin{aligned} \mathbf{T}_m &= \sum_i -R_m^i \int_{\Omega_a^e} (\mathbf{F}_a^r)^{-T} \left(\boldsymbol{\sigma}_a^r \cdot \left((\mathbf{F}_a^{\check{v}})^{-T} \nabla_a \Phi_i \right)^s \right) d\Omega_a^e \\ &+ \sum_i R_m^i \int_{\Omega_a^e} 2 (\mathbf{F}_a^{\check{v}})^T \left((\mathbf{F}_a^{\check{v}})^{-T} \nabla_a \Phi_i \right)^s \boldsymbol{\sigma}_a^r (\mathbf{F}_a^{\check{v}})^{-T} d\Omega_a^e \\ &+ \sum_i R_m^i \left\{ \int_{\Omega_a^e} \left[\left(\frac{\partial \mathbf{S}^r}{\partial \mathbf{C}^r} \right)_a^T \frac{1}{\det \mathbf{F}_a^{\check{v}r}} (\mathbf{F}_a^{\check{v}r})^T \left((\mathbf{F}_a^{\check{v}})^{-T} \nabla_a \Phi_i \right)^s \mathbf{F}_a^{\check{v}r} \right] (\mathbf{F}_a^r)^T d\Omega_a^e \right\}^T \\ &+ \sum_i R_m^i \int_{\Omega_a^e} \mathbf{F}_a^r \left[\left(\frac{\partial \mathbf{S}^r}{\partial \mathbf{C}^r} \right)_a^T \frac{1}{\det \mathbf{F}_a^{\check{v}r}} (\mathbf{F}_a^{\check{v}r})^T \left((\mathbf{F}_a^{\check{v}})^{-T} \nabla_a \Phi_i \right)^s \mathbf{F}_a^{\check{v}r} \right] d\Omega_a^e, \quad (5.5.30) \end{aligned}$$

and

$$\begin{aligned} \mathbf{T}_b &= \sum_i -R_b^i \int_{\Omega_a^e} (\mathbf{F}_a^r)^{-1} \left(\left((\mathbf{F}^{\mathbf{w}})^T \nabla_a \Phi_i \right)^s \cdot \boldsymbol{\sigma}_a^{(\check{v}+\mathbf{w})r} \right) d\Omega_a^e \\ &+ \sum_i R_b^i \int_{\Omega_a^e} 2 (\mathbf{F}_a^{\check{v}})^T \left((\mathbf{F}^{\mathbf{w}})^T \nabla_a \Phi_i \right)^s \boldsymbol{\sigma}_a^{(\check{v}+\mathbf{w})r} (\mathbf{F}_a^{\check{v}})^{-T} d\Omega_a^e \\ &+ \sum_i R_b^i \left\{ \int_{\Omega_a^e} \left[\left(\frac{\partial \mathbf{S}^{(\check{v}+\mathbf{w})r}}{\partial \mathbf{C}^{(\check{v}+\mathbf{w})r}} \right)_a^T \frac{1}{\det \mathbf{F}_a^{\check{v}r}} (\mathbf{F}_a^{\check{v}r})^T \left((\mathbf{F}^{\mathbf{w}})^T \nabla_a \Phi_i \right)^s \mathbf{F}_a^{\check{v}r} \right] (\mathbf{F}_a^{(\check{v}+\mathbf{w})r})^T \mathbf{F}_a^{(\check{v}+\mathbf{w})} d\Omega_a^e \right\}^T, \\ &+ \sum_i R_b^i \int_{\Omega_a^e} (\mathbf{F}_a^{(\check{v}+\mathbf{w})})^T \mathbf{F}_a^{(\check{v}+\mathbf{w})r} \left[\left(\frac{\partial \mathbf{S}^{(\check{v}+\mathbf{w})r}}{\partial \mathbf{C}^{(\check{v}+\mathbf{w})r}} \right)_a^T \frac{1}{\det \mathbf{F}_a^{\check{v}r}} (\mathbf{F}_a^{\check{v}r})^T \left((\mathbf{F}^{\mathbf{w}})^T \nabla_a \Phi_i \right)^s \mathbf{F}_a^{\check{v}r} \right] d\Omega_a^e \quad (5.5.31) \end{aligned}$$

where \mathcal{T} denotes the following transpose operation for an arbitrary fourth order tensor

$$\mathbb{D} = \mathbf{a} \otimes \mathbf{b} \otimes \mathbf{c} \otimes \mathbf{d}: \quad \mathbb{D}^{\mathcal{T}} = (\mathbf{a} \otimes \mathbf{b} \otimes \mathbf{c} \otimes \mathbf{d})^{\mathcal{T}} = \mathbf{c} \otimes \mathbf{d} \otimes \mathbf{a} \otimes \mathbf{b} \quad (5.5.32)$$

Chapter 6

Characterization of residual deformations: numerical examples

6.1 Introduction

In this chapter three numerical examples are presented, proposed to assess the potentiality of the mechanical setting developed in Chapter 5 for the in-vivo characterization of residual recoverable deformations in hemodynamic problems.

The first example is a very simple problem consisting of a 1D clamped bar with a force applied at the midpoint of its domain. This basic case embraces all the necessary ingredients to test the proposed methodology and, because the analytical solution is available, it stands as a conceptual proof of the viability of the approach. As a second example, the characterization of RRDs is performed in an homogeneous thick-walled cylinder subjected to uniform internal pressure. The residual deformation field is defined ad-hoc, and a Neo-Hookean constitutive behavior is considered for the material response. The third example, also featuring a cylindrical geometry, is closer to a more realistic setting of an arterial wall, whose anatomical structures resemble that of an abdominal aorta. For this case, three layers of transversely isotropic hyperelastic material are considered. Moreover, the residual deformation field identified by the optimization problem is based on experimental measures available in the specialized literature.

For each problems, the reference geometry along with the material parameters and objective residual deformations to be identified are described. Next, the forward mechanical problem for different loading states is solved, and, the setting of known configurations is constructed. As last step, the result of the optimization problem is presented. At this point, it is important to remark that we will consider as known input data the material parameters. However, since the measurement of these parameters can be a sensitive issue, and since the reference configuration depends upon the definition of such material properties, having thus an impact in the entire identification process, a sensitivity analysis to explore the relative importance of the different material parameters should be considered as a next step in this research line.

6.2 Clamped bar (1D)

6.2.1 Problem description

In this example, a one-dimensional bar clamped at both ends is considered where the material configuration, Ω_m , occupies the interval $[0, 2L]$. A concentrated load f is applied at the material point P located in the center of Ω_m , i.e. at $x_m = L$. A representative scheme of the problem is presented in Figure 6.1. The constitutive behavior of the material

is characterized by a linear relation between the second Piola-Kirchhoff stress and the deformation tensor, i.e.

$$S = k(F - 1), \quad (6.2.1)$$

where k represents an elastic parameter and $F = F^v F^r$ is the total deformation gradient resulting from the composition between a deformation field due to the displacement v and the RRDs F^r . In particular, due to the kinematical setting of this problem (see Section 6.2.2), a constant field F^r is admitted for the material configuration Ω_m . Consequently, through (6.2.1), S^r is also a constant field.

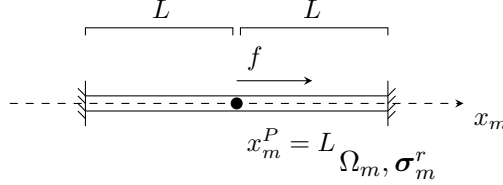


Figure 6.1: Setting for the clamped bar 1D problem

When the concentrated load f is applied, the analytical solution for the equilibrium problem can be easily obtained, resulting in a piece-wise linear displacement field v_m , which presents null values at both ends and maximum at the point $x_m = L$, i.e.

$$v_m(x_m) = \begin{cases} \frac{f}{2(kF^r + S^r)F^r} x_m, & x_m \in [0, L], \\ \frac{f}{2(kF^r + S^r)F^r} (2L - x_m), & x_m \in [L, 2L]. \end{cases} \quad (6.2.2)$$

We introduce the notation $v^f = v(x_m)$ to emphasize the fact that this displacement field is associated to the load f .

From the above displacement field, the equilibrium configuration $\Omega_f = [0, 2L]$ is defined. Observe that despite the fact that Ω_m and Ω_f occupy the same region in the Euclidean space, points in $[0, 2L]$ correspond to different material points depending which configuration is considered. Furthermore, the solution of the problem belongs to the space spanned by linear finite elements shape functions, provided a node is placed at the point $x_m = L$. Thus, despite its simplicity, a validation of the variational framework with an exact solution can be performed with this problem.

6.2.2 Kinematics for the 1D bar

The linear space of kinematically admissible displacements is given by

$$\mathcal{U}_m = \{u_m(x_m) \in H^1(0, 2L) \mid u_m(0) = u_m(2L) = 0\}, \quad (6.2.3)$$

Then, admissible variations of the displacement are in the very same space, that is $\mathcal{U}_m \equiv \mathcal{V}_m$.

For this particular case, the material and spatial expressions for the deformation gradients are given by

$$F^u = 1 + \frac{\partial u_m}{\partial x_m}, \quad (F^u)_a^{-1} = 1 - \frac{\partial u_a}{\partial x_a}, \quad (6.2.4)$$

where $u_m(x_m)$ and $u_a(x_a)$, and the relations (5.2.13), (5.2.15) and (5.2.20) between material

and spatial gradients can be written as

$$\left(\frac{\partial u_m}{\partial x_m}\right)_a = \frac{\frac{\partial u_a}{\partial x_a}}{1 - \frac{\partial u_a}{\partial x_a}}, \quad \left(\frac{\partial u_a}{\partial x_a}\right)_m = \frac{\frac{\partial u_m}{\partial x_m}}{1 + \frac{\partial u_m}{\partial x_m}}. \quad (6.2.5)$$

Furthermore, as $\det F^v = F^v$, the relations between the second Piola-Kirchhoff stress and Cauchy stress are simplified to

$$\sigma_a^{vr} = S_a^{vr} F_a^{vr}, \quad \sigma_a^{(v+w)r} = S_a^{(v+w)r} F_a^{vr}, \quad \sigma_a^r = S_a^r F_a^{vr}. \quad (6.2.6)$$

6.2.2.1 Manufactured solution: data and target

The geometry and constitutive behavior are defined by $L = 1$, $k = 1.0 \cdot 10^3$. The value characterizing the constant RRD field is set as $F^r = 1.01$, defining the objective for the identification problem. Note that, from (6.2.1), the constant RS field is given by $S^r = 10$.

Let us now consider that two equilibrium configurations, Ω_a and Ω_b , are known ($N_B = 1$). $\Omega_a = [0, 2L]$ is at equilibrium with the concentrated load $f_a = 100$. Then, using (6.2.2), we obtain the load application point for the force f_a as $x_a^{f_a} = L + v^{f_a} = 1.0485$. Similarly, $\Omega_b = [0, 2L]$ is at equilibrium with $f_b = 200$, applied at $x_b^{f_b} = L + v^{f_b} = 1.0970$.

Finally, the displacement field w , mapping points from Ω_a into Ω_b is given by

$$w(x_a) = \begin{cases} 0.0485 \frac{x_a}{1.0485}, & x_a \in [0, 1.0485], \\ 0.0485 \frac{x_a - 2L}{1.0485 - 2L}, & x_a \in [1.0485, 2L]. \end{cases} \quad (6.2.7)$$

Summarizing, the data for the identification problem is given by: the constitutive equation (6.2.1), the constitutive parameter k , $\Omega_a = [0, 2L]$, f_a (with its application point $x_a^{f_a}$), $\Omega_b = [0, 2L]$, and f_b (with its application point $x_b^{f_b}$). Additionally, the target RRD field for the identification problem is the constant field $F^r = 1.01$. As consequence, the associated fields S^r , $v = v^{f_a}$ and $u = v^{f_b}$ are also defined as targets.

6.2.3 Optimization problem setting

For the numerical approximation we employ linear finite elements for the displacement field and for the Lagrange multiplier. Then, in this discrete setting, constant RRDs within each element are considered. The spatial discretization is performed in the Ω_a configuration using only two finite elements, considering three nodes: two located at both ends (constrained due to the boundary conditions), and one placed at the load application point P .

The gradient descent method described by Algorithm 3 (see Section 5.4.1) is used. The functional gradient is computed through the sensitivity analysis approach introduced in Section 5.5, which is here particularized for the presented kinematic setting. The initial guess is set as $\tilde{F}_a^r|_{\Omega_a} = 1$, the tolerance for the convergence criterion is $tol^j = 10^{-3}$, and the parameters controlling the update at each iteration are $\gamma = 10^{-7}$, $\Delta^{MAX} = 10^{-2}$ and $\vartheta = 0$. Also, the weighting factors have been set to $\eta_m = 1$ and $\eta_b = 100$. This choice is made considering that with the proposed initial condition any material configuration will be at equilibrium, and, as consequence, at such point the algorithm should be mainly driven by the mechanical imbalance occurring in Ω_b configuration.

Preload problem

As stated in Section 5.5.1, equation (5.5.4) leads to a preload problem, for which the detailed expression is provided by equation (5.5.9). Let us consider the basis $\mathcal{B}_{\mathcal{V}} = \phi_i, i = 1, 2, 3$ for the space \mathcal{V}_a^h approximating \mathcal{V}_a , where $\phi_i(x_a), i = 1, 2, 3$ are the finite element shape functions for the three node discretization proposed.

Then, the preload problem can be particularized for the presented 1D kinematics as follows: Given the equilibrium configuration Ω_a , the applied force f_a , and an estimate of the RD field, say \tilde{F}_a^r , find $\tilde{v}_a \in \mathcal{V}_a \equiv \mathcal{U}_m$ such that

$$\int_{\Omega_a} k \left(F_a^{\tilde{v}} \tilde{F}_a^r - 1 \right) F_a^{\tilde{v}} \tilde{F}_a^r \frac{\partial \hat{v}_a}{\partial x_a} d\Omega_a = f_a \hat{v}_a (L + v_m(L)) \quad \forall \hat{v}_a \in \mathcal{V}_a^h. \quad (6.2.8)$$

Hence, considering the following derivation

$$\left\langle \frac{\partial \left(F_a^{\tilde{v}} \tilde{F}_a^r - 1 \right) F_a^{\tilde{v}} \tilde{F}_a^r}{\partial \tilde{v}_a}, \delta \tilde{v}_a \right\rangle = \left[2 (F_a^{\tilde{v}r})^2 F^{\tilde{v}} - F_a^{\tilde{v}} F_a^{\tilde{v}r} \right] \frac{\partial \delta \tilde{v}_a}{\partial x_a}, \quad (6.2.9)$$

the consistent linearized problem now reads: Given $\Omega_a, f_a, \tilde{F}_a^r$ and \tilde{v}_a (displacement value for the previous Newton-Raphson iteration, index omitted) find $\delta \tilde{v}_a$ such that

$$\begin{aligned} \int_{\Omega_a} k \left[2 (F_a^{\tilde{v}r})^2 F^{\tilde{v}} - F_a^{\tilde{v}} F_a^{\tilde{v}r} \right] \frac{\partial \delta \tilde{v}_a}{\partial x_a} \frac{\partial \hat{v}_a}{\partial x_a} d\Omega_a = \\ \int_{\Omega_a} k \left(F_a^{\tilde{v}} \tilde{F}_a^r - 1 \right) F_a^{\tilde{v}} \tilde{F}_a^r \frac{\partial \hat{v}_a}{\partial x_a} d\Omega_a - f_a \hat{v}_a (L + v_m(L)) \quad \forall \hat{v}_a \in \mathcal{V}_a^h. \end{aligned} \quad (6.2.10)$$

Adjoint problem

Similarly, for the presented 1D kinematics, the adjoint problem introduced by equation (5.5.13) can be written as: Given $\tilde{F}_a^r, f_a, \tilde{v}_a, \tilde{\Omega}_m$ and Ω_a , find χ_{adj} such that

$$\begin{aligned} \sum_{i=1}^3 \eta_m \left[\int_{\Omega_a} \left\langle \frac{\partial \sigma_a^r}{\partial v_a^*}, \hat{v}_a \right\rangle \Big|_{\tilde{v}_a} (\tilde{F}^{\tilde{v}})^{-1} - \sigma_a^r \frac{\partial \hat{v}_a}{\partial x_a} \right] \frac{\partial \phi_i}{\partial x_a} d\Omega_a \Big|_{\tilde{F}_a^r, \tilde{v}_a} + \\ \sum_{i=1}^3 \eta_b \left[\int_{\Omega_a} \left\langle \frac{\partial \sigma_a^{(\tilde{v}+w)r}}{\partial v_a^*}, \hat{v}_a \right\rangle \Big|_{\tilde{v}_a} \left(1 + \frac{\partial w}{\partial x_a} \right) \frac{\partial \phi_i}{\partial x_a} d\Omega_a \right] \Big|_{\tilde{F}_a^r, \tilde{v}_a} + \\ + \int_{\Omega_a} \left\langle \frac{\partial \sigma_a^{\tilde{v}r}}{\partial v_a^*}, \hat{v}_a \right\rangle \Big|_{\tilde{v}_a} \frac{\partial \chi_{\text{adj}}}{\partial x_a} d\Omega_a = 0 \quad \forall \hat{v}_a \in \mathcal{V}_a. \end{aligned} \quad (6.2.11)$$

Note that the particularized expressions for the residuals associated to Ω_m and Ω_b configurations are given by

$$\begin{aligned} R_m^i \Big|_{\tilde{F}_a^r, \tilde{v}_a} = \langle \mathcal{R}_m \left(\tilde{F}_a^r, \tilde{v}_a \right), \phi_i \rangle = \\ \int_{\Omega_a} k \left(\tilde{F}_a^r - 1 \right) \left(1 - \frac{\partial \tilde{v}_a}{\partial x_a} \right) \frac{\partial \phi_i}{\partial x_a} d\Omega_a \quad i = 1, 2, 3, \end{aligned} \quad (6.2.12)$$

$$\begin{aligned} R_b^i \Big|_{\tilde{F}_a^r, \tilde{v}_a} = \langle \mathcal{R}_b \left(\tilde{F}_a^r, \tilde{v}_a \right), \phi_i \rangle = \\ \int_{\Omega_a} k \left(\tilde{F}_a^{(\tilde{v}+w)r} - 1 \right) \left(1 + \frac{\partial w}{\partial x_a} \right) \frac{\partial \phi_i}{\partial x_a} d\Omega_a - f_b \phi_i(x_a^p) \quad i = 1, 2, 3. \end{aligned} \quad (6.2.13)$$

where $\tilde{F}^{(\tilde{v}+w)r} = \tilde{F}^{(\tilde{v}+w)} \tilde{F}_a^r$ is the deformation tensor related to the displacement $(\tilde{v}_a + w_a)$ combined with the residual deformation \tilde{F}_a^r . The derivatives of the Cauchy stress for this 1D setting read

$$\left\langle \frac{\partial \sigma_a^r}{\partial v_a^*}, \hat{v}_a \right\rangle \Big|_{\tilde{v}_a} = k \left(\tilde{F}_a^r - 1 \right) \tilde{F}^{\tilde{v}} \frac{\partial \tilde{v}_a}{\partial x_a} F^{\tilde{v}r}, \quad (6.2.14)$$

$$\left\langle \frac{\partial \sigma_a^{\tilde{v}r}}{\partial v_a^*}, \hat{v}_a \right\rangle \Big|_{\tilde{v}_a} = k \left(2\tilde{F}_a^{\tilde{v}r} - 1 \right) \tilde{F}_a^{\tilde{v}} \frac{\partial \tilde{v}_a}{\partial x_a} \tilde{F}_a^{\tilde{v}r}, \quad (6.2.15)$$

$$\left\langle \frac{\partial \sigma_a^{(\tilde{v}+w)r}}{\partial v_a^*}, \hat{v}_a \right\rangle \Big|_{\tilde{v}_a} = k \left(2\tilde{F}_a^{(\tilde{v}+w)r} - 1 \right) \tilde{F}_a^{\tilde{v}} \frac{\partial \tilde{v}_a}{\partial x_a} \tilde{F}_a^{\tilde{v}r}. \quad (6.2.16)$$

Sensitivity evaluation and update of \tilde{F}_a^r

Once \tilde{v}_a is obtained by iterative solving equation (6.2.8) through the linear form (6.2.10), and after computing χ_{adj} from (6.2.11), it is possible to evaluate the sensitivity of the Lagrangian with respect to changes in \tilde{F}_a^r . Particularly, as we are using piece-wise constant approximation for this RRD field, we are interested in the sensitivity of the functional with respect to local changes in each element. For the following developments we will denote as Ω_a^e and $\tilde{F}_{a,e}^r$ the corresponding element values.

Recalling equation (5.5.19), the form of the sensitivity for the present problem reads

$$\begin{aligned} \left\langle \frac{\partial \mathcal{L}}{\partial \tilde{F}_a^{r,*}}, \hat{F}_a^r \right\rangle \Big|_{\tilde{v}_a, \chi_{\text{adj}}} &= \int_{\Omega_a} k \left(2\tilde{F}_a^{\tilde{v}r} \tilde{F}_a^{\tilde{v}} - F_a^{\tilde{v}} \right) \hat{F}_a^r \frac{\partial \chi_{\text{adj}}}{\partial x_a} d\Omega_a \\ &+ \sum_{i=1}^3 \eta_m \left(\int_{\Omega_a} k \left(2\tilde{F}_a^r \tilde{F}_a^{\tilde{v}} - \tilde{F}_a^{\tilde{v}} \right) \hat{F}_a^r \left(1 - \frac{\partial \tilde{v}_a}{\partial x_a} \right) \frac{\partial \phi_i}{\partial x_a} d\Omega_a \right) R_m^i \Big|_{\tilde{F}_a^r, \tilde{v}_a} \\ &+ \sum_{i=1}^3 \eta_b \left(\int_{\Omega_a} k \left(2\tilde{F}_a^{(\tilde{v}+w)r} \tilde{F}_a^{\tilde{v}} - \tilde{F}_a^{\tilde{v}} \right) \hat{F}_a^r \left(1 + \frac{\partial w_a}{\partial x_a} \right) \frac{\partial \phi_i}{\partial x_a} d\Omega_a \right) R_b^i \Big|_{\tilde{F}_a^r, \tilde{v}_a} \end{aligned} \quad (6.2.17)$$

where $\tilde{F}_a^{\tilde{v}}$ is the deformation tensor arising due to the displacement field \tilde{v}_a and $\tilde{F}_a^{(\tilde{v}+w)r}$ the corresponding to the displacement field $(\tilde{v}_a + w_a)$ combined with the residual deformation tensor \tilde{F}_a^r .

In particular, for changes at element level, it is

$$\begin{aligned} \left\langle \frac{\partial \mathcal{L}}{\partial \tilde{F}_a^{r,*}}, \hat{F}_a^{r,e} \right\rangle \Big|_{\tilde{v}_a, \chi_{\text{adj}}} &= \hat{F}_a^{r,e} |\Omega_a^e| k \left(2\tilde{F}_a^{\tilde{v}r,e} \tilde{F}_a^{\tilde{v},e} - \tilde{F}_a^{\tilde{v},e} \right) \frac{\partial \chi_{\text{adj}}}{\partial x_a} \\ &+ \hat{F}_a^{r,e} \sum_{i=1,2} \eta_m |\Omega_a^e| k \left(2\tilde{F}_a^{r,e} \tilde{F}_a^{\tilde{v}r,e} - \tilde{F}_a^{\tilde{v},e} \right) \left(1 - \frac{\partial v_a}{\partial x_a} \right) \frac{\partial \phi_l^i}{\partial x_a} \langle \mathcal{R}_m, \phi_l^i \rangle \\ &+ \hat{F}_a^{r,e} \sum_{i=1,2} \eta_b |\Omega_a^e| k \left(2\tilde{F}_a^{(\tilde{v}+w)r,e} \tilde{F}_a^{\tilde{v}r,e} - \tilde{F}_a^{\tilde{v},e} \right) \left(1 + \frac{\partial w_a}{\partial x_a} \right) \frac{\partial \phi_l^i}{\partial x_a} \langle \mathcal{R}_b, \phi_l^i \rangle, \end{aligned} \quad (6.2.18)$$

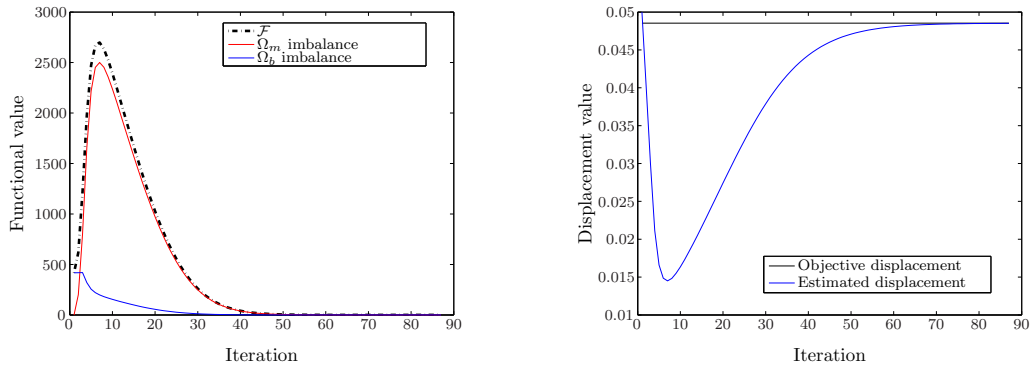
where $|\Omega_a^e|$ stands for the element size, and ϕ_l^i , $i = 1, 2$ for the local shape functions associated with the finite element (one for each node).

For this example the weighting factors have been set to $\eta_m = 1$ and $\eta_b = 100$. This choice is made considering that with the proposed initial condition any material configuration will be at equilibrium, and, as consequence, at such point the algorithm should be mainly driven by the imbalance of Ω_b configuration. The parameters controlling the optimization process are $\Delta^{MAX} = 10^{-2}$, $\gamma = 10^{-7}$ and $tol^j = 10^{-3}$.

6.2.3.1 Results

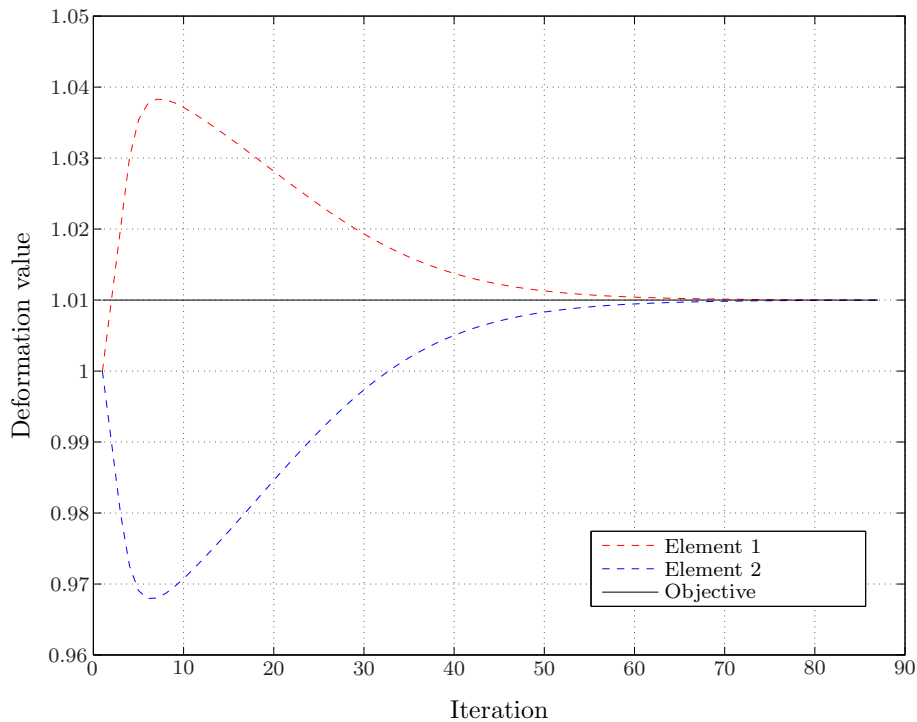
Figure 6.2 summarizes the results. In Figure 6.2(a), the behavior of the descending algorithm through the minimization of the cost functional is shown. In Figure 6.2(b) it is clearly observed that the material configuration is recovered when convergence is achieved. Finally, Figure 6.2(c) displays the convergence of the RRD values for both finite elements.

The results of this basic example show the viability and potentiality of the proposed mechanical setting for the estimation of RRDs (and the corresponding RSs) along with the zero-load (material) configuration.



(a) Minimization of cost functional \mathcal{F} and its components related to the mechanical imbalance at Ω_m and Ω_b . Shown values for the cost functional and components already include weighting factors $\eta_m = 1$ and $\eta_b = 100$.

(b) Convergence of the resulting displacement for the load application point P through the minimization process. The objective value is $v_m(L) = 0.0485$.



(c) Convergence of RRDs at each finite element. Target value for both elements (black horizontal line) and values estimated at each element through the minimization process (red and blue).

Figure 6.2: Clamped bar example: results summary for the RRD characterization problem

6.3 Thick-walled cylinder

6.3.1 Problem description

In this example the identification of RRDs is performed in an homogeneous thick-walled cylinder subjected to uniform internal pressure. Considering such conditions, the problem possess rotational symmetry. As in the previous example, a complete setting will be manufactured from a known material configuration at equilibrium with a known RS field (originated by predefined RRDs), resulting in three known configurations Ω_a, Ω_b^1 and Ω_b^2 at equilibrium with corresponding inner pressures p_a, p_b^1 and p_b^2 as dictated by the mechanical equilibrium problem. Next, considering $\Omega_a, \Omega_b^1, \Omega_b^2$ and $\mathbf{w}^1, \mathbf{w}^2$ given as input data, the RRD identification problem is addressed.

The spatial discretization comprises 1D linear finite elements shape functions to span the space for the radial displacement field. Then, piece-wise constant RRDs are considered within each finite element.

6.3.2 Rotational symmetry kinematics

Consider a cylindrical material configuration, with points defined by

$$\mathbf{x}_m = (\rho_m, \theta_m, z_m), \quad (6.3.1)$$

where as usual, ρ_m denotes the radial coordinate, θ_m the angular coordinate, and z_m the axial coordinate. Considering the rotational symmetry, shear stresses and the tangential component of the displacement field must be null. Moreover, we also consider a pipe of fixed length and constant strains in the axial direction. Thence, the space kinematically admissible displacements is given by

$$\mathcal{U}_m = \{\mathbf{u} = (u^\rho, 0, 0) \mid u^\rho \in \mathcal{U}_m^\rho\}, \quad (6.3.2)$$

with

$$\mathcal{U}_m^\rho = \left\{ u^\rho \in H^1(\Omega_m) \mid \frac{\partial u^\rho}{\partial \theta_m} \Big|_{\Omega_m} = \frac{\partial u^\rho}{\partial z_m} \Big|_{\Omega_m} = 0 \right\}. \quad (6.3.3)$$

Furthermore, for an element $\mathbf{u} \in \mathcal{U}_m$ its gradient takes the following form

$$\nabla_m \mathbf{u} = \begin{bmatrix} \frac{\partial u^\rho}{\partial \rho_m} & 0 & 0 \\ 0 & \frac{u^\rho}{\rho_m} & 0 \\ 0 & 0 & 0 \end{bmatrix}. \quad (6.3.4)$$

6.3.3 Model parameters

For this example we define the material configuration through the inner and external radii $r_i = 5.6$ mm and $r_e = 7$ mm, respectively. An homogeneous compressible Neo-Hookean material is considered, for which the strain energy function is given by

$$\Psi = C_1 (\bar{I}_1 - 3) + k_{vol} (J - 1)^2, \quad (6.3.5)$$

where $\bar{I}_1 = J^{-2/3} \text{tr}(\mathbf{C})$, $J = \det \mathbf{F}$ are invariants of the deformation gradient tensor, and C_1 and k_{vol} represent shear and bulk material parameters, respectively. In this example, the constitutive parameters are set to $C_1 = 15$ kPa (inspired by the values for the media layer presented in (Holzapfel and Ogden, 2010a)) and $k_{vol} = 1490$ kPa, (corresponding to a Poisson coefficient $\nu = 0.49$) while the pressures acting at known spatial configurations Ω_a, Ω_b^1 and Ω_b^2 are considered to be $p_a = 1$ kPa, $p_b^1 = 2$ kPa and $p_b^2 = 3$ kPa, respectively.

6.3.4 Residual stresses

Due to rotational symmetry, any compatible RS field defined in the cylinder presents two characteristics, (a) null shear stresses, and (b) the stress field is only function of the radial coordinate. As a consequence, the RS field can be expressed as

$$\boldsymbol{\sigma}_m^r(\rho_m) = \begin{bmatrix} \sigma_{m,\rho}^r(\rho_m) & 0 & 0 \\ 0 & \sigma_{m,\theta}^r(\rho_m) & 0 \\ 0 & 0 & \sigma_{m,z}^r(\rho_m) \end{bmatrix}. \quad (6.3.6)$$

The associated Euler-Lagrange equation that expresses the mechanical equilibrium in the material configuration (derived from (5.2.10)) reads

$$\frac{\partial \sigma_{m,\rho}^r}{\partial \rho_m} + \frac{1}{\rho_m} (\sigma_{m,\rho}^r - \sigma_{m,\theta}^r) = 0, \quad \rho_m \in (r_i, r_e) \quad (6.3.7)$$

that has to be satisfied in Ω_m along with the homogeneous Neumann boundary conditions $\sigma_{m,\rho}^r(r_i) = \sigma_{m,\rho}^r(r_e) = 0$. Note that, as expressed before, the equilibrium is independent from $\sigma_{m,z}^r$.

For this problem we postulate a linear relation between the circumferential residual stress and the radius, i.e. $\sigma_{m,\theta}^r = a\rho_m + b$. Thus, to satisfy equation (6.3.6), $\sigma_{m,\rho}^r$ takes the following form

$$\sigma_{m,\rho}^r = \frac{a}{2}\rho_m + b + \frac{c}{\rho_m}, \quad (6.3.8)$$

with

$$c = \frac{a}{2}r_e r_i, \quad b = -\frac{a}{2}(r_e + r_i). \quad (6.3.9)$$

Observe that the complete residual stress can be defined by setting only one parameter, in this case $a = -4 \cdot 10^7$.

6.3.5 Residual deformations: Internal Power Approximation (IPA)

Observe that the adopted RS and the associated RRDs are not piece-wise constant fields (as occurred in the previous example). Since the approximation of such fields is performed using element-wise constant functions (consistent with the interpolation for deformation and stress fields, when linear finite elements are considered for the approximation of the displacement field), it is expected that our variational framework will not be able to provide an exact identification of the above fields.

The proposed cost functional is based on the residuals of the equilibrium equations. These equations are expressed through the Virtual Power Principle, i.e. the balance between internal and external virtual powers. Taking into account that the RRD field (through its associated RS field) only takes part in the internal power definition, it is natural to expect that our methodology, which at the discrete level considers element-wise constant RRD fields, will retrieve an element-wise constant field that will exert an internal power equivalent to the one exerted by the proposed nonlinear continuous RRD field, that is, for each elemental domain is satisfied the following equation

$$\int_{\Omega_m^e} \boldsymbol{\sigma}_m^r(\mathbf{F}_m^r) \cdot \nabla_m^s \hat{\mathbf{v}}_i d\Omega_m^e = \bar{\boldsymbol{\sigma}}_m^{r,e}(\mathbf{F}_m^{r,e}) \cdot \int_{\Omega_m^e} \nabla_m^s \hat{\mathbf{v}}_i d\Omega_m^e \quad \forall \hat{\mathbf{v}}_i \in \mathcal{V}_m, \quad (6.3.10)$$

where Ω_m^e denotes de finite element domain and $\bar{\boldsymbol{\sigma}}_m^{r,e}$ the constant RS field induced by the constant RRDs $\mathbf{F}_m^{r,e}$ in such domain.

Note that these constraints are defined for each function basis of \mathcal{V}_m . Moreover, in order to obtain a solution of this equation, the same number of test functions $\hat{\mathbf{v}}_i$ as

non-zero values in $\boldsymbol{\sigma}_m^r$ are needed. For this case, only two test functions are necessary. Hence, linear finite element functions associated with each element are considered for this purpose, leading to

$$\int_{r_i}^{r_e} \left(\sigma_{m,\rho}^r(\mathbf{F}_m^r) \frac{\partial \psi_m^i}{\partial \rho_m} + \sigma_{m,\theta}^r(\mathbf{F}_m^r) \frac{\psi_m^i}{\rho_m} \right) \rho_m d\rho_m = \bar{\sigma}_{m,\rho}^{r,e}(\mathbf{F}_m^{r,e}) \int_{r_i}^{r_e} \frac{\partial \psi_m^i}{\partial \rho_m} \rho_m d\rho_m + \bar{\sigma}_{m,\theta}^{r,e}(\mathbf{F}_m^{r,e}) \int_{r_i}^{r_e} \frac{\psi_m^i}{\rho_m} \rho_m d\rho_m \quad i = 1, 2, \quad (6.3.11)$$

where ψ_m^i represents the local finite element functions associated with the finite element nodes.

As next step, we recall that, for a hyperelastic material, the Cauchy stress tensor due to $\mathbf{F}_m^{r,e}$ deformations is obtained as

$$\boldsymbol{\sigma}_m^{r,e} = \frac{1}{J} \mathbf{F}_m^{r,e} \left(\frac{\partial \Psi}{\partial \mathbf{C}^{r,e}} \right)_m (\mathbf{F}_m^{r,e})^T, \quad (6.3.12)$$

where $\mathbf{C}^{r,e} = (\mathbf{F}_m^{r,e})^T \mathbf{F}_m^{r,e}$, $J = \det \mathbf{F}_m^{r,e}$ and Ψ denotes the strain energy function characterizing the material behavior, in this case given by (6.3.5). For this particular case, (6.3.12) can be written as

$$\boldsymbol{\sigma}_m^{r,e} = \frac{2}{J} C_1 (\mathbf{C}^{r,e})^T - \frac{2}{3J} C_1 \bar{I}_1 \mathbf{I} + 2k_{vol} (J - 1) \mathbf{I}. \quad (6.3.13)$$

Then, to define the piece-wise constant RRDs $\mathbf{F}_m^{r,e}$, we propose a diagonal form for the tensor,

$$\mathbf{F}^r(\rho_m) = \begin{pmatrix} \lambda_\rho(\rho_m) & 0 & 0 \\ 0 & \lambda_\theta(\rho_m) & 0 \\ 0 & 0 & \lambda_z(\rho_m) \end{pmatrix}, \quad (6.3.14)$$

where λ_i , $i = \rho, \theta, z$ are the principal stretches. Also, the RRDs are considered to be incompressible, adding the following constraint

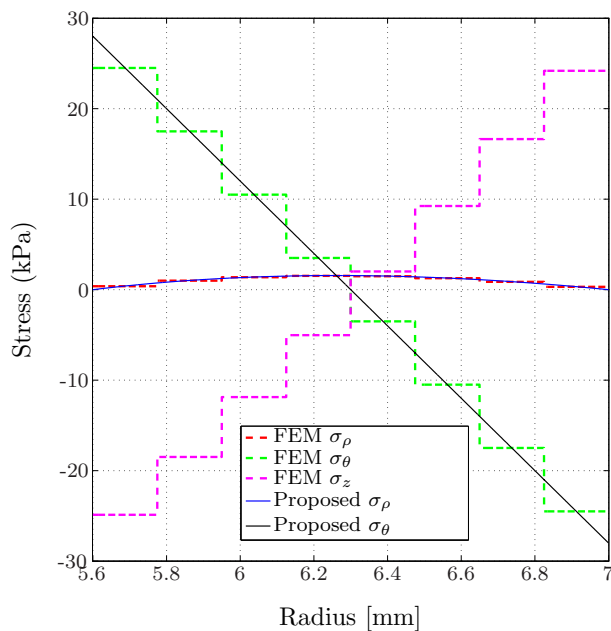
$$\det \mathbf{F}_m^{r,e} = 1. \quad (6.3.15)$$

Finally, considering equations (6.3.11), (6.3.13) and the incompressibility constraint, the RRD tensor is determined from the following nonlinear system of equations

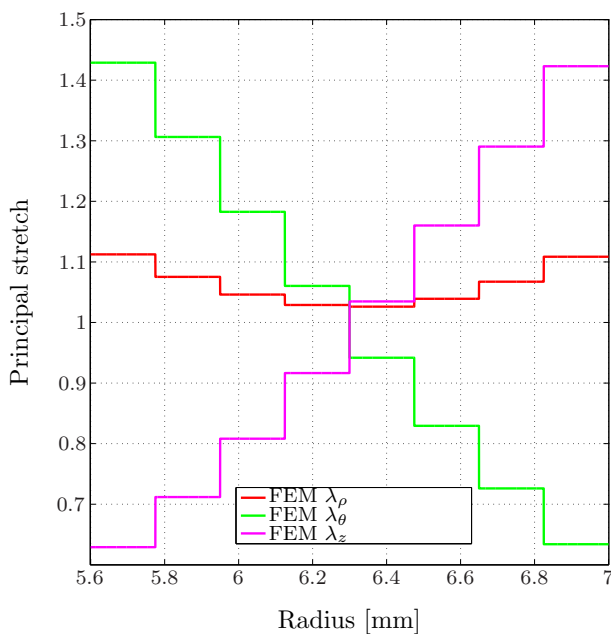
$$\begin{cases} \bar{\sigma}_{m,\rho}^{r,e} = \left(\frac{2}{J} C_1 (\mathbf{C}^{r,e})^T - \frac{2}{3J} C_1 \bar{I}_1 \mathbf{I} + 2k_{vol} (J - 1) \mathbf{I} \right)_{\rho\rho}, \\ \bar{\sigma}_{m,\theta}^{r,e} = \left(\frac{2}{J} C_1 (\mathbf{C}^{r,e})^T - \frac{2}{3J} C_1 \bar{I}_1 \mathbf{I} + 2k_{vol} (J - 1) \mathbf{I} \right)_{\theta\theta}, \\ \det \mathbf{F}_m^{r,e} = 1. \end{cases} \quad (6.3.16)$$

Hereafter, the described element-wise constant field will be referred to as the *Internal Power Approximation* (IPA) of the corresponding RRD field. In particular, Figure 6.3 displays the continuous fields and the IPA obtained for a discretization with 8 equally-sized finite elements. As will be demonstrated through the numerical experiments, our proposed variational framework accurately identifies such approximations.

As a final remark, there are techniques available to obtain better approximations of the real target fields based on the constant piece-wise solution. As a simple example, a nodal field can be defined as the mean value of the reported for the associated elements. These techniques are extensively used for computation of stresses using finite elements, for more details see Zienkiewicz and Taylor (1989).



(a) Proposed residual stress field (solid black lines) and piece-wise constant approximation using 8 finite elements (dashed color lines).



(b) Principal stretches defining the objective RD tensor for a piece-wise constant approximation with 8 finite elements.

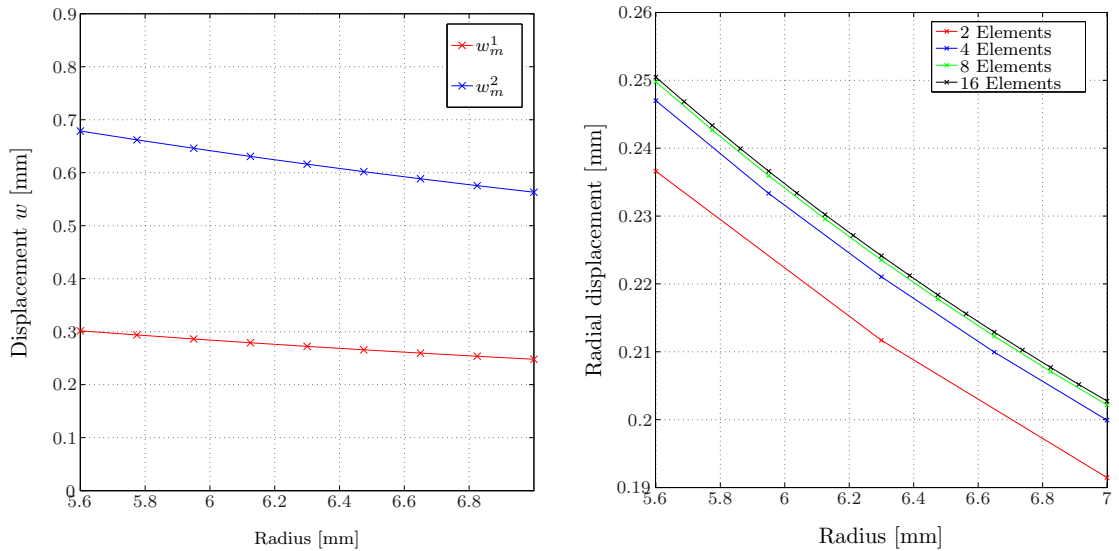
Figure 6.3: Thick-walled cylinder example: objective residual deformations and stresses

6.3.5.1 Manufactured solution

The mechanical equilibrium problem is solved for different values of internal pressure to obtain the *known* equilibrium configurations Ω_a , Ω_b^1 and Ω_b^2 . The linearization of this problem is performed following the ideas presented in Blanco et al (2015). Observe that since the gradient operators (e.g. ∇_m) depend on ρ , associated quantities (e.g. stresses, deformation gradient tensors) are not uniform within each element.

In this example, three different spatial discretizations are explored, using 2, 4 and 8 equally-sized finite elements in the radial directions. The spatial integration is performed using a Gaussian quadrature with 4 Gauss-points.

Figure 6.4(c) displays a representative scheme of the problem, highlighting geometrical landmarks (inner and external radii) for the involved configurations. In this context, Figure 6.4(a) shows the radial displacement fields w_m^1 and w_m^2 mapping Ω_a into Ω_b^1 and Ω_b^2 for an 8 finite elements discretization. Additionally, Figure 6.4(b) shows the displacement fields obtained for a fixed internal pressure $p = 1$ kPa. These figures illustrate the convergence of the finite element method.



(a) Radial displacement fields w_m^j mapping Ω_a into Ω_b^j for the 8 finite element discretization.

(b) Solution of the mechanical problem with $p = 1$ kPa. Displacement field obtained for the different discretization levels expressed terms of material coordinates.

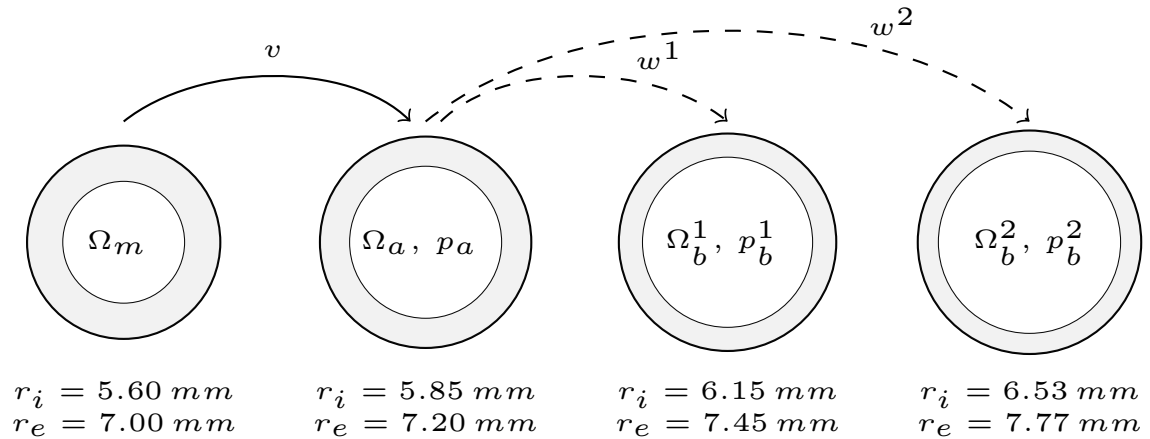


Figure 6.4: Thick-walled cylinder example: results for the mechanical problem

6.3.6 Optimization problem setting

For this problem we make use of the implementation of the interior-point algorithm introduced in Section 5.4.2 available in the MATLAB Optimization Toolbox through the function *fmincon*. For the configuration options we considered:

- *AlwaysHonorConstraints* set to *none* (constraints are not satisfied at each iteration),
- *GradObj* set to *off* (gradient is computed using finite differences),
- *Hessian* set to *bfgs* (Hessian is updated with a BFGS algorithm),
- *InitTrustRegionRadius* set to 40 ($\epsilon_T = 40$, see equation (5.4.27)),
- *TolCon* set to 10^{-12} ($tol^j = 10^{-12}$, see Algorithm 4),
- *TolFun* set to 10^{-8} ($tol^g = tol^h = 10^{-8}$, see Algorithm 4),
- *MaxFunEvals* set to 10^6 (maximum number of function evaluations), and
- *MaxIter* set to 10^5 (maximum number of optimization iterations).

The rest of the options are taken by default. As a constraint, a functional depending on the determinant for the residual deformation at each element is incorporated, assuming the form

$$\mathcal{C} = \sum_e (\det \mathbf{F}_m^{r,e} - 1). \quad (6.3.17)$$

Note that, in this manner the incompressibility of the RRD field is enforced. This fact also contributes to reduce the number of possible solutions for the problem and, consequently, the chances that the optimization process will lead to a local minimum.

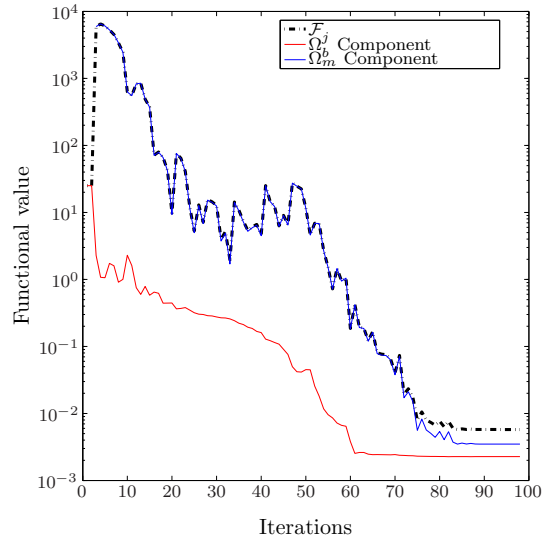
For the setting of the initial conditions we consider $\mathbf{F}_a^r = \mathbf{I}$ for the discretization containing 2 finite elements. Once the solution for this case is achieved, the result is employed as an initial condition for the refined mesh containing 4 finite elements. We proceed this way with successive refinements.

Three stages of optimization are used, using a different set of weighting factors each time; for the second and third optimization stages initial conditions are taken from the previous run. For the first optimization routine, weights are set as $\eta_b^1, \eta_b^2 = 100$ and $\eta_m = 0.1$, emphasizing the influence of the residuals corresponding to the equilibrium in Ω_b^1 and Ω_b^2 . For the second stage weighting factors are $\eta_b^1, \eta_b^2 = 1$ and $\eta_m = 0.1$. Finally, $\eta_b^1 = \eta_b^2 = \eta_m = 1$ is considered for the third stage.

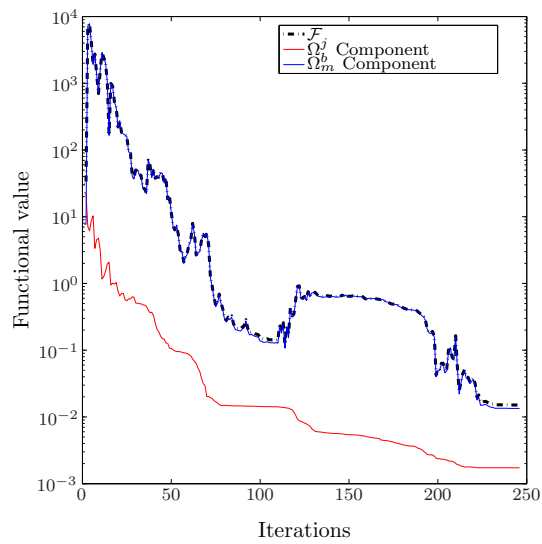
We considered 4 Gauss points for the spatial integration required in the evaluation of the cost functional.

6.3.7 Results

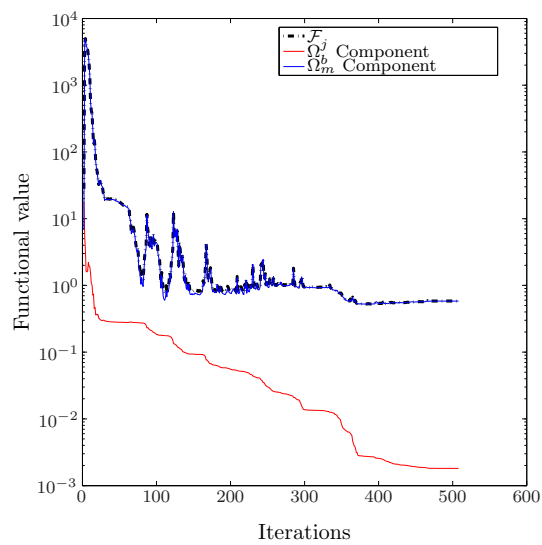
Figure 6.5 evidences the suitability of the proposed algorithm for the minimization of the cost functional, presenting the convergence of the cost functional \mathcal{F} for the three proposed spatial discretizations. The displayed values for the functionals are corresponding to normalized weights $\eta_b^1 = \eta_b^2 = \eta_m = 1$ in order to track to progression of the minimization process considering the three optimization cycles. The minima achieved for each case are $\mathcal{F}^2 = 5.8 \cdot 10^{-3}$, $\mathcal{F}^4 = 1.51 \cdot 10^{-2}$ and $\mathcal{F}^8 = 5.83 \cdot 10^{-1}$, where superscript indicate the number of elements of the discretization for the corresponding functional. The initial large values for the functionals can be explained by the rapid increase of the Ω_m component due to the initial weight values. Furthermore, for the 2 finite elements discretization, the initial condition implies that this component is initially null and any perturbation will inevitably produce a raise of its value.



(a) 2 Finite elements



(b) 4 Finite elements



(c) 8 Finite elements

Figure 6.5: Thick-walled cylinder example: minimization process showing functional value for the three optimization stages. Functional values are corresponding to normalized weights $\eta_b^1 = \eta_b^2 = \eta_m = 1$.

Figure 6.6 presents the results of the obtained RSs for each case, displaying a comparison between the results and their corresponding objective values. Similarly, Figure 6.7 presents the identified RRD fields. Table 6.1 summarizes the results for this problem, showing the discrepancy between the obtained results and target solutions. Here, e_σ indicates the relative discrepancy in RSs and $e_{\mathbf{F}^r}$ the corresponding relative discrepancy in RRDs measured in the L^2 norm. Additionally, e_σ^F and $e_{\mathbf{F}^r}^F$ denote the discrepancy between the obtained results and the IPA of the target RRD for each different discretization (see Section 6.3.4). Similarly, e_v^F measures in the L^2 norm the relative discrepancy between the obtained radial displacement field v (mapping from Ω_m into Ω_a) and the corresponding field obtained through the mechanical equilibrium problem when RRDs are given by the IPA of the target RRD. Finally, the minimum value achieved for the functional \mathcal{F} and the number of iterations are displayed.

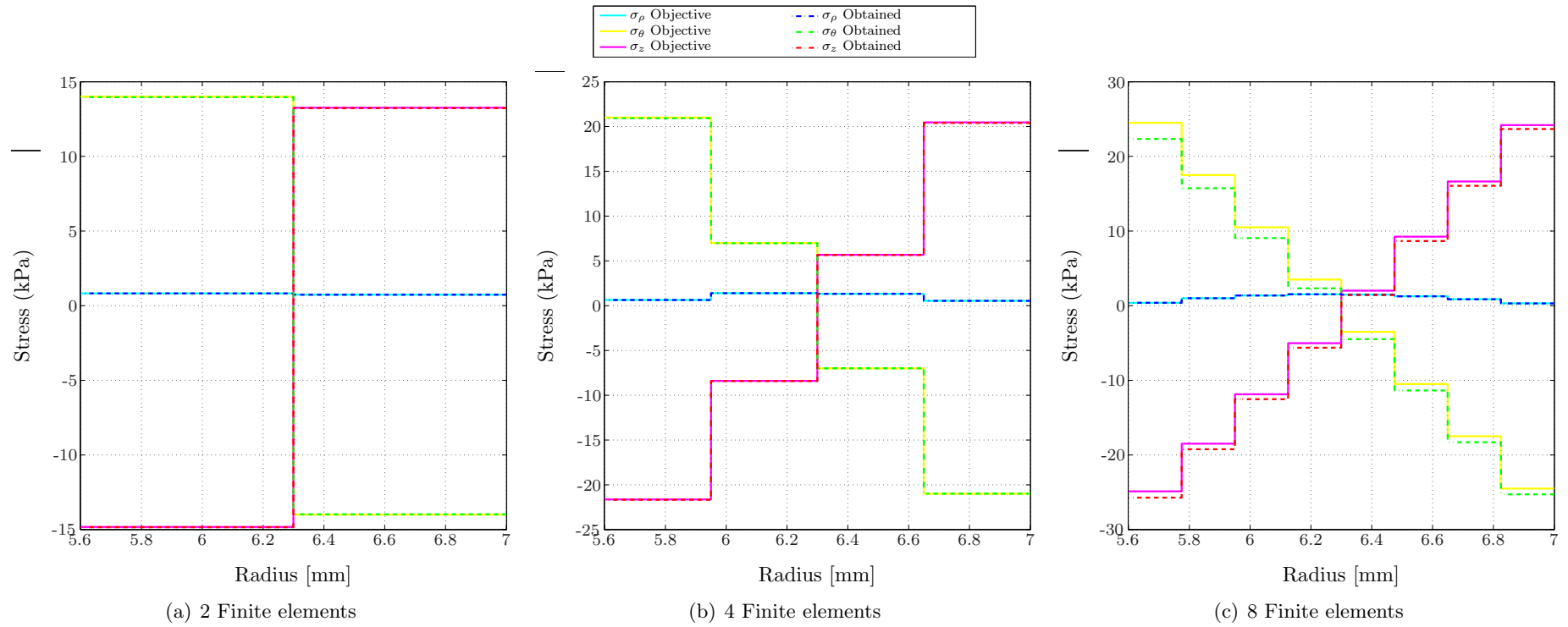


Figure 6.6: Thick-walled cylinder example: residual stresses for different discretizations. Comparison between obtained results (dashed) and values corresponding to the IPA of the target RRD field (solid).

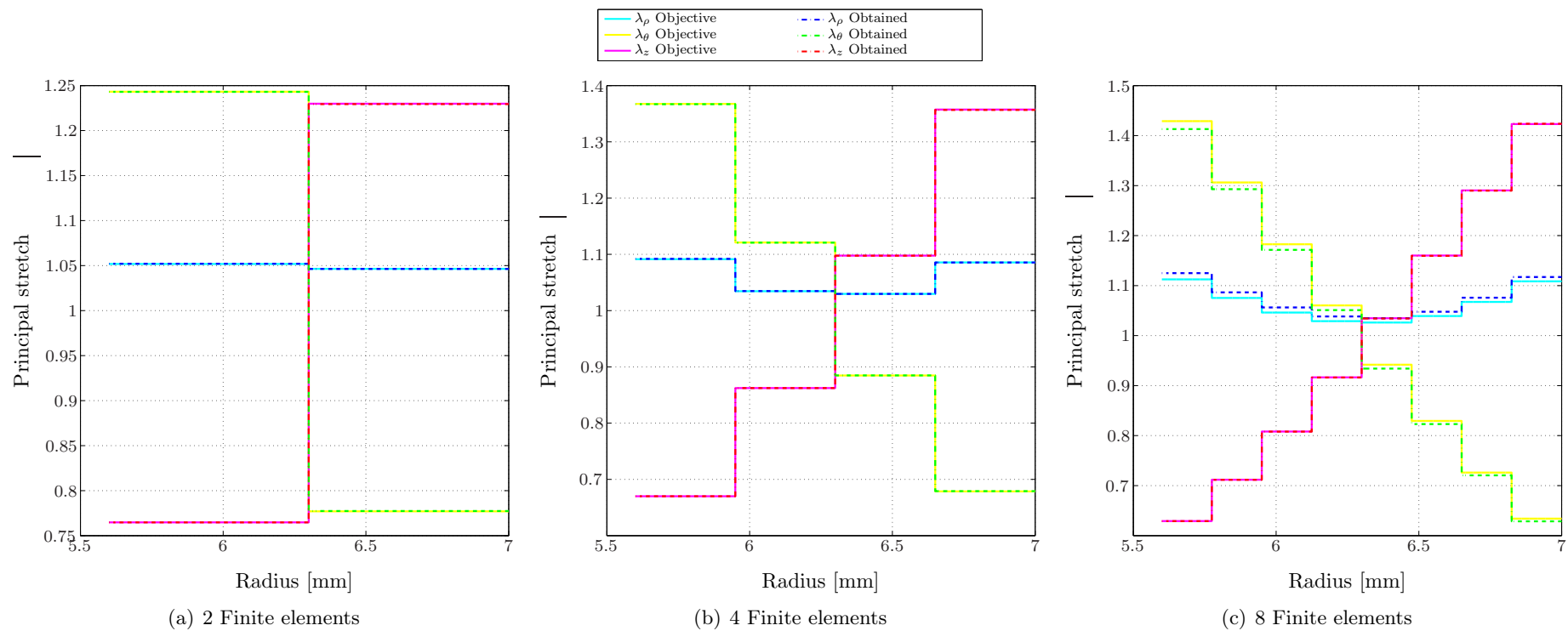


Figure 6.7: Thick-walled cylinder example: principal stretches characterizing the RRDs for different discretizations. Comparison between obtained results (dashed) and the IPA of the target RRD field (solid).

Result overview: discrepancies with target fields.							
Elements	e_σ	e_σ^F	$e_{\mathbf{F}r}$	$e_{\mathbf{F}r}^F$	e_v^F	\mathcal{F}	Iterations
2	$4.99 \cdot 10^{-1}$	$1.95 \cdot 10^{-3}$	$1.02 \cdot 10^{-1}$	$2.66 \cdot 10^{-4}$	$6.41 \cdot 10^{-4}$	$5.76 \cdot 10^{-3}$	92
4	$2.49 \cdot 10^{-1}$	$3.24 \cdot 10^{-3}$	$5.11 \cdot 10^{-2}$	$3.64 \cdot 10^{-4}$	$4.18 \cdot 10^{-3}$	$1.51 \cdot 10^{-2}$	240
8	$1.85 \cdot 10^{-1}$	$8.39 \cdot 10^{-2}$	$2.77 \cdot 10^{-2}$	$8.39 \cdot 10^{-3}$	$2.52 \cdot 10^{-1}$	$5.83 \cdot 10^{-1}$	502

Table 6.1: Thick-walled cylinder example: identification error summary.

It can be observed that the proposed methodology is able to adequately characterize the mechanical setting making possible the identification of RRDs. For the obtained RRD field, the relative error encountered is below 1% in all cases, when compared with the IPA of the target RRD.

It is worthwhile to remark that, although the accuracy in the estimation of the values at the element level decreases (see discrepancies with fields corresponding to the IPA of the target field) when the number of variables characterizing the fields is incremented, the increasing number of elements in the spatial discretization leads to a better identification of the continuous target fields.

One strategy to circumvent the ill-conditioning of the problem as the number of unknowns increases is to replace the element-wise unknown approach with predefined whole-domain functions, with small number of parameters, which will be used to minimize the cost functional. Such approach would bound the number of unknowns as the finite element mesh becomes finer. Note that the use of this type of functions could also contribute to obtain more accurate approximations for the initially proposed continuous RS field with a reduced number of variables. This issue is beyond the scope of the present work and is a matter of current investigation.

6.4 Three-layered arterial wall

6.4.1 Problem description

In this example, RRDs in the case of a vessel resembling the setting of the arterial wall of an abdominal aorta, are characterized. For modeling purposes, we consider the arterial wall to be a cylindrical tube, consisting of three-layers of uniform thickness, the intima, the media and the adventitia. Moreover, the material in each layer features uniform properties and is assumed to behave according to the constitutive equation proposed in Holzapfel and Gasser (2000) (presented in Section 3.6.1). For this example, a quasi-incompressible arterial wall response is considered, and the cited constitutive equation is modified accordingly, yielding

$$\Psi = \frac{c_{elast}}{2}(\bar{I}_1 - 3) + \frac{k_1}{2k_2} \sum_{i=4,6} \delta_i \left\{ e^{k_2(\bar{I}_i - \lambda_i^0)^2} - 1 \right\} + k_{vol}(J - 1)^2. \quad (6.4.1)$$

In this context, k_{vol} is the bulk modulus, $J = \det \mathbf{F}_m$ and $\bar{\mathbf{F}}_m = \mathbf{F}_m J^{-1/3}$ is the isochoric deformation tensor. Associated to this deformation we have $\bar{\mathbf{C}}_m = \bar{\mathbf{F}}_m^T \bar{\mathbf{F}}_m$ and the isochoric invariants

$$\bar{I}_1 = \mathbf{I} \cdot \bar{\mathbf{C}}_m, \quad \bar{I}_i = \bar{\mathbf{C}}_m \cdot (\mathbf{a}_i \otimes \mathbf{a}_i), \quad i = 4, 6. \quad (6.4.2)$$

It is worthwhile to mention that recruitment stretches λ_i^0 are defined in such a way that in the material configuration collagen fibers store null energy, i.e.

$$\lambda_i^0 = \bar{\mathbf{C}}_m^r \cdot (\mathbf{a}_i \otimes \mathbf{a}_i), \quad \bar{\mathbf{C}}_m^r = \bar{\mathbf{F}}_m^r (\bar{\mathbf{F}}_m^r)^T. \quad (6.4.3)$$

This fact implies that the collagen load bearing starts when the vessel is inflated beyond the null pressure level and they have no influence in the residual stress state induced by residual deformations. This is motivated by the remodeling process experienced by the collagen (Humphrey, 1999) (through continuous degradation and synthesis), enabling the adoption of different configurations of the fibers and avoiding residual deformations.

Four scenarios are analyzed, where Ω_a is considered to be the solution of the forward problem obtained for an internal pressure $p_a = 6$ kPa. In addition to this known Ω_a configuration, we explore different scenarios, each of which is regarded with a different number of additional known configurations according to the following

- (a) 1 additional configuration (at equilibrium with $p = 14$ kPa),
- (b) 2 additional configurations (at equilibrium with $p = 8/14$ kPa),
- (c) 3 additional configurations (at equilibrium with $p = 8/10/14$ kPa),
- (d) 4 additional configurations (at equilibrium with $p = 8/10/12/14$ kPa).

These scenarios are proposed to evaluate the capabilities of the identification problem to deliver the correct RRDs as the amount of input data is increased.

6.4.2 Kinematic setting

The kinematic setting for this problem is the same to the presented for the Neo-Hookean cylinder introduced in Section 6.3.2.

6.4.3 Model parameters and residual deformations

Based on experimental measurements for each individual layer (experimental data available in Holzapfel et al (2007)), Holzapfel and Ogden (2010a) propose a methodology to define a field of RRDs (here denoted \mathbf{F}_m^{exp}). In this work, an idealized cylindrical geometry for the material configuration and an incompressible Neo-Hookean material are considered. This RRD field is expressed in terms of the principal stretches λ_ζ , $\zeta \in (\rho, \theta, z)$, adopting the following forms for each of the corresponding layers

$$\begin{aligned} \mathbf{F}_m^{exp,(I)}(\rho) &= \begin{pmatrix} \lambda_\rho^{(I)}(\rho) & 0 & 0 \\ 0 & \lambda_\theta^{(I)}(\rho) & 0 \\ 0 & 0 & \lambda_z^{(I)}(\rho) \end{pmatrix}, \\ \mathbf{F}_m^{exp,(M)}(\rho) &= \begin{pmatrix} -\lambda_\rho^{(M)}(\rho) & 0 & 0 \\ 0 & 0 & \lambda_\theta^{(M)}(\rho) \\ 0 & \lambda_z^{(M)}(\rho) & 0 \end{pmatrix}, \\ \mathbf{F}_m^{exp,(A)}(\rho) &= \begin{pmatrix} \lambda_\rho^{(A)}(\rho) & 0 & 0 \\ 0 & \lambda_\theta^{(A)}(\rho) & 0 \\ 0 & 0 & \lambda_z^{(A)}(\rho) \end{pmatrix}, \end{aligned} \quad (6.4.4)$$

where superscripts (I) , (M) , (A) indicate that the field corresponds to the intima, media or adventitia layer, respectively. Considering the setting presented in Figure 6.8, Holzapfel and Ogden (2010a) calculated the principal stretches using the mechanical equilibrium equation of the material domain, resulting in functions of geometrical parameters characterizing the excised and separated layers ($A^{(I)}$, $B^{(I)}$, $L^{(I)}$, $k^{(I)}(\alpha^{(I)})$, $A^{(M)}$, $B^{(M)}$, $L^{(M)}$, $k^{(M)}(\alpha^{(M)})$, $L_1^{(A)}$, $L_2^{(A)}$, $L_3^{(A)}$) and the *intact* (i.e. before excising and separating the material layers) material configuration ($a^{(I)}$, $b^{(I)}$, l , β_c , l_m , $a^{(M)}$, $b^{(M)}$, $a^{(A)}$, $b^{(A)}$). As previously

mentioned, the set of geometrical parameters was obtained from experimental data. Two of the parameters corresponding to the material configuration are given (in this example $a^{(I)}$ and $b^{(I)}$), and the remaining are computed through the incorporation of equations corresponding to the interface matching between layers and to the continuity of radial stresses. Therefore, the principal stretches take the following form

$$\begin{aligned}
\lambda_\rho^{(I)}(\rho) &= \frac{L^{(I)}}{\rho k^{(I)} l} \left[(A^{(I)})^2 + k^{(I)} \frac{l}{L^{(I)}} ((\rho)^2 - (a^i)^2) \right]^{1/2}, \\
\lambda_\rho^{(M)}(\rho) &= \frac{L^{(M)} \pi}{\rho \beta_c l^{(M)} k^{(M)}} \left[(A^{(M)})^2 + \frac{\beta_c l^{(M)} k^{(M)}}{L^{(M)} \pi} ((b^{(M)})^2 - (\rho)^2) \right]^{1/2}, \\
\lambda_\rho^{(A)}(\rho) &= \frac{L_2^{(A)} L_3^{(A)}}{\pi \rho l}, \\
\lambda_\theta^{(I)}(\rho) &= \frac{\rho k^{(I)}}{\left[(A^{(I)})^2 + k^{(I)} \frac{l}{L^{(I)}} ((\rho)^2 - (a^i)^2) \right]^{1/2}}, \\
\lambda_\theta^{(M)}(\rho) &= \frac{r^{(M)} \beta_c}{L^{(M)}}, \\
\lambda_\theta^{(A)}(\rho) &= \frac{\pi \rho}{L_2^{(A)}}, \\
\lambda_z^{(I)}(\rho) &= \frac{l}{L^{(I)}}, \\
\lambda_z^{(M)}(\rho) &= \frac{l^{(M)} k^{(M)}}{\pi \left[(A^{(M)})^2 + \frac{\beta_c l^{(M)} k^{(M)}}{L^{(M)} \pi} ((b^{(M)})^2 - (\rho)^2) \right]^{1/2}}, \\
\lambda_z^{(A)}(\rho) &= \frac{l}{L_3^{(A)}}. \tag{6.4.5}
\end{aligned}$$

Note that the dependence of these stretches with respect to the Neo-Hookean stiffness parameters for each layer $c^{(I)}, c^{(M)}$ and $c^{(A)}$ is contained in the definition of β_c . The geometric parameters used for this example were extracted from Holzapfel and Ogden (2010a) and are summarized in Table 6.2. Figure 6.9 displays the resulting principal stretches λ_ζ , $\zeta \in (\rho, \theta, z)$ and the associated RSs.

Intima	Media	Adventitia
$A^{(I)} = 7.50$ mm	$A^{(M)} = 8.41$ mm	$L_1^{(A)} = 0.205$ mm
$B^{(I)} = 7.76$ mm	$B^{(M)} = 9.99$ mm	$L_2^{(A)} = 18.3$ mm
$L^{(I)} = 2.58$ mm	$L^{(M)} = 2.52$ mm	$L_3^{(A)} = 2.29$ mm
$k^{(I)} = 1.19$	$k^{(M)} = 1.19$	
$a^{(I)} = 5.61$ mm	$a^{(M)} = 5.91$ mm	$a^{(A)} = 6.72$ mm
$b^{(I)} = 5.91$ mm	$b^{(M)} = 6.72$ mm	$b^{(A)} = 7.05$ mm
	$l^{(M)} = 4.80$ mm	
Common parameters		
$\beta_c = 0.58$	$l = 2.48$ mm	

Table 6.2: Summary of geometrical parameters employed for the three-layered vessel wall

The material parameters characterizing the isotropic term of the strain energy function are taken from the same bibliographic reference, as $c_{elast}^{(I)} = 39.8$ kPa, $c_{elast}^{(M)} = 31.4$ kPa, and $c_{elast}^{(A)} = 17.3$ kPa, where superscripts I, M, A indicate that the field corresponds to the intima, media or adventitia layer, respectively. The bulk moduli are considered as $k_{vol}^{(I)} = 484.23$ kPa, $k_{vol}^{(M)} = 382.03$ kPa, and $k_{vol}^{(A)} = 210.48$ kPa, consistent with a Poisson

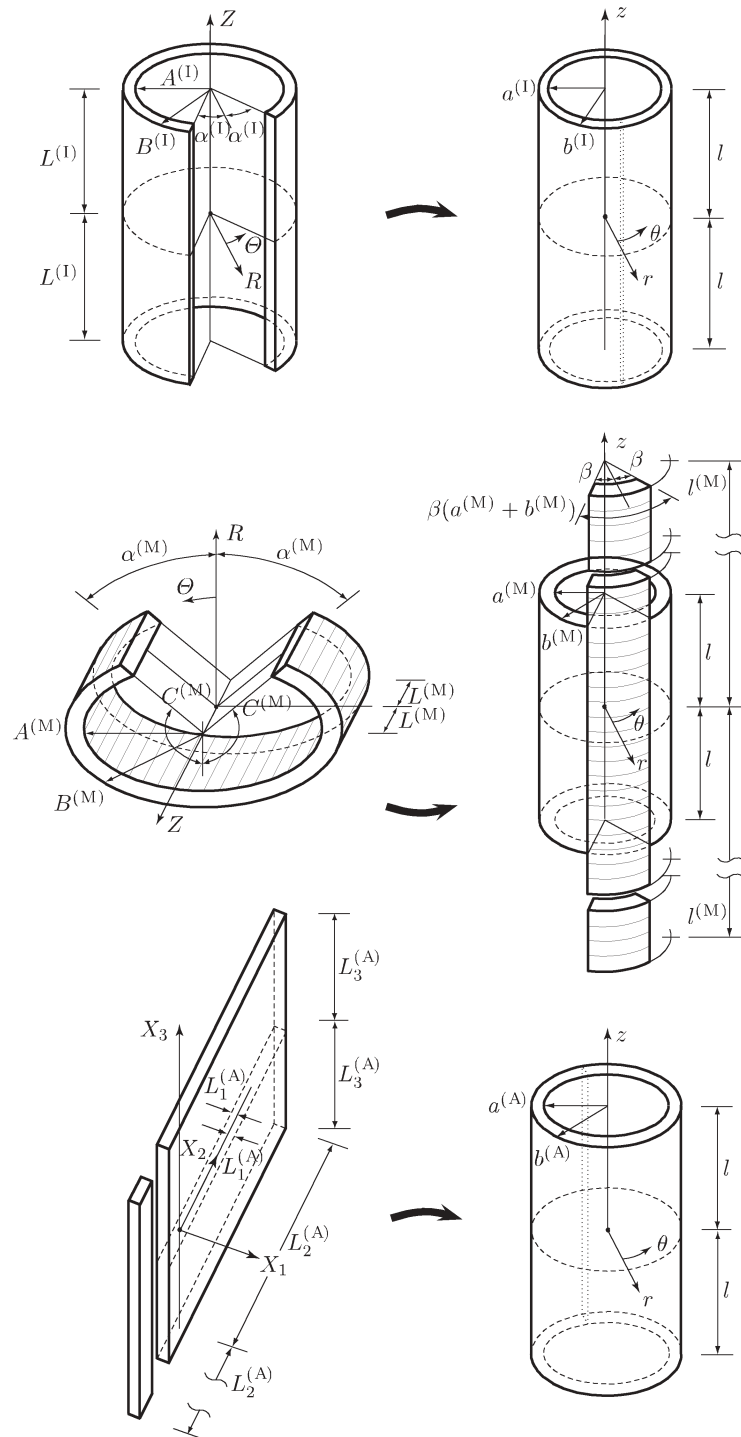


Figure 6.8: Coordinate system and related geometries for the individual layers (intima, media, adventitia) in their virtual (left) and the *intact* material configurations (right). Figure adapted from Holzapfel and Ogden (2010a)

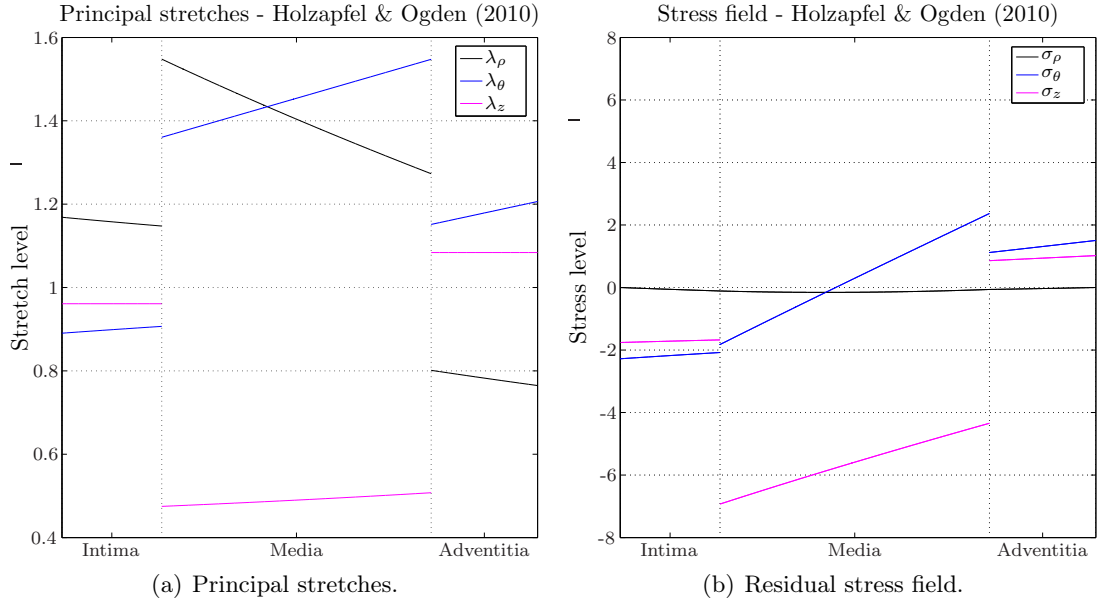


Figure 6.9: Principal stretches shaping the residual deformation field and the associated residual stresses through the wall radius as introduced in Holzapfel and Ogden (2010a).

modulus of $\nu = 0.49$ is considered only the stiffness of the isotropic contribution. Material parameters characterizing the collagen behavior are taken from Weisbecker et al (2012) and are $k_1^{(I)} = 10.1$ MPa, $k_1^{(M)} = 0.81$ MPa, $k_1^{(A)} = 0.38$ MPa, $k_2^{(I)} = 0.01$, $k_2^{(M)} = 12.4$ and $k_2^{(A)} = 3.35$. Two collagen fiber families are considered, oriented with angles of $\beta^{(I)} = 40.5^\circ$, $\beta^{(M)} = 39.1^\circ$, and $\beta^{(A)} = 40.6^\circ$ with respect to the azimuthal axis. Table 6.3 summarizes the information regarding the material parameter setting for this example.

Material parameter	Intima	Media	Adventitia
Thickness [mm]	0.30	0.81	0.32
k_{elast} [kPa]	39.8	31.4	17.3
k_{vol} [10^2 kPa]	4.84	3.82	2.10
k_1 [MPa]	10.1	0.81	0.98
k_2	0.01	12.4	3.35
β [$^\circ$]	40.5	39.1	40.6

Table 6.3: Summary of material parameters for three-layered wall example

We employ different finite element discretizations, and, in every case, we approximate the RRD field with a piece-wise constant field. As in the previous example, our methodology is expected to find the IPA of the RRD field provided in Holzapfel and Ogden (2010a).

Figure 6.10 shows the IPAs of the RRD field corresponding to two different discretizations. The first one consisting in 1 finite element per layer (3 elements total), and the second one with 2, 4 and 2 finite elements for the intima, media and adventitia layers, respectively. These fields are compared with the RRDs given in Holzapfel and Ogden (2010a). Additionally, Figure 6.11 displays the RS fields related to the RRDs.

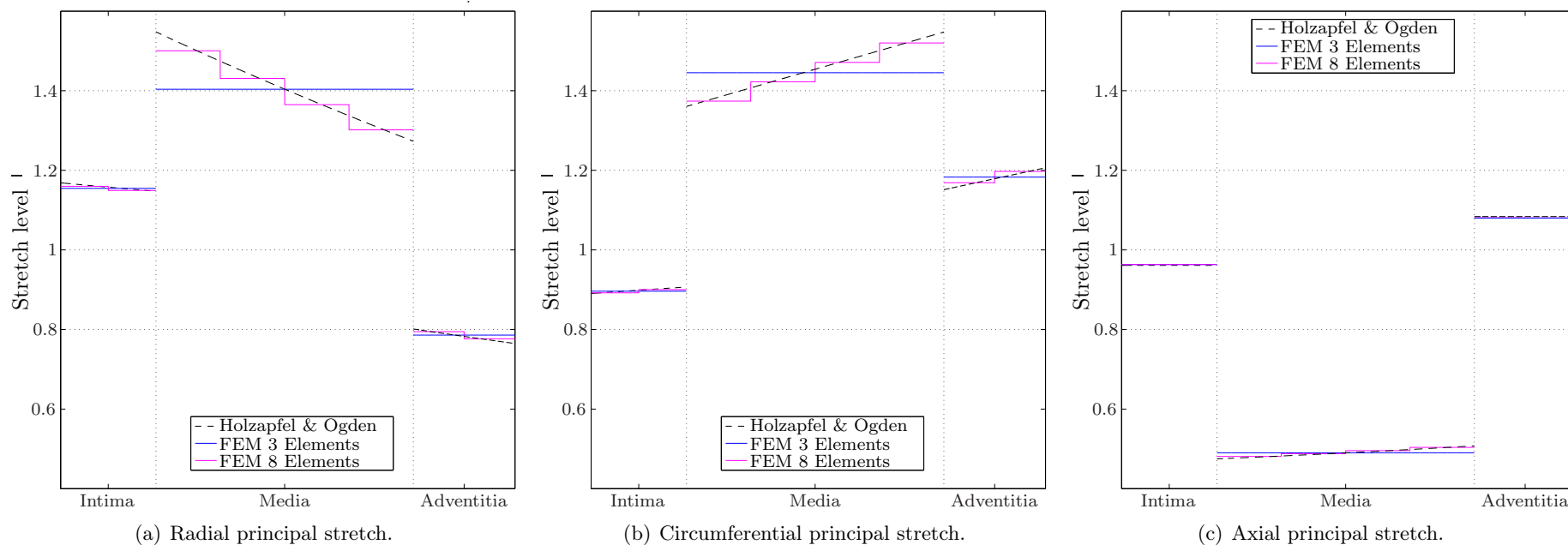


Figure 6.10: Principal stretches shaping the IPA of the target RRD field using element-wise constant RRDs for the 3 and 8 finite elements discretizations. Comparison with target RRDs proposed in Holzapfel and Ogden (2010a).

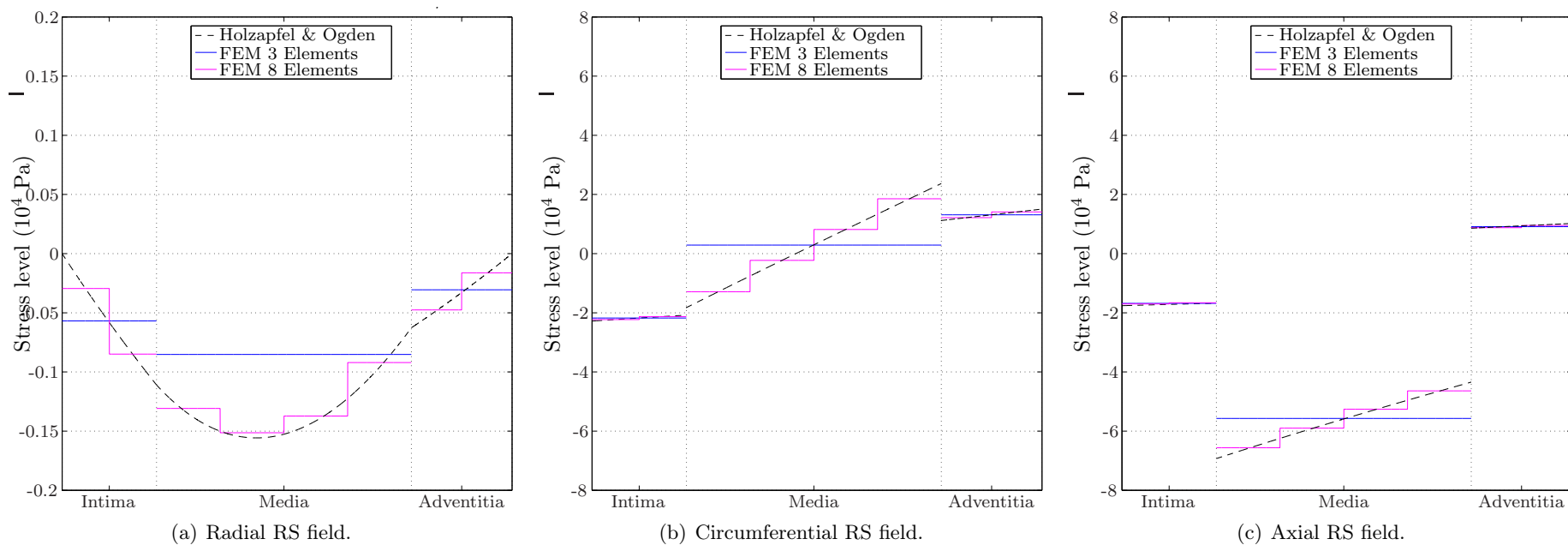
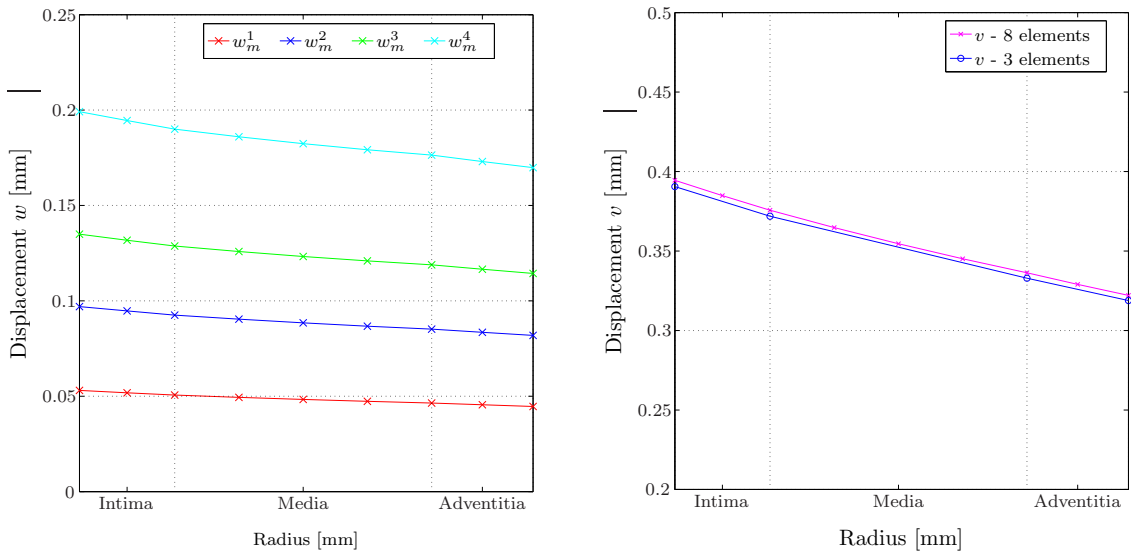


Figure 6.11: RS fields associated with the IPA of the target RRD for the 3 and 8 finite element discretizations. Comparison with the RS field proposed in Holzapfel and Ogden (2010a).

6.4.4 Manufactured solution

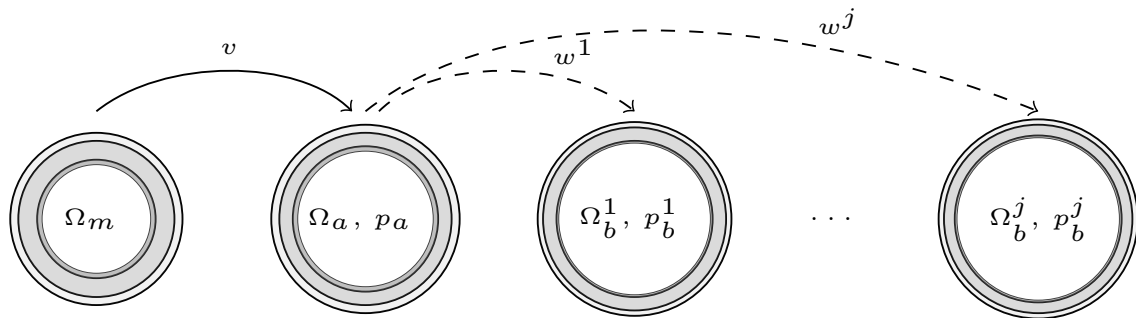
With the material configuration and RRDs already defined, the mechanical problem is solved for different levels of inner pressure. This is done for the two proposed discretizations.

Figure 6.12(c) displays a representative scheme of the problem, while Table 6.4 presents the geometrical landmarks for the involved configurations in scenario (d). Figure 6.12(a) shows the radial displacement fields w_m^j for each of the four additional known configurations proposed in scenario (d), while Figure 6.12(b) shows the radial displacement field obtained for an inner pressure $p = 6$ kPa for the 3 and 8 finite elements approximations. The numerical integration is performed using 4 Gauss points.



(a) Radial displacement fields w_m^j mapping Ω_a into Ω_b^j (for the set of known configurations proposed in scenario (d)) for the 8 finite element discretization.

(b) Displacement fields obtained as solution of the forward problem for internal pressure $p = 6$ kPa for both proposed spatial discretizations (3 and 8 finite elements).



(c) Problem representative scheme.

Figure 6.12: Three-layered aorta: Numerical solution of the forward mechanical problem.

6.4.5 Optimization problem setting

For the 3 finite elements discretization the initial condition is set as $\mathbf{F}^{e,m} = \mathbf{I}$. Next, the solution obtained for this case is given as initial condition for the discretization with 8 finite elements. The options setting for the MATLAB *fmincon* function is identical to the presented in Section 6.3.6.

Three stages of optimization are used, using a different set of weighting factors

Three-layered aorta: geometrical landmarks of manufactured solution for scenario (d)						
Configuration	Pressure [kPa]	Inner radius [mm]	Intima thickness	Media thickness	Adv. thickness	
Ω_m	0	5.61	0.301	0.812	0.324	
Ω_a	6	6.00	0.282	0.774	0.335	
Ω_b^1	8	5.66	0.299	0.809	0.323	
Ω_b^2	10	5.71	0.297	0.806	0.324	
Ω_b^3	12	5.75	0.295	0.803	0.326	
Ω_b^4	16	5.81	0.292	0.799	0.328	

Table 6.4: Three-layered aorta example: geometrical landmarks.

each time; for the second and third optimization stages, the initial condition is the result obtained in the previous run. For the 3 finite elements discretization the following weights are used: $\eta_m = 0.01$, $\eta_{b,j} = 10$ for the first stage, $\eta_m = 10$, $\eta_{b,j} = 0.1$ for the second stage, and $\eta_m = 1$, $\eta_{b,j} = 100$ for the third stage. Note that $j = 1, \dots, N_B$, with N_B representing the number of known configurations -additional to Ω_a - (see list of scenarios in Section 6.4.1) for the corresponding case.

This set of weighting parameters was defined based on the functional values achieved through the minimization process. It is important to remark that the chosen initial condition leads to a null initial value for the generalized residual of the mechanical problem in Ω_m , then, the contributions of the residuals in the remaining configurations drive the minimization process.

For the 8 finite elements discretization the weights are defined as follows, $\eta_m = 1$, $\eta_{b,j} = 1$ for the first stage, $\eta_m = 10$, $\eta_{b,j} = 10$ for the second stage, and $\eta_m = 1$, $\eta_{b,j} = 1$ for the third stage.

As a constraint, a functional depending on the determinant of the RRD for each element is considered. This constraint is expressed as

$$\mathcal{C} = \sum_e (\det \mathbf{F}_m^{r,e} - 1)^2 < \varpi, \quad (6.4.6)$$

with $\varpi = 0.01$.

The integration required for the numerical computation of the preload problem and the evaluation of generalized residuals is performed using 4 Gauss points in each element.

6.4.6 Results

Results for the 3 finite elements discretization

An overview of the results for the four proposed scenarios is presented in Table 6.5, where the identification errors are summarized. Here, the number of functional evaluations for each scenario and the value achieved for the cost functional \mathcal{F} (normalized with $\eta_{b,j} = \eta_m = 1$) are shown. Like in the previous example, error measures for the RRDs, RSs and displacement fields are presented.

Result overview: Three-layered wall example (3 finite elements)							
Scenario	e_σ	e_σ^F	$e_{\mathbf{F}^r}$	$e_{\mathbf{F}^r}^F$	e_v^F	\mathcal{F}	Iterations
(a)	$6.08 \cdot 10^{-1}$	$5.77 \cdot 10^{-1}$	$2.18 \cdot 10^{-1}$	$2.05 \cdot 10^{-1}$	$4.28 \cdot 10^{-2}$	$9.35 \cdot 10^{-1}$	165
(b)	$4.88 \cdot 10^{-1}$	$4.57 \cdot 10^{-1}$	$1.73 \cdot 10^{-1}$	$1.56 \cdot 10^{-1}$	$8.07 \cdot 10^{-4}$	$4.02 \cdot 10^{-1}$	337
(c)	$4.22 \cdot 10^{-1}$	$3.84 \cdot 10^{-1}$	$1.39 \cdot 10^{-1}$	$1.21 \cdot 10^{-1}$	$3.85 \cdot 10^{-3}$	$4.49 \cdot 10^{-1}$	221
(d)	$1.68 \cdot 10^{-1}$	$1.64 \cdot 10^{-3}$	$4.21 \cdot 10^{-2}$	$4.53 \cdot 10^{-4}$	$4.25 \cdot 10^{-5}$	$5.70 \cdot 10^{-2}$	583

Table 6.5: Three-layered aorta example: summary of results corresponding to the 3 finite elements approximation. Values for the functional \mathcal{F} are normalized using $\eta_{b,j} = \eta_m = 1$ ($j = 1, \dots, N_B$).

As can be seen in Table 6.5, the proposed methodology is capable of fully characterizing the target RRD field and the associated RSs, with discrepancies up to 0.07% in RRDs, 0.004% in the displacement field values and 0.3% in the RSs, for scenario (d). Moreover, with this simple discretization using only one finite element in each layer is obtained a 4.2% discrepancy with the RRD field reported in Holzapfel and Ogden (2010a).

The achieved functional values for the different scenarios reveal the existence of local minima. Improvement of optimization algorithms to improve the minimization process deserves further research and is out of the scope of the present manuscript. The information provided by the additional known configurations enables the optimization algorithm to reduce the value of the cost functional and of the discrepancies in the identification problem. In other words, the mechanical setting is consistent in the sense that as we add more data, the identification problem becomes better-conditioned and the objective solution is ultimately found. This is fundamental, because no previous works had addressed the questions risen in this work.

Figure 6.13 features a comparison between the obtained principal stretches, characterizing the RRD state (see equation (6.4.4)), for the four proposed scenarios and the objective values (corresponding to the IPA of the target RRD) for each case. From this figure it can be noted that the most relevant discrepancies are primarily in the adventitia layer deformations. This fact can be explained due to the lower stiffness of the material and its reduced thickness when compared with the media layer, both facts leading to a smaller contribution to the internal virtual power. As consequence, the proposed cost functional is less sensitive to changes in the deformations affecting that layer. Additionally, Figure 6.14 presents a similar comparison for the obtained RS field. As it is natural, these results reflect the discrepancies previously observed for the RRD field.

The identification with only two configurations (scenario (a)) could be considered satisfactory depending upon the specific interest. In fact, observe that except for the adventitia, the identification problem yields mechanically consistent RRDs fields. That is, the local minima found by the algorithm are not only close to the solution, but they have physical meaning.

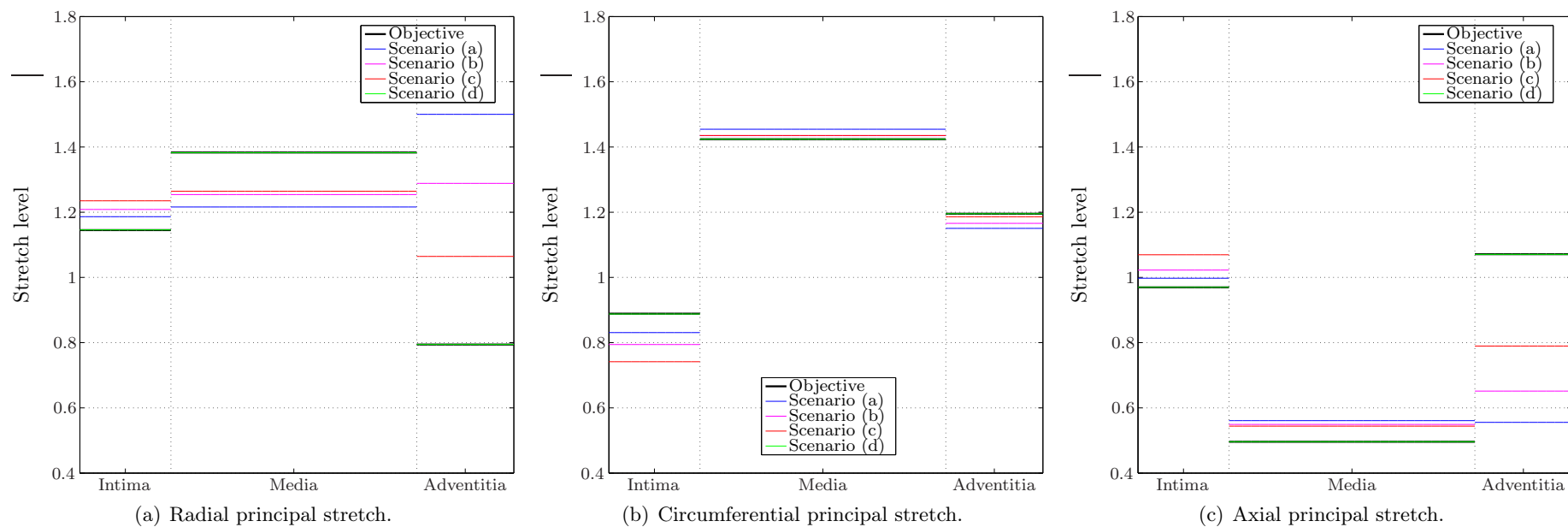


Figure 6.13: Three-layered wall example: results for the three finite elements approximation. Residual deformations obtained as result of the optimization process for the four proposed scenarios compared with the IPA of the objective field.

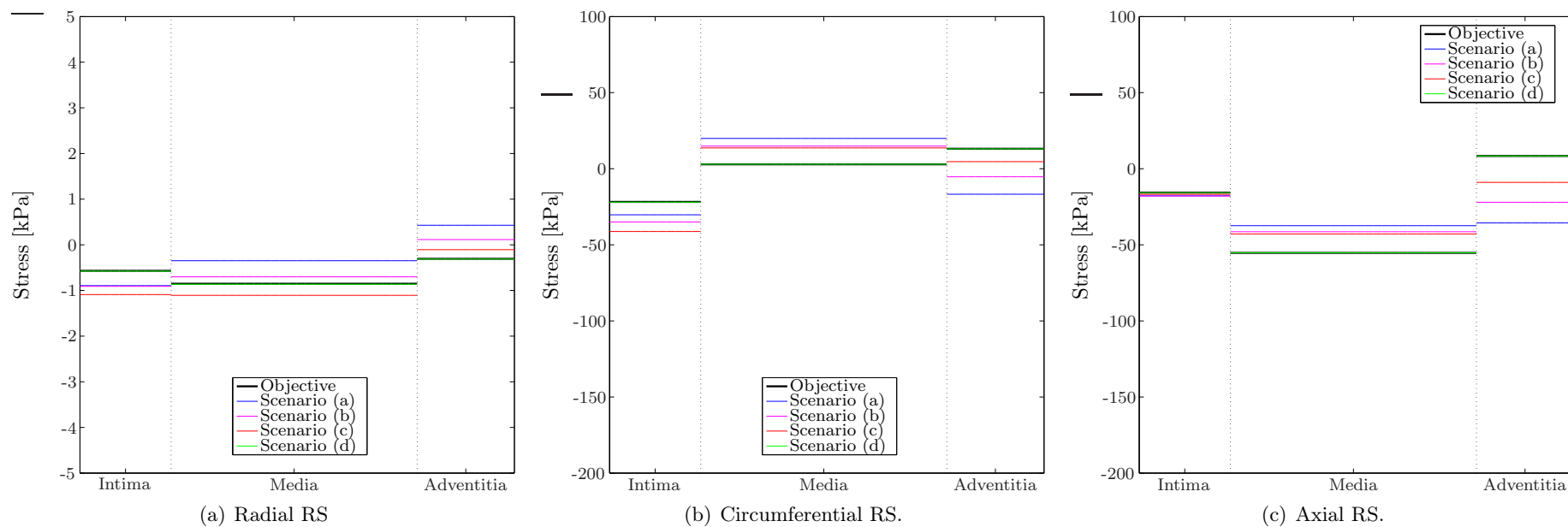


Figure 6.14: Three-layered wall example: results for the three finite elements approximation. Residual stresses arising from the residual deformation field obtained as result of the optimization process for the four proposed scenarios, compared with the RSs associated to the IPA of the RRDs.

Results for the 8 finite elements discretization

As before, an overview of the results for the four proposed scenarios is presented in Table 6.6, where the identification errors are summarized. Here, the number of functional evaluations for each scenario and the value achieved for the functional \mathcal{F} (normalized with $\eta_{b,j} = \eta_m = 1$) are also shown. Furthermore, error measures for the RRDs, RSs and displacement fields are presented. It can be clearly seen the impact of the amount of

Result overview: Three-layered wall example (8 finite elements)							
Scenario	e_σ	e_σ^F	$e_{\mathbf{F}^r}$	$e_{\mathbf{F}^r}^F$	e_v^F	\mathcal{F}	Iterations
(a)	$5.48 \cdot 10^{-1}$	$5.46 \cdot 10^{-1}$	$1.97 \cdot 10^{-1}$	$1.93 \cdot 10^{-1}$	$1.13 \cdot 10^{-1}$	$1.94 \cdot 10^0$	290
(b)	$4.41 \cdot 10^{-1}$	$4.36 \cdot 10^{-1}$	$1.54 \cdot 10^{-1}$	$1.51 \cdot 10^{-1}$	$4.08 \cdot 10^{-3}$	$8.45 \cdot 10^{-1}$	232
(c)	$3.62 \cdot 10^{-1}$	$3.58 \cdot 10^{-1}$	$1.22 \cdot 10^{-1}$	$1.18 \cdot 10^{-1}$	$6.49 \cdot 10^{-3}$	$8.65 \cdot 10^{-1}$	223
(d)	$1.02 \cdot 10^{-1}$	$9.15 \cdot 10^{-2}$	$2.98 \cdot 10^{-2}$	$2.44 \cdot 10^{-2}$	$7.26 \cdot 10^{-5}$	$2.11 \cdot 10^{-1}$	175

Table 6.6: Three-layered wall example: summary of results corresponding to the 8 finite elements approximation. Values for the functional \mathcal{F} are normalized using $\eta_{b,j} = \eta_m = 1$ ($j = 1, \dots, N_B$).

available data in the ability of the minimization procedure to find the stationary point close to the objective solution. In this case, the initial conditions were supplied by the solutions obtained using 3 finite elements, correspondingly.

We highlight that the functional value shows a strong correlation with the quality of the estimation of RRDs. The precision achieved for scenario (d) is excellent, identifying the IPA of the target field with discrepancies of $e_{\mathbf{F}^r}^F = 2.44 \cdot 10^{-2}$, $e_v^F = 7.26 \cdot 10^{-5}$ and $e_\sigma^F = 9.15 \cdot 10^{-2}$. The radial displacement v (which defines the material configuration) presents excellent agreement with the objective field, with maximum relative discrepancies up to approximately 11% for scenario (a), 0.4% for scenario (b), 0.6% for scenario (c) and 0.01% for scenario (d). The use of a finer discretization leads to an accuracy gain in the representation of the target RRD and RS fields; the discrepancy in RSs decreased from 17% to 10% and the corresponding to RRDs from 4.2% to 3% when comparing achieved results for the 3 and 8 elements discretizations.

Additionally, Figures 6.15 and 6.16 present the identified RRD and RS fields for the four described scenarios. As observed for the 3 finite elements case, scenario (d) results show an exceptional agreement with the IPA of the target RRD. In absolute terms, the most relevant discrepancies are primarily in the adventitia layer deformations, in line with the results described in the previous case with a smaller number of finite elements. Also, in relative terms, the discrepancy in the radial deformations are particularly relevant for scenarios (a), (b) and (c). This is due to the relatively low radial stress values and their small influence in the contribution to the internal power.

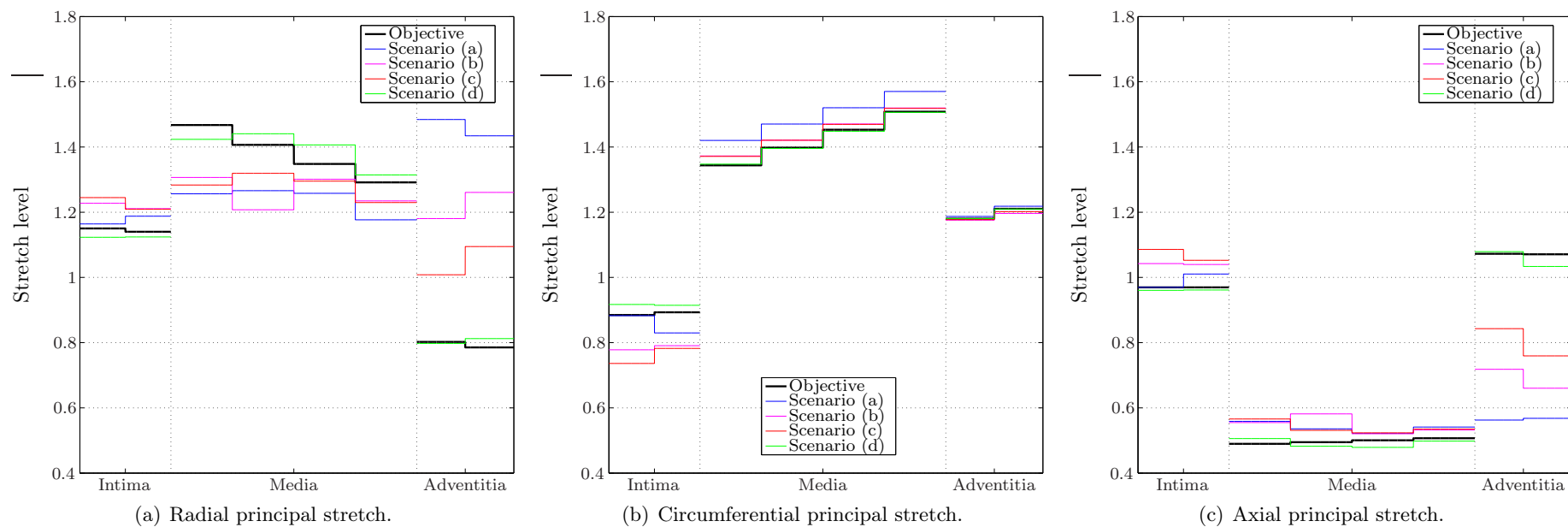


Figure 6.15: Three-layered wall example: results for the eight finite elements approximation. Residual deformations obtained as result of the optimization process for the four proposed scenarios compared with the IPA of the objective field.

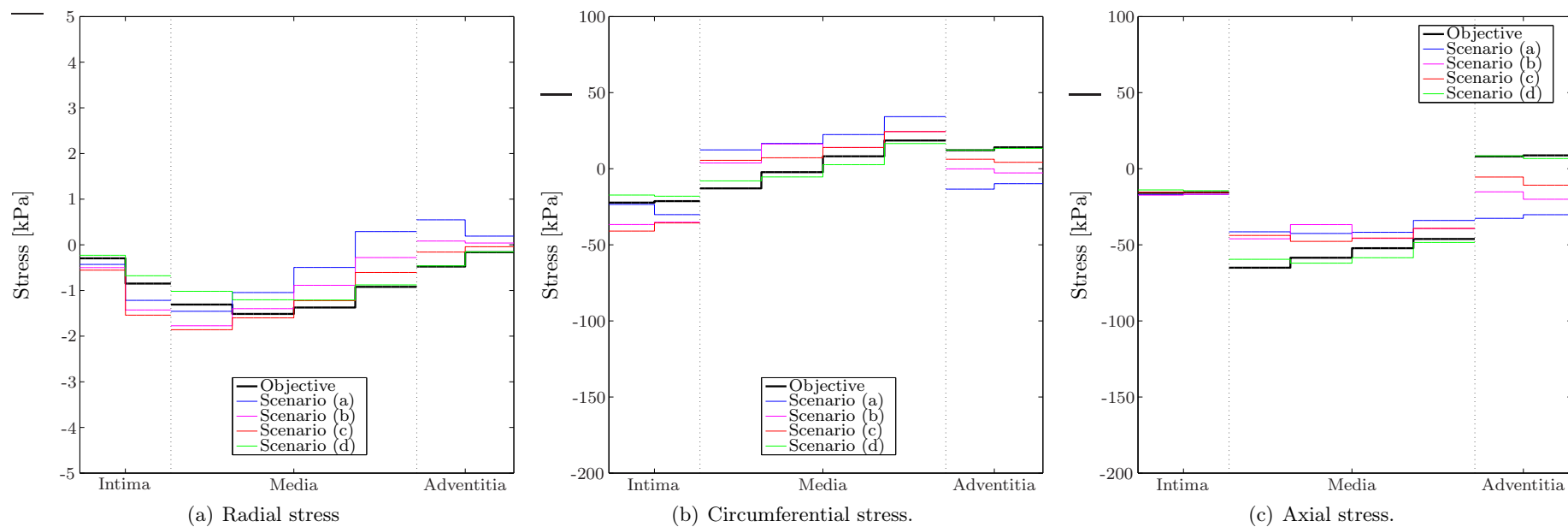


Figure 6.16: Three-layered wall example: results for the eight finite elements approximation. Residual stresses arising from the residual deformation field obtained as result of the optimization process for the four proposed scenarios, compared with the RSs associated to the IPA of the RRDs.

6.5 Discussion

As described in Chapter 5, a novel variational framework was proposed for the in-vivo characterization of RRDs in arterial walls. In this process, the load-free configuration of that vessel is also obtained. The proposed approach relies on a cost functional which measures the mechanical imbalance caused by an inconsistent RRD field. Then, the RRDs characterization problem is transformed into the minimization problem of such functional.

The examples shown in this work highlight the suitability and consistency of this novel approach, evidencing that the minimization of the proposed functional successfully leads to the characterization of RRDs, obtaining excellent results for the three explored cases. Moreover, in the first simple example, the sensitivity analysis detailed in Section 5.5 has also been validated. We emphasize that this methodology has proven to be able to identify the objective fields inspired by experimental ex-vivo measures on real human arterial vessels with great accuracy. This is encouraging, since these results suggest that the present method (or variants based on the present ideas), when coupled with adequate image acquisition techniques, could successfully result in the in-vivo identification of RRDs.

Observe that the proposed methodology could also be applicable to the estimation of constitutive parameters. While such questions has been increasingly addressed in the literature (Wittek et al, 2013; Bertagna et al, 2014) in the last years (using, however, completely different approaches), the lack of contributions regarding the estimation of RRDs motivated the subject of the present work.

As a matter of fact, although the proof-of-concept examples discussed are problems with rotational symmetry, it is important to remark that the presented framework has been developed in 3D space with no additional kinematic simplifications whatsoever. This also constitutes a fundamental characteristic for its subsequent application in patient-specific settings. On the one hand, this is noteworthy, because the proposed mechanical formulation proved to be effective towards the formalization of the RRD identification problem. This constitutes a step forward towards the development of truly realistic patient specific models. On the other hand, it is also true that the proposed formulation requires a large amount of input data for the successful identification of RRD. Nowadays, this could be viewed as restrictive or excessively demanding. However, cutting-edge advances in medical image acquisition systems together with interpolation techniques, which enable to limit the number of unknown parameters as the number of finite elements is increased, will definitely mitigate, and ultimately overcome, this limitation.

It is also important to note that the presented functional depends on weighting factors η_m and η_b^j , $j = 1, \dots, N_B$. The criteria for the definition of such parameters requires further analysis and is matter of future research. The values for these parameters are problem dependent and must account for the “quality” of the reconstruction of the related domains and displacement fields as well as for the impact of the different levels of stresses and external loads involved in the equilibrium of each known configuration.

As a final remark, we state that it is not within the scope of this work the development of novel optimization techniques for the minimization of the presented cost functional. In this thesis the use of the optimization methods is limited to the finding of adequate solutions for the listed set of problems.

Chapter 7

Conclusion

7.1 Integrative modeling framework

In this thesis, a variational framework for the analysis of the mechanical equilibrium of arterial wall tissues and its interaction with the blood flow was presented and tested. Within this framework, the *forward* and *preload* mechanical problems were formulated, emphasizing that the equilibrium equations are identical and the difference between them only relies on the known data. That is, for the forward and preload problems, it is assumed that the material and the spatial configurations are respectively given. The definition of such preload problem is necessary to realistically assess the mechanical regime of the arterial wall. This is due to the fact that the geometrical information provided by image acquisition devices corresponds to a loaded state of the vessel. Thence, solving this preload problem allows us to obtain the material configuration of the arterial structure, where the constitutive equations can effectively be defined. It is also worthwhile to mention that consistent linearizations and numerical implementations were provided for both mechanical problems. In this context, the influence of the preload pressure and the tethering forces acting on the artificial boundaries of the arterial segments was studied, concluding that taking any simplifying approach that overlooks the complete load state acting on the wall leads to an unrealistic quantification of the in-vivo stresses in the tissue.

The constitutive modeling considered in this thesis accounts for the complex composition of the arterial wall tissue, where the behavior of each layer is represented as a hyperelastic composite material. In the strain energy function characterizing the hyperelastic material, the elastin matrix is taken into account through a Neo-Hookean isotropic contribution, and the collagen fibers are considered by means of an anisotropic contribution acting in two given directions. Moreover, the forces exerted by the bodies surrounding the arterial wall as well as the interaction with the blood flow dynamics are considered in the evaluation of the mechanical regime of the solid.

The blood flow dynamics is modeled using the *Arbitrary Lagrangean Eulerian* formulation for the Navier-Stokes equations in the specific arterial vessel of interest, which, furthermore, is coupled with a dimensionally reduced model that provides the interaction with the cardiovascular system. It has been shown in the featured examples that it is possible to use simplifying hypotheses if the analysis is limited to the study of blood flow dynamics. Although the influence of the preload pressure can not be neglected, a low sensitivity of the blood flow dynamics with respect to the presence of tethering forces was reported.

As a contribution of this thesis, we emphasize that the integration of these modeling ingredients had not had precedents in the specialized literature. Furthermore, the comprehensive approach described in this work proved to be crucial (i) to understand the interaction between the different components involved in the physical phenomena and their

influence in arterial function, (ii) to accurately quantify the impact of different modeling hypotheses, and (iii) to provide a realistic hemodynamic environment for the simulation and analysis of adaptive processes in the cardiovascular system.

7.2 Characterization of residual deformations

A variational framework was proposed for the in-vivo characterization of residual deformations in arterial walls. As input data, the present approach requires a set of known arterial configurations, the load setting corresponding to each of those configurations, and the displacement field relating material points between them. This information can be retrieved from image acquisition and processing techniques paired with motion tracking tools. It is worthwhile to mention that the sensitivity of the methodology with respect to the precision and accuracy of the input data is still uncertain and constitutes a matter of future research. The variational formulation of the mechanical equilibrium related to the given configurations leads to the definition of a cost functional that measures the mechanical imbalance of such configurations when inconsistent residual deformations are assumed. In this approach, the cost functional is constructed using the generalized residuals of the corresponding set of variational equations.

Several examples using synthetic data were presented, where the viability of the present approach was studied and discussed in detail, concluding that the minimization of the cost functional successfully leads to the characterization of residual deformations. The results are encouraging, and suggest that the methodology could lead to the successful in-vivo identification of residual deformations.

It is important to bring attention to the fact that there are no previous works that targeted the in-vivo characterization of residual stresses and/or deformations. Furthermore, the presented approach can potentially be extended to simultaneously estimate constitutive parameters, thus, performing a fundamental step towards truly patient-specific simulations.

7.3 Future work

Let us now discuss some future work and open problems related to the topics addressed in this thesis.

Considering the capabilities of the integrative modeling framework, the tools already available can be used to gain insight into specific topics in patient-specific computational hemodynamics. Also, through the incorporation of damage, growth and remodeling models, the realistic environment provided by the proposed framework will definitely be increased, leading to a better understanding of such adaptive processes in a physiologically-consistent mechanical environment. Moreover, aligned with the objective of developing each time more realistic hemodynamic simulations, this framework could be enriched by the addition of further details, such as the incorporation of more complex constitutive models which may account for the active component smooth muscle cells.

Although promising results were shown for the proposed methodology for the in-vivo characterization of residual deformations, there is yet a great deal of work to be done for its application in real patient-specific scenarios. In this line, the next steps should include:

- (i) an analysis of different approximation techniques for the residual deformation field in the characterization problem,
- (ii) a sensitivity analysis with respect to the uncertainty of the input data,
- (iii) an evaluation of alternative cost functionals or the incorporation of regularizing terms to improve conditioning,

- (iv) an examination of different optimization techniques for the minimization procedure, and
- (v) the extension of the theoretical basis to include the simultaneous estimation of constitutive parameters.

Chapter 8

Appendices

8.1 Appendix A: basic relations in continuum mechanics

Consider a displacement field \mathbf{u}_m which is perturbed producing $\mathbf{u}_{m,\tau} = \mathbf{u}_m + \tau \delta \mathbf{u}_m$. With this perturbation we have the deformation gradient, originally given by $\mathbf{F}_m = \mathbf{I} + \nabla_m \mathbf{u}_m$, results in $\mathbf{F}_{m,\tau} = \mathbf{I} + \nabla_m \mathbf{u}_{m,\tau} = \mathbf{I} + \nabla_m (\mathbf{u}_m + \tau \delta \mathbf{u}_m)$. Let us compute the expressions of the derivatives of several quantities involving $\mathbf{F}_{m,\tau}$, with respect to τ . This will be employed in the linearization procedures whenever the material configuration is known. Then, we have

$$\left. \frac{d}{d\tau} \mathbf{F}_{m,\tau} \right|_{\tau=0} = \nabla_m \delta \mathbf{u}_m = (\nabla_s \delta \mathbf{u}_s)_m \mathbf{F}_m, \quad (8.1.1)$$

$$\left. \frac{d}{d\tau} \mathbf{F}_{m,\tau}^{-1} \right|_{\tau=0} = -\mathbf{F}_m^{-1} (\nabla_m \delta \mathbf{u}_m) \mathbf{F}_m^{-1} = -\mathbf{F}_m^{-1} (\nabla_s \delta \mathbf{u}_s)_m, \quad (8.1.2)$$

$$\left. \frac{d}{d\tau} \det \mathbf{F}_{m,\tau} \right|_{\tau=0} = \det \mathbf{F}_m (\mathbf{F}_m^{-T} \cdot \nabla_m \delta \mathbf{u}_m) = \det \mathbf{F}_m (\operatorname{div}_s \delta \mathbf{u}_s)_m, \quad (8.1.3)$$

$$\left. \frac{d}{d\tau} \mathbf{E}_{m,\tau} \right|_{\tau=0} = (\mathbf{F}_m^T (\nabla_m \delta \mathbf{u}_m))^S = \mathbf{F}_m^T (\nabla_s \delta \mathbf{u}_s)_m^S \mathbf{F}_m. \quad (8.1.4)$$

$$\begin{aligned} \left. \frac{d}{d\tau} |\mathbf{F}_{m,\tau}^{-T} \mathbf{n}_0| \right|_{\tau=0} &= \left. \frac{d}{d\tau} \sqrt{\mathbf{F}_{m,\tau}^{-T} \mathbf{n}_0 \cdot \mathbf{F}_{m,\tau}^{-T} \mathbf{n}_0} \right|_{\tau=0} \\ &= \frac{1}{|\mathbf{F}_{m,\tau}^{-T} \mathbf{n}_0|} \left(-\mathbf{F}_m^{-T} (\nabla_m \delta \mathbf{u}_m)^T \mathbf{F}_m^{-T} \right) \mathbf{n}_0 \cdot \mathbf{F}_m^{-T} \mathbf{n}_0 \\ &= - \left[(\nabla_s \delta \mathbf{u}_s)^T \mathbf{n}_s \cdot \mathbf{n}_s \right]_m |\mathbf{F}_{m,\tau}^{-T} \mathbf{n}_0| \end{aligned} \quad (8.1.5)$$

$$\begin{aligned} \left. \frac{d}{d\tau} |\mathbf{F}_{m,\tau}^{-T} \mathbf{n}_0|^{-1} \right|_{\tau=0} &= -|\mathbf{F}_{m,\tau}^{-T} \mathbf{n}_0|^{-3} \left(-\mathbf{F}_m^{-T} (\nabla_m \delta \mathbf{u}_m)^T \mathbf{F}_m^{-T} \right) \mathbf{n}_0 \cdot \mathbf{F}_m^{-T} \mathbf{n}_0 \\ &= |\mathbf{F}_{m,\tau}^{-T} \mathbf{n}_0|^{-1} (\nabla_s \delta \mathbf{u}_s)_m^T (\mathbf{n}_s)_m \cdot (\mathbf{n}_s)_m \end{aligned} \quad (8.1.6)$$

$$\begin{aligned}
\left. \frac{d}{d\tau} \frac{\mathbf{F}_{m,\tau}^{-T} \mathbf{n}_0}{|\mathbf{F}_{m,\tau}^{-T} \mathbf{n}_0|} \right|_{\tau=0} &= -(\nabla_s \delta \mathbf{u}_s)_m^T \frac{\mathbf{F}_m^{-T} \mathbf{n}_0}{|\mathbf{F}_{m,\tau}^{-T} \mathbf{n}_0|} \\
&+ \frac{\mathbf{F}_m^{-T} \mathbf{n}_0}{|\mathbf{F}_{m,\tau}^{-T} \mathbf{n}_0|^2} \frac{(\nabla_s \delta \mathbf{u}_s)_m \mathbf{F}_m^{-T} \mathbf{n}_0 \cdot \mathbf{F}_m^{-T} \mathbf{n}_0}{|\mathbf{F}_{m,\tau}^{-T} \mathbf{n}_0|} \\
&= - \left[(\nabla_s \delta \mathbf{u}_s)^T \mathbf{n}_s \right]_m + \left[\left[(\nabla_s \delta \mathbf{u}_s)^T \mathbf{n}_s \cdot \mathbf{n}_s \right] \mathbf{n}_s \right]_m \\
&= \left\{ \left[-(\nabla_s \delta \mathbf{u}_s)^T + \left((\nabla_s \delta \mathbf{u}_s)^T \mathbf{n}_s \cdot \mathbf{n}_s \right) \mathbf{I} \right] \mathbf{n}_s \right\}_m \quad (8.1.7)
\end{aligned}$$

Now, consider the displacement field \mathbf{u}_s which is perturbed producing $\mathbf{u}_{s,\tau} = \mathbf{u}_s + \tau \delta \mathbf{u}_s$. Then $\mathbf{F}_s^{-1} = \mathbf{I} - \nabla_s \mathbf{u}_s$ results in $\mathbf{F}_{s,\tau}^{-1} = \mathbf{I} - \nabla_s \mathbf{u}_{s,\tau} = \mathbf{I} - \nabla_s (\mathbf{u}_s + \tau \delta \mathbf{u}_s)$. The derivatives of several quantities involving $\mathbf{F}_{s,\tau}$ with respect to τ are

$$\left. \frac{d}{d\tau} \mathbf{F}_{s,\tau}^{-1} \right|_{\tau=0} = -\nabla_s \delta \mathbf{u}_s, \quad (8.1.8)$$

$$\left. \frac{d}{d\tau} \mathbf{F}_{s,\tau} \right|_{\tau=0} = \mathbf{F}_s (\nabla_s \delta \mathbf{u}_s) \mathbf{F}_s, \quad (8.1.9)$$

$$\left. \frac{d}{d\tau} \det \mathbf{F}_{s,\tau} \right|_{\tau=0} = \det \mathbf{F}_s (\mathbf{F}_s^T \cdot \nabla_s \delta \mathbf{u}_s), \quad (8.1.10)$$

$$\left. \frac{d}{d\tau} \mathbf{E}_{s,\tau} \right|_{\tau=0} = \mathbf{F}_s^T (\mathbf{F}_s (\nabla_s \delta \mathbf{u}_s))^S \mathbf{F}_s. \quad (8.1.11)$$

Bibliography

- Alastrué V, Rodríguez J, Calvo B, Doblaré M (2007) Structural damage models for fibrous biological soft tissues. *International Journal of Solids and Structures* 44(18-19):5894–5911
- Ambrosi D, Mollica F (2002) On the mechanics of a growing tumor. *International Journal of Engineering Science* 40(12):1297–1316
- Antiga L, Piccinelli M, Botti L, Ene-Iordache B, Remuzzi A, Steinman DA (2008) An image-based modeling framework for patient-specific computational hemodynamics. *Medical & Biological Engineering & Computing* 46(11):1097–1112
- Avolio A (1980) Multi-branched model of the human arterial system. *Medical & Biological Engineering & Computing* 18:709–718
- Baek S, Rajagopal K, Humphrey J (2005) Competition between radial expansion and thickening in the enlargement of an intracranial saccular aneurysm. *Journal of Elasticity* 80(1-3):13–31
- Balzani D, Brinkhues S, Holzapfel GA (2012) Constitutive framework for the modeling of damage in collagenous soft tissues with application to arterial walls. *Computer Methods in Applied Mechanics and Engineering* 213-216:139–151
- Bellini C, Ferruzzi J, Roccabianca S, Di Martino E, Humphrey J (2014) A microstructurally motivated model of arterial wall mechanics with mechanobiological implications. *Annals of Biomedical Engineering* 42(3):488–502
- Bertagna L, D’Elia M, Perego M, Veneziani A (2014) Fluid-Structure Interaction and Biomedical Applications, Springer Basel, Basel, chap Data Assimilation in Cardiovascular Fluid–Structure Interaction Problems: An Introduction, pp 395–481
- Bharadvaj B, Mabon R, Giddens D (1982) Steady flow in a model of the human carotid bifurcation. Part I - flow visualization. *Journal of biomechanics* 15(5)
- Blanco PJ, Feijóo RA (2013) A dimensionally-heterogeneous closed-loop model for the cardiovascular system and its applications. *Medical Physics and Engineering* 35:652–667
- Blanco PJ, Feijóo RA, Urquiza SA (2007) A unified variational approach for coupling 3d-1d models and its blood flow applications. *Computer Methods in Applied Mechanics and Engineering* (41-44):4391–4410
- Blanco PJ, Pivello MR, Urquiza SA, Feijóo RA (2009) On the potentialities of 3d-1d coupled models in hemodynamics simulations. *Journal of Biomechanics* 42(7):919–930
- Blanco PJ, Urquiza SA, Feijóo RA (2010) Assessing the influence of heart rate in local hemodynamics through coupled 3d-1d-0d models. *International Journal for Numerical Methods in Biomedical Engineering* 26:890–903.

- Blanco PJ, Deparis S, Malossi ACI (2013a) On the continuity of mean total normal stress in geometrical multiscale cardiovascular problems. *Journal of Computational Physics* 251:136–155
- Blanco PJ, Leiva JS, Buscaglia GC (2013b) A black-box decomposition approach for coupling heterogeneous components in hemodynamics simulations. *International Journal for Numerical Methods in Biomedical Engineering* .:408–27
- Blanco PJ, Watanabe S, Passos MARF, Feijóo RA (2014a) An anatomically detailed arterial network model for one-dimensional computational hemodynamics. *IEEE transactions on bio-medical engineering* 9294(c):1–18
- Blanco PJ, Watanabe SM, Dari EA, Passos MARF, Feijóo RA (2014b) Blood flow distribution in an anatomically detailed arterial network model: criteria and algorithms. *Biomechanics and modeling in mechanobiology* 13(6):1303–30
- Blanco PJ, Ares GD, Urquiza SA, Feijóo RA (2015) On the effect of preload and pre-stretch on hemodynamic simulations: an integrative approach. *Biomechanics and Modeling in Mechanobiology* DOI 10.1007/s10237-015-0712-y
- Blum J, Le Dimet FX, Navon IM (2009) Data Assimilation for Geophysical Fluids. *Handbook of Numerical Analysis* 14(08):385–441
- Byrd RH, Hribar ME, Nocedal J (1999) An Interior Point Algorithm for Large-Scale Nonlinear Programming. *SIAM Journal on Optimization* 9:877–900
- Byrd RH, Gilbert JC, Nocedal J (2000) A trust region method based on interior point techniques for nonlinear programming. *Mathematical Programming* 89(1):149
- Cao Y, Miller MI, Winslow RL, Younes L (2005) Large deformation diffeomorphic metric mapping of vector fields. *IEEE transactions on medical imaging* 24(9):1216–30
- Castro MA, Putman CM, Cebal JR (2011) Computational analysis of anterior communicating artery aneurysm shear stress before and after aneurysm formation. *Journal of Physics: Conference Series* 332(1):012,001
- Cebal MA J R Castro, Appanaboyina S, Putman CM, Millan D, Frangi AF (2005) Efficient pipeline for image-based patient-specific analysis of cerebral aneurysm hemodynamics: Technique and sensitivity. *IEEE Trans Med Imaging*
- Cowin SC (2004) Tissue growth and remodeling. *Annual review of biomedical engineering* 6:77–107
- Crosetto P, Reymond P, Deparis S, Kontaxakis D, Stergiopoulos N, Quarteroni A (2011) Fluid-structure interaction simulation of aortic blood flow. *Computers & Fluids* 43(1):46–57
- Cyron CJ, Humphrey JD (2014) Vascular homeostasis and the concept of mechanobiological stability. *International journal of engineering science* 85:203–223
- Delfino A, Stergiopoulos N, Moore J, Meister JJ (1997) Residual strain effects on the stress field in a thick wall finite element model of the human carotid bifurcation. *J Biomech* 30:777–786.
- D’Elia M, Mirabella L, Passeri T, Perego M, Piccinelli M, Vergara C, Veneziani A (2012) *Modelling of Physiological Flows*, Springer-Verlag Italia, chap Application of variational data assimilation in computational hemodynamics.

- Dempere-Marco L, Oubel E, Castro M, Putman C, Frangi A, Cebral J (2006) Cfd analysis incorporating the influence of wall motion: application to intracranial aneurysms. *Medical Image Computing and Computer-Assisted Intervention - MICCAI 2006* pp 438–445
- Deparis S, Fernandez M, Formaggia L, Nobile F (2003) Acceleration of a fixed point algorithm for fluid structure interaction using transpiration conditions. In: Bathe KJ (ed) *Computational Fluid and Solid Mechanics 2003*, Elsevier Science Ltd, Oxford, pp 1307 – 1311
- Deparis S, Discacciati M, Fourestey G, Quarteroni A (2006) Fluid-structure algorithms based on steklov-poincaré operators. *Computer Methods in Applied Mechanics and Engineering* 195(41-43):5797–812
- Destrade M, Liu Y, Murphy J, Kassab G (2012) Uniform transmural strain in pre-stressed arteries occurs at physiological pressure. *J Theor Biol*
- DN Arnorld MF F Brezzi (1984) A stable finite element for the Stokes equations. *Calcolo* 21:337–344
- Donea J, Huerta A (2003) *Finite Element Methods for Flow Problems*. John Wiley & Sons, Ltd., Chichester, UK
- Driessen N, Wilson W, Bouten C, Baaijens F (2004) A computational model for collagen fibre remodelling in the arterial wall. *Journal of Theoretical Biology* 226(1):53–64
- Feng B, Li By, Nauman Ea, Schild JH (2007) Theoretical and electrophysiological evidence for axial loading about aortic baroreceptor nerve terminals in rats. *American journal of physiology Heart and circulatory physiology* 293(6):H3659–72
- Ferruzzi J, Bersi M, Uman S, Yanagisawa H, Humphrey J (2015) Decreased elastic energy storage, not increased material stiffness, characterizes central artery dysfunction in fibulin-5 deficiency independent of sex. *J Biomech Eng*
- Fischer C, Rossman JS (2009) Effect of non-newtonian behavior on hemodynamics of cerebral aneurysms. *J Biomech Eng*
- Fletcher R (1987) *Practical Methods of Optimization*, Second Edition. Wiley-Interscience, New York, NY, USA
- Formaggia L, Nobile F, Quarteroni A, Veneziani A (1999) Multiscale modelling of the circulatory system: a preliminary analysis. *Computing and visualization in science* 2(2-3):75–83
- Formaggia L, Gerbeau J, Nobile F, Quarteroni A (2001) On the coupling of 3d and 1d navier-stokes equations for flow problems in compliant vessels. *Computer Methods in Applied Mechanics and Engineering* 191:561–582
- Formaggia L, Lamponi D, Quarteroni A (2003) One-dimensional models for blood flow in arteries. *Journal of Engineering Mathematics* 47(3-4):251–276
- Formaggia L, Lamponi D, Tuveri M, Veneziani A (2006) Numerical modeling of 1D arterial networks coupled with a lumped parameters description of the heart. *Computer methods in biomechanics and biomedical engineering* 9(5):273–288
- Fung YC (1991) What are the residual stresses doing in our blood vessels? *Annals of Biomedical Engineering* 19:237–249

- Fung YC (1993) *Biomechanics: Motion, Flow, Stress, and Growth*, vol 60. Springer-Verlag New York, Inc.
- Fung YC, Liu SQ (1989) Change of residual strains in arteries due to hypertrophy caused by aortic constriction. *Circulation research* 65:1340–1349
- Gasser TC, Ogden RW, Holzapfel GA (2006) Hyperelastic modelling of arterial layers with distributed collagen fibre orientations. *Journal of The Royal Society Interface* 3(6):15–35
- Gee M, Reeps C, Eckstein H, Wall W (2009) Prestressing in finite deformation abdominal aortic aneurysm simulation. *Journal of Biomechanics* 42:1732–1739
- Gee MW, Forster C, Wall WA (2010) A computational strategy for prestressing patient-specific biomechanical problems under finite deformation. *International Journal for Numerical Methods in Biomedical Engineering* 26(1):52–72
- Germain P (1973) The Method of Virtual Power in Continuum Mechanics. Part 2: Microstructure. *SIAM Journal on Applied Mathematics* 25(November):556–575
- Ghil M, Malanotte-Rizzoli P (1991) Data Assimilation in Meteorology and Oceanography. *Advances in Geophysics* 33:141–266
- Gill PE, Murray W, Wright MH (1981) *Practical optimization*. Academic Press, London
- Govindjee S, Mihalic PA (1996) Computational methods for inverse finite elastostatics. *Computer Methods in Applied Mechanics and Engineering* 136(1-2):47 – 57
- Govindjee S, Mihalic PA (1998) Computational methods for inverse deformations in quasi-incompressible finite elasticity. *International Journal for Numerical Methods in Engineering* 43(5):821–838
- Grinberg L, Karniadakis GE (2008) Outflow boundary conditions for arterial networks with multiple outlets. *Annals of Biomedical Engineering* 36(9):1496–1514
- Gundiah N, B Ratcliffe M, A Pruitt L (2007) Determination of strain energy function for arterial elastin: Experiments using histology and mechanical tests. *Journal of Biomechanics* 40(3):586–594
- Hariton I, DeBotton G, Gasser TC, Holzapfel GA (2007) Stress-driven collagen fiber remodeling in arterial walls. *Biomechanics and Modeling in Mechanobiology* 6:163–175
- Heidenreich PA, Trogdon JG, Khavjou OA, Butler J, Dracup K, Ezekowitz M, Finkelstein EA, Hong Y, Johnston ALJD S Cand Khera, Lloyd-Jones D, Nelson SA, Nichol G, Orenstein D, Wilson PW, Woo YJ (2011) Forecasting the future of cardiovascular disease in the united states: A policy statement from the american heart association. *Circulation* 123(8):933–944
- Hernández-Sabaté A, Gil D, Garcia-Barnés J, Martí E (2011) Image-based cardiac phase retrieval in intravascular ultrasound sequences. *IEEE transactions on ultrasonics, ferroelectrics, and frequency control* 58(1):60–72
- Hill MR, Duan X, Gibson GA, Watkins S, Robertson AM (2012) A theoretical and non-destructive experimental approach for direct inclusion of measured collagen orientation and recruitment into mechanical models of the artery wall. *Journal of Biomechanics* 45(5):762–771
- Holzapfel GA, Gasser TC (2000) A new constitutive framework for arterial wall mechanics and a comparative study of material models. *J Elast* 61:1–48

- Holzappel GA, Ogden R (2010a) Constitutive modelling of arteries. *Proceedings of the Royal Society A: Mathematical, Physical and Engineering Science* 466(2118):1551–1597
- Holzappel GA, Ogden RW (2010b) Modelling the layer-specific three-dimensional residual stresses in arteries, with an application to the human aorta. *Journal of The Royal Society Interface* 7(46):787–799
- Holzappel GA, Sommer G, Auer M, Regitnig P, Ogden RW (2007) Layer-specific 3D residual deformations of human aortas with non-atherosclerotic intimal thickening. *Annals of biomedical engineering* 35(4):530–45
- Honda Y, Fitzgerald PJ (2008) Frontiers in intravascular imaging technologies. *Circulation* 117(15):2024–37
- Hsu M, Bazilevs Y (2011) Blood vessel tissue prestress modeling for vascular fluid-structure interaction simulation. *Finite Elements in Analysis and Design* 47(6):593 – 599
- Hughes TJR (1987) *The Finite Element Method: Linear Static and Dynamic Finite Element Analysis*. Prentice-Hall, Inc.
- Hughes TJR, Lubliner J (1973) On the one-dimensional theory of blood flow in the larger vessels. *Math Biosci* 18:161–170.
- Hughes TJR, Liu WK, Zimmermann TK (1981) Lagrangian-eulerian finite element formulation for incompressible viscous flows. *Computational Methods in Applied Mechanics and Engineering* 29:329–349
- Hughes TJR, Franca LP, Mallet M (1987) computational fluid dynamics: VI. Convergence analysis of the generalized SUPG formulation for linear time-dependent multidimensional advective-diffusive systems. *Computer Methods in Applied Mechanics and Engineering* 63(604912):97–112
- Humphrey JD (1999) Remodeling of a collagenous tissue at fixed lengths. *Journal of biomechanical engineering* 121:591–597
- Humphrey JD, Rajagopal KR (2002) A constrained mixture model for growth and remodeling of soft tissues
- Joosten MM, Dettmer WG, Perić D (2009) Analysis of the block gauss-seidel solution procedure for a strongly coupled model problem with reference to fluid-structure interaction. *International Journal for Numerical Methods in Engineering* 78(7):757–778
- Kim H, Figueroa C, Hughes T, Jansen K, Taylor C (2009a) Augmented lagrangian method for constraining the shape of velocity profiles at outlet boundaries for three-dimensional finite element simulations of blood flow. *Computer Methods in Applied Mechanics and Engineering* 198(45-46):3551–3566
- Kim HJ, Vignon-Clementel IE, Figueroa CA, LaDisa JF, Jansen KE, Feinstein JA, Taylor CA (2009b) On coupling a lumped parameter heart model and a three-dimensional finite element aorta model. *Annals of Biomedical Engineering* 37(11):2153–2169
- Kirchner H, Niemann H (1992) Finite element method for determination of optical flow. *Pattern Recognition Letters* 13:131–141
- Kivity Y, Collins R (1974) Nonlinear wave propagation in viscoelastic tubes: application to aortic rupture. *Journal of biomechanics* 7(1):67–76

- Korakianitis T, Shi Y (2006) Numerical simulation of cardiovascular dynamics with healthy and diseased heart valves. *Journal of Biomechanics* 39:1964–1982
- Lewis M, Kerckhoffs R (2010) Current progress in patient-specific modeling. *Brief Bioinform* 11(1):111–126
- Li D, Robertson AM (2009) A structural multi-mechanism damage model for cerebral arterial tissue. *Journal of biomechanical engineering* 131(10):101,013
- Liang F, Takagi S, Himeno R, Liu H (2009) Multi-scale modeling of the human cardiovascular system with applications to aortic valvular and arterial stenoses. *Medical & Biological Engineering & Computing* 47:743–755
- Löhner R (2008) *Applied Computational Fluid Dynamics Techniques: An Introduction Based on Finite Element Methods*, John Wiley & Sons, Ltd, pp 227–243
- Lu J, Zhou X, Raghavan ML (2007) Inverse elastostatic stress analysis in pre-deformed biological structures: Demonstration using abdominal aortic aneurysms. *Journal of Biomechanics* 40(40):693–696
- Lu J, Zhou X, Raghavan M (2008) Inverse method of stress analysis for cerebral aneurysms. *Biomechanics and Modeling in Mechanobiology* 7(6):477–486
- Malossi ACI, Blanco PJ, Crosetto P, Deparis S, Quarteroni A (2013) Implicit coupling of one-dimensional and three-dimensional blood flow models with compliant vessels. *Multiscale Modeling & Simulation* 11(2):474–506
- Maso Talou G, Larrabide I, Blanco P, Guedes Bezerra C, Lemos P, Feijoo R (2015) Improving cardiac phase extraction in ivus studies by integration of gating methods. *Biomedical Engineering, IEEE Transactions on* 62(12):2867–2877
- Matthys KS, Alastruey J, Peiró J, Khir AW, Segers P, Verdonck PR, Parker KH, Sherwin SJ (2007) Pulse wave propagation in a model human arterial network: assessment of 1-D numerical simulations against in vitro measurements. *Journal of Biomechanics* 40(15):3476–3486
- Mendis S, Puska P, B N (2011) *Global Atlas on Cardiovascular Disease Prevention and Control*, World Health Organization, chap 1, p 155
- Migliavacca F, Balossino R, Pennati G, Dubini G, Hsia TY, de Leval MR, Bove EL (2006) Multiscale modelling in biofluidynamics: Application to reconstructive paediatric cardiac surgery. *Journal of Biomechanics* 39(6):1010–1020
- Mintz GS, Nissen SE, Anderson WD, Bailey SR, Erbel R, Fitzgerald PJ, Pinto FJ, Rosenfield K, Siegel RJ, Tuzcu E, Yock PG, O’Rourke RA, Abrams J, Bates ER, Brodie BR, Douglas PS, Gregoratos G, Hlatky MA, Hochman JS, Kaul S, Tracy CM, Waters DD, Winters WL Jr (2001) American college of cardiology clinical expert consensus document on standards for acquisition, measurement and reporting of intravascular ultrasound studies (ivus) 33a report of the american college of cardiology task force on clinical expert consensus documents developed in collaboration with the european society of cardiology endorsed by the society of cardiac angiography and interventions. *Journal of the American College of Cardiology* 37(5):1478–1492
- Moireau P, Xiao N, Astorino M, Figueroa C, Chapelle D, Taylor CA, Gerbeau JF (2012) External tissue support and fluid - structure simulation in blood flows. *Biomechanics and modeling in mechanobiology*

- Morales HG, Larrabide I, Geers AJ, Aguilar ML, Frangi AF (2013) Newtonian and non-newtonian blood flow in coiled cerebral aneurysms. *J Biomech*
- Orth RC, Wallace MJ, Kuo MD (2009) C-arm Cone-beam CT: General Principles and Technical Considerations for Use in Interventional Radiology. *Journal of Vascular and Interventional Radiology* 20(7):S538–S544
- Pierce DM, Fastl TE, Rodriguez-Vila B, Verbrugghe P, Fourneau I, Maleux G, Herijgers P, Gomez EJ, Holzapfel GA (2015) A method for incorporating three-dimensional residual stretches/stresses into patient-specific finite element simulations of arteries. *Journal of the Mechanical Behavior of Biomedical Materials* 47:147–164
- Quarteroni A, Veneziani A, Zunino P (2001) Mathematical and numerical modeling of solute dynamics in blood flow and arterial walls. *SIAM Journal on Numerical Analysis* 39(5):1488–1511 (electronic)
- Rausch MK, Kuhl E (2013) On the effect of prestrain and residual stress in thin biological membranes. *Journal of the Mechanics and Physics of Solids* 61(9):1955–1969
- Reymond P, Crosetto P, Deparis S, Quarteroni A, Stergiopoulos N (2013) Physiological simulation of blood flow in the aorta: Comparison of hemodynamic indices as predicted by 3-d FSI, 3-d rigid wall and 1-d models. *Medical Engineering & Physics* 35(6):784–791
- Robertson AM, Sequeira A, Kameneva MV (2008) Hemodynamical Flows: Modeling, Analysis and Simulation, Birkh{ä}user Basel, chap Hemorheology, pp 63–120
- Rodriguez EK, Hoger A, McCulloch AD (1994) Stress-dependent finite growth in soft elastic tissues. *Journal of Biomechanics* 27:455–467
- van Rooij WJ, Sprengers ME, de Gast AN, Peluso JPP, Sluzewski M (2008) 3D rotational angiography: the new gold standard in the detection of additional intracranial aneurysms. *AJNR American journal of neuroradiology* 29(5):976–9
- Southern J, Pitt-Francis J, Whiteley J, Stokeley D, Kobashi H, Nobes R, Kadooka Y, DGavaghan (2008) Multi-scale computational modelling in biology and physiology. *Progress in Biophysics and Molecular Biology* 96(1-3):60 – 89
- Steinman DA, Thomas JB, Ladak HM, Milner JS, Rutt BK, Spence JD (2002) Reconstruction of carotid bifurcation hemodynamics and wall thickness using computational fluid dynamics and mri. *Magnetic Resonance in Medicine* 47(1):149–159
- Stergiopoulos N, Young D, Rogge T (1992) Computer simulation of arterial flow with applications to arterial and aortic stenoses. *Journal of Biomechanics* 25:1477–1488
- Taber La, Humphrey JD (2001) Stress-modulated growth, residual stress, and vascular heterogeneity. *Journal of Biomechanical Engineering* 123(6):528–535
- Takamizawa K, Hayashi K (1987) Strain energy density function and uniform strain hypothesis for arterial mechanics. *Journal of Biomechanics* 20(1):7–17
- Taylor C, Hughes T, Zarins C (1998) Finite element blood flow modeling in arteries. *Computer Methods in Applied Mechanics and Engineering* 158:155–196
- Tezduyar TE, Takizawa K, Moorman C, Wright S, Christopher J (2010) Multiscale sequentially-coupled arterial FSI technique. *Computational Mechanics* 46(1):17–29
- The MathWorks I (2013) Matlab optimization toolbox r2013b

- Torii R, Oshima M, Kobayashi T, Takagi K, Tezduyar TE (2006) Computer modeling of cardiovascular fluid-structure interactions with the deforming-spatial-domain/stabilized space-time formulation. *Computer Methods in Applied Mechanics and Engineering* 195(13-16):1885–1895
- Torii R, Oshima M, Kobayashi T, Takagi K, Tezduyar TE (2008) Fluid-structure interaction modeling of a patient-specific cerebral aneurysm: influence of structural modeling. *Computational Mechanics* 43(1):151–159
- Čanić S, Tambača J, Guidoboni G, Mikič A, Hartley CG, Rosenstrauch D (2006) Modeling viscoelastic behavior of arterial walls and their interaction with pulsatile blood flow. *SIAM J Appl Math*
- Urquiza SA, Blanco PJ, Vénere MJ, Feijóo RA (2006) Multidimensional modeling for the carotid blood flow. *Computer Methods in Applied Mechanics and Engineering* 195:4002–4017
- Valentín A, Humphrey JD (2009) Evaluation of fundamental hypotheses underlying constrained mixture models of arterial growth and remodelling. *Philosophical transactions Series A, Mathematical, physical, and engineering sciences* 367(1902):3585–3606
- Vavourakis V, Papaharilaou Y, Ekaterinaris J (2011) Coupled fluid-structure interaction hemodynamics in a zero-pressure state corrected arterial geometry. *Journal of Biomechanics* 44(13):2453–2460
- Vignon-Clementel IE, Alberto Figueroa C, Jansen KE, Taylor CA (2006) Outflow boundary conditions for three-dimensional finite element modeling of blood flow and pressure in arteries. *Computer Methods in Applied Mechanics and Engineering* 195(29-32):3776–3796
- Watanabe SM, Blanco PJ, Feijóo RA (2013) Mathematical model of blood flow in an anatomically detailed arterial network of the arm. *ESAIM: Mathematical Modelling and Numerical Analysis* 47:961–985
- Watton PN, Selimovic A, Raberger NB, Huang P, Holzapfel GA, Ventikos Y (2011) Modelling evolution and the evolving mechanical environment of saccular cerebral aneurysms. *Biomechanics and Modeling in Mechanobiology* 10(1):109–32
- Weisbecker H, Pierce DM, Regitnig P, Holzapfel Ga (2012) Layer-specific damage experiments and modeling of human thoracic and abdominal aortas with non-atherosclerotic intimal thickening. *Journal of the Mechanical Behavior of Biomedical Materials* 12:93–106
- Witte A, Karatolios K, Bihari P, Schmitz-Rixen T, Moosdorf R, Vogt S, Blase C (2013) In vivo determination of elastic properties of the human aorta based on 4D ultrasound data. *Journal of the Mechanical Behavior of Biomedical Materials* 27:167–183
- Wu Y, Cai XC (2014) A fully implicit domain decomposition based ALE framework for three-dimensional fluid-structure interaction with application in blood flow computation. *J Comput Phys* 258:524–537
- Zhou X, Raghavan ML, HarbRag RE, Lu J (2010) Patient-specific wall stress analysis in cerebral aneurysms using inverse shell model. *Ann Biomed Eng*
- Zienkiewicz OC, Taylor RL (1989) *The finite element method*, vol 1, 4th edn. McGraw-hill London

- Zulliger MA, Fridez P, Hayashi K, Stergiopoulos N (2004a) A strain energy function for arteries accounting for wall composition and structure. *Journal of Biomechanics* 37:989–1000
- Zulliger Ma, Rachev A, Stergiopoulos N (2004b) A constitutive formulation of arterial mechanics including vascular smooth muscle tone. *American journal of physiology Heart and circulatory physiology* 287(3):H1335–43